University of Alberta

Library Release Form

Name of Author: Ryan R. Chladny

Title of Thesis: Modeling and Control of Automotive Gas Exchange Valve Solenoid Actuators

Degree: Doctor of Philosophy

Year this Degree Granted: 2007

Ryan R. Chladny
7924 91 Ave
Edmonton, Alberta,
T6C 1R1, Canada

Submission Date

University of Alberta

Modeling and Control of Automotive Gas Exchange Valve Solenoid Actuators

by

Ryan R. Chladny

A thesis submitted to the Faculty of Graduate Studies and Research in partial fulfillment of the requirements for the degree of Doctor of Philosophy.

Department of Mechanical Engineering

Edmonton, Alberta

Fall 2007

University of Alberta

Faculty of Graduate Studies and Research

The undersigned certify that they have read, and recommend to the Faculty of Graduate Studies and Research for acceptance, a thesis entitled Modeling and Control of Automotive Gas Exchange Valve Solenoid Actuators submitted by Ryan R. Chladny in partial fulfillment of the requirements for the degree of Doctor of Philosophy.

Dr. C.R. (Bob) Koch

Dr. Jeff Pieper

Dr. Tongwen Chen

Dr. Alan Lynch

Dr. M. David Checkel

To my wife Melanie. Thank you for your continued love, understanding and countless personal sacrifices that you have made in order for me to further my education.

Abstract

A promising method for enhancing automotive internal combustion engine efficiency uses solenoid actuators to directly control the gas exchange valves. Mitigation of valve seating velocities is challenging due to phenomena such as magnetic saturation and combustion gas force disturbances. A comprehensive control strategy is presented for a hinged solenoid actuator. Gas forces on the exhaust valve are particularly problematic due to the potential for large cycle-to-cycle variations. Soft seating is achieved using a flatness-based landing algorithm with a nonlinear disturbance estimator. The estimator is used with an energy-based feedforward controller to reject exhaust gas force disturbances. Feedback is provided through the use of flux and current measurements and an accurate inductance model. Overviews of the employed modeling and simulation techniques and experimental testbench results are also presented. Both simulated and experimental results indicate the proposed control methodology is capable of compensating for the nonlinear magnetic dynamics and combustion gas force disturbances experienced by exhaust valve solenoid actuators.

Acknowledgements

I would like to take this opportunity to acknowledge the following individuals and organizations who helped me during the course of this work.

Dr. Koch for his willingness to help, patience and understanding throughout my career as a graduate student. Your positive attitude, contribution of time, insight and invaluable wealth of knowledge certainly made all of my challenges much easier to cope with as they arose.

Dr. Lynch and Thomas Grochmal for their controls expertise and advice.

Dr. Kostiuk and the Department of Mechanical Engineering for continued financial aid and genuine concern during my mountain bike accident recovery.

DaimlerChrysler AG for the generous donation of the solenoid actuators, schematics and single cylinder head.

No amount of thanks (or donuts) can repay technicians, Bernie Faulkner, Greg Miller and Rick Bubenko or machinists, Dirk Kelm, Albert Yeun and Dave Pape for their expert skills, advice and the countless occasions where they sacrificed time from their projects for my own.

Thanks are also deserved to Terry Nord and Bill Bizuk for their assistance and support with the various custom electronic devices that were accrued over the course of this work.

Thanks to my colleagues of room 4-28 for advice, support and otherwise keeping moral levels up.

Finally, I would like to thank my parents for their continued love and encouragement throughout all of my challenges, academic or otherwise.

Table of Contents

List of Tables

List of Figures

Nomenclature

Note that bold typeface denotes a vector or matrix quantity.

ADC ..... Analog to digital converter

α ..... Saturable flux linkage model parameter [A^{-1}]

A_t ..... Valve position dependent effective throat flow area [m^2]

A_v ..... Exhaust valve area [m^2]

$\boldsymbol{B}$ ..... Magnetic field flux density [T]

BDC ..... Bottom dead centre

b ..... Effective viscous damping coefficient [$\frac{\text{Ns}}{\text{m}}$]

$\hat{b}$ ..... Viscous damping coefficient associated with the armature [$\frac{\text{Nms}}{\text{rad}}$]

β ..... Flux linkage parameter [m/A]

b_v ..... Viscous damping coefficient associated with the valve [$\frac{\text{Ns}}{\text{m}}$]

$\boldsymbol{E}$ ..... Electric field [$\frac{\text{V}}{\text{m}^2}$]

C_d ..... Effective flow discharge coefficient

C_{gf} ..... Effective gas force flow coefficient

DAC ..... Digital to analog converter

ECU ..... Engine control unit

EMF ..... Electromotive force

ϵ_0 ..... Permittivity constant $= 8.85 \times 10^{-12} \frac{\mathrm{F}}{\mathrm{m}}$

EVO ..... Exhaust valve opening

FEA ..... Finite element analysis

FEM ..... Finite element method

$F_{m,c}$ ..... Magnetic closer force on the armature [N]

F_g ..... Gas force acting upon the valve [N]

F_{gs} ..... Simplified gas force [N]

$F_{m,o}$ ..... Magnetic opener force on the armature [N]

F_v ..... Valve spring pre-load [N]

f_1 ..... Normalized gas force disturbance simplification

f_2 ..... Rate of change of the normalized gas force disturbance simplification

γ ..... Initial gas force amplitude [N]

$\boldsymbol{H}$ ..... Magnetic field strength $[\frac{\mathrm{A}}{\mathrm{m}}]$

ICE ..... Internal combustion engine

IGBT ..... Insulated gate bipolar transistor

I_o ..... Armature and torsion bar moment of inertia about the pivot point [kgm^2]

i ..... Coil current [A]

$\boldsymbol{J}$ ..... Current density $[\frac{\mathrm{A}}{\mathrm{m}^2}]$

KVL ..... Kirchoff voltage law

k_1 ..... Linear error dynamics controller gain [1/s]

k_2 ..... Linear Error dynamics controller gain $[1/\mathrm{s}^2]$

k_3 ..... Linear Error dynamics controller gain $[1/\mathrm{s}^3]$

k ..... Effective spring constant $[\frac{\mathrm{N}}{\mathrm{m}}]$

$\hat{k}$ ..... Angular torsion bar spring constant $[\frac{\mathrm{Nm}}{\mathrm{rad}}]$

κ ..... Flux linkage parameter [m]

k_t ..... Specific heat ratio of the in-cylinder gas

k_v ..... Valve spring constant $[\frac{\mathrm{N}}{\mathrm{m}}]$

L ..... Inductance [H]

LHP ..... Left-hand plane

LPM ..... Lumped parameter model

LTI ..... Linear time invariant

LVDT ..... Linear variable differential transformer

ℓ_v ..... Radial distance from the armature pivot point to where the longitudinal armature and valve axes intersect [m]

ℓ_m ..... Radial distance from the armature pivot point to where the resultant opener magnetic force acts on the armature [m]

λ ..... Magnetic flux linkage [Wb-turns]

M ..... Local Mach number at the exhaust valve throat

MMF ..... Magnetomotive force [A-turns]

m ..... Effective moving mass [kg]

m_g ..... Mass of the gas inside the cylinder [kg]

m_v ..... Effective valve and moving spring mass [kg]

μ_0 ..... Permeability constant $= 4\pi \times 10^{-7} \frac{\mathrm{H}}{\mathrm{m}}$

μ_r ..... Relative permeability

N ..... Number of coil turns [turns]

N_{fc} ..... Number of turns of flux measurement coil [turns]

N_{ec} ..... Number of turns of excitation coil [turns]

ν ..... Reluctivity [$\frac{\mathrm{m}}{\mathrm{H}}$]

ODE ..... Ordinatry differential equation

P ..... Cylinder pressure [Pa]

P_{atm} ..... Atmospheric pressure [Pa]

P_o ..... Initial cylinder pressure [Pa]

PDE ..... Partial differential equation

PI ..... Proportional integral

PPC ..... PowerPC

PSD ..... Position sensitive device

PWM ..... Pulse width modulation

ϕ ..... Magnetic flux [Wb]

ψ ..... Flux linkage model parameter [Wb]

QP ..... Quadradic programming

R ..... Coil resistance [Ω]

RPM ..... Revolution per minute

$\Re$ ..... Reluctance [$\frac{1}{\mathrm{H}}$]

R_g ..... Ideal gas constant for in-clinder gas

ρ ..... Electric charge density [$\frac{C}{\mathrm{m}^3}$]

S ..... Total valve stroke, 8 mm

SQP ..... Sequential quadratic programming

σ ..... Conductivity [S]

T ..... In-cylinder gas temperature [K]

TDC ..... Top dead centre

θ_c ..... Crank angle [rad]

t_0 ..... Initial end-control time [s]

t_f ..... Final end-control time [s]

u ..... Control input

V ..... Electric scalar potential [V]

V_c ..... Cylinder volume at valve opening [m^3]

V_{res} ..... Combined cylinder head and crevice volume [m^3]

v ..... Coil voltage [V]

VVT ..... Variable valve timing

W_c ..... Co-energy function [J]

x ..... Valve displacement, $\epsilon\{[-4\text{mm},\ 4\text{mm}]\}$

x_L ..... Valve lift $\epsilon\{[-8\text{mm},\ 0\text{mm}]\}$

x_{lc} ..... Landing control engagement position

$\dot{x}$ ..... Valve velocity [m/s]

$\ddot{x}$ ..... Valve acceleration [m/s^2]

y ..... Flat output [m]

y_d ..... Desired position [m]

$\dot{y}_d$ ..... Desired velocity [m/s]

$\dot{y}_d$ ..... Desired acceleration [m/s^2]

$y_d^{(3)}$ ..... Desired jerk [m/s^3]

Chapter 1

Introduction

1.1 Background

Rising fuel costs and greenhouse gas emissions (GHG) have garnered increasing public and political concern in recent years. These trends are expected to continue as developing nations such as India and China continue to rapidly industrialize while conventional oil reserves wane. A significant contribution to worldwide energy consumption and GHG emissions is the transportation sector, accounting for two thirds, or 8.4 million m^3 (53 million US barrels) of crude oil a day (4.6 million m^3 of which are used for land transport of people) and 25% of global GHG emissions [Heywood, 2006]. Adding to the transportation energy demand is the increase in global vehicle production, which by the end of 2006, is expected to reach approximately 70 million vehicles; an increase of 5% over the previous year [Gottschalk, 2006]. Although Canada ranks as the eighth largest vehicle producer with over 2.6 million vehicles in 2005 [OICA, 2005a, OICA, 2005b], Canada's per-capita oil consumption of 3 gallons per day ranks it as a leading energy consumer [Energy Information Agency (EIA), 2006]. Similarly, Canada is a leading per-capita GHG emitter with 26% coming from the transportation sector [Canada, 2005]. Consequently, even modest improvements in transportation engine efficiency could poten-

tially have profound economic and environmental effects at national and international scales.

1.2 Variable Valve Timing

Without a feasible alternative to the internal combustion engine (ICE) foreseeable within the next ten to fifteen years [Atkins and Koch, 2003], methods of improving existing ICE efficiency have become increasingly important. One promising method of improving ICE efficiency is through independent control of gas exchange valve timing. Traditional ICE gas exchange valve timing is mechanically fixed in proportion to crankshaft position. This timing determines when valves open and close, thereby affecting the air-fuel mixture and exhaust flow. At high engine speeds and loads, a delayed closing of the intake valve is desired to take advantage of air-fuel momentum, otherwise known as the ram effect. Conversely, at low engine speeds and loads, ram-charging is negligible and intake valve closing should occur early to maximize the effective compression ratio and to avoid exhaust gas recirculation (EGR). Since timing cannot be altered without significant engine modifications, a compromise between low and high engine speed efficiency is assigned [Schechter and Levin, 1996]. Although the variable valve timing concept is not new [Payne, 1899], a confluence of increasing fuel prices, stringent emissions standards, efficient and affordable power-electronics and microprocessor technologies have motivated automotive researchers to investigate a variety of variable valve timing methods. Already available to consumers are engines with variable valve timing over limited ranges of crank angle. It is now common to find manufacturers implementing mechanical devices capable of altering the valve phase [Dugdale et al., 2005], duration [Borgmann et al., 2004, Hara et al., 2000] and lift [Golovatai-Schmidt et al., 2004, Nakamura et al., 2001]. BMW's Valvetronic, Porsche's Vario-Cam Plus and Honda's IVTEC are just a few examples of mechan-

ical variable valve systems which are currently in production and offer some flexibility in valve actuation. Although such configurations do improve low to mid-speed torque and fuel economy, the do not offer the ability to change the timing or duration of the individual valve events. In each of the aforementioned production systems, all intake or exhaust valves will be changed to a new profile rather than altering an individual valve trajectory. Independent valve control is desirable for a multitude of reasons such as when performing a cylinder deactivation procedure, internal EGR management, or for a staggered intake valve opening operation [Wilson et al., 1993]. In addition, an extensive host of engine operation modes also become available with independent valve control, ranging from one cylinder starting to regenerative engine braking [Turner et al., 2004, Schechter and Levin, 1996]. As a result, the design and implementation of individual actuators which allow the ability to independently influence each valve irrespective of crank angle or other valves is being actively pursued. Laboratory engines have already been fitted with hydraulic [Shen et al., 2006, Allen and Law, 2002, Barros da Cunha et al., 2000], pneumatic [Trajkovic et al., 2006, Richeson and Erickson, 1989], motor [Henry, 2001] and electromagnetic actuators [Cope and Wright, 2006], [Niţu et al., 2005],
[Pischinger et al., 2000], [Lequesne, 1990] to demonstrate the various benefits of VVT on engine performance (usually while disregarding valve actuation performance). These studies have shown low to mid-speed torque output has been increased by 10%, fuel economy has been improved by 15% and a reduction of NO_x emissions by 20% [Pischinger et al., 2000, Moro et al., 2001, Lancefield et al., 1993] compared with a conventional fixed timing valvetrain.

1.2.1 Electromagnetic Variable Valve Timing

A number of designs for variable valve actuators have been proposed. These include valve control through electrical motors (linear and rotary) [A. Warburton et al., 2005,

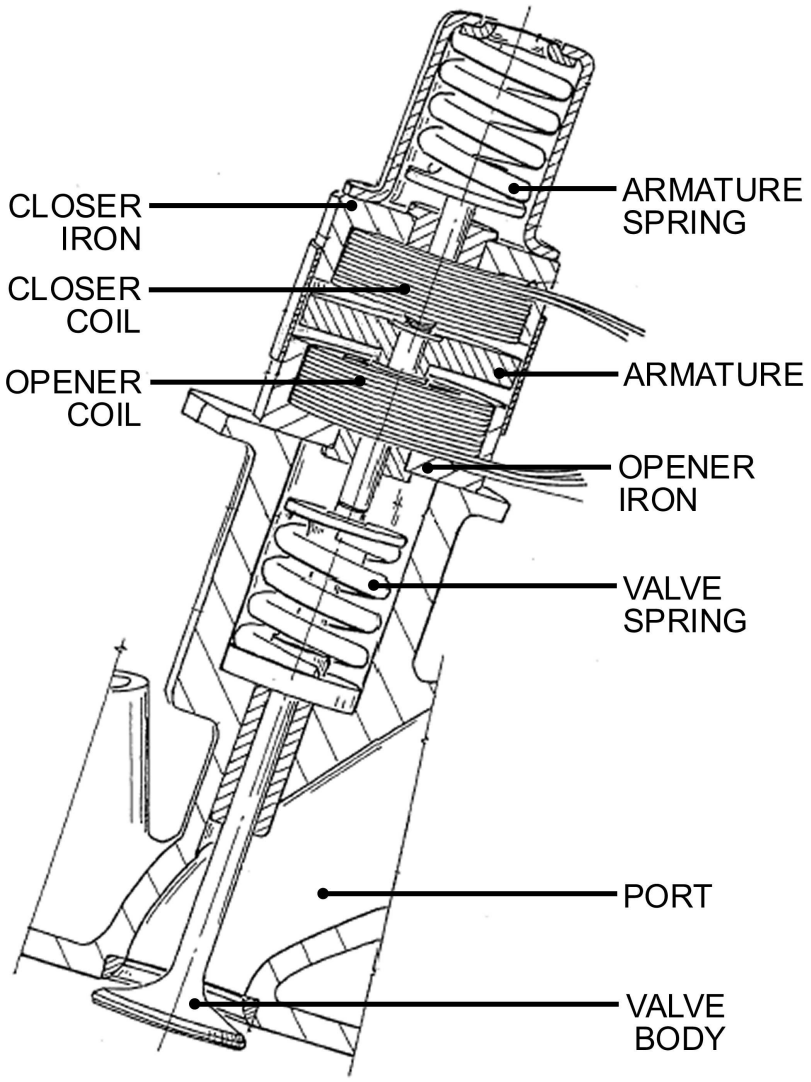

Figure 1.1: Schematic of prototype solenoid valve actuator [Gladel et al., 1999]

Qiuz et al., 2004, Henry, 2001], piezoelectric [Weddle and Leo, 1998], pneumatic [Richeson and Erickson, 1989, Gould et al., 1991], hydraulic [Allen and Law, 2002], [Barros da Cunha et al., 2000], and solenoid actuators [Pischinger et al., 2000], [Lequesne, 1990]. Many of these approaches cannot provide sufficiently fast, efficient and precise control of cylinder charge during engine transients. Transient cylinder charge control is of particular importance in the transition between combustion modes such as homogeneous charge compression ignition (HCCI) in spark

ICEs [Shahbakhti et al., 2007, Koopmans et al., 2003]. Although no clear actuation method has been proven to be superior, solenoids are ideal in that they work through non-contacting forces, provide sufficiently fast transition times, are relatively energy efficient and are inexpensive to mass produce.

Typically, the solenoid actuator consists of a linear-moving armature with two coils and two preloaded springs as described in [Gladel et al., 1999] and shown in Figure 1.1. The springs can achieve rapid flight times while minimizing electrical energy input and are essential in overcoming the significant combustion pressures imposed on the exhaust valve. The electromagnets are required for 'catching' the armature at either stroke bound. In addition, they are used to overcome friction and pressure disturbances. Permanent magnets have also been employed to "catch" the armature at the stroke bounds with electromagnets providing a release force [Lequesne, 1999, Theobald et al., 1994].

Other designs include hinged or clapper-type configurations [Kawase et al., 1991, Montanari et al., 2004, Mianzo et al., 2005], such as the prototype used in this work. An example of a typical hinged solenoid actuator is shown in Figure 1.2. In the hinged armature design, the armature equilibrium is balanced between a torsion bar and a linear compression spring. Pole geometry is considered 'U' shaped and made of laminated steel for eddy current suppression.

A production solenoid actuator based variable valvetrain is estimated to increase the parasitic engine load by 1% over a conventionally driven cam-roller valvetrain [Flierl and Klüting, 2000]. However, there is a low to mid-speed improvement of 15-20% in fuel economy through volumetric efficiency enhancement [Moro et al., 2001], [Pischinger et al., 2000, Lancefield et al., 1993]. Similar performance and energy consumption characteristics are expected to be achieved using the prototype actuator described in this work. In addition, higher efficiency of the actuator itself can be attained through improved control strategies [Gunselmann and Melbert, 2003] and

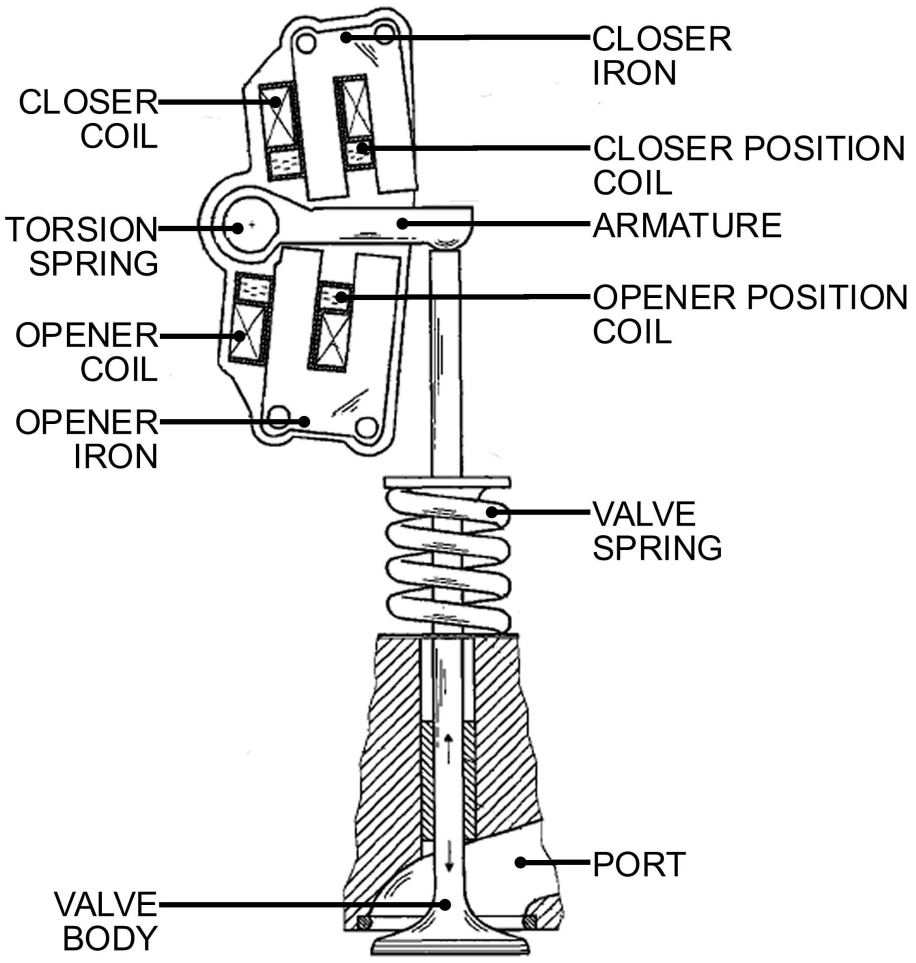

Figure 1.2: Hinged electromagnetic gas exchange valve actuator [Stolk and Gaisberg, 2001]

actuator design [Clark et al., 2005]. Arguably the greatest advantage of fully flexible valvetrain over variable valve timing systems already in production is the ability to affect individual valves on a cycle-by-cycle basis. Such ability potentially enables a host of advanced engine management strategies such as varying the effective compression ratio, operating on alternative combustion cycles (HCCI, Miller) thereby enhancing efficiency over a broad range of operating conditions.

1.3 Problem Identification and Research Scope

One of the challenges remaining in the implementation of solenoid actuators in production engines is the achievement of robust valve landing control subject to practical constraints. These constraints have already been identified in literature
[Koch et al., 2002] and include:

- maximum available voltage of 42V
- maximum valve seating velocities of 0.1m/s [Wang et al., 2002] (for maintaining acceptable engine acoustical noise levels and ensuring valve seating and wear requirements are met)
- transition times of no more than 4.5ms [Peterson and Stefanopoulou, 2004] (in order to meet maximum engine speeds of 5000 - 6000 RPM)
- practical feedback sensor technology

Performing efficient solenoid valve control is a challenging problem due to these stringent constraints and the nonlinear actuator characteristics. Depending on the actuator design, control may be complicated due to eddy currents, magnetic saturation, limited range of authority, and sensitivity to parameter variations and combustion gas force disturbances.
Given the above constraints, intermediate objectives are identified in relation to the overall research scope. They are:

- **Modeling and Simulation:** An accurate yet simple model of the actuator system is derived and experimentally validated in order to design control strategies and algorithms. The simulations offer an expeditious and cost effective method for model and control performance refinement prior to implementation.

- **Control Design:** Identification, derivation and implementation of a control methodology and design. Algorithms are evaluated in simulation using the developed models.

- **Experimental Testbench Control Validation:** Experimental validation of the models and control simulations on an idealized engine test platform. Performance is evaluated with respect to valve seating velocities, transition times and energy efficiency while subject to the outlined constraints.

A "V-cycle" or rapid prototyping flow chart of these objectives within the context of the overall VVT actuator design and implementation process is presented in Figure 1.3. The focus of this work is on refining and evaluating the developed control algorithms on an experimental engine testbench simulator in preparation for implementation on an operational single cylinder engine. These aspects are indicated by the dashed outline in Figure 1.3. Additionally, the modeling and simulation done in previous work [Chladny, 2003] are extended to accommodate the latest prototype and additional physical effects, such as gas force disturbances.

1.3.1 Contribution

The overall objective of this work is to provide the hardware and software required for implementation of electromagnetic valvetrain actuators for use on an experimental single cylinder ICE. In pursuing this goal, the following contributions have been made related to control of electromagnetic VVT actuators:

- A method for position feedback using a finite element model and magnetic flux measurement technique.

- The simplification of a compressible flow model for online cycle-by-cycle gas force identification.

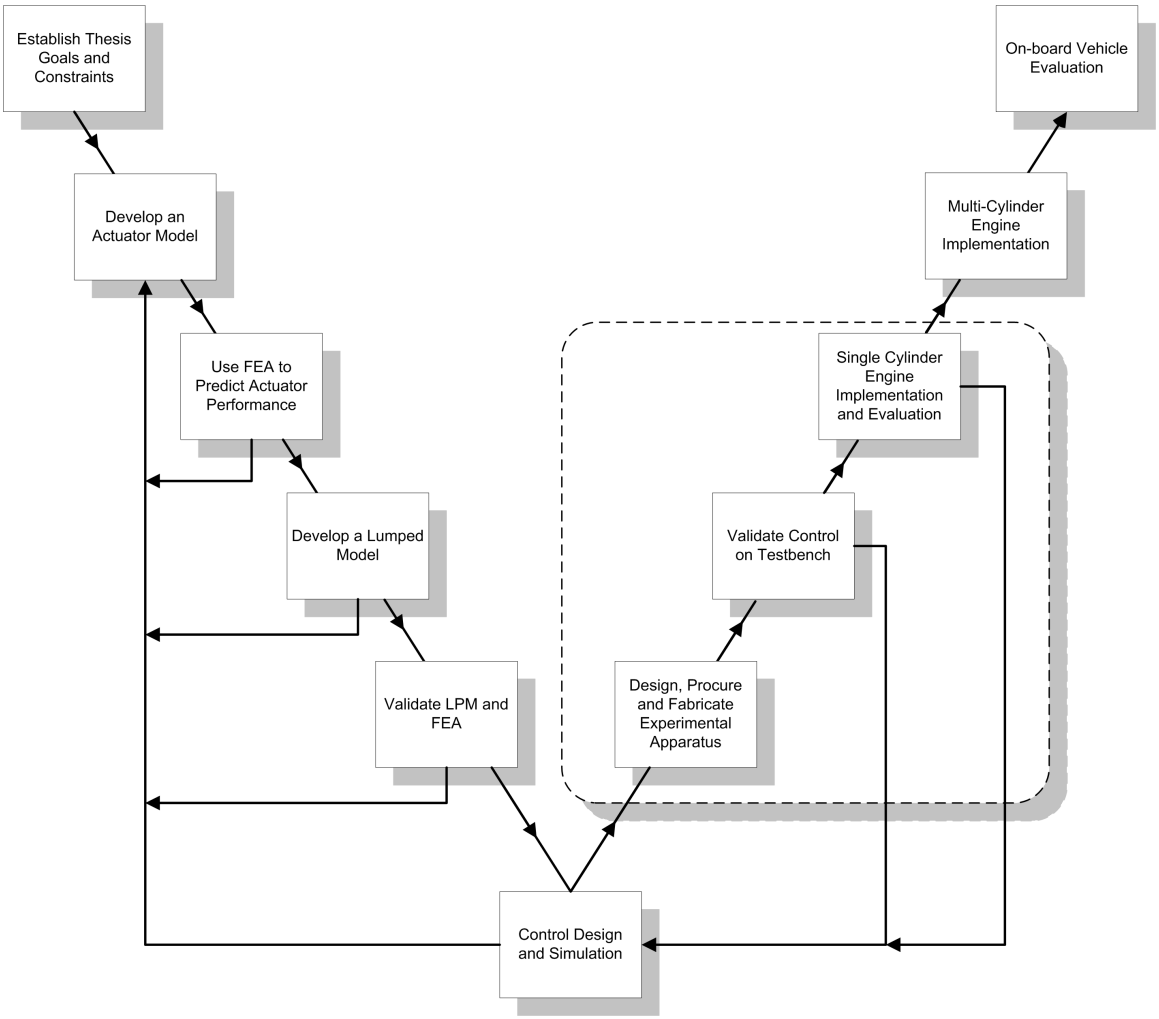

Figure 1.3: V-Cycle workflow of overall research objectives

- An experimental testbench method for exhaust gas disturbance emulation and control performance evaluation.
- The development of a nonlinear observer for gas force disturbance identification.
- The design and implementation of feedforward and nonlinear landing controllers subject to practical physical constraints and gas force disturbances using the aforementioned feedback sensing and disturbance identification techniques.
- Demonstration of advanced nonlinear control on a highly-nonlinear system which

requires a detailed understanding of the actuator system physics, use of a novel feedback sensor concept, implementation of a feed-forward and disturbance estimator to reject large disturbances on a cycle-by-cycle basis and integration of the derived feed-forward and closed loop controllers.

In the following chapters, an overview of these contributions and the related supplementary material are provided within the context of relevant literature. The chapters are organized as follows. A survey of relevant literature is presented in Chapter 2. Proposed variable valve actuators, modeling, feedback, control and implementation methods are compared and contrasted. Chapter 3 provides a summary of the related modeling and control theory with respect to the solenoid variable valve actuator problem. Details of the modeling and simulations undertaken are provided in Chapter 4. The overall proposed controller topology is presented in Chapter 5. In this chapter, the constituent algorithms that comprise the overall control method such as the state estimation and landing controller are described in detail. Chapter 6 describes the experimental procedures and equipment used to qualify the developed simulation models and evaluate control performance. Experimental results and principal findings are discussed in Chapter 7. A summary of key conclusions and supplementary reference material are provided in Chapter 8 and appendices, respectively.

Chapter 2

A Review Of Current Variable Valve Actuator Technology, Modeling and Control

2.1 Introduction

Currently, a myriad of variable valve timing (VVT) actuators have been implemented on laboratory engines. Electric motor, pneumatic, hydraulic and electromagnetic actuators have all been implemented and documented. Although such actuators have demonstrated the benefits of VVT on engine performance, their designs often neglect many of the issues which must be addressed prior to being implemented in a production vehicle. Means of preventing excessive valve seating velocity and the resulting wear and acoustic emissions are of particular concern. Other considerations include methods of feedback, opening/closing (transition) time and power consumption. This chapter highlights some of the current efforts to implement VVT technology with respect to actuator types, modeling, feedback control and exhaust gas disturbance rejection strategies.

2.2 Various Actuator Technologies

The following sections provide an overview of current and proposed VVT actuation technology.

2.2.1 Pneumatic & Hydraulic Actuators

Presently, pneumatic and electro-hydraulic valve actuators for spark ignition engines are not expected to be mass produced in a production vehicle due to the relatively high unrecoverable energy input required to operate them [Henry, 2001]. In addition, these actuators tend to require considerable maintenance and their performance and accuracy are temperature sensitive. Pneumatic or hydraulic pumps, with coolers, filters and all the related accessories required to deliver the air or fluid are necessary to allow these actuators to operate in an on-board vehicle environment. Some hydraulic actuators rely on a traditional camshaft that provides pressure to small cylinders located above the valve body. Timing and lift may be then varied with a valve that controls the amount of fluid in the cylinders [Gecim, 1993, Kim et al., 1997, Barros da Cunha et al., 2000]. Aside from the increased parasitic load on the engine, such systems will increase associated engine manufacturing costs. Further costs may be associated with the safety equipment required to protect personnel and the environment from any system failures due to the presence of fluid pressures in excess of 20 MPa (3000 psi) [Sun and Cleary, 2003]. As well, advanced control systems and electronics are required to coordinate appropriate valve motion. Pneumatic and hydraulic actuators are also susceptive to the same constraints as electromagnetic actuators such as cost, seating noise and speed requirements. It is for these reasons that successful use of such actuators has been primarily limited to either laboratory or to high output (and relatively low mileage) race engines.

2.2.2 Rotary & Linear Motors

Electric rotary motors which use permanent magnets have also been proposed for use as valve actuators. They typically employ mechanical devices which transform rotary motion into reciprocating linear motion. These systems appear relatively

easy to control since valve position can be considered fixed with respect to the motor displacement. However, they are far less developed than pneumatic and hydraulic devices [Giglio et al., 2002], perhaps due to the relatively large physical volumes required to achieve the necessary response and valve speeds. Due to the challenging task of overcoming exhaust gas force disturbances, there appears to be renewed interest in the motor driven desmodromic valve actuators [Parlikar et al., 2005, A. Warburton et al., 2005]. Such actuators are relatively simple to control, and in some cases, are capable of variable lift and zero holding current. However, the issues of soft landing, transition time, under-hood volume and power consumption still appear problematic in some cases. In [Parlikar et al., 2005], zero engine load (no gas disturbance) transition time is achieved within 3.5 ms however, full load (6000rpm, open throttle) power consumption is estimated to be 160 W. Seating velocities of 0.15 to 0.27 m/s are reported. Power consumption in [A. Warburton et al., 2005] is lower (100 W), with similar transition times and seating estimated to be below 0.24 m/s. If further refitments can be made, the motor driven valve actuator may become a viable flexible VVT candidate.

Linear motors have also been applied as variable valve actuators [Braune et al., 2006], [Mercorelli et al., 2003]. They were initially predicted to be better suited to valve strokes in excess of 20 mm when compared with solenoid electromagnetic actuators [Lequesne, 1996]. This is because the high frequencies and the resulting duty cycle required in a VVT application cause significant power consumption and their relatively slow response (due to large moving mass). In [Mercorelli et al., 2003], simulated results indicate landing speeds of approximately 0.01 m/s, however the transition time is approximately 5 ms and a voltage in excess of 100 V is used. Later in [Braune et al., 2006], the same group provides considerably poorer experimental results with transition times in excess of 15 ms (with zero pressure disturbances) and holding currents (while open) in excess of 30 A. No landing speeds or velocity trajec-

tories are explicitly reported. The armature is separated from the valve stem when fully closed (1 mm gap) which, aside from potential wear and acoustical noise caused by internal impacts, results in an unusual opening lift trajectory. A potentiometer is used for position feedback and the supply voltage used is not indicated. Susceptibility of permanent magnets to under-hood temperature variations is also of concern [Trout, 2001]. Despite those shortcomings, there are few reported linear motor results and in time, they may also become a viable VVT actuation option.

2.2.3 Piezoelectric Actuators

Actuators using piezoelectric crystals have been proposed in [Weddle and Leo, 1998]. The benefits of such a system would be through the exploitation of the fast response and high forces inherent with piezoelectric systems. However, displacement is quite limited from the crystals themselves, thus a lever arm and rack and pinion gearing are used to amplify crystal deflection. To minimize system inertia, a 'flapper' or butterfly type of valve is proposed instead of a typical valvetrain poppet valve. The authors discuss several concerns that arose while testing an initial prototype. Aside from flow and sealing concerns of a different gas exchange valve, variation of valve displacement with frequency occurred as a result of the excitation of various modes. As well, dimensional tolerances (and the additional expenses) are of concern due to the mechanical amplification through the lever arm. To date, no further prototypes have been documented.

2.2.4 Electroactive Polymer Actuators

Presently an emerging technology, electroactive polymer (EAP) actuators have also been proposed for VVT applications [Ashley, 2003]. Such actuators consist of a dielectric polymer (acrylic or silicon for example) laminated between two conductive

sheets. A high voltage (1-5kV) is applied to the conducting layers, establishing an electric field sufficiently strong enough to squeeze the polymer layer which in turn, expands in area. The actuation technique offers large strain rates with respect to force per unit density compared to magnetic and piezoelectric devices, however many issues must be resolved before a production actuator could be viable. Aside from the need to generate high voltages, these include fatigue and temperature susceptibility / sensitivity.

2.2.5 Solenoid Actuators

Another promising actuator configuration for independent valve control is the electromagnetic solenoid. Electromagnetic actuators for valve control were patented at least as early as the 1970s [Longstaff and Holmes, 1975, Pischinger and Kreuter, 1984] and are perhaps the most popular of the production fully flexible VVT actuator candidates. Unlike the aforementioned hydraulic and pneumatic actuators, electromagnetic actuators are often designed with two springs which provide most of the necessary energy for a given valve cycle. After the armature is released it accelerates to the middle position, then the valve is decelerated with an opposing spring which stores the kinetic energy for the the next valve event. In the non-powered rest position, the two springs force the armature to the mid-stroke position. In this way, electromagnetic energy is only required to influence the valve behavior at either end of the valve trajectory and to overcome any losses due to friction or gas forces. They are compact in size, relatively inexpensive to mass produce and are not as temperature dependant as their hydraulic counterparts. Like the motor based actuators, they require sophisticated electronic hardware and control software. A relatively large alternator / permanent magnet induction motor must also be employed to supply approximately 70W of peak electrical power per actuator at maximum engine speed and load. However, the extra electrical power requirement (3% of total engine output) is expected

to be offset by the friction energy saved through the absence of camshafts (2% of total engine output for a roller-bearing valve-train) [Flierl and Klüting, 2000]. One potential drawback to solenoid actuators is that the springs often dominate valve motion, especially near the mid-stroke position, making variable valve lift (VVL) a challenging issue. However, even this limitation has been addressed with some success in [Peterson et al., 2006, Wolters et al., 2003].

Successful implementation of electromagnetic actuators has also been generally limited to the laboratory, although several prototype vehicles have been built with an electromagnetic valve-train [Pischinger et al., 2000]. Control with combustion pressure disturbances has been particularly challenging. Manually tuned feedforward control has been implemented within laboratory settings [Tai and Tsao, 2001]. However, such systems are unable to account for the significant combustion pressure fluctuations. In order to implement a reliable control system it must be robust to variations of the valve / actuator system. These variations include abrupt disturbances from combustion pressure variations as well as the relatively gradual parameter changes caused by component fatigue, friction and temperature variations. In addition to these variations, the relatively high speed of the actuators, the non-linear magnetics and the short distance over which control is feasible has motivated many to develop closed loop control systems [Koch et al., 2002, Wang et al., 2002, Tai and Tsao, 2001, W. Hoffmann and A. Stefanopoulou, 2001]. Due to the design goals and the necessity for closed loop control, it has been determined that high armature position sensor resolution and frequency response are required. Such sensors are often expensive and difficult to calibrate in a mass production environment. However, efforts are being made to develop alternative cost effective sensors or sensing methods with sufficient response and resolution [Lynch et al., 2003, Rossi and Alberto, 2001, Takashi and Iwao, 1995, Roschke and Bielau, 1995].

2.3 Feedback Sensors

The majority of experimental literature makes use of external valve and/or armature-based position measurements for state reconstruction. These include position or velocity measurements via linear variable differential transducer (LVDT)
[Sun and Cleary, 2003], potentiometer [Braune et al., 2006], laser [Peterson, 2005],
[Tai and Tsao, 2003, Wang et al., 2002, Stubbs, 2000] or eddy current
[Peterson et al., 2006, Chung et al., 2007] displacement sensors.
Although these sensors provide sufficient precision, accuracy and response, efforts are being made to develop alternative cost effective sensors or sensing methods with equivalent performance. These include the flux-based coil type [Chladny and Koch, 2006a, Scacchioli, 2005, Montanari et al., 2004],
[Rossi and Alberto, 2001], [Rossi and Tonielli, 2001], [Roschke and Bielau, 1995],
observer-based [Lynch et al., 2003, Eyabi and Washington, 2006a, Eyabi, 2003] and self inductive [Butzmann et al., 2000, Takashi and Iwao, 1995] schemes. In the latter case, it is proposed that the driving coil itself be used to relate the measured rate of change of induced coil current to the armature position and velocity. This may be done by momentarily deactivating the drive coil and relating velocity-induced currents to position. Drive currents are readily measurable through hall-effect devices and generally used in all control schemes. Using this method of sensing, landing speeds of 0.2m/s are claimed. However, the authors indicate that the system is limited by its sensitivity to disturbances in addition to temporary loss of control authority while sensing [Butzmann et al., 2000] and is therefore of limited practical use.
Observer-based state reconstruction makes use of partial state measurements and estimated initial state conditions to predict plant output. A sliding mode observer is used to predict valve position and velocity using only a measured current signal in [Eyabi and Washington, 2006a]. The algorithm is implemented successfully on a

actuator with relatively soft springs (peak velocities $\leq$ 1.5 m/s, transition times $\geq$ 25 ms) and gas force disturbances are not considered. In [Peterson et al., 2002] position and current are used to estimate velocity in a nonlinear reduced order observer. Although observer-based feedback systems reduce the number or eliminate the need for sensors, such schemes may be sensitive to initial state estimates and require high gain for the relatively rapid estimation convergence needed for landing control. As a result, landing control performance may be compromised when subjected to excessive noise or disturbances.

Another feedback system demonstrated includes a microphone to adaptively improve impact speeds from sound intensity measurement [Peterson and Stefanopoulou, 2004]. Although proven successful in laboratory testbench experiments, such a sensor scheme is likely not practical in an engine environment due to multiple valves in operation and other possible acoustic sources. The method also requires several cycles to converge from one operating condition to another and is thus perhaps more suitable for slowly changing conditions.

In the case of [Montanari et al., 2004], using flux-based position reconstruction, two functions are used to relate reluctance and excitation to air gap. Improved accuracy is achieved with a similar measurement technique but through the use of a numerical look-up table with finite element analysis (FEA) results in [Chladny and Koch, 2006a]. At this time, it appears that no other group has documented a FEA derived flux-based position sensing technique. In both cases, the sensor is cost effective, practical and capable of achieving landing speeds below 0.1 m/s.

2.4 Actuator Modeling

With many electromagnetic devices, simplified geometry and linear approximations are often satisfactory in estimating device performance. In the context of variable

valve timing actuator design, control is to be applied in an operating region in which the air gap is small and at excitation levels sufficiently large that material saturation is significant, making linear theory unsatisfactory for accurately predicting actuator performance [Chladny, 2003]. The following highlights some of the work that has contributed to the advancement of solenoid actuator modeling.

2.4.1 Lumped Parameter Models

Nearly all solenoid VVT control algorithms described in literature are derived from some variation of a lumped parameter model (LPM). Most use heuristic flux and force relations that take on a form that neglect magnetic material saturation like below:

$$\lambda(x) = \frac{\beta}{\kappa - x} \tag{2.1}$$
$$F_{mag}(x, i) = \frac{\beta i^2}{(\kappa - x)^2}$$

where λ represents the magnetic flux linkage, x is the valve/armature position, i is the coil current and F_{mag} is the resulting magnetic force. Coefficients β and κ are determined by performing linear regression fits to experimentally obtained data [Tai and Tsao, 2001, Peterson and Stefanopoulou, 2004]. A similar approach is used in [Wang et al., 2002, Butzmann et al., 2000], but another analytic function is appended to approximate the saturated operating points (with constraints to prevent discontinuities). Later, [Tai and Tsao, 2003] improved the model by adding a current and position dependant gain to compensate for saturation effects. An inductance relation proposed by [Ilic'-Spong et al., 1987] that accounts for magnetic saturation is used by [Chladny and Koch, 2006b, Chung et al., 2007, Koch et al., 2004] using two different actuators. The authors fit the LPM parameters to FEA generated data and demonstrate good agreement with static and transient experimental measurements. Four methods for establishing LPMs to describe linear and rotary electromagnetic sys-

tems are investigated in [Melgoza and Rodger, 2002]. The methods are evaluated for computational time and accuracy. It is acknowledged that it is not practical to fully simulate the overall performance of the actuator through a discretization processes. Rather, a more practical approach is the use of a simplified model that combines the accuracy of off-line FEA results with the computational speed of a LPM.

A model that includes saturation and hysteresis is presented in
[Eyabi and Washington, 2006b]. Also considered is the effect of mutual inductance between the opener and closer magnets. Here (as in [Vaughan and Gamble, 1996]) net coil current, i, is composed of dissipative current, i_d, and restoring current (or the current related to the coenergy stored in the magnetic field), i_r, such that $i = i_r + i_d$ with i_r and i_d defined by:

$$i_r = f(x, \lambda) = g_4\lambda^4 + g_3\lambda^3 + g_2\lambda^2 + g_1\lambda g_0 \tag{2.2}$$

$$i_d = f_1(v) - \tau_j \frac{di_d}{dt} \tag{2.3}$$

where i_r is a function of flux linkage λ and coefficients g_i are dependent on position, x, as follows:

$$g_i = n_{i,6}x^6 + n_{i,5}x^5 + n_{i,4}x^4 + n_{i,3}x^3 + n_{i,2}x^2 + n_{i,1}x + n_{i,0} \tag{2.4}$$

Coefficients $n_{i,j}$ are fit to experimental data. Hysteresis is accounted for in the i_d term which is a nonlinear function of voltage, v, and a dissipation term, τ_j, such that:

$$f_1(v) = \begin{cases} d_{1,1}|v|^{d_{1,2}(x)}\mathrm{sgn}(v), & v \geq 0 \\ d_{2,1}|v|^{d_{22}(x)}\mathrm{sgn}(v), & v < 0 \end{cases} \tag{2.5}$$

and

$$\tau_j = \begin{cases} \tau_1, & v > 0 \\ \tau_2, & v < 0, \quad x < x_v \\ \tau_3, & v < 0, \quad x > x_v \end{cases} \tag{2.6}$$

where parameters τ_j, $d_{i,j}$ and x_v are determined experimentally. Finally, a relationship between magnetic force, F_m, position and flux is defined as:

$$F_m = m_2\lambda^2 + m_1\lambda + m_0, \tag{2.7}$$

with

$$m_i = p_{i,8}x^8 + p_{i,7}x^7 + p_{i,6}x^6 + p_{i,5}x^5 + p_{i,4}x^4 + p_{i,3}x^3 + p_{i,2}x^2 + p_{i,1}x + p_{i,0} \tag{2.8}$$

where again, coefficients $p_{i,j}$ are fit to data (it is unspecified if it is simulated or experimentally generated). The model is contrasted with experimentally acquired results with reasonably good agreement with a significant reverse magnetization effect due to hysteresis losses. The work is relatively unique since others' contributions have found, including this work, that in practice, hysteresis is not significant and thus not modeled.

Other LPMs are derived through the use of reluctance networks [Mercorelli et al., 2003, Chillet and Voyant, 2001, Piron et al., 1999]. This technique parallels an electric circuit approach to predicting actuator static and transient performance. By discretizing portions of the magnetic circuit into elements, each with their own permeability and geometric identity, the same methods of solving electric circuits may be used to solve the reluctance network. It is acknowledged in [Piron et al., 1999] that a preliminary FEA analysis may need to be performed to accurately predict flux and eddy current

paths.

Other LPM magnetic models have been derived from fitting polynomial functions to FEA data [Haskara et al., 2004] or experimental force and excitation data [Vaughan and Gamble, 1996].

2.4.2 Finite Element Analysis

In [Chladny et al., 2005, Chladny, 2003] methods of FEA modeling and validation of a solenoid VVT actuator are documented using two dimensional static and transient models. Comparable work has been documented in [Clark et al., 2005]. The techniques used in [Clark et al., 2005] differ in that a 3D FEA model is used to investigate pole geometry on force response over a variety of operating ranges. The benefits of using FEA to shape the pole face to improve stability (minimize reluctance and increase flux density) is highlighted in [Chladny, 2003, Lequesne, 1999, Lequesne, 1990]. Despite the greater computational load of a 3D model, there appears to be no gain in model accuracy compared with existing results attained by 2D models. More commonly, FEA is used to evaluate reluctance network models [Chillet and Voyant, 2001, Piron et al., 1999, Xiang, 2002] or for thermal rise due to coil heating [Stubbs, 2000]. Experimental evaluation of solenoid prototypes has been well documented for the purposes of control design [Giglio et al., 2002, Wang et al., 2002, Tai and Tsao, 2001, Stubbs, 2000]. Static force data as a function of excitation and position are typically measured for fitting parametric functions to. However, FEA simulation and experimental results (static) documented in the same work are less common [Lequesne, 1999, Clark et al., 2005, Hartwig et al., 2005]. At this time, there does not appear to be any published results of transient FEA modeling in contrast with comparable experiments other than [Chladny et al., 2005, Chladny, 2003, Koch et al., 2002]. In addition, [Chladny et al., 2005] describes a method of parameterizing an eddy current model by utilizing FEA results for a linear motion solenoid actuator.

2.4.3 Mechanical System Modeling

Most literature follows a similar mechanical system structure based on a one dimensional second order mass spring system [Peterson and Stefanopoulou, 2004],
[Montanari et al., 2004]. Others attempt to capture additional dynamics which take place when a flexible lash adjuster is considered [Haskara et al., 2004],
[Lambrechts et al., 2004, Tai and Tsao, 2003]. The mechanical models that include lash dynamics consist of a two mass-spring system representing a valve, armature with additional relative stiffness and viscous damping coefficients. Although such a model more accurately reflects expected valve and armature behavior, lash-armature position mismatch is not predicted to be a critical design consideration if incorporated into the trajectory design [Koch et al., 2004]. Other groups have modeled valve-seat impacts
[Eyabi and Washington, 2006b] by modeling the magnetic pole faces as stiff mass-spring-damper systems in order to approximate a collision. According to those authors, bounce is not present provided landing speeds are below 0.3 m/s. Given the low impact speed specification of 0.1m/s, the benefits of an impact model will thus be most apparent in a landing control failure.

2.5 Control

In many proposed designs, motion control is performed in two stages
[Gunselmann and Melbert, 2003]. The first stage of motion is usually performed in open-loop due to the relatively limited force authority at larger airgaps and low bandwidth inherent to solenoid actuators (high inductance and restricted source voltage). A common approach is to use a feedforward controller to provide desirable initial conditions for the landing controller. Feedforward controllers are also used to overcome any gas forces that may be present, perhaps in combination with an

adaptive scheme [Peterson and Stefanopoulou, 2004] or engine load and speed maps [Haskara et al., 2004]. Typically, such feedforward schemes are highly tuned to a particular operating condition [Chung, 2005] and not suited to accommodate potentially large gas force cycle-to-cycle variations, due to a misfire for example. During the second stage, closed loop feedback is used to achieve the stringent landing requirements. Irrespective of the control algorithm used, control performance variations can be expected due to the various actuator designs, feedback techniques and voltage sources. Even the power electronics and control thereof play a significant role in overall actuator performance [Mercorelli and Liu, 2005, Mianzo et al., 2005]. Thus, caution must be used when comparing one control algorithm to another unless done with equivalent systems (simulation or experiments). Provided a sufficiently accurate model is used, nonlinear control (feedback linearization, backstepping, flatness, sliding mode) generally results in superior performance and minimal control effort compared to linear techniques. However, the algorithms may be computationally expensive, sensitive to disturbances and sensitive parameter variations when compared to classical techniques.

2.5.1 Landing Control

A wide variety of control algorithms for the end-control or landing problem have been proposed. They include: passive permanent magnets to 'catch' the armature at either stroke bound with excitation currents applied to temporarily neutralize the magnets during armature release [Lequesne, 1999], classical linearized model control [Konrad, 1998], an energy-based method [Schmitz, 1995] where mechanical system energy is regulated about a desired constant, proportional integral (PI) control [Tai and Tsao, 2001, Stubbs, 2000], linear quadratic regulator (LQR) control [Tai and Tsao, 2003], sliding mode feedback linearization [Haskara et al., 2004], [Eyabi, 2003], flatness-based control [Chladny and Koch, 2006b, Chung et al., 2007,

Chung, 2005, Koch et al., 2004, Mercorelli et al., 2003].

Also of interest is a sensorless, constant ratio approach that alleviates the need for external position and velocity measurements [Butzmann and Melbert, 2003], [Butzmann et al., 2000]. Here, armature motion is inferred from coil measurements using the following relationship:

$$\frac{di}{dt} = \frac{1}{1 + H_0\, x}\left(\frac{v\, x}{\mu_0 N^2 A_c} - \frac{i\, \dot{x}}{x}\right) \tag{2.9}$$

where x is the air gap between armature and pole face, μ_0 is the permeability constant, H_0 is a constant accounting for flux leakage, A_c is the core flux path area, i is the coil current, v is the coil voltage and N is the number of coil turns. If the supply voltage source, v, is set to zero (for measurement during landing control), and the $H_0\, x$ leakage term is neglected, the above relation simplifies to

$$\frac{di/dt}{i} = -\frac{\dot{x}}{x} \tag{2.10}$$

For landing control, a predefined desired velocity-position ratio is compared to the measured $\frac{di/dt}{i}$ signal. The coil is then switched to regulate the velocity-position ratio to the desired constant.

Under laboratory testbench conditions, most methods of feedback are able to achieve landing speeds of 0.2 m/s or less with variations in transition times between 3.5 and 20 ms. There is large variation reported among the voltage sources, feedback techniques and power consumption used; all of which play a significant role in the overall suitability for production implementation.

2.5.2 Feedforward Control

The approximate $\frac{1}{x^2}$ drop in magnetic force with air gap limits the effectiveness of the closed loop controller to regions close to the pole face and is thus only used for landing control [Tai and Tsao, 2002]. Due to the relatively wide range of typical ICE operating conditions imposed on solenoid VVT actuators, the control scheme must compensate both for slowly varying conditions and rapid disturbances. Changes occurring over many valve opening and closing cycles are classified as slow changes. Examples of slow changes are variations in coil resistance and friction as a function of temperature or mechanical wear. Such variations can be accounted for through a cyclical adaptive approach as illustrated in [Wang et al., 2002, Peterson and Stefanopoulou, 2004, Tai and Tsao, 2003, Butzmann et al., 2000]. However, rapidly varying disturbances, such as those due to combustion gas forces (particularly those on the exhaust gas valve), can vary significantly from one cycle to the next (over 250 N for the actuator in this study). A feedforward controller will have to accommodate gas force disturbances because the majority of gas work occurs during the initial valve stroke and must therefore adjust the imparted magnetic force accordingly to setup reasonable initial conditions for the landing controller. The design is further complicated since in-cylinder pressure sensors are not present in current production engines. As a result, some form of online disturbance estimation scheme is required.

2.5.2.1 Cyclic-Adaptive Compensation

Controllers designed to compensate for parameter variations or disturbances occurring over many valve opening and closing cycles are classified as cyclic adaptive or iterative learning controllers (ILC). Work such as [Peterson and Stefanopoulou, 2004, Hoffmann et al., 2003, Tai and Tsao, 2003, Wang et al., 2002, Butzmann et al., 2000] exploits the repetitive nature of the actuator operation to tune performance over many

cycles. For example, in [Peterson, 2005, Peterson and Stefanopoulou, 2004] impact acoustical intensity is measured via a microphone to tune the controller over several cycles via an extremum seeking controller:

$$U_c = \frac{K_1}{\gamma + x}\,\dot{x} + \frac{K_2}{\beta + x} \tag{2.11}$$

where control output, U_c, is subject to tuning parameters K_1, K_2, γ and β. In practice, only β is adjusted to reduce impact velocity based on impact sound intensity via the following cost function:

$$Q = [S_{des} - S_{meas}(k)]^2 \tag{2.12}$$

where the difference between the desired and measured sound intensity (S_{des} and $S_{meas}(k)$ respectively) is is minimized over k cycles. Using this method impact velocities below 0.1 m/s and transition times of less than 4.0 ms are achieved with a 100 V source. Convergence occurs in approximately 40 cycles. Velocity, $\dot{x}$, is estimated with the nonlinear observer presented in [Peterson et al., 2002].

An iterative learning controller (ILC) is presented in [Hoffmann et al., 2003] that uses observer output feedback. The magnitude of simulated transient force disturbances on the order of 20 N (intake or low-load exhaust pressure disturbances) are varied by 2 N over 10 cycles to demonstrate how the ILC adjusts open-loop input based on the actual and desired armature position weighted errors. A linear-quadratic regulator (LQR) landing controller is used to track a trajectory in the latter part of the valve stroke. Convergence is achieved after approximately 35 valve cycles with impact velocities of 0.04 m/s using a 200 V power source.

In [Chen et al., 2005], gas force disturbances are heuristically parameterized using an exponential decay function in which the amplitude and time constant are estimated over several combustion cycles via a hybridized multi-step least squares - Kalman

filter. Although the disturbance is parameterized as a function of time only (no coupling to engine speed, exhaust valve opening (EVO) angle or valve position) simulated results appear promising. However as acknowledged by the authors, the technique is not suited to the extreme pressure fluctuations experienced during transient engine operation or misfires. Even when with a moderate change in initial exhaust valve opening pressure, four consistent cycles are required for convergence.

2.5.2.2 Exhaust Gas Force Disturbance Compensation

Exhaust valve opening with solenoid actuators is a challenging control problem because the opening pressure can vary significantly from one cycle to the next. After combustion, the engine piston is driven down and the EVO occurs usually 40 to 60 degrees of crank angle before bottom dead centre (BDC) [Heywood, 1988]. The pressure at valve opening varies depending on the combustion process and the crank angle at which the valve opens. This is of concern as pressure significantly affects the force required by the electromagnet for successful soft landing (while opening). In-cylinder pressure sensors are not present in current production engines so this disturbance is not known. Furthermore, since feedforward is used for control in the initial opening of the valve, an online identification scheme is required. These rapid changes present a challenging control problem [Hartwig et al., 2005] and have, at least in part, motivated researchers to develop alternative actuators such as the motor driven cam actuators described in Section 2.2.2. One of the earliest incorporations of gas force disturbances in valve control is in [Wang et al., 2000] where an experimental cylinder pressure trace was input in simulation. Valve force was related to gas pressure through valve area times the difference in pressure between cylinder and exhaust port. Later, [Hoffmann et al., 2003] simulates a similar version of the disturbance in an iterative learning controller. The disturbance was taken at a light engine load (peak force of 20 N) and assumed to be unknown to the controller (varied by 2N every 10

cycles). In [Hartwig et al., 2005], it is proposed to use solenoid actuators only on the intake valves, and driving the exhaust valves with a camshaft to avoid controlling the exhaust opening process altogether. Similarly, automotive supplier Valeo announced plans for a 'half camless' engine to be in production by 2009 [Alexander, 2006] where solenoids are to be used only on the intake valves while exhaust valves will remain cam-driven. However, no plans have yet been set for production of a fully camless system, likely because of the added complexity of rejecting exhaust gas disturbances. Indeed, there are very few published proposals for opening of solenoid exhaust valve actuators while maintaining landing and transition criteria. In [Haskara et al., 2004], the use of either a calibrated engine load-speed dependent feedforward current input or a recursive estimation scheme is proposed. The mapping technique is ideal for most operating conditions provided consistent maps and combustion can be maintained from one cycle to the next. This is not the case in the event of a misfire or partial combustion. The speed-load (and presumably EVO timing) mapping technique is also time consuming to calibrate and may be unique from one engine to the next. Reduction of calibration effort is currently an important priority for automotive manufactures [Ohata and Butts, 2005]. [Haskara et al., 2004] suggest the map is updated online by adjusting the feedforward current input to maintain a specific kinetic and potential energy at the point where the landing controller is engaged. The disturbance, $\hat{\delta}$, is estimated using a sliding mode observer with the following error dynamics:

$$\begin{bmatrix} \dot{e} \\ \ddot{e} \end{bmatrix} = \mathbf{A} \begin{bmatrix} e \\ \dot{e} \end{bmatrix} + \mathbf{B} \left[f_{fbk} + \hat{\delta} \right]$$

with

$$\mathbf{A} = \begin{bmatrix} 0 & 1 \\ -\frac{k}{m} & -\frac{b}{m} \end{bmatrix} \text{ and, } \mathbf{B} = \begin{bmatrix} 0 \\ \frac{1}{m} \end{bmatrix} \tag{2.13}$$

and control input, f_{fbk}, spring stiffness, k, moving mass, m, and friction, b parameterizing the mechanical response. Sampling discretization of the error dynamics is approximating through a zero order hold resulting in:

$$\mathbf{e}_{k+1} = \mathbf{\Phi}\mathbf{e}_k + \mathbf{\Gamma}\left[f_{fbk,k} + \delta_k\right] \tag{2.14}$$

where $\mathbf{\Phi} = e^{\mathbf{A}T}$ and $\mathbf{\Gamma} = (e^{\mathbf{A}T} - \mathbf{I})\mathbf{A}^{-1}\mathbf{B}$ and δ_k represents the average disturbance during a sampling interval. A sliding surface, s_k, is defined as:

$$s_k = \mathbf{C}\begin{bmatrix} e_k \\ \dot{e}_k \end{bmatrix} \tag{2.15}$$

$$s_{k+1} = \mathbf{C}\mathbf{\Phi}\mathbf{e}_k + \mathbf{C}\mathbf{\Gamma}\left[f_{fbk,k} + \delta_k\right] \tag{2.16}$$

a control input, v_k, is defined as:

$$v_k = -f_{fbk,k-1} + (\mathbf{C}\mathbf{\Gamma})^{-1}\mathbf{C}\mathbf{e}_k - (\mathbf{C}\mathbf{\Gamma})^{-1}\mathbf{C}\mathbf{\Phi}\mathbf{e}_{k-1} \tag{2.17}$$

with the disturbance estimate and compensated feedback given by:

$$\hat{d}_k = \hat{d}_{k-1} + \gamma(v_k - \hat{d}_{k-1}) \tag{2.18}$$

$$f_{fbk,k} = -\hat{d}_k$$

where γ is a convergence tuning parameter. Disturbance dynamics are considered constant (un-modeled) between sampling intervals and thus, as reported by the authors, the latter technique is ideal for slowly varying disturbances. Details of the technique with respect to convergence performance or even if it was used in the results presented are not given.

2.6 Summary

A brief overview of the progress towards designing and implementation of variable valve actuators is given. Replacing the camshafts of traditional ICEs is a nontrivial task, and as such, design considerations and constraints are numerous. Most published work focuses on the soft landing issue with little to no regard of exhaust gas force disturbances. Some of the proposed control schemes are able to attain seating velocities of 0.1 m/s or less, often with the use of in-cylinder and / or expensive feedback sensors, voltages exceeding 100 V or transition times exceeding 5ms (at low engine load). Cyclically adaptive controllers or ILCs have also been demonstrated which are capable of accommodating slowly time varying changes that occur over many opening/closing events. One of the most significant remaining challenges is exhaust valve opening control under the influence of significant in-cylinder gas force disturbance variations. The landing controller scheme proposed in this study addresses the issue of exhaust gas force disturbances and landing control. The intake actuator gas disturbances are of lesser concern because their magnitudes and variations are less significant and more predictable. The proposed controller augments the flatness-based landing controller used in [Chung et al., 2007, Chladny and Koch, 2006b, Chung, 2005] with exhaust gas disturbance estimation and feedforward capability using coil current and a practical magnetic flux measurement for feedback while using a 42 V source.

Chapter 3

Theory

3.1 Introduction

Due to the multidisciplinary nature of electromechanical VVT actuators, a relatively large scope of physical phenomena must be examined when modeling and controlling such devices. The following presents a brief overview of the modeling and control techniques used with respect to the hinged solenoid actuator considered in this study.

3.2 Finite Element Modeling

The hinged electromagnetic actuator used in this study has different opener and closer geometry and thus current and force response. Static and transient finite element models of the opener and closer magnetic paths are analyzed to obtain an accurate characterization of actuator behavior for control design. In static analyses, force and path flux values are generated as a function of current and armature (valve) positions. These results constitute a data set which characterize the electrical and mechanical response of the actuator for later use in lumped parameter model (LPM) development. Transient analyses are used to estimate system response and the extent to which it is inhibited by eddy currents. Furthermore, the finite element method

(FEM) results provide qualitative results which may offer insight into aspects such as flux leakage and saturation regions. The following sections provide a brief overview of the FEM process.

3.2.1 Maxwell's Equations

James Clerk Maxwell recognized four general unifying relations which now make up the foundation of all classical electromagnetic field theory [Maxwell, 1864]. These equations provide a means of coupling time varying electric and magnetic fields [Griffiths, 1999]. They are briefly derived in Appendix A and summarized below.

$$\nabla \cdot \boldsymbol{E}(\mathbf{r}, t) = \frac{\rho}{\epsilon_0}, \tag{3.1}$$

$$\nabla \times \boldsymbol{B}(\mathbf{r}, t) = \mu \boldsymbol{J}(\mathbf{r}, t) + \mu\epsilon_0 \frac{\partial \boldsymbol{E}(\mathbf{r}, t)}{\partial t}, \tag{3.2}$$

$$\nabla \times \boldsymbol{E}(\mathbf{r}, t) = -\frac{\partial \boldsymbol{B}(\mathbf{r}, t)}{\partial t}, \tag{3.3}$$

$$\nabla \cdot \boldsymbol{B}(\mathbf{r}, t) = 0 \tag{3.4}$$

where $\mathbf{r}$ is a position vector and t represents a time scalar. Equation 3.1 relates charge density, ρ, to an electric field $\boldsymbol{E}$ and free space permittivity, ϵ_0, through Gauss' law. In Equation (3.2), Maxwell extended Ampére's original expression relating magnetic flux density, $\boldsymbol{B}$, and current density, $\boldsymbol{J}$, by adding the far right hand side term, $\mu\epsilon_0 \frac{\partial \boldsymbol{E}}{\partial t}$, known as displacement current, to account for time varying electric fields displacing electrons resulting in current. Equation (3.3) is a form of Faraday's law (through Stokes theorem) which states that a time-varying magnetic field produces a corresponding electric field. The relationship is such that the electric field lines produced tend to encircle the magnetic field lines. Equation (3.4), known as Gauss' Law, indicates that no net flux may emanate from any given region of space (magnetic

monopoles do not exist). Thus, the net magnetic flux, ϕ_B, through an arbitrary closed surface is always zero.

3.2.1.1 Simplifying Assumptions

These relations are general enough to account for electromagnetic waves ranging from radio to gamma radiation. However, in the study of electromechanical devices, wave phenomenon are often disregarded as the electrical excitation frequencies are usually low enough that the system may be regarded as quasi-static, or slowly varying with time. This means that although the time dependency of the magnetic induction term $-\frac{\partial \boldsymbol{B}}{\partial t}$ of Equation (3.3) is of interest during transient analyses, the magnetic field may be approximated by ignoring the displacement current term in Equation (3.2), as nearly all the energy will be stored in the magnetic field rather than an electric field. For example, electromagnetic devices are often not limited by the propagation speed of electromagnetic fields traveling at the speed of light because their dimensions are relatively small. As such, the general solution of a given problem without the quasi-static assumption will likely have some portion depending on a ratio between the system geometry and the speed of light, and may be approximated as zero. The result is an approximation that a slowly varying electric excitation produces only a slowly varying magnetic field. Generally speaking, either the electric or magnetic field will dominate over the other depending on the problem configuration. This fact is used to simplify the above complex relations to more practical expressions. For example, when a short circuit exists as in the case of a coil of wire, a large current typically exists and a large static magnetic field results. Accordingly, the displacement current is of negligible importance. In contrast, two isolated plates when excited with a constant electric potential result in an electric field but not a magnetic one, as the magnetic induction term is negligible. The quasi-static approximation allows the assumption that only one field is dominant and thus it is possible to de-couple the

electric and magnetic relations and only consider the dominant field. The revised Maxwell's equations with the quasi-static limit imposed for the case of a dominant magnetic field are shown below:

$$\nabla \cdot \boldsymbol{E}(\mathbf{r}, t) = \frac{\rho}{\epsilon_0}, \tag{3.5}$$

$$\nabla \times \boldsymbol{B} = \mu \boldsymbol{J}, \tag{3.6}$$

$$\nabla \times \boldsymbol{E} = -\frac{\partial \boldsymbol{B}}{\partial t}, \tag{3.7}$$

$$\nabla \cdot \boldsymbol{B} = 0 \tag{3.8}$$

Note that the displacement current in Equation (3.2) is no longer present in Equation (3.6), yet the magnetic field still has a time dependency through Equation (3.7). Material behavior is accounted for through the following constituent equations (neglecting temperature dependence, permanent magnets and relative motion):

$$\boldsymbol{B} = \boldsymbol{\mu} \boldsymbol{H} \tag{3.9}$$

$$\boldsymbol{J} = \sigma \boldsymbol{E} \tag{3.10}$$

where $\boldsymbol{\mu}$ represents material magnetic permeability and σ the material conductivity. When material saturation is considered (field intensity dependent) μ may be defined by a relation between magnetic field intensity, $\boldsymbol{H}$, and magnetic flux density, $\boldsymbol{B}$. Equation (3.10) represents the relationship between an electric field, $\boldsymbol{E}$, and applied current density, $\boldsymbol{J}$. Material conductivity, σ, may be assumed orthotropic, and thus a scalar quantity.

Equations (3.5) through (3.10) may be used to express the four vector fields $\boldsymbol{B}$, $\boldsymbol{H}$, $\boldsymbol{J}$ and $\boldsymbol{E}$ as Poisson's (or Laplacian) equations that may be numerically solved with finite element methods.

Magnetic Field Intensity By substituting (3.9) into (3.6) and taking the curl of both sides results in:

$$\nabla \times (\nabla \times \boldsymbol{H}) = \nabla \times \boldsymbol{J} \tag{3.11}$$

With constant permeability, Equation (3.8) $\Rightarrow \nabla \cdot \boldsymbol{H} = 0$. Thus, with the use of the identity:

$$\nabla \times (\nabla \times \boldsymbol{P}) = \nabla(\nabla \cdot \boldsymbol{P}) - \nabla^2 \boldsymbol{P} \tag{3.12}$$

where $\boldsymbol{P}$ is an arbitrary three dimensional field quantity. the left side of the above equation may be simplified to:

$$\nabla \times (\nabla \times \boldsymbol{H}) = -\nabla^2 \boldsymbol{H} \tag{3.13}$$

Using Equations (3.7), (3.10), the right side of (3.11) may be expressed as:

$$\nabla \times \boldsymbol{J} = \sigma \nabla \times \boldsymbol{E} = -\sigma\mu \frac{\partial \boldsymbol{H}}{\partial t} \tag{3.14}$$

which results in a partial differential equation (PDE) in Poisson's form [Kreyszig, 1993]:

$$\boxed{\nabla^2 \boldsymbol{H} = \sigma\mu \frac{\partial \boldsymbol{H}}{\partial t}} \tag{3.15}$$

Electric Field Taking the curl of both sides of (3.7) and using the identity in (3.12) results in :

$$\nabla \times (\nabla \times \boldsymbol{E}) = \nabla(\nabla \cdot \boldsymbol{E}) - \nabla^2 \boldsymbol{E} = -\nabla \times \frac{\partial \boldsymbol{B}}{\partial t} \tag{3.16}$$

Assuming constant permittivity and negligible static charge implies $\nabla \cdot \boldsymbol{E} = 0$ and thus:

$$\nabla^2 \boldsymbol{E} = \nabla \times \frac{\partial \boldsymbol{B}}{\partial t} \tag{3.17}$$

Using constituent Equations (3.6) and (3.10), the right hand side is simplified to:

$$\nabla \times \frac{\partial \boldsymbol{B}}{\partial t} = \mu \frac{\partial}{\partial t} \boldsymbol{J} = \mu\sigma \frac{\partial \boldsymbol{E}}{\partial t} \tag{3.18}$$

resulting in the Poisson PDE for an electric field:

$$\boxed{\nabla^2 \boldsymbol{E} = \sigma\mu \frac{\partial \boldsymbol{E}}{\partial t}} \tag{3.19}$$

Current Density Substituting (3.10) into (3.7) and taking the curl of both sides yields:

$$\nabla \times (\nabla \times \boldsymbol{J}) = -\sigma \frac{\partial}{\partial t} (\nabla \times \boldsymbol{B}) \tag{3.20}$$

Again using the identity in (3.12) with the $\nabla \cdot \boldsymbol{J}$ condition and substituting (3.6) into the right side results in:

$$\boxed{\nabla^2 \boldsymbol{J} = \sigma\mu \frac{\partial \boldsymbol{J}}{\partial t}} \tag{3.21}$$

Magnetic Flux Density The Poisson PDE for magnetic flux density is obtained by first substituting (3.10) into 3.6 yielding

$$\nabla \times \boldsymbol{B} = \sigma\mu \boldsymbol{E}. \tag{3.22}$$

Solving for $\boldsymbol{E}$, substituting the result into (3.7) and using (3.8) and (3.12) gives:

$$\boxed{\nabla^2 \boldsymbol{B} = \sigma\mu\frac{\partial \boldsymbol{B}}{\partial t}} \tag{3.23}$$

3.2.2 Magnetic Vector Potential

For the magnetic field solution of the actuator, 2D models are constructed with the commercially available FEA software, ANSYS, by ANSYS Inc. In all of the model types conducted, ANSYS utilizes the vector potential method for both static and transient cases to solve the equations previously defined. Here a potential representing the magnetic field is introduced as it is numerically easier to determine the vector potential than the magnetic field directly. The magnetic field $\boldsymbol{B}$ may be expressed as a magnetic vector potential $\boldsymbol{A}$ by observing that a magnetic field is divergence free as shown in Equation (3.8) (may be proven with the Biot-Savart law) and thus it may be stated that:

$$\nabla \cdot \boldsymbol{B} = 0 \Rightarrow \boldsymbol{B} = \nabla \times \boldsymbol{A} \tag{3.24}$$

For 2D cases, the flux density $\boldsymbol{B}$ has only in-plane components $\boldsymbol{B} = B_x\hat{i} + B_y\hat{j}$ and current density, $\boldsymbol{J} = J_z\hat{k}$ and potential $\boldsymbol{A} = A_z\hat{k}$ have only out of plane components. Thus, magnetic flux density may be expressed as:

$$\boldsymbol{B} = B_x\hat{i} + B_y\hat{j} = \frac{\partial A_z}{\partial y}\hat{i} - \frac{\partial A_z}{\partial x}\hat{j} \tag{3.25}$$

or

$$B_x\hat{i} = \frac{\partial A_z}{\partial y}\hat{i} \tag{3.26}$$

$$B_y\hat{j} = -\frac{\partial A_z}{\partial x}\hat{j} \tag{3.27}$$

Given $\nabla \times \boldsymbol{B} = \mu \boldsymbol{J}$, current density may be related to magnetic potential by:

$$\nabla \times \nabla \times \boldsymbol{A} = \nabla(\nabla \cdot \boldsymbol{A}) - \nabla^2 \boldsymbol{A} = \mu \boldsymbol{J} \tag{3.28}$$

However, the vector potential does not offer uniqueness. Any function with zero curl, or a gradient of a scalar function may be added to the potential $\boldsymbol{A}$ since the curl of a gradient is always zero. Thus, the divergence of $\boldsymbol{A}$, has no physical significance and may be chosen to be zero:

$$\nabla \cdot \boldsymbol{A} = 0 \tag{3.29}$$

This stipulation is known as the Coulomb gauge condition. Thus, Poisson's equation for the magnetic potential is found using the above condition and the identity (3.12):

$$\boxed{\nabla^2 \boldsymbol{A} = -\mu_0 \boldsymbol{J}} \tag{3.30}$$

Since there is no variation in the out of plane direction for 2D cases, Poisson's equation for the magnetic potential is found by equating out of plane terms,

$$\frac{\partial^2 A_z}{\partial x^2}\hat{j} + \frac{\partial^2 A_z}{\partial y^2}\hat{j} = -\mu J_z \hat{j} \tag{3.31}$$

Physically, magnetic flux (per unit length) is the difference in magnetic potential between any two points. Considering a 2D surface, S, and orthonormal contour, C, as shown in Figure 3.1, flux, ϕ, and potential are related through:

$$\phi = \int_S \boldsymbol{B} \cdot ds = \int_S \nabla \times \boldsymbol{A} \cdot ds = \oint_C \boldsymbol{A} \cdot d\ell \tag{3.32}$$

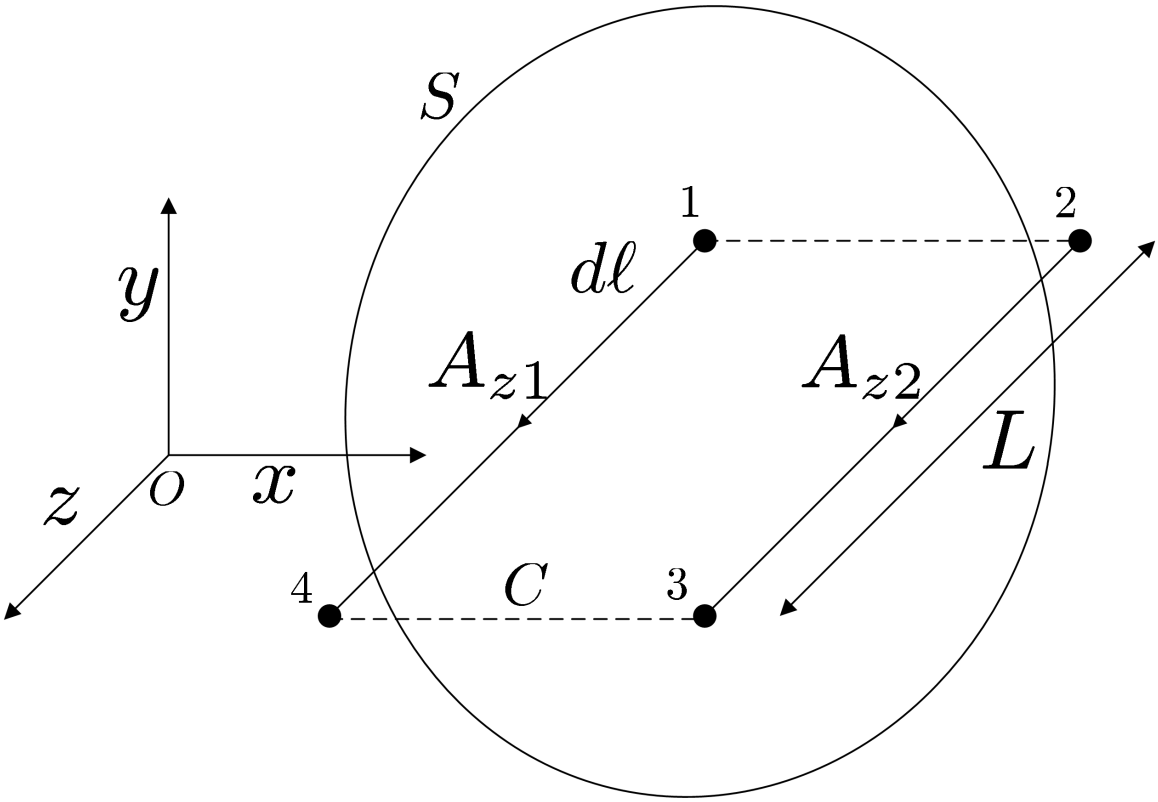

Figure 3.1: Magnetic vector potential interpretation as a the change in magnetic flux per unit depth for 2D geometry

Since there is no net contribution to the circulation integral where A_z is perpendicular to the path, C, flux is expressed as:

$$\phi = (A_{z1} - A_{z2})L \tag{3.33}$$

where L represents the depth of the system. Because flux is defined by the difference in potential, the potential must be explicitly defined (usually at the domain boundary) through a boundary condition.

3.2.2.1 Time Dependance

The magnetic potential is also applicable for time dependant fields. In such cases, a time varying electric potential (voltage) may be coupled to the magnetic domain. In the quasi-static case, the electric field $\boldsymbol{E}$ is a vector field which is always irrotational or has a zero curl component (proven with Coulomb's Law) and therefore is not influenced by time varying magnetic fields. This property may be used to transform the problem of solving for the vector $\boldsymbol{E}$ into a problem of solving for a scalar quantity known as the electric scalar potential, V. Since an irrotational vector may be represented as the gradient of a scalar function the electric field may be expressed as:

$$\boldsymbol{E} = -\nabla V \tag{3.34}$$

Substituting this expression into Equation (3.3) results in:

$$\nabla \cdot \boldsymbol{E} = \nabla \cdot (-\nabla V) = -\nabla^2 V = \frac{\rho}{\epsilon_0} \tag{3.35}$$

Which is known as Poisson's equation, or in non-conducting regions ($\rho = 0$), Laplace's equation. Thus the electric potential can be solved for with one differential equation and then related to $\boldsymbol{E}$ rather than solving for both the divergence and curl of $\boldsymbol{E}$.

Substituting Equation (3.24) into Faraday's law, equation (3.7), yields:

$$\nabla \times \boldsymbol{E} = -\frac{\partial}{\partial t}(\nabla \times \boldsymbol{A}) \tag{3.36}$$

or rearranging,

$$\nabla \times \left(\boldsymbol{E} + \frac{\partial \boldsymbol{A}}{\partial t} \right) = 0 \tag{3.37}$$

When written as the gradient of a scalar potential, V

$$\boldsymbol{E} = -\nabla V - \frac{\partial \boldsymbol{A}}{\partial t} \tag{3.38}$$

Equations (3.24) and (3.38) satisfy Maxwell's equations (3.7) and (3.8). Substituting Equation (3.10) into the expression for divergence free current density ($\nabla \cdot \boldsymbol{J} = 0$) results in:

$$\sigma \nabla \cdot \boldsymbol{E} = 0 \tag{3.39}$$

Substituting in Equation (3.38), the electric scalar potential yields:

$$\boxed{\nabla \cdot \left(-\nabla V - \frac{\partial \boldsymbol{A}}{\partial t} \right) = 0} \tag{3.40}$$

The finite element code (ANSYS) must also solve this equation.

Finally, the relations $\nabla \times \boldsymbol{H} = \boldsymbol{J}$ and Equations (3.9) and (3.10) are combined to yield:

$$\nu \nabla \times \boldsymbol{B} = \sigma \boldsymbol{E} \tag{3.41}$$

Substituting in the magnetic and electric potentials results in:

$$\nu \nabla \times (\nabla \times \boldsymbol{A}) = \sigma \left(-\nabla V - \frac{\partial \boldsymbol{A}}{\partial t} \right) \tag{3.42}$$

This may be simplified using the identity in Equation (3.12) and the Coulomb gauge condition to

$$\boxed{-\nu \nabla^2 \boldsymbol{A} + \sigma \frac{\partial \boldsymbol{A}}{\partial t} + \sigma \nabla V = 0} \tag{3.43}$$

It should be noted that equations (3.30), (3.40) and (3.43) will vary depending on the material properties. For conducting (steel and copper coil) regions, the following

equations result:

$$\nabla^2 \boldsymbol{A} = -\mu(\boldsymbol{H})\boldsymbol{J} \tag{3.44}$$

$$\nabla \cdot \left(\frac{\partial \boldsymbol{A}}{\partial t} - \nabla V \right) = 0 \tag{3.45}$$

$$\sigma \frac{\partial \boldsymbol{A}}{\partial t} - \frac{1}{\mu(\boldsymbol{H})} \nabla^2 \boldsymbol{A} + \sigma \nabla V = 0 \tag{3.46}$$

For nonconducting, or air regions, the following equations apply:

$$\nabla^2 \boldsymbol{A} = -\mu_0 \boldsymbol{J} \tag{3.47}$$

$$\nabla \cdot \left(\frac{\partial \boldsymbol{A}}{\partial t} - \nabla V \right) = 0 \tag{3.48}$$

$$\nabla^2 \boldsymbol{A} = 0 \tag{3.49}$$

3.2.3 Static Elements

The commercially available finite element software ANSYS was used to solve the magnetic potential PDEs by discretizing the model domain into appropriately configured elements. For the static models, two element types were used. The two dimensional element type PLANE13 is used throughout the iron and air regions. Although this element may be used in non-magnetic studies, the nodal degree of freedom (DOF) that is solved for in the static analyses is the magnetic vector potential in the z or normal direction. The PLANE13 quadrilateral element is defined by four nodes at each corner [ANSYS Inc., 2005]. Nonlinear magnetic materials are permitted by associating an appropriate property table with the element type. Magnetic forces are

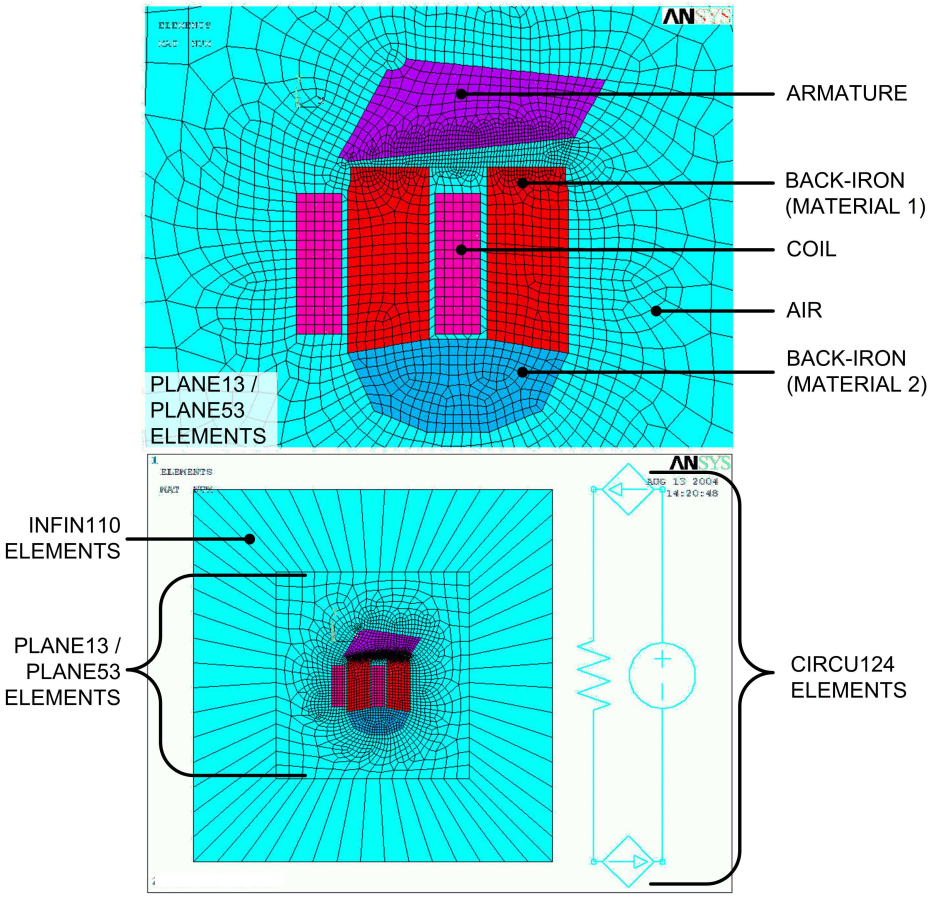

Figure 3.2: Static and transient model mesh and element types for the opener FEA model

determined using both a Maxwell stress tensor calculation and virtual work calculation on surfaces in contact with air regions by using a macro that recognizes surfaces that have been identified or 'flagged' for such force calculations. An example of the meshed opener magnetic path is shown in Figure 3.2 with a complete description of the modeling process provided in Chapter 4, Section 4.3. The elements making up the armature region of the model are identified for such a force calculation. A steady-state current density body load is applied to the elements which make up the coil region. Note that this element does not possess voltage forced capability. During simulation postprocessing, magnetic flux density is calculated with respect to the two

dimensions of the element co-ordinate system. Magnetic flux through the device is calculated by first defining a two point path. A macro then defines a pre-specified number of points along the path over which flux density is integrated. For all elements used, a default coordinate system orientation was used. These default systems are right-handed, orthogonal and parallel to the global cartesian coordinate system.

To model far-field decay without solving for a large amount of additional elements, a single layer of INFI110 infinite boundary elements were used to surround the air region of the actuator model. These elements use four nodes and shape functions which force the magnetic potential to zero at infinity [ANSYS Inc., 2005]. These elements have both four node and eight node capability and only offer the magnetic potential DOF. When used with PLANE13 elements, ANSYS documentation recommends using the four node option.

3.2.4 Transient Elements

The transient model elements used are similar to those of the static analyses, with a few minor exceptions. In order to simulate the response of predetermined voltage input, a model with a circuit coupled voltage source was used. Here, PLANE53 elements were used throughout the air, iron and coil regions instead of PLANE13. This element is defined by eight nodes, each possessing up to four possible DOFs. These include the magnetic vector potential, a time-integrated electric scalar potential, electric current, and electromotive force (EMF). It is these additional degrees of freedom that make PLANE53 applicable to low frequency transient electromagnetic-circuit coupled analyses. However, only the magnetic vector potential degree of freedom was considered through the air and iron regions. In the coil region, the electric current and EMF degrees of freedom were also activated to allow for nodal coupling to the circuit domain. The circuit consists of three CIRCU124 elements, each of a different configuration. CIRCU124 elements are based on Kirchhoff's Current Law with stiff-

ness matrices based on a lumped circuit model. Independent voltage source, stranded coil and resistor elements were meshed in series to represent the actuator circuit. The resistor was typically set to a value close to zero as it was only added to enhance model flexibility. The resistor only possesses a voltage degree of freedom. An independent voltage source was used to represent the actuator power supply. The voltage source element has voltage and current degrees of freedom. The voltage degrees of freedom are specified by terminating one node as a ground, or 0 V, and another node as a piecewise linear voltage function of time. This allows for the ability to input a simulated or measured voltage signal for direct comparison with other simulations or experiments. Finally, the stranded coil element has voltage, current and EMF degrees of freedom. The voltage degrees of freedom are coupled to the resistor and ground nodes. The EMF and current DOFs are coupled to a node in the coil region in the FEA domain. Similarly, all nodes in the coil region have the current and EMF DOFs coupled to one another. Physical coil properties are implied by the elements from the coil region FEA domain and specified material constants. As shown in Figure 3.2, INFIN110 elements were used to surround the air region, however, with the 8 node option activated, as recommended by ANSYS documentation for use with PLANE53 elements.

3.2.4.1 Eddy Currents

Eddy currents are characterized as local circulating currents which exist in the core material. These are physically existing currents produced within the material due to a time varying core flux. They may be thought of as a short circuit consisting of a coil wrapped around the external core material path in that the change in flux induces a current which in turn generates its own magnetic flux in the opposite sense (obeying Lenz's law) and ultimately opposes the change or rise of flux of the overall circuit. Thus, the observed flux rise or magnetization curve will be lower than the that of

the static case. The energy difference between the static and rapid field buildup is defined through resistive losses and hence heating. In summary, the two effects of eddy currents are: an internal magnetomotive force (MMF) is generated which tends to counteract the applied MMF and an irreversible heating loss of energy with the i^2 Joule heating losses in the core. Thus, greater changes in flux tend to generate more losses. A widening of the hysteresis loop is an indication of the eddy current magnitudes. They may be minimized by using materials with low conductivity and by laminating the core structure (through thin sheets) or sintered powder metallurgy techniques. The laminations succeed by increasing the circulating path length and by breaking the eddy current paths into many smaller loops with lower magnitude and subsequently reduce the counter flux generated. In the actuator studied, the back iron and armature are made from 0.3 mm silicon steel laminae to mitigate the effect of eddy currents. Eddy currents are not to be confused with the electrodynamic Amperian currents generated by electron spin which are used to explain material magnetism.

3.2.5 Element Shape Functions

Figure 3.3 illustrates the PLANE13, PLANE53 and INFIN110 elements. Coordinates s and t represent the local element nodal coordinate system. When the coordinates are used with the shape functions, they are normalized, going from -1.0 on one side of the element to +1.0 on the other. It should also be noted that s and t are not necessarily orthogonal to one another. The shape functions for the 2D magnetic vector potential (z component only) for each of the elements are as follows for PLANE13, PLANE53 and INFIN110 respectively:

$$\begin{aligned} A_{zPLANE13} &= \tfrac{1}{4}(A_{zI}(1-s)(1-t) + A_{zJ}(1+s)(1-t) \\ &\quad + A_{zK}(1+s)(1+t) + A_{zL}(1-s)(1+t)) \end{aligned} \tag{3.50}$$

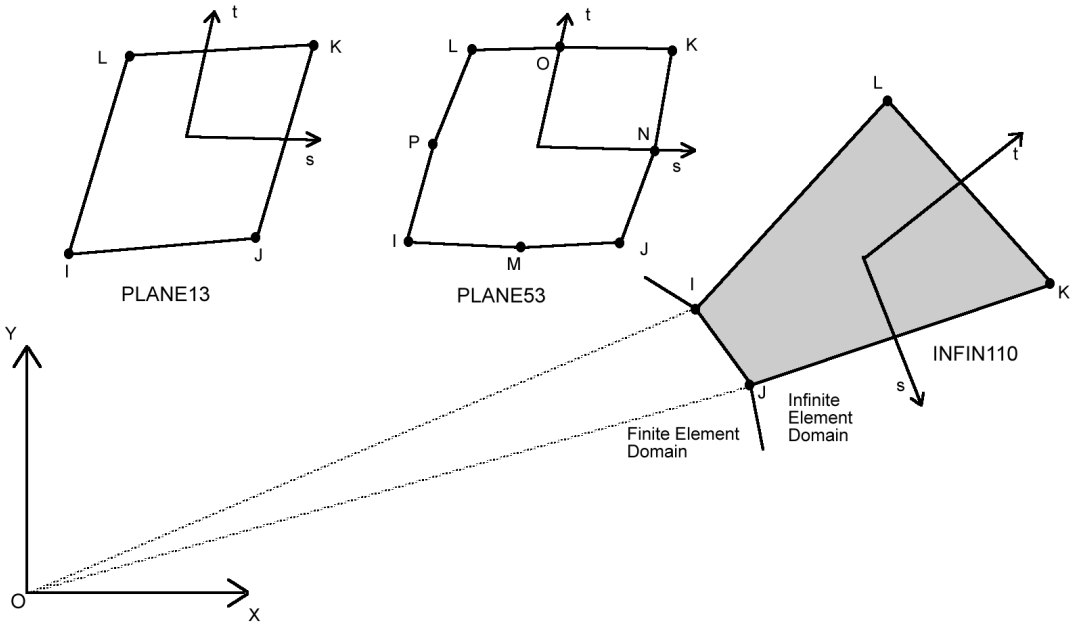

Figure 3.3: Element Configurations

$$\begin{aligned} A_{zPLANE53} &= \tfrac{1}{4}(A_{zI}(1-s)(1-t) + A_{zJ}(1+s)(1-t) \\ &\quad + A_{zK}(1+s)(1+t) + A_{zL}(1-s)(1+t)) \\ &\quad + \tfrac{1}{2}(A_{zM}(1-s^2)(1-t) + A_{zN}(1+s)(1-t^2) \\ &\quad + A_{zO}(1-s^2)(1+t) + A_{zP}(1-s)(1-t^2)) \end{aligned} \tag{3.51}$$

$$\begin{aligned} A_{zINFIN110} &= \tfrac{1}{4}(A_{zI}(1-s)(t^2-t) + A_{zJ}(1+s)(t^2-t)) \\ &\quad + \tfrac{1}{2}(A_{zK}(1+s)(1-t^2) + A_{zL}(1-s)(1-t^2)) \end{aligned} \tag{3.52}$$

The shape functions for voltage are analogous, and can be formed by substituting the scalar voltage with the magnetic vector potential terms. ANSYS assembles these functions for each element in shape function matrices. Hence the magnetic potential $\boldsymbol{A}$ and the scalar electric potential V may be represented by matrices $\boldsymbol{N_A}$ and $\boldsymbol{N}_V$

respectively:

$$\boldsymbol{A} = \boldsymbol{N_A}^T \boldsymbol{A_N} = \boldsymbol{N_A}^T \begin{bmatrix} 0 \\ 0 \\ \boldsymbol{A_{zN}} \end{bmatrix} \tag{3.53}$$

and

$$\boldsymbol{V} = \boldsymbol{N}_V^T \boldsymbol{V_N} \tag{3.54}$$

ANSYS then uses $\boldsymbol{N_A}$ to calculate the flux density as follows:

$$\boldsymbol{B} = \nabla \times \boldsymbol{N_A} \boldsymbol{A_N} \tag{3.55}$$

Where $\boldsymbol{A_N}$ and $\boldsymbol{V_N}$ are the nodal magnetic and electric potentials.

3.2.6 Solution Process

The FEA discretization process results in a series of simultaneous nonlinear equations that are numerically solved depending on the material properties (conductive, field intensity dependent) and if the system is time dependent or not. The following provides a brief overview of the solution procedure (see [ANSYS Inc., 2005, Chladny, 2003] for more details).

3.2.7 Matrix Assembly

After the 2D model is meshed and appropriate boundary conditions and loads are applied, ANSYS solves equations of the following form:

$$[C]\dot{\boldsymbol{d}} + [K]\boldsymbol{d} = \boldsymbol{J} \tag{3.56}$$

Where the degree of freedom vector is represented by

$$\boldsymbol{d} = \begin{bmatrix} \boldsymbol{A_z} \\ \boldsymbol{V} \end{bmatrix} \tag{3.57}$$

$\boldsymbol{A_z}$ represents the magnetic vector potential in the Z direction (into the model/page) as this is the only relevant potential direction for the 2D axis-symmetric case. Note that this is a relatively large vector as it represents all elements. $\boldsymbol{V}$ is the time integrated electric scalar potential, $\boldsymbol{V} = \int V dt$ which is input as a voltage excitation (if one exists).

Matrices $[C]$ and $[K]$ are the coefficient matrices defined as:

$$[K] = \begin{bmatrix} [K^L] + [K^N] + [K^G] & 0 \\ 0 & 0 \end{bmatrix} \tag{3.58}$$

and,

$$\begin{aligned} \left[K^L\right] &= \int_{Vol} (\nabla \times \boldsymbol{N_A}^T)^T \nu (\nabla \times \boldsymbol{N_A}^T) dV, \\ \left[K^N\right] &= \int_{Vol} (\nabla \times \boldsymbol{N_A}^T)^T \nu (\nabla \cdot \boldsymbol{N_A}^T) dV, \\ \left[K^G\right] &= 2 \int_{Vol} \tfrac{d\nu}{d|B|^2} (\boldsymbol{B}^T (\nabla \times \boldsymbol{N_A}^T))^T (\boldsymbol{B}^T (\nabla \times \boldsymbol{N_A}^T)) dV \end{aligned}$$

Where the element shape function matrices are integrated over their respected volumes. If the model is axis-symmetric, the element positions are mapped to the global coordinate system so that the appropriate volume can be derived for the entire actuator. As before, ν represents the reluctivity matrix, $[\mu]^{-1}$, but for the case of orthotropism, is considered a magnetic field intensity dependant scalar. The nonlinear input B-H cure is converted to a spline fit function of ν vs $|\boldsymbol{B}|^2$ from which the

derivative $\frac{d\nu}{d|B|^2}$ may be taken. The transient coefficient matrices are as follows:

$$[C] = \begin{bmatrix} \left[C^{AA}\right] & \left[C^{Av}\right] \\ \left[C^{Av}\right] & [C^{vv}] \end{bmatrix} \tag{3.59}$$

where,

$$\begin{aligned} \left[C^{AA}\right] &= \int_{Vol} \boldsymbol{N_A} \sigma \boldsymbol{N_A}^T dV, \\ \left[C^{Av}\right] &= \int_{Vol} \boldsymbol{N_A} \sigma \nabla \cdot \boldsymbol{N}_V^T dV, \\ [C^{vv}] &= \int_{Vol} (\nabla \cdot \boldsymbol{N}_V^T)^T \sigma \nabla \cdot \boldsymbol{N}_V^T dV \end{aligned}$$

For static analyses (no time dependant potentials or fields), only the K matrices and magnetic vector potential DOFs are required as Equations (3.44) through (3.49) will be further simplified when $\boldsymbol{B}$ is time invariant.

The load vector is defined as:

$$\boldsymbol{J} = \begin{bmatrix} \int_{Vol} \boldsymbol{J_s} \boldsymbol{N_A}^T dV \\ \int_{Vol} \boldsymbol{J_t} \boldsymbol{N_A}^T dV \end{bmatrix} \tag{3.60}$$

Where $\boldsymbol{J_s}$ is the source current density vector (also referred to as current segments) and $\boldsymbol{J_t}$ is the total current density vector. The total current density vector is equal to the summation of the source currents, eddy currents, $\boldsymbol{J_e}$ and induced velocity currents, $\boldsymbol{J_v}$, (not present as the armature is fixed in all simulations).

$$\boldsymbol{J_t} = \boldsymbol{J_e} + \boldsymbol{J_s} + \boldsymbol{J_v} \tag{3.61}$$

The eddy current density vector is solved for through the conductivity matrix, $[\sigma]$ and rate of change of magnetic potential:

$$\boldsymbol{J_e} = -[\sigma]\frac{\partial A_z}{\partial t} \tag{3.62}$$

$$= -[\sigma]\frac{1}{n}\Sigma_{i=1}^{n}\boldsymbol{N_A}^T\boldsymbol{A_e} \tag{3.63}$$

where $n = 4$ is the number of integration points for the quadrilateral elements and $\boldsymbol{A_e}$ is the magnetic vector potential time derivative. The source current is related to the electric scalar potential as:

$$\boldsymbol{J_s} = -[\sigma]\nabla \cdot V \tag{3.64}$$

$$= [\sigma]\frac{1}{n}\Sigma_{i=1}^{n}\nabla \cdot \boldsymbol{N}^T\boldsymbol{V_N} \tag{3.65}$$

where $\boldsymbol{N}$ is the element shape functions for the electric scalar potential $\boldsymbol{V_N}$ at the integration points.

3.2.8 Static Model Solution

As shown in the previous section, the FEA discretization process results in a series of simultaneous nonlinear equations as represented by Equation (3.56). For static models, the time dependant magnetic potential vector and coefficient matrices can be disregarded and an incremental Newton-Raphson method is used to solve nonlinear systems by:

$$[K_{n,i}^T]\Delta\boldsymbol{A_{z,i}} = \boldsymbol{J_n} - \boldsymbol{J_{n,i}^{nr}} \tag{3.66}$$

Where $[K_{n,i}^T]$ is the Dirichlet matrix for sub-step n, and iteration i. $\boldsymbol{A_{z,i}}$ is the magnetic potential vector at iteration i and $\Delta\boldsymbol{A_{z,i}} = \boldsymbol{A_{z,i+1}} - \boldsymbol{A_{z,i}}$. $\boldsymbol{J_n}$ is the applied current density vector for a given sub-step, n, and $\boldsymbol{J_{n,i}^{nr}}$ is referred to as the resisting

load vector which is calculated from element magnetic fluxes. The right-hand side of Equation (3.66) is referred to as the residual or out-of-balance load vector and represents the amount the system is out of equilibrium. A predetermined number of sub-steps are required for solution convergence when the system is highly nonlinear or path-dependent. These intermediate steps are performed so that the final current density vector $\boldsymbol{J}$ is achieved by applying it in increments. At each sub-step the Newton-Raphson procedure is performed by assuming a potential vector $\boldsymbol{A_{z,o}}$, which is usually obtained from the last converged iteration, $\boldsymbol{A_{z,i}}$. An updated coefficient matrix, $[K^T_{n,i}]$ and load vector, $\boldsymbol{J^{nr}_{n,i}}$ are determined from the magnetic potential vector, $\boldsymbol{A_{z,i}}$. Next $\Delta\boldsymbol{A_{z,i}}$ is solved for from Equation (3.66). Then $\boldsymbol{A_{z,i+1}}$ is computed by adding $\Delta\boldsymbol{A_{z,i}}$ to $\boldsymbol{A_{z,i}}$ or $\boldsymbol{A_{z,o}}$ if it is the first iteration. These equilibrium iterations are repeated until convergence is achieved for each sub-step and the current density vector is fully applied. Convergence checking can be based on either magnetic potentials, current segments, or both. However, for 2D models, ANSYS recommends convergence to be determined by current segments as:

$$\sqrt{\sum(\boldsymbol{J} - \boldsymbol{J^{nr}_i})^2} < \zeta_J J_{Ref} \tag{3.67}$$

Where ζ_J is a specified tolerance of a typical current segment value, J_{Ref}, which is taken as $\|\boldsymbol{J}\|$. For magnetic potential convergence, ANSYS compares the change in nodal potential values between successive equilibrium iterations to a similar criterion as above.

3.2.9 Transient Model Solution

For the transient models, a generalized trapezoidal rule

$$\boldsymbol{A_{z,n+1}} = \boldsymbol{A_{z,n}} + \Delta t \dot{\boldsymbol{A}}_{\boldsymbol{z,n+1}} \tag{3.68}$$

is used to numerically integrate Equation 3.56 over a series of pre-specified time steps, $\Delta t = t_{n+1} - t_n$ prior to the application of the incremental Newton-Raphson method as discussed in the static analyses. A sufficiently small time step is required to ensure the applied voltage load waveform is captured and for solution convergence. The magnetic potentials at time t_n are represented by $\boldsymbol{A_{z,n}}$ and the respective time derivative $\dot{\boldsymbol{A}}_{\boldsymbol{z,n}}$ is calculated at the previous time step. Substituting the trapezoidal approximation at time t_{n+1} into Equation 3.56 results in:

$$\left(\frac{1}{\Delta t}[C] + [K]\right) \boldsymbol{A_{z,n+1}} = \boldsymbol{J} + \frac{1}{\Delta t}[C]\boldsymbol{A_{z,n}} \tag{3.69}$$

This equation set is then solved in a similar fashion to the static models. However, sub-steps are now replaced with a time step, (ie. the load is no longer ramped). Therefore, to ensure convergence, a sufficiently small time step size must be used. Upon calculation of $\boldsymbol{A_{z,n+1}}$, Equation (3.68) is used to update $\dot{\boldsymbol{A}}_{\boldsymbol{z,n+1}}$.

3.3 Lumped Parameter Modeling

Although FEA techniques are ideal for providing accurate field solutions to relatively complex nonlinear and coupled problems, the time and computational resources required are potentially untenable. Additionally, the models are not conducive to application of modern control design. As a result, a simplified lumped parameter model is sought that sufficiently describes the actuator behavior yet is still computationally simple enough to incorporate into a real-time control algorithm. The actuator may be characterized by electromagnetic and mechanical subsystems as discussed in the following sections and shown schematically in Figure 3.4.

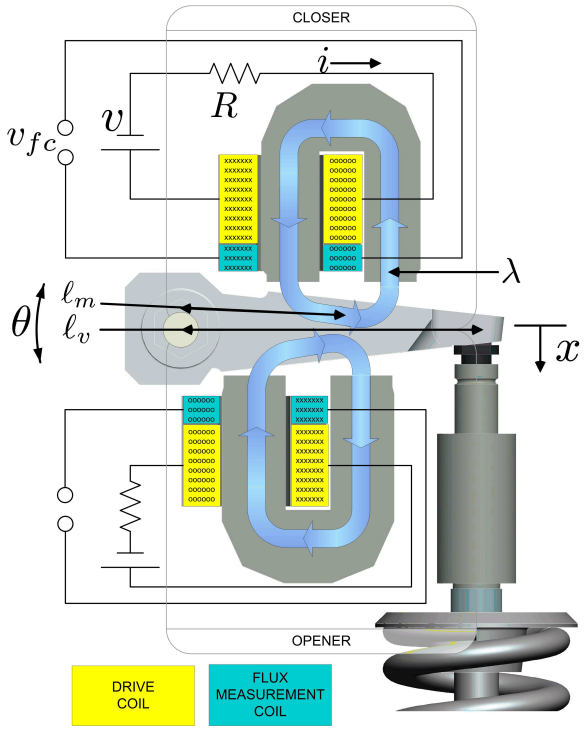

Figure 3.4: Cross-sectional schematic of hinged actuator indicating armature motion and magnetic flux

3.3.1 Reluctance Network

A common approach to modeling magnetic circuits is through construction of a reluctance network. Often, linear induction is assumed so that the relative permeabilities of the backiron and armature materials are independent of field intensity. For most magnetic devices, this assumption is reasonable for lower field intensities. Since the linear permeability of steel is approximately 1000 times greater than air, the steel material properties are expected to be of little significance in the inductance calculation at large air gaps (or prior to the onset of saturation). Upon material saturation, the steel permeability is the same as free space, μ_0, or air, and hence the reluctance of the steel flux path lengths become as significant as the air gaps. Saturation is expected to occur at relatively large excitation levels and small air gaps, as it is at those operating points where the magnetic field intensity will be greatest.

By taking advantage of the linear permeability relationship, $B = \mu_r H$, between flux density B, and applied field intensity, H, flux may be related to the material properties as:

$$\phi = \mu_r H A_{path} \tag{3.70}$$

where A_{path} is the path cross sectional area. Note that for nonlinear or saturable materials $\mu_r = \mu_r(H)$. H can be related to the number of turns of the coil, N, the current, i, and the length of the flux path, l by:

$$H = \frac{Ni}{l} = \frac{M}{l} \tag{3.71}$$

where M is the magnetomotive force (MMF). Equation 3.70 can now be rearranged as:

$$\phi = \frac{\mu_r A_{path} N i}{l} \tag{3.72}$$

This expression can be used to discretize the geometry and material of a linear magnetic device which results in a network of regions that can be solved in a similar fashion as classical circuit analysis. Thus, flux for a device consisting of n different linear materials in series can be expressed as:

$$\phi = \sum_{i=1}^{n} \frac{\mu_j A_j N i_j}{l_j} \tag{3.73}$$

In such cases, each of the elements are analogous to resistors in an electric circuit. In magnetic terms, they are cumulatively known as the system reluctance, $\Re$, where

$$\Re = \frac{M}{\phi} = \frac{Hl}{\phi} = \frac{Bl}{\mu_r \phi} = \frac{l}{\mu A} \tag{3.74}$$

or by definition of inductance, $\Re = \frac{N^2}{L}$. Note that in devices with air gaps, it is often possible to neglect the reluctance of materials with high permeability much in the

same way the resistance of wires in an electric circuit can often be neglected. Consequently, for devices such as solenoids, flux linkage, $\lambda = \lambda(x, i)$, is highly dependant on the air gap, or position of the armature, as well as current excitation or MMF. Flux can finally be stated as:

$$\phi(x, i) = M \sum_{j=1}^{n} \frac{1}{\Re_j} \tag{3.75}$$

Where the magnetic system is discretized into n regions of unique reluctance elements, $\Re_j$.

3.3.2 Nonlinear Induction

As a means of providing an accurate inductance model, magnetic material saturation is considered. Saturation effects will be present at high MMF values, particularly at small armature/pole face air gaps and/or high current excitation [Chladny et al., 2005]. The following function is intended to approximate the net magnetic circuit flux linkage response with magnetic material saturation as in [Ilic'-Spong et al., 1987]:

$$\lambda(x, i) = \psi(1 - e^{-ig(x)}), \tag{3.76}$$

where,

$$g(x) = \frac{\beta}{\kappa - x} + \alpha. \tag{3.77}$$

The parameters ψ, β, κ and α are identified with MATLAB using a nonlinear least squares fit to the FEA model data. Specifically, the `nlinfit.m` m-function uses the Gauss-Newton algorithm with Levenberg-Marquardt modifications for global convergence.

3.3.3 Electric Coupling

By making use of Kirchhoff's second law and Faraday's law, a differential equation relating a DC source, coil resistance and flux linkage may be expressed as

$$v_{Source} = Ri + \frac{d\lambda(i,x)}{dt} \tag{3.78}$$

Eddy currents are not modeled as preliminary FEA modeling and experimental tests indicated negligible contribution to overall current response [1]. A lumped parameter method of accommodating eddy currents using FEA data was developed for a similar actuator in [Chladny et al., 2005].

3.3.4 Magnetic Co-energy

When the actuator armature moves, energy is exchanged among three forms. Namely, the mechanical system, the electrical system and the magnetic field. It is possible to consider an energy balance of the entire system when observing the nature of the force development so that a complex field analysis may be avoided [Schmitz and Novotny, 1965]. The general energy balance equation for the three systems may be expressed as:

$$\Delta W_e = \Delta W_c + \Delta W_m \tag{3.79}$$

where ΔW_e, ΔW_c, ΔW_m represent changes in electrical, magnetic and mechanical energies respectively.

Since mechanical force may be expressed as a change of energy over a change in

[1] The actuator back iron and armature are constructed from laminated silicon steel sheets. The laminations succeed by breaking the eddy current paths into many smaller loops with lower magnitude and subsequently reduce the counter flux generated.

displacement, Δx the average force on the armature may be stated as:

$$F_{avg}\Delta x = \Delta W_m \tag{3.80}$$

Implicitly, it may be observed from Equation 3.79 that for any given position, the mechanical energy may be determined from either magnetic flux linkage, λ, or electrical current, i. Thus, the average force may be expressed as:

$$F_{avg} = \frac{\Delta W_e(i,x)}{\Delta x} - \frac{\Delta W_c(i,x)}{\Delta x} \tag{3.81}$$

or

$$F_{avg} = \frac{\Delta W_e(\lambda,x)}{\Delta x} - \frac{\Delta W_c(\lambda,x)}{\Delta x} \tag{3.82}$$

For a simple air-coil-resistor circuit, W_c can be expressed as the stored energy in the coil over a change in time, $\Delta t = t_2 - t_1$, as:

$$W_c = \int_{t_1}^{t_2} iV_{Coil}dt \tag{3.83}$$

Using Faraday's law of induction, $V_{Coil} = \frac{d\lambda}{dt}$, yields:

$$W_c = \int_{t_1}^{t_2} \frac{d\lambda}{dt} idt = \int_{\lambda_1}^{\lambda_2} id\lambda \tag{3.84}$$

For such linear systems, the relationship between flux linkage, λ, and current, i is often expressed as the coil self-inductance, L as:

$$L = \frac{\lambda}{i} \tag{3.85}$$

Inductance is analogous to mechanical inertia or mass as it resists any change in current due to an applied voltage, just as a mass resists a change in velocity due to

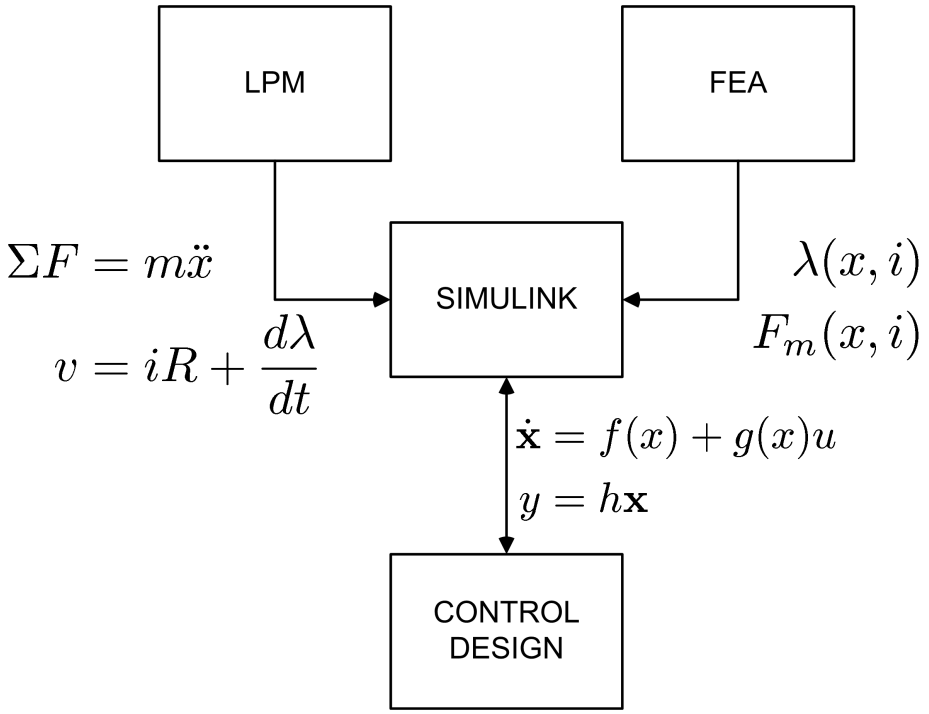

Figure 3.5: Schematic of Simulink modeling process

an applied force. If the system is excited from $\lambda_1 = 0$, the stored field energy may be expressed as:

$$W_c = \int_0^{\lambda} id\lambda = \frac{1}{2}Li^2 \tag{3.86}$$

3.4 Simulink Model

As a means of hybridizing the accuracy of a FEA field solution with the expedient solution time and flexibility of a LPM, a MATLAB-Simulink model of the actuator system is designed. The intent of this model is to accurately represent the actuator system for control algorithm evaluation. Perhaps the most significant aspect of the modeling approach is the use of FEA generated data in look-up tables to simulate the electromagnetic response. Here, flux and force FEA data are input with respect to armature position and excitation current. Faraday's equation is numerically integrated to derive flux linkage subject to applied coil voltage and coil resistance. As Figure 3.5

indicates, the model may be considered a LPM-FEA hybrid model as, technically, it is neither but incorporates elements of both in an attempt to use the accuracy of a field solution with the computational simplicity of solving a system of ODEs. Thus, it has greater accuracy than a strictly ODE based model, but is not amenable to analytic control design. Rather, its primary purpose is to simulate the experimental testbench conditions for evaluating control performance with model-plant mismatch. After models of the circuit and mechanical dynamics were implemented and experimentally validated (see Chapter 6), representations of the power electronics and gas force dynamics were added. Descriptions of the sub-models are provided in Chapter 4. Due to the coupled multi-disciplinary nature of the model and the switched nature of the power electronics, a stiff solver was used. In such instances, MATLAB recommends use of the multi-step solver `ode15s` based on numerical differentiation formulas (NDFs) [Shampine and Reichelt, 1997].

3.5 Differential Flatness

The feedback control algorithm used in this work exploits a property of the actuator system known as "flatness" as first outlined in [Martin, 1992, Fliess et al., 1992] using differential algebraic techniques. Most simply stated, a system may be considered (differentially) flat if the state(s) and input(s) may be expressed explicitly as a function of the 'flat' output(s) and a finite number of output time derivatives [Lévine, 2004, Martin et al., 1997]. More specifically, a system, $\dot{x} = f(x, u)$, may be considered flat provided the state variables, $x \epsilon \mathbb{R}^n$, and inputs, $u \epsilon \mathbb{R}^m$, can be parameterized by an m-dimensional flat output $y \epsilon \mathbb{R}^m$ of the form:

$$y = \gamma\left(x,\ u,\ \dot{u}, \ldots,\ u^{(\alpha)}\right), \tag{3.87}$$

satisfying:

$$x = \phi\left(y, \ldots, y^{(\beta)}\right)$$
$$u = \psi\left(y, \ldots, y^{(\beta)}\right) \tag{3.88}$$

The outputs may correspond to physically measurable parameters or to some fictitious output. This endogenous feedback results in an equivalent linearization such that an expression of the system dynamics can be related to the output without the need for numerical integration [Mercorelli et al., 2003, Martin et al., 1997]. Figure 3.6 provides a graphical representation of how a trajectory may be designed in flat output space, then one-to-one mapped (smoothly) to the original input and state space. Consequently, the property is useful for solving motion planning and control tracking problems since the problem of solving a dynamic system is reduced to an algebraic (non-differential) one [Fliess et al., 1995]. Many mechanical systems may be characterized as being differentially flat [Murray et al., 1995]. For example, linear controllable systems are flat as well as input-output linearizable systems (by definition). Although no necessary and sufficient conditions have yet been determined, some equivalence theorems exist [Rathinam and Sluis, 1995, van Nieuwstadt et al., 1994]. As a result, in most cases the only way to demonstrate that a system is flat is through finding an appropriate output (or set thereof) that satisfy the conditions (3.87) and (3.88). The flatness definition in (3.87) was later extended using differential geometry techniques to include outputs with infinite coordinate dependance [Fliess et al., 1999] and time transformations or orbital flatness [Fliess et al., 1994].

3.6 Summary

The preceding sections briefly summarize the key analytic and numerical tools used during the course of the actuator modeling and control. Specifically, Maxwell's general

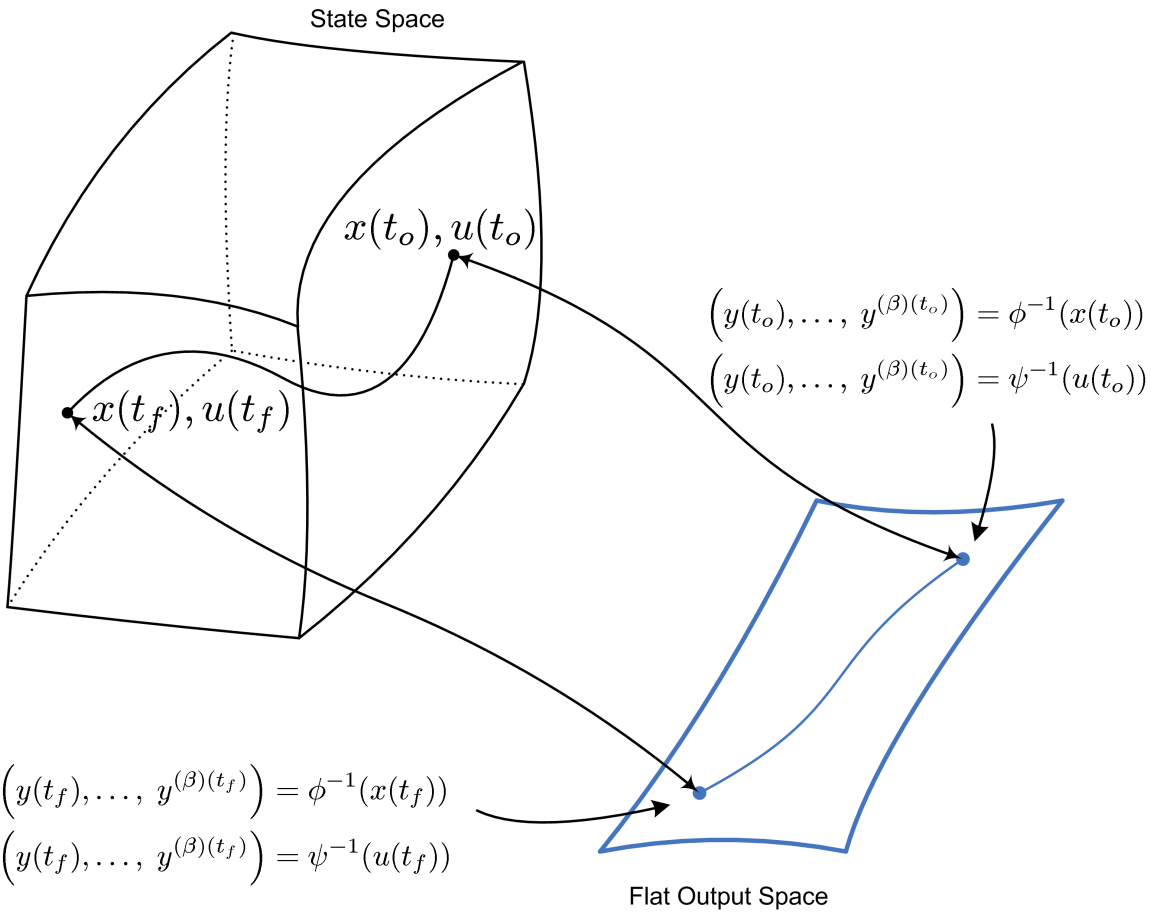

Figure 3.6: Correspondence between flat output space and state space [Chung, 2005]

equations are subjected to the quasi-static approximation and the magnetic vector and electric scalar potentials are used to provide differential equations which govern air and iron regions of a 2D system. ANSYS applies these equations over discretized regions and assembles them into a system of equations which are then solved using a Newton-Raphson procedure. As well, methods of modeling magnetic circuits for the purpose of control design are outlined. The hinged actuator is simulated using the MATLAB-Simulink numerical solving environment for preliminary control performance evaluation. Finally, the concept of differential flatness is summarized which provides a system characterization framework that allows for trajectory planning and tracking development without the need for numerical integration. The remaining

chapters will expand on these techniques and the assumptions used in the context of the hinged solenoid actuator system and in contrast to experimentally measured results.

Chapter 4

Modeling and Simulation

4.1 Introduction

As part of the overall goal for implementation of the hinged actuator on a single cylinder research engine, extensive modeling and simulation are conducted for control design and visualization purposes. Solid modeling is performed as part of the finite element analysis and testbench design. Finite element and lumped parameter models are developed and experimentally validated for control design purposes. The results of the these models are implemented in a MATLAB-Simulink model that also includes representations of the power electronics and exhaust gas force disturbances to further improve model scope and fidelity. A strong emphasis is placed on modeling in part due to the nonlinear control algorithms used. Controllers derived through feedback linearization techniques are model dependant and thus poor model fidelity could adversely affect performance. All models are essential in the development, evaluation and debugging of potential control algorithm candidates prior to hardware implementation.

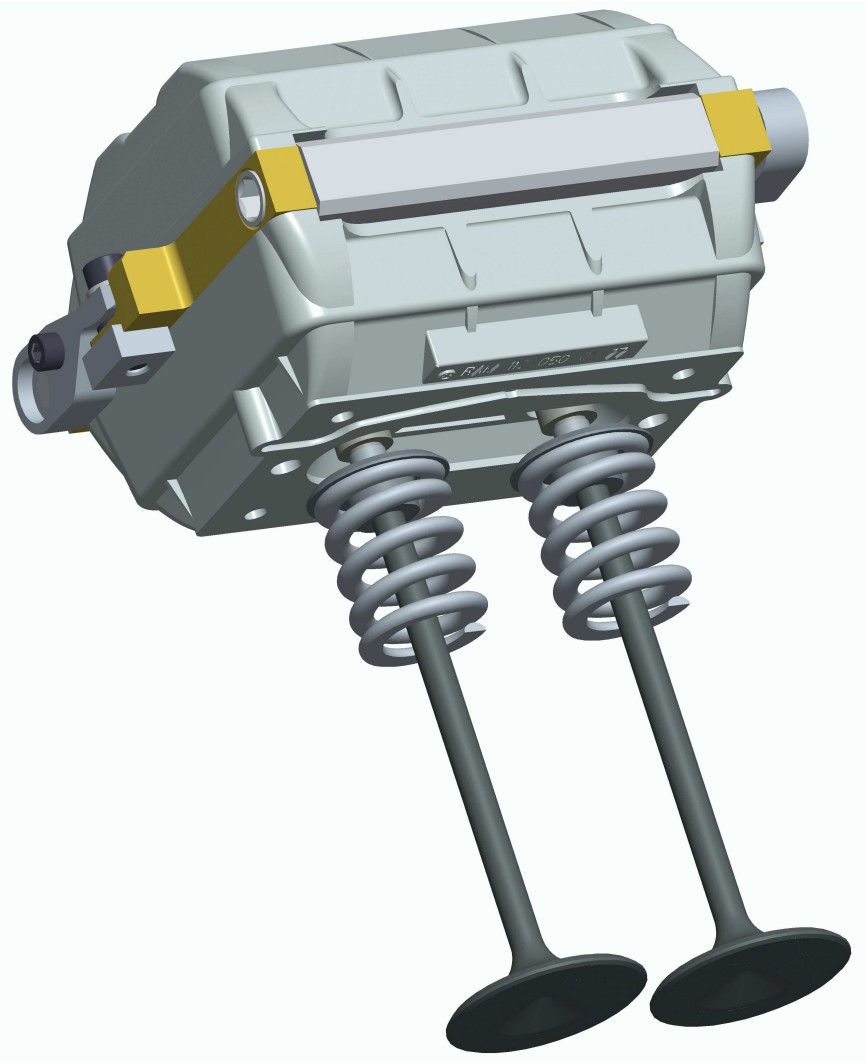

Figure 4.1: 3D solid model of the prototype actuator

4.2 3D Solid Modeling

An accurate geometric representation of the prototype actuator is desired for modeling, experimental design and visualization purposes. A model of a cylinder head is also required for the testbench and custom single cylinder engine designs. The modeling package Pro/Engineer, by Parametric Technology Corporation (PTC), is used to generate models of the actuator, cylinder head and related experimental hardware. The armature and back-iron geometry is exported from Pro/E to ANSYS to

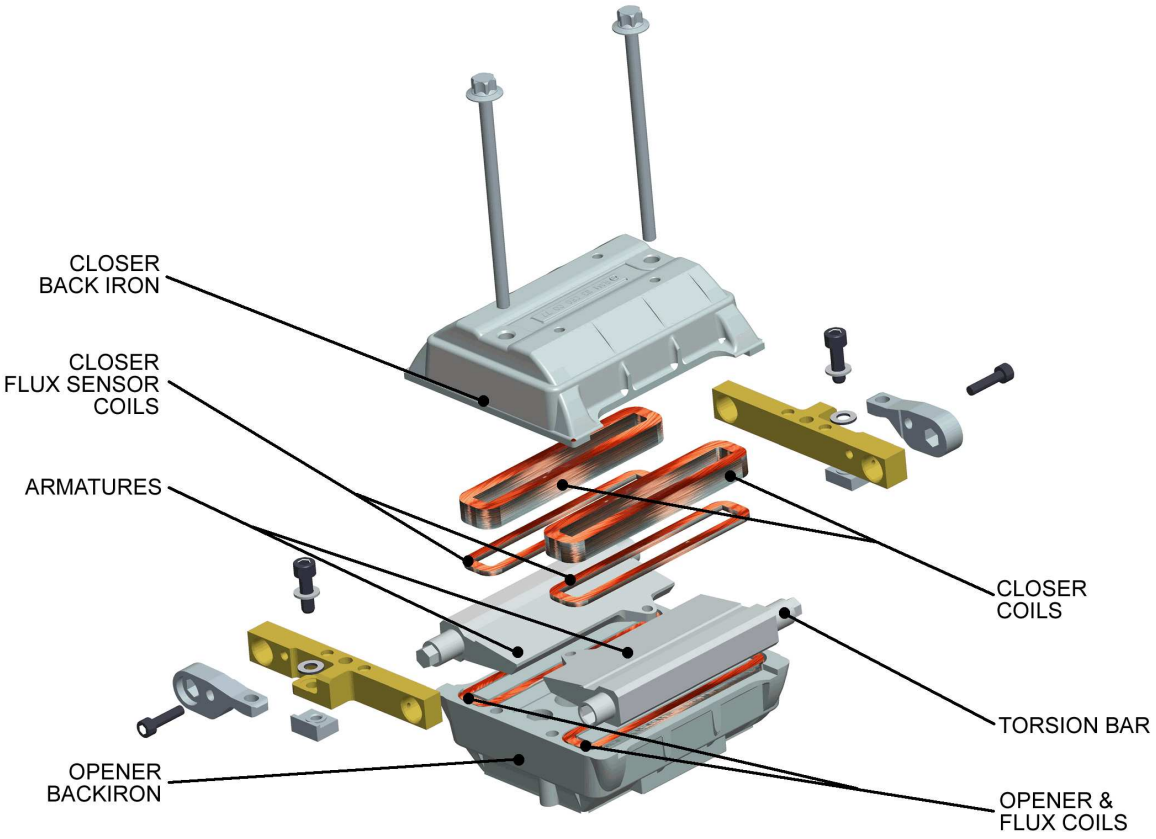

Figure 4.2: 3D solid model of the actuator, exploded view

simplify the input during geometry definition. An example of the modeled actuator unit is shown in Figure 4.1. An exploded view of the actuator and two actuator units mounted to a cylinder head and cylinder are provided in Figures 4.2 and 4.3, respectively. The intake and exhaust actuator units differ slightly to accommodate differences between intake and exhaust valve requirements (such as spring stiffness and valve geometries). Although there are two valve actuators per actuator unit (for a four valve cylinder head), the actuation operations need not be coupled.

The model of the armature is also used in solid mechanics type finite element analysis (using PTC's Pro/Mechanica analysis software) to investigate the effect of torsion bar deflection on nominal magnetic airgap.

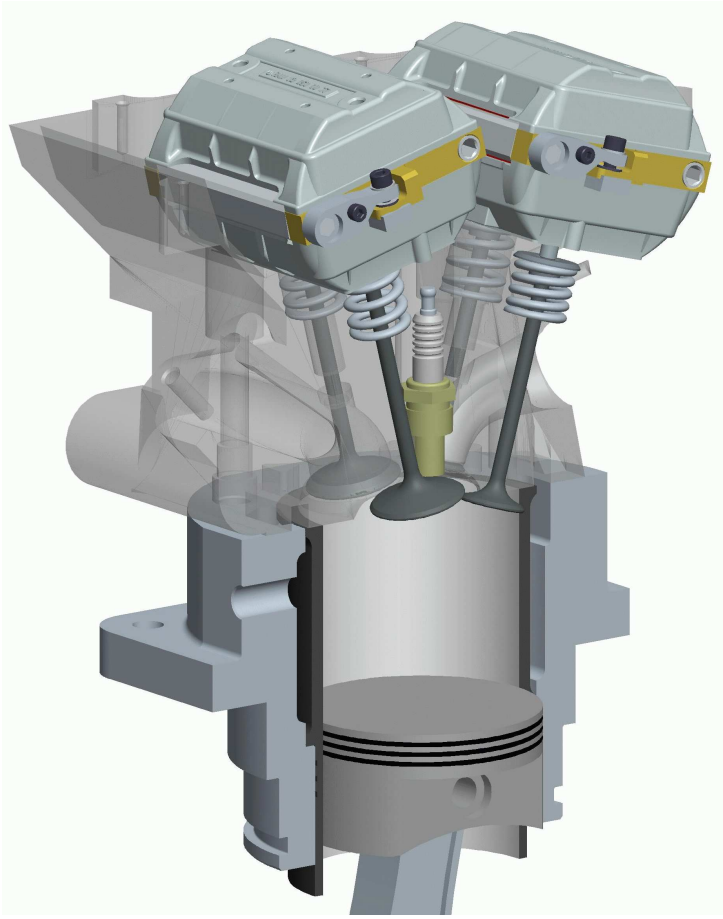

Figure 4.3: 3D solid model of the actuator, cylinder head and custom engine cylinder

4.3 Finite Element Modeling

Two dimensional representations of the opener and closer are separately modeled to minimize model complexity and computational time and because they have different geometry. Due to flux path geometry, the magnetic field is expected to vary most significantly in only two dimensions. The 2D simplification may be justified provided the actuator has a sufficiently large depth, small air gap and minimal eddy currents [Takahashi et al., 1991]. The actuator in this study has a depth over eight times greater than the flux path width and is constructed from laminate silicon steel sheets (0.3 mm thick) for eddy current suppression. The maximum air gap is approximately

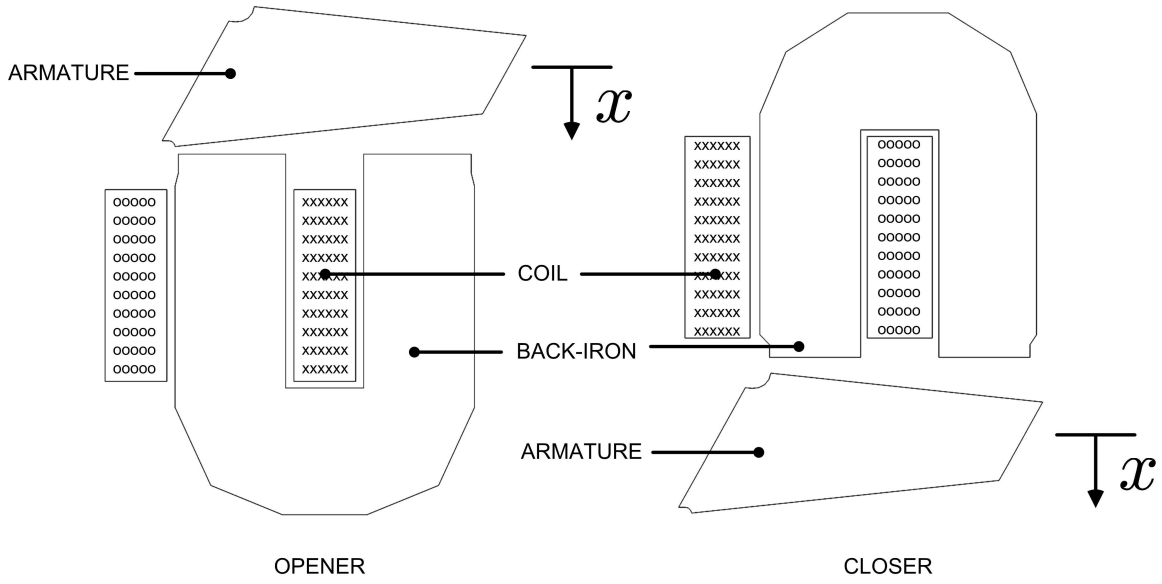

Figure 4.4: Modeled actuator flux path sections

the same as the flux path width. Using 2D geometry for the 3D actuator assumes that the more complex 3D eddy current paths during transients and fringing in the corners of the back iron and armature are negligible. Aside from the added computational load, full 3D analyses are also subject to potentially greater accuracy and convergence issues [Prieto et al., 2005]. Additionally, no flux path scaling or transformation is required since the modeled and actual flux path areas are the same (since the device is not modeled as axis-symmetric) [Li and McEwan, 1993]. The simplification of modeling the opener and closer components separately is justified through the high permeability of the armature, relatively large distance between the two magnets, and since in practice, only one coil is active at any time. Although similar data could be gathered through experimental studies, a more expedient design process would be to simulate the actuator response and control performance prior to prototype fabrication and evaluation. Figure 4.4 illustrates the modeled opener and closer coil and steel cross-sections that will most significantly influence the flux path. In both static and transient studies, reference is made to air gaps or the distance from the armature to

Table 4.1: Air gap and excitation operating points

Air gaps [mm]									
0.02	0.03	0.05	0.07	0.10	0.13	0.20	0.33	0.49	0.66
0.99	1.32	1.98	2.63	3.29	3.95	4.61	5.27	6.58	8.00
Coil excitations / MMF [Ampere-turns]									
10	25	50	100	200	300	400	500	600	800
1000	1250	1500	1750	2000	2250	2500	3000	3750	5000

the respective magnet pole face. Due to the hinged nature of the actuator, the air gap distance is ambiguous and therefore all air gap references are made with respect to valve position. For example an opener air gap of 0.50 mm corresponds to a valve position that is 0.50 mm away from being fully opened (or $x = 3.50$ mm). Similarly, a closer air gap of 1.50 mm corresponds to a valve position that is 1.50 mm away from being fully closed (or $x = -2.50$ mm). This is done to explicitly acknowledge the affect the air gap has on the magnetic response while still referencing a state variable.

4.3.1 Static Modeling and Simulation

Static 2D models of the opener and closer are created using geometry generated from Pro/Engineer and the ANSYS Parametric Design Language (APDL). For each operating point, macros are called from a submitted batch file that assigns appropriate geometry, mesh, material properties, boundary conditions and current excitations. The resulting force and flux data are exported to file for further processing with MATLAB. Results for the opener are determined for each of the operating points listed in Table 4.1 for a total of 400 static solutions. The operating points were selected to provide a relatively smooth force and flux relation as a function of air gap and current. A higher number of data points are required for a smooth data set at low air gaps due to the dramatic change in magnetic flux and force in these regions. Similarly, due to material saturation, a higher resolution of data are required at

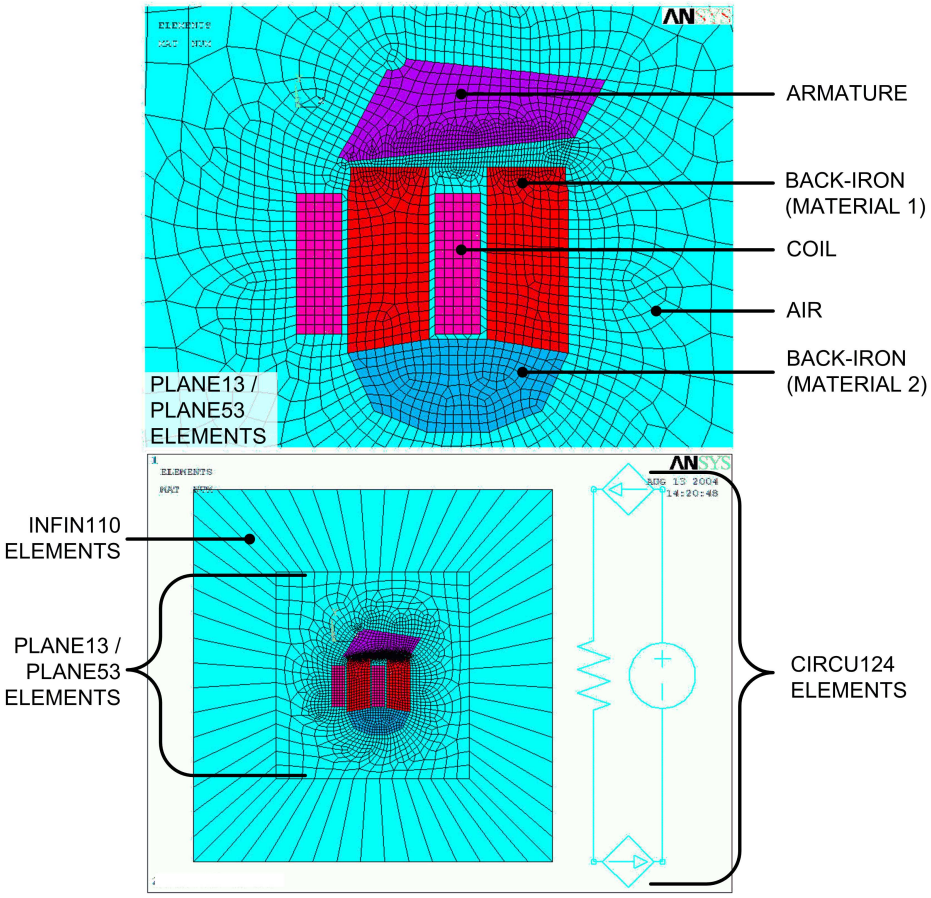

Figure 4.5: Static and transient model mesh and material types for the opener FEA model

lower excitation. Mesh refinement is determined by inspection as well as by ensuring force and flux convergence with respect to an increase in element density. In order to prevent elements with poor aspect ratios, active mesh control is established in the back iron, armature and air gap regions in addition to the model boundaries. The default auto-mesh generator is used to mesh the remaining regions with the finest mesh refinement possible. In order to ensure appropriate element densities and shapes at extreme armature positions, a linear function is used to control the element mesh in the air gap region over the 8 mm range of valve motion. For both iron and air regions, 2D quadrilateral elements with a magnetic potential degree of freedom

are used. Figure 4.5 illustrates a full and close up view of a typical mesh over the armature, air and opener back iron. A single layer of boundary elements is used around the perimeter of the model to model far field decay. These infinite elements use shape functions which require the magnetic potential to be zero at infinity. The backiron region is divided into two material type regions to better represent the anisotropic induction resulting from aligned grain structures of the laminate sheet. Unlike the transient simulations, where coil current is coupled to circuit elements, excitation is applied directly to the coil elements in the form of current density. Validity of the model is assessed by comparing simulation results to experimental measurements (see Chapter 6).

4.3.2 Transient Modeling and Simulation

The transient behavior of the model is determined by applying a voltage step at a constant air gap to a quasi-static transient FEA model. A step voltage is chosen as it is a typical output waveform of driver circuits [Xiang, 2002, Amato and Meuller-Heiss, 2001, Lequesne, 1990]. Quadrilateral elements with additional electromotive force (EMF) and current degrees of freedom are used for circuital excitation and to account for transient effects such as eddy currents. A voltage source, resistor, and stranded coil element are modeled to excite the actuator finite element domain as represented in Figure 4.5. The circuit elements are not part of the field solution. Rather, the stranded coil element's current and EMF degrees of freedom are coupled to the coil elements in the actuator domain. The coil resistance, assumed independent of temperature, is accounted for through the geometry of the FEA and the specified conductivity of copper. Approximate step waveform voltages, measured from an actual experiments, are applied to the FEA model to allow model validation and comparison with experimental data (see Chapter 6).

For further details of the finite element solution process, see [Chladny et al., 2005,

Chladny, 2003].

4.4 Plant Derivation

In the following sections, two types of lumped parameter models of the hinged actuator are presented for use in the development of control algorithms. In both cases, the actuator system can be considered to be comprised of magnetic, electrical and mechanical domains.

4.4.1 Magnetic Subsystem

Two magnetic models are presented for the hinged actuator. The first neglects changes in magnetic path caused by material saturation and is derived from the material properties and through a reluctance network method. A second magnetic model is presented based on the work of [Ilic'-Spong et al., 1987]. The latter model heuristically represents the net magnetic circuital response and is parameterized through numerical fitting to a FEA data set.

4.4.1.1 Reluctance Network - Linear Induction

The following details the derivation of a plant model for the hinged actuator assuming linear induction and the reluctance network method. A schematic of the magnetic path for the hinged opener magnet is shown in Figure 4.6. In this case, the path has been discretized into eight regions represented by various path lengths and the four relative permeabilites. The net reluctance may be thus expressed (using a small angle approximation) as:

$$\Re = \frac{1}{A}(\alpha_\ell + \delta_\ell + \gamma_\ell + \xi_\ell) \tag{4.1}$$

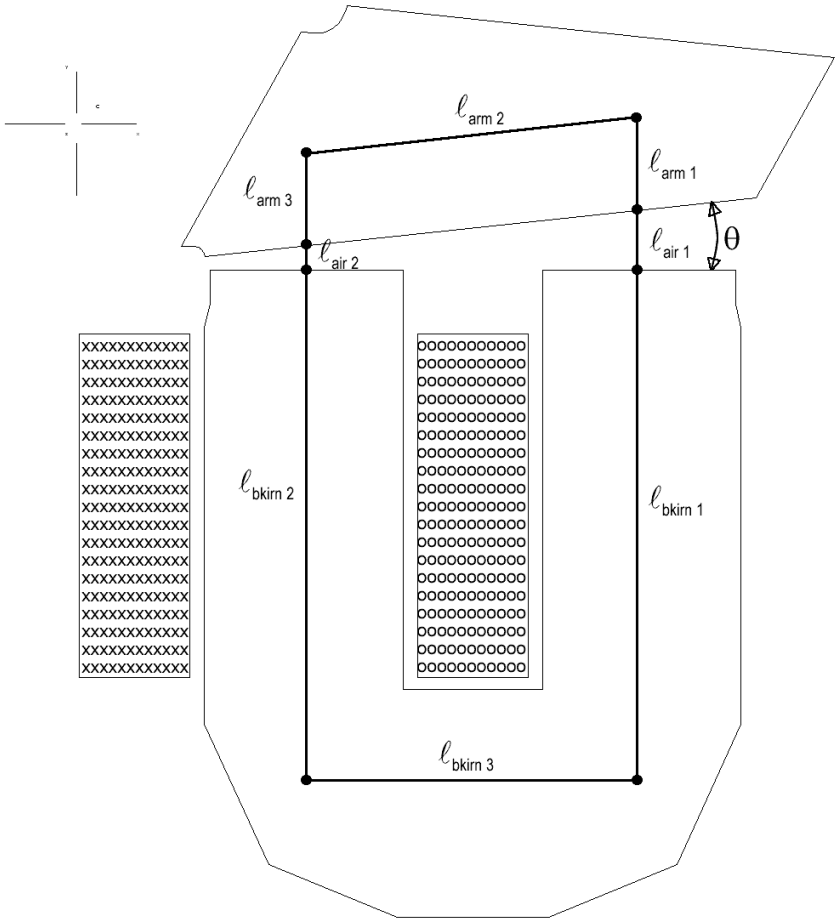

Figure 4.6: Opener magnetic path

where,

$$\alpha_\ell = \frac{\ell_{arm1} + \ell_{arm2} + \ell_{arm3}}{\mu_{arm}} \tag{4.2}$$

$$\delta_\ell = \frac{\ell_{bkirn1} + \ell_{bkirn2}}{\mu_{irnlg}}$$

$$\gamma_\ell = \frac{\ell_{bkirn3}}{\mu_{irnrt}}$$

$$\xi_\ell = \frac{\ell_{air1} + \ell_{air2}}{\mu_{air}}$$

$A =$ flux path cross-sectional area

Note that the air gap path lengths, ℓ_{air1} and ℓ_{air2}, only vary in relation to valve position x. The derived reluctance may be related to inductance by:

$$L = \frac{N^2}{\Re} = \frac{N^2 A}{\alpha_\ell + \delta_\ell + \gamma_\ell + \xi_\ell} \tag{4.3}$$

This expression can then take a more general form by combining the fixed path terms and relating the changing airgap to valve position, x. Specifically,

$$L(x) = \frac{\beta_\ell}{\kappa_\ell - x} \tag{4.4}$$

where β_ℓ and κ_ℓ are constants determined by the reluctance of the magnetic core, air and armature flux path. For improved accuracy, these constants may be fit to experimental or FEA simulated data. Recall from Chapter 3 Equation (3.85), that inductance may also be defined as the ratio of path flux to applied current. The expression for flux linkage is thus:

$$\lambda_\ell = \frac{\beta_\ell i}{\kappa_\ell - x} \tag{4.5}$$

4.4.1.2 Nonlinear Induction Model

As a means of providing a more accurate model of the physical system, magnetic material saturation is considered. Saturation effects will be present at high magnetomotive force (MMF) values. Specifically, at small armature/pole face air gaps and or high current excitation. Due to the soft landing requirements of this system, the feedback control is active during such conditions (and thus requiring accurate modeling). The following function, proposed in [Ilic'-Spong et al., 1987], is intended to

heuristically approximate the flux linkage response with magnetic material saturation:

$$\lambda(x, i) = \psi(1 - e^{-ig(x)}) \tag{4.6}$$

where

$$g(x) = \frac{\beta}{\kappa - x} + \alpha \tag{4.7}$$

Using this form, the parameters ψ, β, κ and α are obtained with a nonlinear least squares fit of collected experimental or numerically simulated force, position and current excitation data and listed in Appendix B.

4.4.2 Electric Subsystem

The following sections provide details of the derivation of the electrical domain of the actuator system in the case of the linear and nonlinear magnetic induction models.

4.4.2.1 Electric Subsystem - Linear Induction

The magnetic and electric domains are coupled through a source voltage and circuit current which can be represented by an RL circuit described by Faraday's law of induction and the following KVL equation:

$$\begin{aligned} v &= iR + \frac{d\lambda(i, x)}{dt} \\ &= iR + L(i, x)\frac{di}{dt} + \Psi(i, x)\dot{x} \end{aligned} \tag{4.8}$$

with applied voltage, v, coil current, i, $\lambda(i, x)$ representing the magnetic flux linkage of the electromagnet and $L(i, x)$ the self-inductance of the electromagnet. In addition, $\Psi(i, x)$ represents the back EMF, R, the total resistance of the coil winding and, x,

the valve position (and thus relates to the effective air gap between the armature and magnetic core pole face). Substituting the flux linkage model from (4.5) into the defining KVL relation, (4.8), yields the following ODE:

$$\begin{aligned} v &= iR + L(x)\dot{i} + i\frac{dL(x)}{dx}\dot{x} \\ &= iR + (\frac{\beta}{\kappa - x})\frac{di}{dt} + \frac{\beta i}{(\kappa - x)^2}\dot{x} \end{aligned} \tag{4.9}$$

Solving for rate of change of current yields

$$\frac{di}{dt} = -\frac{i}{(\kappa - x)}\dot{x} + \frac{(\kappa - x)}{\beta}(v - iR) \tag{4.10}$$

4.4.2.2 Electric Subsystem - Nonlinear Induction

For the nonlinear induction model, a similar procedure is used to derive the following KVL equation which considers magnetic material saturation:

$$\begin{aligned} v &= iR + \frac{d\lambda(x,i)}{dt} \\ &= iR + \frac{d}{dt}\left(\psi\left(1 - e^{-ig(x)}\right)\right) \\ &= iR + \frac{\psi g'(x)}{g^2(x)}\left(1 - (1 + ig(x))e^{-g(x)i}\right). \end{aligned} \tag{4.11}$$

where $g'(x)$ is

$$g'(x) = \frac{\beta}{(\kappa - x)^2} \tag{4.12}$$

Solving for rate of change of current yields

$$\frac{di}{dt} = \frac{-\beta\psi i\dot{x} + e^{i(\frac{\beta}{\kappa-x}+\alpha)}(\kappa-x)^2(v-iR)}{\psi(\beta+\alpha(\kappa-x))(\kappa-x)} \tag{4.13}$$

$$= \frac{1}{g(x)}\left(\frac{e^{g(x)i}(v-iR)}{\psi} - ig'(x)\dot{x}\right) \tag{4.14}$$

4.4.3 Magnetic Force Calculation

A relationship between magnetic force, airgap and current is derived through co-energy, W_c. Here, the change in field energy is related to a change in armature position [Woodson and Melcher, 1968]. To derive the co-energy of the system based on the linear induction model, flux linkage, λ_ℓ, is integrated with respect to current, i:

$$\begin{aligned} W_{c\ell}(x,i) &= \int_0^i \lambda_\ell(x,\xi)d\xi \\ &= \frac{i^2\beta}{\kappa-x} \end{aligned} \tag{4.15}$$

where $W_{c\ell}$ represents coenergy of the linear induction model. Differentiating with respect to x yields the expression for magnetic force:

$$\begin{aligned} F_{m\ell}(x,i) &= \frac{dW_{c\ell}(x,i)}{dx} \\ &= -\frac{i^2\beta_\ell}{(\kappa_\ell-x)^2} \end{aligned} \tag{4.16}$$

4.4.3.1 Magnetic Force - Nonlinear Induction

In a similar procedure, the nonlinear inductance model described in Section 4.4.1.2 is used to develop a relationship between magnetic force, airgap and current through

co-energy, W_c.

$$\begin{aligned} W_c(x,i) &= \int_0^i \lambda(x,\xi)d\xi \\ &= \int_0^i \psi\left(1 - e^{-\xi(\frac{\beta}{\kappa-x}+\alpha)}\right)d\xi \\ &= \frac{\psi e^{-i(\frac{\beta}{\kappa-x}+\alpha)}}{\beta+\alpha(\kappa-x)}\left(\kappa + e^{i(\frac{\beta}{\kappa-x}+\alpha)}(\beta i + (-1+\alpha i)(\kappa-x)) - x)\right) \end{aligned} \tag{4.17}$$

Differentiating with respect to x yields the expression for magnetic force:

$$\begin{aligned} F_m(x,i) &= \frac{dW_c(x,i)}{dx} \\ &= \frac{\psi e^{-i(\frac{\beta}{\kappa-x}+\alpha)}}{(\beta+\alpha(\kappa-x))^2(\kappa-x)}\left(-\beta i + (-1+e^{i(\frac{\beta}{\kappa-x}+\alpha)} - \alpha i)(\kappa-x)\right) \\ &= \frac{\psi g'(x)}{g^2(x)}\left(1-(1+ig(x))e^{-g(x)i}\right) \end{aligned} \tag{4.18}$$

4.4.4 Mechanical System

The mechanical subsystem is represented through application of Newton's second law relating the system forces to the armature and valve acceleration. Due to the way in which the armature of the hinged actuator is constrained (see Figure 3.4), the imparted magnetic force may be expressed as a moment. The moment can be calculated by using the radial distance from the armature revolute joint to the position where the distributed magnetic load may be equivalently resolved as a point load, ℓ_m. Due to the relatively small change in angle, this parameter is assumed constant with air gap. Valve force can be resolved with the radial distance from the armature pivot point to where the longitudinal armature and valve axes intersect, ℓ_v. In this way, Newton's second law can be applied to derive valve motion as a function of effective magnetic, torsion bar, spring, and viscous damping forces with respect to

valve position:

$$\ddot{x}(m_v + \frac{I_o}{\ell_v^2}) + \dot{x}(b_v + \frac{\hat{b}}{\ell_v^2}) + x(k_v + \frac{\hat{k}}{\ell_v^2}) + F_{vpl} + F_g = \frac{F_{m,j}(i,x)\ell_m}{\ell_v} \tag{4.19}$$

where: x is the valve position, m_v is the valve and moving spring mass, b_v is the friction damping coefficient associated with the valve, $\hat{b}$ is the viscous damping coefficient associated with the armature, k_v is the valve spring constant, $\hat{k}$ is the angular torsion bar spring constant, F_v is the valve spring pre-load, F_g is the gas force acting upon the valve and $F_{m,j} = -F_{m,o}, F_{m,c}$ is the magnetic force on the armature, with $j \epsilon o, c$ to indicate the opener or closer magnet respectively. Typically only one magnet is in operation at any given time. This may be further reduced to:

$$\ddot{x} = -\frac{1}{m}\left(\dot{x}b + xk - F_v + F_g - \frac{\ell_m}{\ell_v}F_{m,j}(x,i)\right) \tag{4.20}$$

with $m = m_v + \frac{I_o}{\ell_v^2}$ representing the effective system inertia, $k = k_v + \frac{\hat{k}}{\ell_v^2}$ the effective spring constant and $b = b_v + \frac{\hat{b}}{\ell_v^2}$ the effective damping coefficient. The valve and armature are considered to be rigidly coupled. Sufficiently small angles are assumed such that $\sin\theta \sim \theta$, since θ is limited to $\pm 6^o$. Armature and valve impacts are ignored since in experimental results in this work and in [Eyabi, 2003] it is reported that impact speed less than ≈ 0.2 m/s produced negligible armature or valve bounce. Thus, armature impacts are modeled simply by setting acceleration and velocity to zero when the armature reaches the stroke bounds. Impact speeds of approximately 0.1m/s or less are needed for successful control. The total valve stroke is represented by: $S = 8.00$ mm. External forces such as those caused by gravity are considered negligible. Effective moving mass, spring pre-load, spring constant and friction parameters are determined using a grey-box model system identification technique described in Appendix B.

4.4.5 State Space Formulation

With the magnetic, electrical and mechanical relations now derived, the state vector is defined as: $\mathbf{x} = [x_1\ x_2\ x_3]^T$ where $x_2 = \kappa - x$ for notational convenience.

4.4.5.1 State Space Model - Linear Induction

For the linear induction model, the resulting state space model is:

$$\begin{pmatrix} \dot{x}_1 \\ \dot{x}_2 \\ \dot{x}_3 \end{pmatrix} = \begin{pmatrix} \frac{x_1 x_3}{x_2} \\ -x_3 \\ \frac{x_3 b + (x_2 - \kappa)k - F_g - F_v}{m} + \frac{x_1^2 \beta \ell_m}{m \ell_v x_2^2} \end{pmatrix} + \begin{pmatrix} \frac{x_2}{\beta} \\ 0 \\ 0 \end{pmatrix} u \tag{4.21}$$

where input u is defined as $u = v - iR$.

4.4.5.2 State Space Model - Nonlinear Induction

Again substituting $x_2 = \kappa - x$ and defining the state vector $\mathbf{x} = [x_1\ x_2\ x_3]^T$ results in the following nonlinear state space model which includes saturation effects:

$$\begin{pmatrix} \dot{x}_1 \\ \dot{x}_2 \\ \dot{x}_3 \end{pmatrix} = \begin{pmatrix} \frac{x_1 g'(x_2) x_3}{g(x_2)} \\ -x_3 \\ -\frac{1}{m}\left(-x_3 b + (\kappa - x_2)k - F_v + F_g - \frac{\ell_m}{\ell_v} F_m(x_1, x_2)\right) \end{pmatrix} + \begin{pmatrix} \frac{e^{g(x_2)x_1} u}{\psi g(x_2)} \\ 0 \\ 0 \end{pmatrix}$$

Note that both systems are in control affine form [Isidori, 1997]:

$$\begin{aligned} \dot{\mathbf{x}} &= f(x) + g(x)u \\ \bar{y} &= [0\ 1\ 0]\,\mathbf{x} \end{aligned} \tag{4.22}$$

4.5 Gas Model

Motion control of the valve subject to cycle-to-cycle gas force disturbances adds an additional challenge to the soft landing objectives. In-cylinder pressures at exhaust valve opening may change from over 5 bar to about 1 bar in consecutive cycles in depending on the engine operating point (or even less in the event of a misfire). Identifying and rejecting these disturbances is crucial to successful exhaust actuator implementation in a real engine. Negative pressures such as those potentially encountered during regenerative braking are not considered and at any rate, will likely be more predictable due to the change in operating mode.

4.5.1 Gas Pressure

To predict the transient pressure disturbance, a compressible flow model is used assuming an initially sealed volume (cylinder with valves closed) which contains a mass of exhaust gas at a given pressure and temperature. The gas is expelled through the time varying valve opening. The cylinder volume varies with piston position which is a function of engine crank position and time. Upon valve opening, mass transfer takes place between the volume and atmosphere. The flow is considered isentropic through a duct (exhaust port) with area, A_t, defined as a function of valve position. The gas is assumed to be homogeneous (either pure air or exhaust depending on the case simulated) and the Mach number at the minimum port area is dependent on the in-cylinder and downstream exhaust pressure ratio. Using the aforementioned idealizations, mass flow rate may be approximated as compressible flow through a nozzle:

$$\dot{m}_g = \frac{C_d A_t M P \sqrt{k_t/(R_g T)}}{(1+(k_t-1)M^2/2)^{\frac{(k_t+1)}{2(k_t-1)}}} \qquad \text{[Çengel and Boles, 1993]} \qquad (4.23)$$

where: m_g is the mass of the gas inside the cylinder, C_d is the effective flow discharge coefficient, R_g is the ideal gas constant for the gas, T is the gas temperature, A_t is

the valve-position-dependent effective throat flow area, M is the local Mach number at the effective valve throat, k_t is the specific heat ratio of the gas (k_t is 1.4 for air and 1.3 for exhaust gas [C. R. Ferguson, 2000]). Local Mach number is expressed as a function of heat ratio and pressure ratio (in this case, back pressure is assumed to be atmospheric, P_{atm}). Mach number at the valve throat is limited to unity [Blair, 1999] and is expressed as:

$$M(P) = \sqrt{\frac{2}{k_t - 1}\left(\frac{P_{atm}}{P}\right)^{\frac{-(k_t-1)}{k_t}-1}} \tag{4.24}$$

Mass flow rate and pressure flow rate are related using the ideal gas relation

$$PV_c = mR_gT \tag{4.25}$$

Cylinder volume, V_c, varies as a function of engine crank angle, θ_c,

$$V_c = -\frac{\pi d_b^2}{4}\left(-L_r - \frac{L_s}{2} + (\frac{L_s}{2}\cos(\theta_c) + \sqrt{L_r^2 - \left[\frac{L_s}{2}\sin(\theta_c)\right]^2}\right) + V_{res} \quad \text{[Heywood, 1988]} \tag{4.26}$$

where: θ_c varies from 0^o to 360^o with TDC at $0^o, 360^o$ and BDC at 180^o, d_b is the cylinder bore diameter, L_r is the connecting rod length, L_s is the piston stroke length, V_{res} is the combined cylinder head and crevice volume.

The volume time derivative is

$$\dot{V}_c = \frac{1}{8}d_b^2 L_s \pi \sin(\theta_c)\left(\frac{L_s\cos(\theta_c)}{\sqrt{4L_r^2 - L_s^2\sin^2(\theta_c)}} + 1\right)\dot{\theta}_c \tag{4.27}$$

Crank angle as a function speed, N_e (in revolutions per minute), initial crank angle θ_o and time, t may be expressed as

$$\theta_c = \pi \sin(\frac{\pi N_e}{30} t + \theta_o) \tag{4.28}$$

The time derivative of crank angle is

$$\dot{\theta}_c = \frac{\pi^2 N_e}{30} \cos(\frac{\pi N_e}{30} t + \theta_o) \tag{4.29}$$

Thus, an approximate expression for pressure as a function of initial pressure, P_o, valve lift, $x_L = (x + S/2)$ m, crank angle and time

$$P = P_o - \frac{C_d V}{R_g T} \int_0^t \frac{A_t(x_L) M(P) P \sqrt{k_t/(R_g T)}}{(1 + (k_t - 1) M(P)^2/2)^{\frac{(k_t+1)}{2(k_t-1)}}} dt \tag{4.30}$$

The discharge coefficient, C_d, of 0.9 is estimated based on other four-valve geometries [Blair, 1999]. Valve curtain area, A_t, is valve lift dependant and may be represented as a frustum of a cone [Blair, 1999]. For a valve seat angle of 45^o, area may be expressed by

$$A_t = \begin{cases} \frac{\pi(d_{os}+d_{is})}{2} \sqrt{(d - \frac{d_{os}-d_{is}}{2})^2 + (\frac{d_{os}-d_{is}}{2})^2}, d \leq d_{lim} \\ \\ \frac{\pi d}{\sqrt{2}}(d_{is} + \frac{d}{2}), d > d_{lim} \end{cases} \tag{4.31}$$

where d_{is} and d_{os} are the respective inner and outer valve seat diameters. For a valve with a seat angle of $\phi_v = 45^o$, a lift limit beyond which the distance between the valve and valve seat is no longer normal to the seat occurs at $d_{lim} = \frac{d_{os}-d_{is}}{\sin 2\phi} = d_{os} - d_{is}$. Flow area as a function of valve lift is plotted in Figure 4.7.

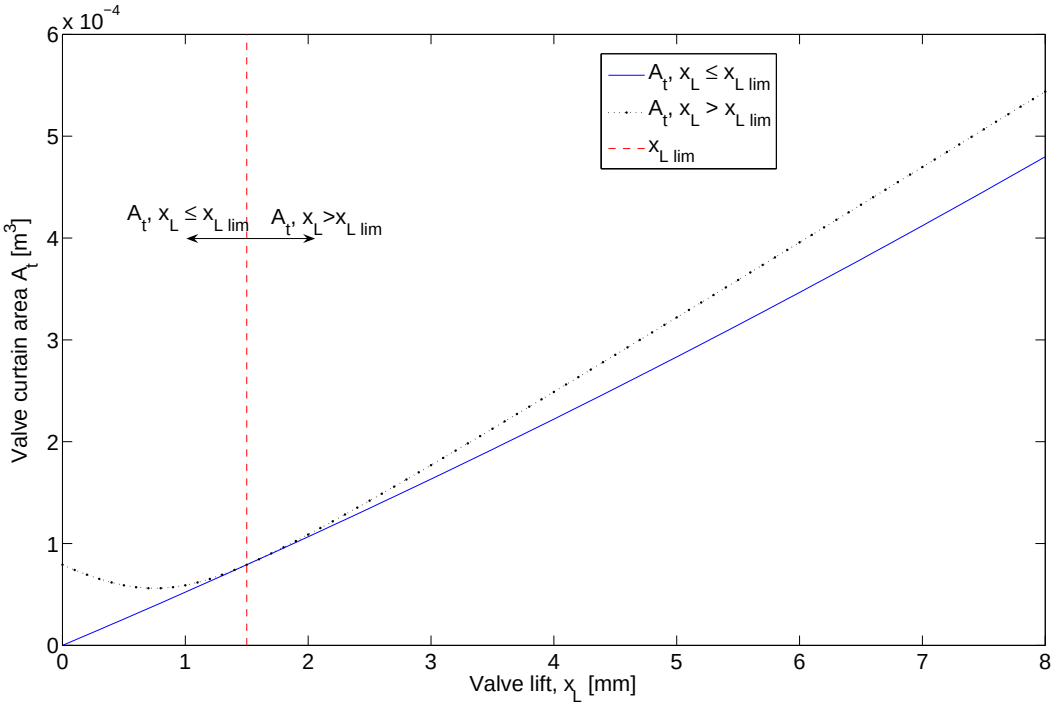

Figure 4.7: Valve flow area as a function of lift for valve seat diameters d_{os}, d_{is}

4.5.2 Gas Force

Combustion gas pressure disturbances may be related to valve force through the following:

$$F_g = C_{gf} P(x, P_o, t) A_v \tag{4.32}$$

where the valve face area is A_v and C_{gf} is a gas force coefficient that approximates the affect of flow losses behind the valve during opening. In [Schernus et al., 2002], C_{gf} is found to range from approximately 0.85 to 0.7 over the valve stroke. For simplicity, a constant value of $C_{gf} = 0.8$ is used throughout this study to approximate this stagnation flow effect. As shown in Section 4.5.1, cylinder pressure, P, depends on time, initial pressure, P_o, and effective flow area, A_t. Upon investigation, it is found that a quadratic functional form of gas force, F_{gs}, approximates this phenomenological

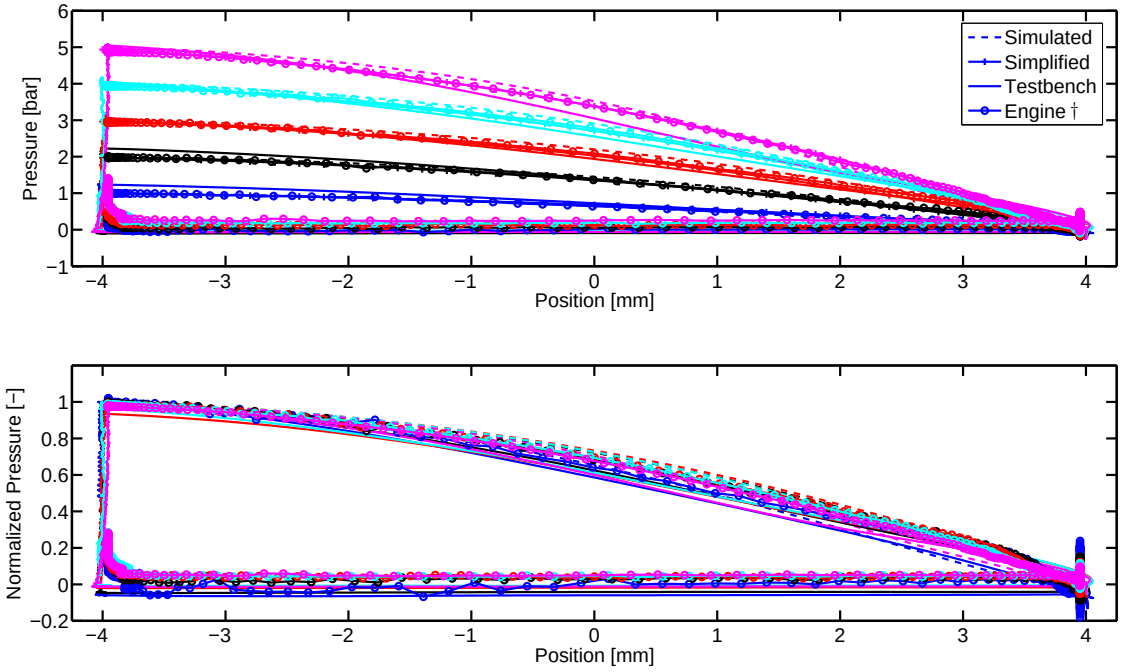

Figure 4.8: Comparison of the quadratic gas model to simulated, experimental testbench and engine† measurements

gas flow model and may be expressed as:

$$F_{gs} = C_{gf} P_o A_v f_1(x) = \gamma f_1(x) \tag{4.33}$$

with

$$f_1 = c_1 + c_2 x_L + c_3 x_L^2 \tag{4.34}$$

where the constants c_i are obtained using least squares fit to simulated or measured compressible flow pressure transients. The initial gas force magnitude is represented by $\gamma = C_{gf} P_o A_v$ and is considered constant throughout the opening cycle. Comparisons between this simplified relation, the numerical gas flow model, testbench experiments (see Section 6.3) and single cylinder engine tests are shown in Figure 4.8 over pressures ranging from 1 to 5 bar. Agreement between the simplified model

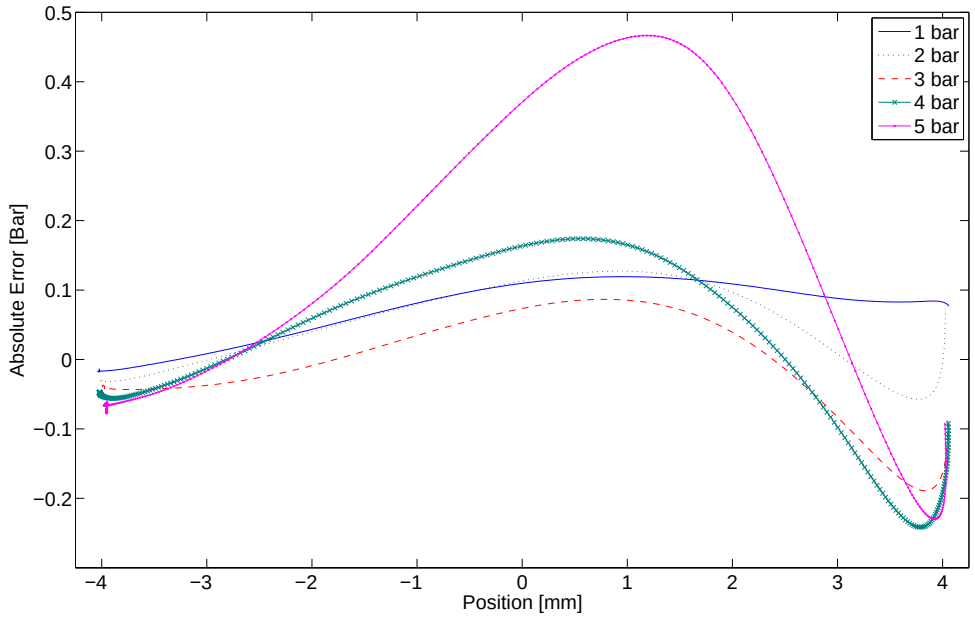

Figure 4.9: Absolute error of the quadratic gas model with respect to experimental testbench results over various pressure ranges

and experimental testbench measurements is good with a plot of the error between the simplified model and measured testbench results over various pressures provided in Figure 4.9. Maximum error tends to occur at higher pressure levels (in excess of 4 bar) at the 1 mm position with magnitudes of approximately 0.5 bar. Through (4.32), errors of 0.5 bar translate to valve force errors of approximately 20 N. The relatively good agreement attainable with a relatively computationally simple gas force model makes the quadratic gas model an ideal candidate to be used in disturbance estimation.

Taking the time derivative of (4.33) results in an expression for the rate of change of

[†]These data are provided by DaimlerChrysler AG from a single cylinder research engine equipped with linear motion type solenoid actuators

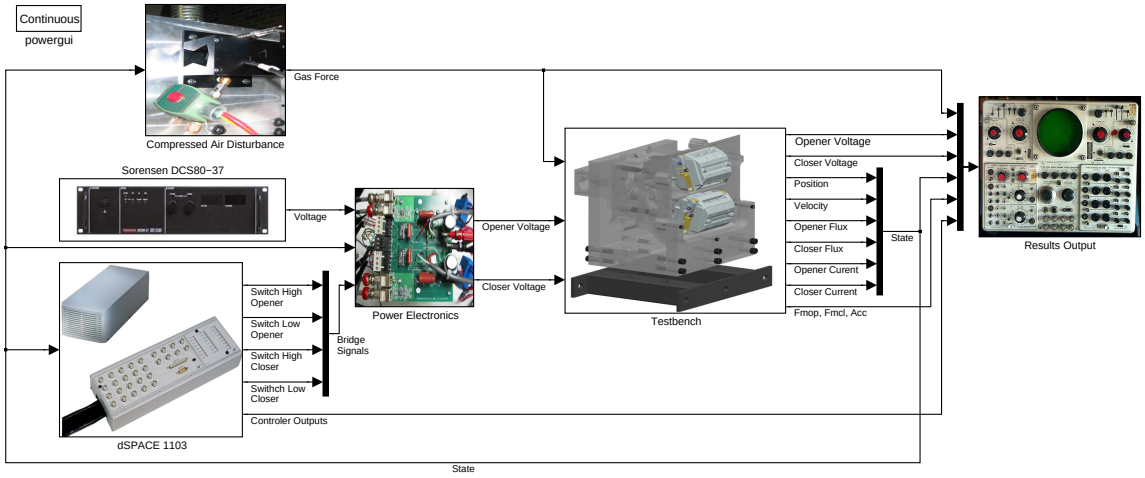

Figure 4.10: Simulink Model - top level

gas force:

$$\dot{F}_{gs} = C_{gf} P_o A_v (c_2(\dot{x}) + 2c_3(x + S/2)\dot{x}) = \gamma f_2(x, \dot{x}) \tag{4.35}$$

At higher engine speeds, gas forces caused by the time varying piston volume, V can be approximated. In that case, f_1 and f_2 from (4.34) and (4.35) can be augmented to reflect the crank position, θ_c, dependence:

$$f_{1c} = \frac{f_1 V_o}{V(\theta_c)} \tag{4.36}$$

$$f_{2c} = \frac{V_o f_2}{V(\theta_c)} - \frac{V_o f_1 \dot{V}}{V^2(\theta_c)} \tag{4.37}$$

where cylinder volume, V and its time derivative are detailed in Section 4.5.1. Estimates for both F_{gs} and $\dot{F}_{gs}$ are required in the landing control law derived in Chapter 5.

4.6 Simulink Model

A flexible simulation model capable of incorporating the various physical domains of the hinged actuator is developed using the MATLAB-Simulink environment. The model is designed to simulate prospective control algorithms and to predict actuator performance over a opening or closing cycle. The top-level of the model is shown in Figure 4.10 which indicates the major sub-models which are briefly explained in the following subsections. This model has been validated experimentally for the hinged actuator in [Chladny and Koch, 2006b] and for a linear VVT actuator (including an eddy current model, but without gas disturbances) in [Chladny et al., 2005].

4.6.1 Power Supply and Electronics

The actuator is excited through the use of a switched bridge amplifier circuit. In this way, digital pulse width modulated (PWM) signals from the controller are amplified as described in Chapter 6, Section 6.5.14. Through the use of one digital and one PWM controller outputs, this 'H-bridge' circuit provides the ability to apply three coil voltages: 42 V, 0 V and -42 V. The circuit is modeled using data from schematics and component manufacturer data. The SimPower Toolbox is used to represent the individual circuit components within the Simulink model. A representation of the opener drive circuit is shown in Figure 4.11.

Presently, the 3 kW power supply used in experiments is modeled simply as a constant source with a value of 42 V. This assumption is shown to be valid for the relatively short pules such as those in Section 7.2.2.

4.6.2 Testbench Model

The testbench sub-model (shown in Figure 4.12) consists of the mechanical, opener and closer coil dynamics models. Voltages from the power electronics are passed to

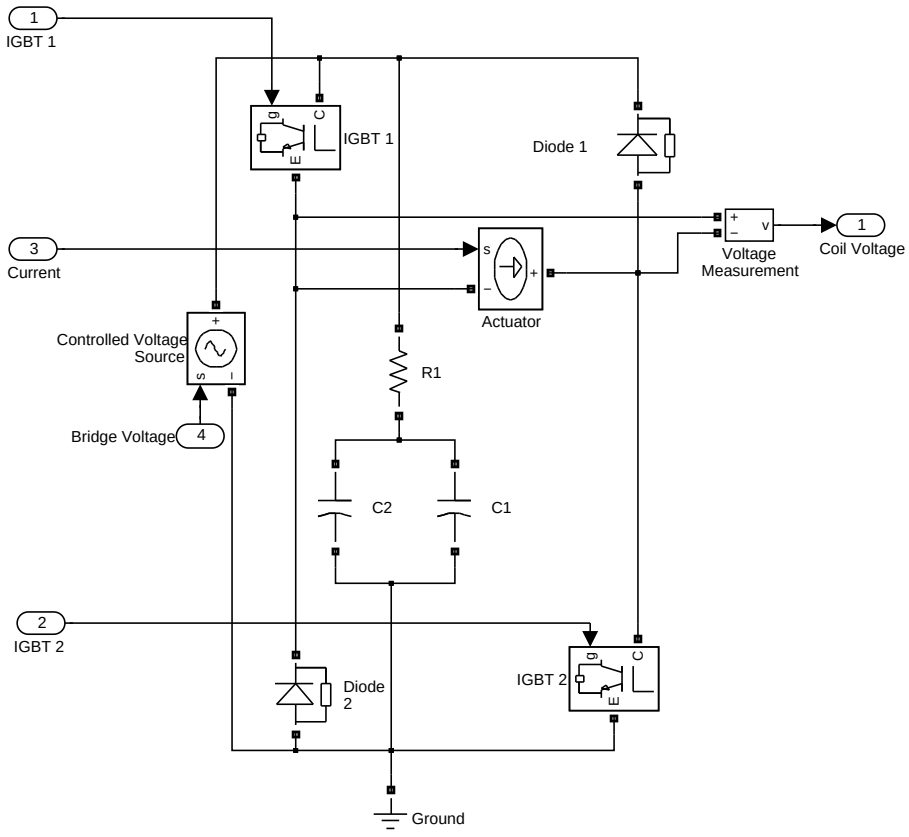

Figure 4.11: Simulink Model - Power Electronics (Opener)

the respective opener and closer coil dynamics which are described in the following section.

4.6.2.1 Coil Dynamics Model

To accurately represent the magnetic response of the hinged actuator, flux and force data from the FEA studies are implemented in lookup tables as shown in Figure 4.13. In this way, the difference in applied voltage and Ohmic losses is integrated and related to flux linkage and position to coil current. Coil current and position are then used to predict magnetic force through another data set. The coil dynamics models are coupled to the power electronics sub-systems through the applied voltage and coil

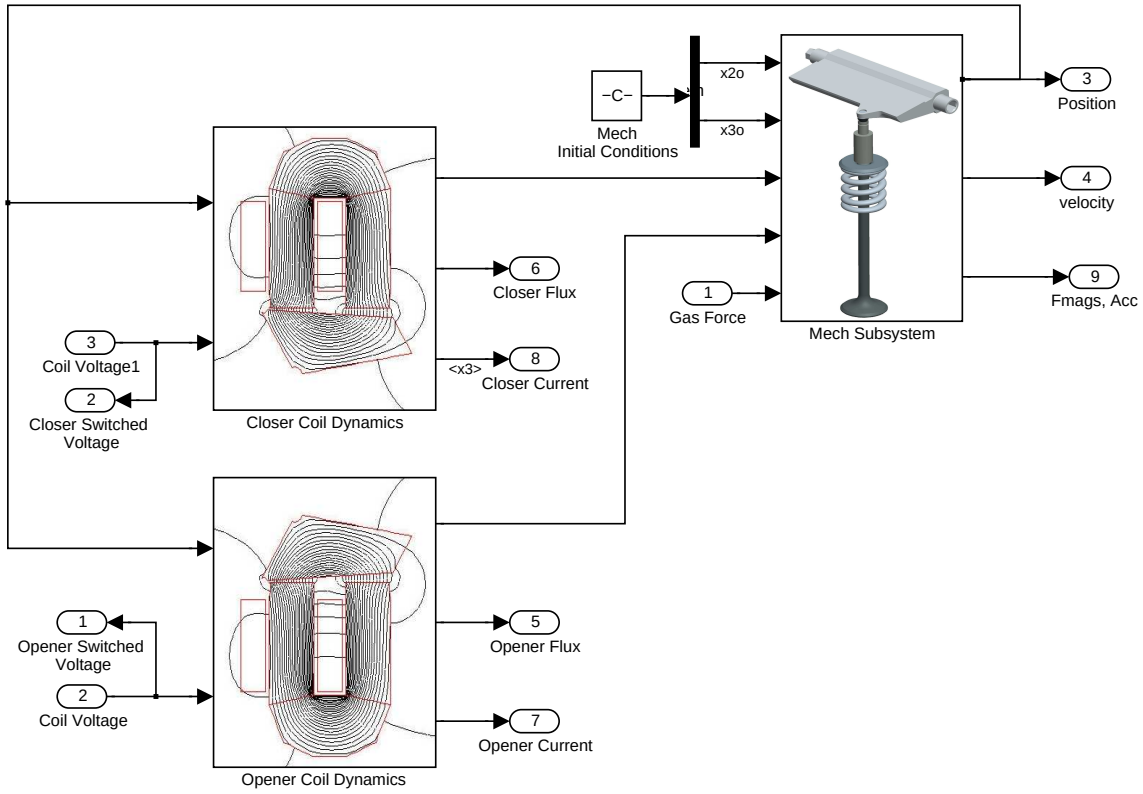

Figure 4.12: Simulink Model - Testbench

current. The system is also coupled to the mechanical system through armature position and magnetic force. Magnetic flux and current are output for control feedback which are experimentally measured through analog integration of measurement coil voltage and a hall effect sensor, respectively.

4.6.3 Mechanical Model

The actuator and valve mechanics are modeled using Newton's Law as shown in Figure 4.14. The model is coupled to the coil dynamics and gas disturbance models through their respective forces and armature position. Position and velocity data are output for feedback (in the case of full state feedback simulations) and analysis purposes. If required, this model could be extended to include a valve / armature

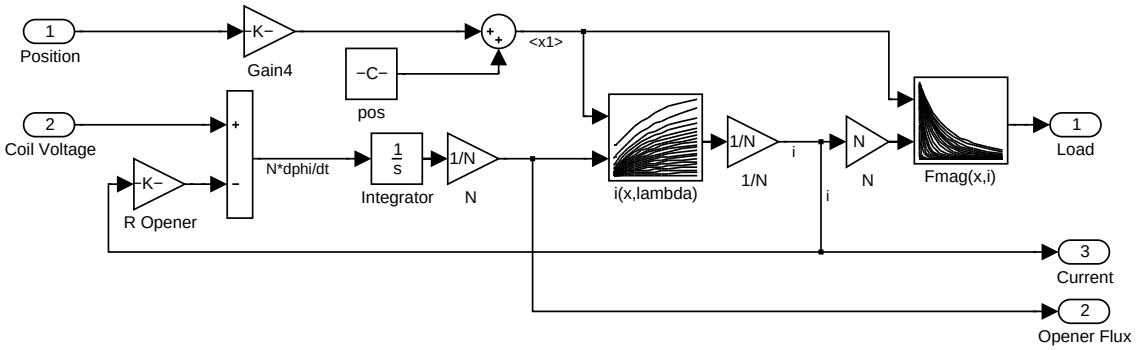

Figure 4.13: Simulink Model - Coil Dynamics (Opener)

impact model or a flexible element linking the armature and valve masses to represent a hydraulic lash adjuster.

4.6.4 Gas Force Disturbance Model

To investigate the effects of time varying gas force disturbances on valve trajectory, the numerical gas model presented in Section 4.5 is incorporated into the hinged actuator system Simulink model. The model is coupled to the mechanical system through valve position and gas force. Pressure changes caused by engine piston motion can be selected as well (via engine speed and EVO crank angle input). Time dependent experimental pressure traces can also be used from within this model, however such simulation results are viewed as less reliable due to the lack of valve throat area coupling.

4.6.5 dSPACE Controller Model

Given the myriad combinations of feedback, estimation and control algorithms available for evaluation, the control sub-system is implemented in modules. It contains a series of logical operations, or state machine, that co-ordinate the various control states and their respective algorithms at a simulated sample and execution rate of

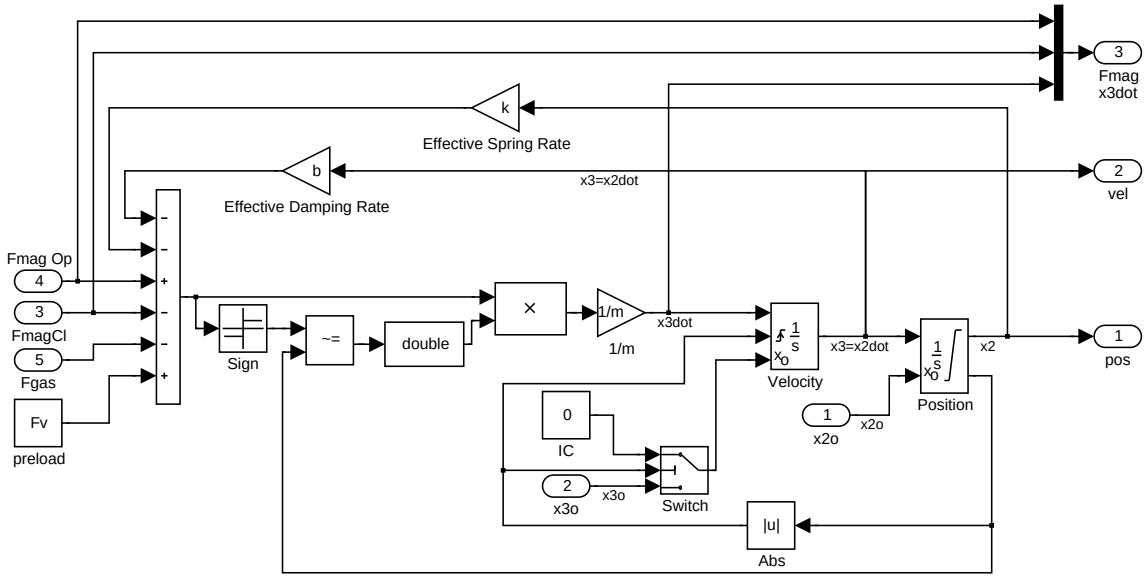

Figure 4.14: Simulink Model - Mechanical Dynamics

50 kHz. The controller model also has modules to co-ordinate what kinds of feedback and landing controllers are to be used. Conversion of the controller voltage output into a set of opener and closer PWM and logic signals for the power electronics is also included to emulate the physical dSPACE 1103 control hardware output. Information such as armature position, coil currents and magnetic flux are input for control calculation purposes while control output and feedback estimation data are output for analysis and debugging.

4.7 Computer Software & Hardware

All modeling software suites were run on a 300W ATX desktop computer consisting of an Intel Pentium 4 (2.80GHz) CPU, 1.0 Gbyte of RAM, 7200 rpm ATA hard disk, using a Microsoft Windows XP operating system and MATLAB versions 6.5 to 7.1.

4.8 Summary

The preceding sections highlight the key modeling methods and techniques undertaken with specific reference to the hinged actuator system investigated. Static and transient finite element analyses are conducted to establish and parameterize analytic magnetic models. The analytic models are to be used in the derivation of control algorithms. Power electronics circuits, FEA data and mechanical and electric systems are incorporated into a Simulink model intended to represent the complete hinged actuator system for control system performance evaluation. Also provided is an idealized compressible flow model used to approximate the affects of gas pressure on valve motion during exhaust valve opening. Where applicable, contrast of the various models with equivalent experimental data are provided in Chapter 6.

Chapter 5

Control Design

5.1 Introduction

Based on derivation and validation of an actuator model and identification of design constraints, a control strategy is formulated. In the following sections, an overview of the proposed control methodology is presented. Auxiliary algorithms for position feedback and exhaust gas disturbance force are also provided for use with the proposed feedforward and feedback controllers. Also presented are the derivations of classical linear and proportional integral (PI) landing controllers to contrast with the proposed flatness-based algorithm. Simulated performance results comparing the various feedback controllers for both the linear and and nonlinear induction models are included to justify the use of a model that accounts for magnetic saturation. The techniques used to derive the control reference trajectories are also discussed.

5.2 Controller Topology

As discussed in Chapter 1, the actuator and controller design must satisfy several performance and physical constraints. These include maximum valve seating velocities of 0.1m/s, transition times (time from open to close or close to open) of no more than 4.5ms, the use of practical feedback sensor technology and a maximum avail-

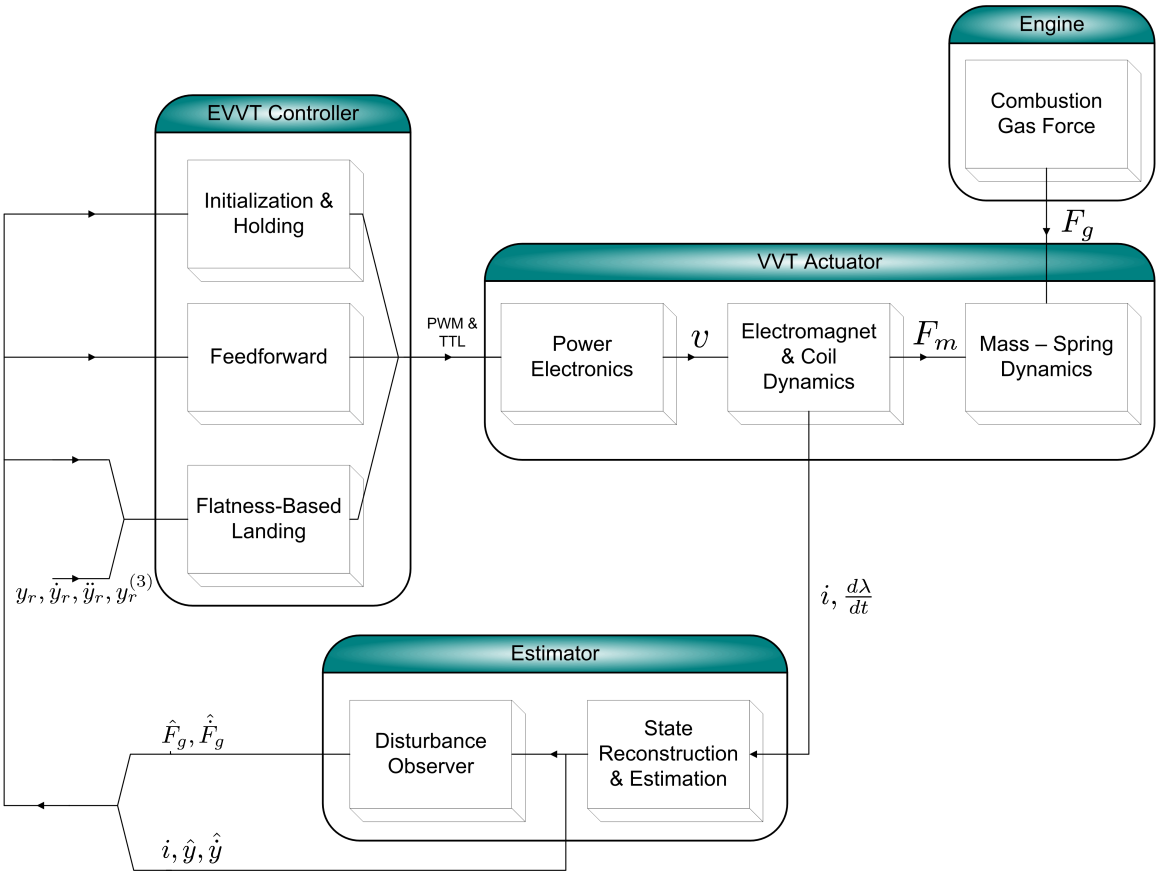

Figure 5.1: Control flowchart from closed to open and open to close

able voltage of 42V. Given these control constraints and actuator characteristics, the design of the actuator controller is divided into the following primary areas:

- Initialization and holding routines
- Closed-loop landing controller
- Landing control reference trajectory design
- State and disturbance estimation
- Feedforward controller

The control system is a combination of feedforward and feedback landing controllers with online disturbance estimation through measured current and flux-based state

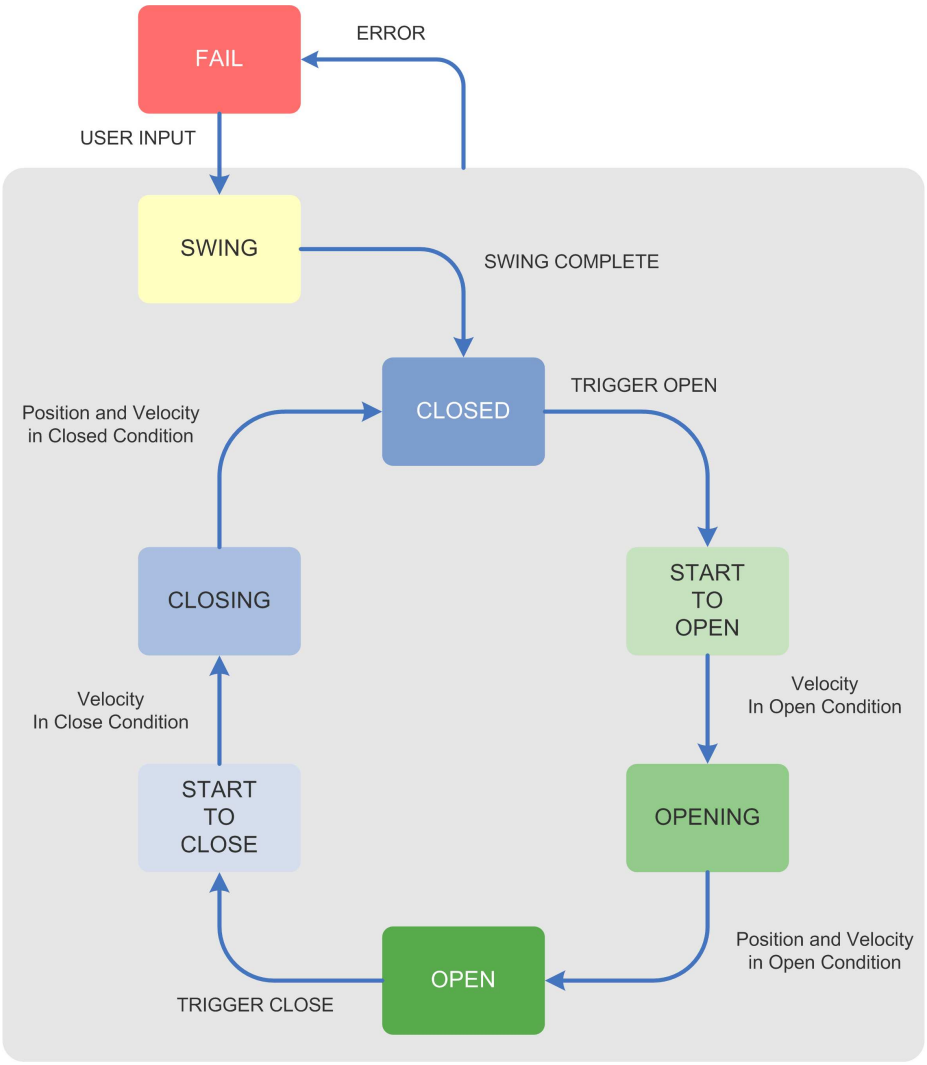

Figure 5.2: State machine flowchart [Chung, 2005]

reconstruction. A block diagram of the above structure with respect to the actuator plant and engine disturbances is presented in Figure 5.1. The individual control stages are executed according to a set of logical conditions or state machine as shown in Figure 5.2. Starting from an inactive state, an open-loop initialization routine is called which moves the armature and valve into a closed position. Then, as shown in Figure 5.3, a holding controller is engaged until a command is given to move the valve to an open state. The closer holding controller is released and position, velocity and disturbance estimation begins along with an energy-based feedforward controller.

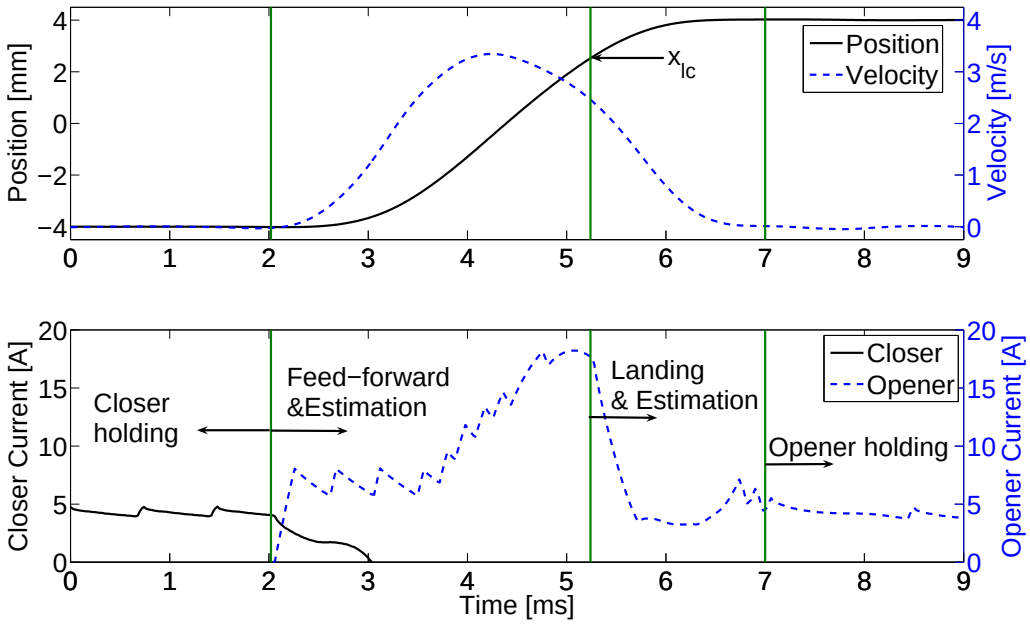

Figure 5.3: Control stages from closed to open position with respect to experimentally measured position, velocity and coil current at 2 bar EVO

These routines are used to set up favorable initial conditions for the landing controller which is engaged at position $x = x_{lc}$. After this point, the feedforward controller is disengaged and the closed-loop landing controller takes over to seat the armature and valve with a low impact speed. When a pre-determined open position and velocity are reached the valve is determined to be in the open state and the estimation and closed-loop controller are disengaged and an opener holding routine is enabled. To close, a similar procedure is used, although instead of an energy-based feedfoward controller, a simpler position based routine is used instead (see [Chung, 2005]. This is because minimal gas force disturbances are expected during the closing cycle. A plot of the different control modes with respect to an experimental opening cycle at an EVO pressure of 2 bar is provided in Figure 5.3. Figure 5.4 provides a flowchart overview of the closed-to-open and open-to-closed control cycles and the following sections describe in detail the individual routines.

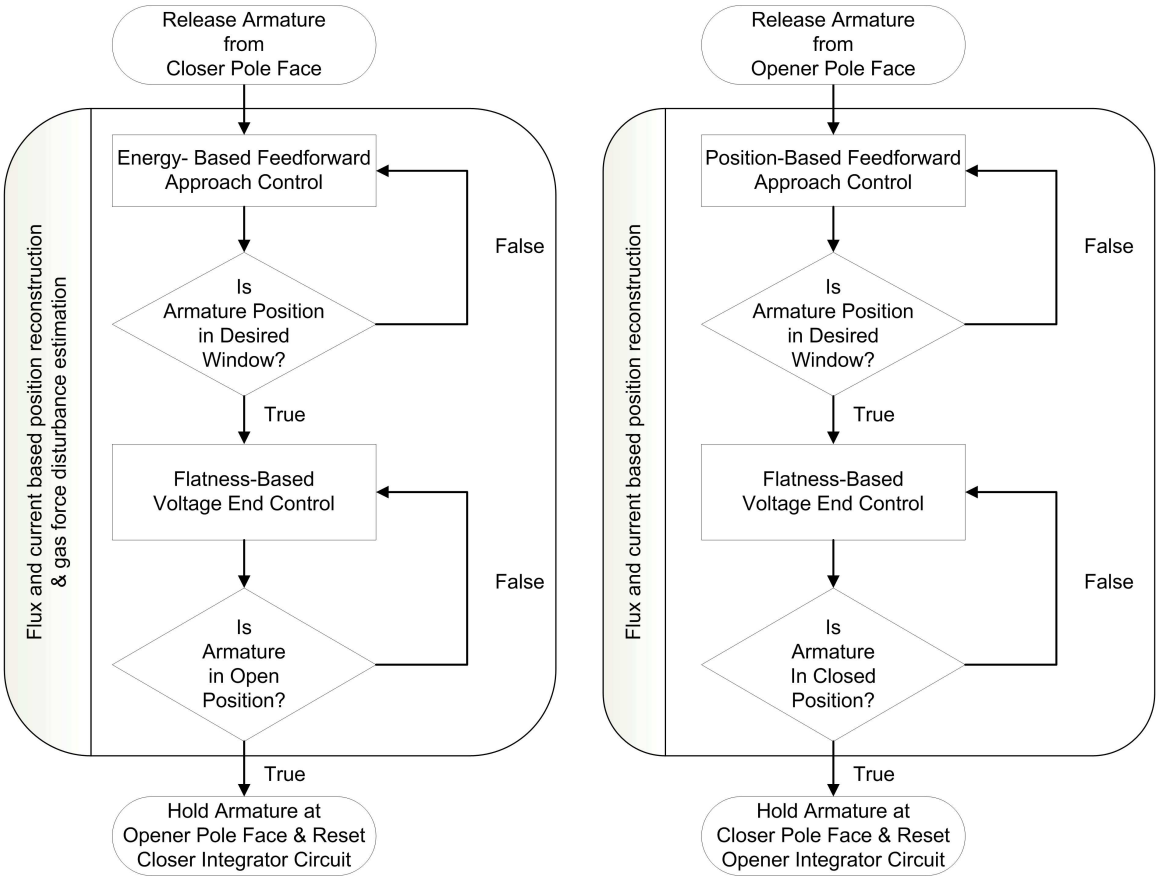

Figure 5.4: Control flowchart from closed to open and open to close

5.3 Initialization and Holding Control

When the valve is not in transition it is either inactive, being initialized into the closed position or being held open or closed. The initialization and holding processes have relatively little impact on overall control performance, but are essential for practical operation and are thus included for completeness.

5.3.1 Initialization

Prior to engine startup, or when the actuator is otherwise inactive, the armature and valve equilibrium is at approximately a mid-stroke position. Due to the limited force authority of the magnets and relatively high spring and torsion bar stiffness, a

time-based open loop controller alternatively pulses the opener and closer magnet to 'swing' the armature into the closed position utilizing the natural frequency of the mass-spring system.

5.3.2 Holding Control

After initialization or at the end of a valve opening or closing cycle, the armature and valve are held in an open or closed state. During this time, a pre-specified holding current is regulated through a coil current measurement and holding controller until a release command is issued by a software RPM generator (in the case of testbench experiments) or ECU (in the case of a real engine). Current is typically regulated at approximately 4.0 A through a simple 'on-off' controller that switches the holding coil current on (+42 V mode) or off (0 V mode) if the actual current level is respectively 0.1 A less than or greater than the set-point. Switching is relatively inactive because of the high inductance at these positions (minimal air gap). When a release command is issued, the coil current is driven to 0 A with the -42 V mode to drive the holding force to zero and minimize the time until motion is incipient.

5.4 Closed-loop Landing Control

To justify the use of a nonlinear controller and an induction model that accounts for magnetic saturation, four closed loop landing controllers are derived and simulated for comparison purposes. They are: two classical linear controllers based on both the linear and nonlinear induction models, a PI controller and a flatness controller based on the nonlinear induction model. The benefits of the flatness technique and nonlinear induction model are apparent in simulation so only the flatness controller is implemented with hardware.

5.4.1 Plant Models

With reference to the plant models derived in Chapter 4 Section 4.4, below are the linear and nonlinear induction state space models. In both cases the state vector is defined as $\mathbf{x} = [x_1\ x_2\ x_3]^T = [i\ \bar{x}\ \dot{x}]^T$ where $\bar{x} = \kappa - x$ and input u is defined as $u = v - iR$ for notational convenience.

5.4.1.1 Linear Induction Model

As introduced earlier, the resulting linear induction state space model is:

$$\begin{pmatrix} \dot{x}_1 \\ \dot{x}_2 \\ \dot{x}_3 \end{pmatrix} = \begin{pmatrix} \frac{x_1 x_3}{x_2} \\ -x_3 \\ \frac{x_3 b + (x_2 - \kappa)k - F_g - F_v}{m} + \frac{x_1^2 \beta \ell_m}{m \ell_v x_2^2} \end{pmatrix} + \begin{pmatrix} \frac{x_2}{\beta} \\ 0 \\ 0 \end{pmatrix} u \tag{5.1}$$

5.4.1.2 Nonlinear Induction Model

The resulting state space model for the nonlinear induction model is:

$$\begin{pmatrix} \dot{x}_1 \\ \dot{x}_2 \\ \dot{x}_3 \end{pmatrix} = \begin{pmatrix} \frac{x_1 g'(x_2) x_3}{g(x_2)} \\ -x_3 \\ -\frac{\left(-x_3 b + (\kappa - x_2)k - F_v + F_g - \frac{\ell_m}{\ell_v} F_m(x_1, x_2)\right)}{m} \end{pmatrix} + \begin{pmatrix} \frac{e^{g(x_2)x_1} u}{\psi g(x_2)} \\ 0 \\ 0 \end{pmatrix} \tag{5.2}$$

5.4.2 Linear Full State Feedback - Linear Induction System

In order to obtain an LTI compliant model, the nonlinear state equations in Section 5.4.1.1 are linearized about an equilibrium point $\mathbf{x}_e = [x_{1e}\ x_{2e}\ x_{3e}]$.

It is apparent that the equilibrium velocity, x_{3e}, must be zero from solving $\dot{x}_2 = 0$. The equilibrium current may then be solved for an arbitrary position, $x_{2e} = \kappa - x_e$. This operating point is chosen to be $x_e = 3.25$ mm, or 0.75 mm from the stroke

bounds, as that is the midpoint of the range over which control is typically executed.

$$x_{1e} = \frac{\sqrt{\beta \ell_v \ell_m (F_g + F_v + k(\kappa - x_{2e}))} x_{2e}}{\beta \ell_m} \tag{5.3}$$

Solving for the equilibrium input voltage, v, is accomplished by setting $\dot{x}_1 = 0$:

$$v = R \frac{\sqrt{\beta \ell_v \ell_m (F_g + F_v + k(\kappa - x_{2e}))} x_{2e}}{\beta \ell_m} \tag{5.4}$$

To generate the linearized A matrix, the Jacobian of the nonlinear system is computed with respect to the state vector x at the derived equilibrium point. The result of which is provided below:

$$A = \begin{pmatrix} 0 & 0 & \frac{\sqrt{\beta \ell_m \ell_v (\kappa - x_{2e}) k + F_v + F_g)}}{\beta \ell_m} \\ 0 & 0 & -1 \\ \frac{2\sqrt{-\ell_m \beta \ell_v ((x2e - \kappa) k - Fv - Fg)}}{\ell_v x_{2e} m} & k/m + \frac{2((x_{2e} - \kappa) k - F_v - F_g)}{x_{2e} m} & \frac{b}{m} \end{pmatrix} \tag{5.5}$$

The corresponding linearized B matrix is:

$$B = \begin{pmatrix} \frac{x_{2e}}{\beta} \\ 0 \\ 0 \end{pmatrix} \tag{5.6}$$

The tracking problem is solved locally through static state feedback. To simplify the following analysis, the linearized system described by matrices (5.5) and (5.6) is

redefined as follows:

$$\dot{\mathbf{x}} = \begin{pmatrix} 0 & 0 & a_{13} \\ 0 & 0 & 1 \\ a_{31} & a_{32} & a_{33} \end{pmatrix} \mathbf{x} + \begin{pmatrix} b_1 \\ 0 \\ 0 \end{pmatrix} u \tag{5.7}$$

$$y = (0\ 1\ 0)\mathbf{x} \tag{5.8}$$

where

$$\begin{aligned} a_{13} &= -\frac{\sqrt{-\beta\ell_m\ell_v((x_{2e}-\kappa)k - F_v - F_g)}}{\beta\ell_m} \quad a_{31} = \frac{2\sqrt{-\ell_m\beta\ell_v((x_{2e}-\kappa)k - Fv - Fg)}}{\ell_v x_{2e} m} \\ a_{32} &= k/m + \frac{2((x_{2e}-\kappa)k - F_v - F_g)}{x_{2e}m} \qquad a_{33} = -\frac{b}{m} \\ b_1 &= \frac{x_{2e}}{\beta} \end{aligned} \tag{5.9}$$

A change of coordinates and a state feedback control law is sought such that local exponentially stable error dynamics, and hence asymptotic tracking is achieved. Successive derivatives of 5.8 are taken to determine the relative degree, ρ.

$$\begin{aligned} y &= x_2 \\ \dot{y} &= \dot{x}_2 \\ &= x_3 \\ \ddot{y} &= \dot{x}_3 \\ &= a_{31}x_1 + a_{32}x_2 + a_{33}x_3 \\ y^{(3)} &= a_{31}\dot{x}_1 + a_{32}\dot{x}_2 + a_{33}\dot{x}_3 \\ &= a_{31}a_{13}x_3 + a_{31}b_1u + a_{32}\dot{x}_2 + a_{33}\dot{x}_3 \end{aligned}$$

By inspection, the input appears in the third derivative. Therefore the relative degree is well defined and equal to the system order. Furthermore, analysis of the transfer function representation of (5.7),

$$\frac{\hat{y}(s)}{\hat{u}(s)} = \frac{b_1 a_{31}}{s(s^2 - s a_{33} - a_{32} - a_{31} a_{13})} \tag{5.10}$$

confirms that unstable zeros do not exist and hence the tracking dynamics are locally bounded input, bounded state. Therefore, the tracking problem is locally solvable by static state feedback.

The coordinate transformation is defined by $z = Tx = [y\ \dot{y}\ \ddot{y}]^T$, where

$$T = \begin{pmatrix} 0 & 1 & 0 \\ 0 & 0 & 1 \\ a_{31} & a_{32} & a_{33} \end{pmatrix} \tag{5.11}$$

and the feedback law

$$\begin{aligned} u = & \frac{1}{b_1 a_{31}} (\bar{u} - (a_{31} a_{13} + a_{32}) x_3 \\ & - a_{33}(a_{31} x_1 + a_{32} x_2 + a_{33} x_3)) \end{aligned} \tag{5.12}$$

where $\bar{u}$ is an auxiliary input. The linearized system can thus be transformed into Brunovsky controller form:

$$\dot{z} = \begin{pmatrix} 0 & 1 & 0 \\ 0 & 0 & 1 \\ 0 & 0 & 0 \end{pmatrix} z + \begin{pmatrix} 0 \\ 0 \\ 1 \end{pmatrix} \bar{u} \tag{5.13}$$

By choosing

$$\begin{aligned}\bar{u} = &- k_1(z_1 - y_r(t)) - k_2(z_2 - \dot{y}_r(t)) \\ &- k_3(z_3 - \ddot{y}_r(t)) + y_r^{(3)}(t)\end{aligned} \tag{5.14}$$

yields the exponentially stable tracking error equation

$$e^{(3)} + k_1 e + k_2 \dot{e} + k_3 \ddot{e} = 0 \tag{5.15}$$

where $e^{(i)} = (y^{(i)} - y_r^{(i)})$ is defined for $0 \leq i \leq 3$ and $k_i > 0$. These error dynamics guarantee local exponential tracking to a desired reference trajectory. Since the reference trajectories, $y_r^{(i)}$, are assumed to be bounded, then so are the states z_1, z_2, and z_3, whereby under transformation, the states, x_1, x_2, and x_3, are also bounded. Pole placement is selected with respect to convergence rate and plant saturation (42 V and stroke limitations). The composite control law in x-coordinates is derived through combining (5.13) and (5.15) and applying the derived transformation $z = Tx$ as shown below:

$$\begin{aligned}u =& \frac{1}{b_1 a_{31}} \left(-k_1(z_1 - y_r(t)) - k_2(z_2 - \dot{y}_r(t))\right. \\ &- k_3(z_3 - \ddot{y}_r(t)) + y_r^{(3)}(t) - (a_{31}a_{13} + a_{32})x_3 \\ &\left. -a_{33}(a_{31}x_1 + a_{32}x_2 + a_{33}x_3)\right) \Big|_{z=Tx} \\ =& \frac{1}{b_1 a_{31}} \left(-k_1(x_2 - y_r(t)) - k_2(x_3 - \dot{y}_r(t))\right. \\ &- k_3(a_{31}x_1 + a_{32}x_2 + a_{33}x_3 - \ddot{y}_r(t)) + y_r^{(3)}(t) \\ &\left. - (a_{31}a_{13} + a_{32})x_3 - a_{33}(a_{31}x_1 + a_{32}x_2 + a_{33}x_3)\right)\end{aligned}$$

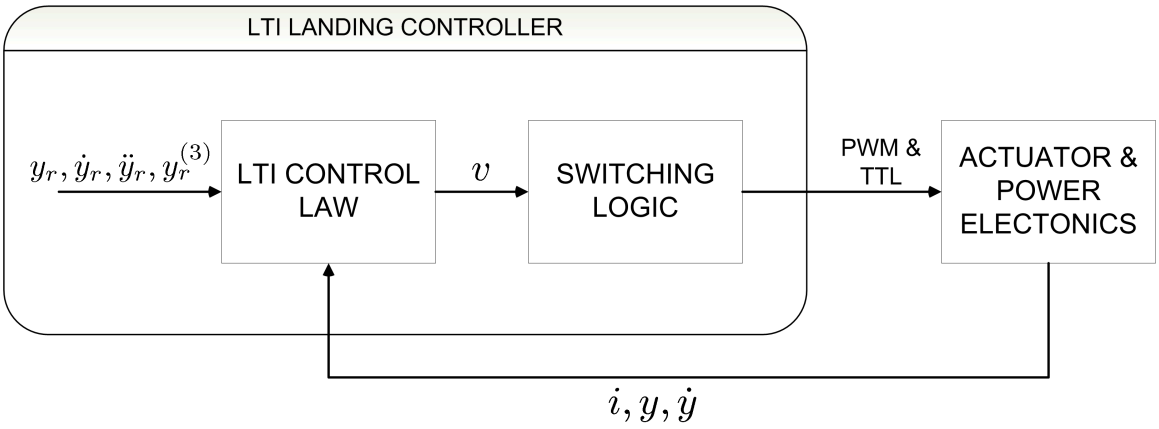

Figure 5.5: Simulated linear time invariant landing control block diagram

Finally, accounting for the substitution $u = v - iR$, the exponentially tracking control law is:

$$\begin{aligned} v =& x_1 R + \frac{1}{b_1 a_{31}} \left(-k_1(x_2 - y_r(t)) - k_2(x_3 - \dot{y}_r(t)) \right. \\ & - k_3(a_{31}x_1 + a_{32}x_2 + a_{33}x_3 - \ddot{y}_r(t)) + y_r^{(3)}(t) \\ & \left. - (a_{31}a_{13} + a_{32})x_3 - a_{33}(a_{31}x_1 + a_{32}x_2 + a_{33}x_3) \right) \end{aligned}$$

Note that this controller requires either full state feedback or estimates thereof. For the purposes of controller comparison simulations, it is assumed the full state is available and that gas forces are negligible. A block diagram of the LTI end-controller structure is shown in Figure 5.5

5.4.3 Linear Full State Feedback - Nonlinear Induction

An identical process to that described in Section 5.4.2 is used to derive an LTI model based upon the nonlinear induction model. The equilibrium current is:

$$x_{1e} = -\frac{x_2 e}{\beta + \alpha x_{2e}} \left(W_{-1}(z) + 1 \right) \tag{5.16}$$

where $W_{-1}(z)$ is a real-valued branch of the Lambert's function $w(z)e^{w(z)}$ (see Appendix A, Section A.6 or [Corless et al., 1996] for details)

$$W_{-1}(z) = \frac{1}{\psi\beta e\ell_m}\left(\beta^2\ell_v(F_g + F_v + k(\kappa - x_{2e})) + (\alpha x_{2e})^2\ell_v(F_g + F_v + k(\kappa - x_{2e}))\right. \tag{5.17}$$

$$\left. + \beta(-\ell_m\psi + 2\alpha\ell_v x_{2e}(F_g + F_v + k(\kappa - x_{2e})))\right)$$

Thus, the state space representation of the system about the equilibrium point is

$$\dot{\mathbf{x}} = \begin{pmatrix} 0 & 0 & a_{13} \\ 0 & 0 & -1 \\ a_{31} & a_{32} & a_{33} \end{pmatrix}\mathbf{x} + \begin{pmatrix} b_1 \\ 0 \\ 0 \end{pmatrix} u \tag{5.18}$$

$$y = (0\ 1\ 0)\mathbf{x} \tag{5.19}$$

where

$$\begin{aligned} a_{13} =& \frac{x_{1e}\beta}{x_{2e}(\beta + \alpha x_{2e}} & a_{31} =& \frac{\ell_m\beta\psi x_{1e}e^{(-\frac{x_{1e}(\beta+\alpha x_{2e})}{x_{2e}})}}{m\ell_v x_{2e}^2} \\ a_{32} =& \frac{e^{-x_{1e}\left(\alpha+\frac{\beta}{x_{2e}}\right)}}{\ell_v m x_{2e}^3(\beta + \alpha x_{2e})^3}\left(x_{2e}^3 e^{x_{1e}\left(\alpha+\frac{\beta}{x_{2e}}\right)}\zeta_1 + \zeta_2\right) & & \\ a_{33} =& \frac{b}{m} & & \\ b_1 =& \frac{(x_{2e} + \alpha)}{\psi\beta}e^{\frac{\beta x_{1e}}{x_{2e}+\alpha}} & & \end{aligned} \tag{5.20}$$

with

$$\begin{aligned} \zeta_1 =& \left(k\ell_v\beta^3 + 3\alpha k\ell_v x_{2e}\beta^2 + \alpha\left(3\alpha k\ell_v x_{2e}^2 - 2\ell_m\psi\right)\beta + \alpha^3 k\ell_v x_{2e}^3\right) \\ \zeta_2 =& \beta\ell_m\psi\left(-x_{1e}^2\beta^3 - 2\alpha x_{1e}^2 x_{2e}\beta^2 - \alpha x_{1e}(\alpha x_{1e} - 2)x_{2e}^2\beta + 2\alpha(\alpha x_{1e} + 1)x_{2e}^3\right) \end{aligned} \tag{5.21}$$

The system control law derivation and form is identical to that described in the case of the linear induction controller with exception of the coefficients.

5.4.4 Proportional-Integral Control

A classical PI landing controller is presented as a benchmark comparison to the linear and flatness-based controllers. The control technique is commonplace in industrial applications due to the relative ease in design, tuning, robustness and computational demands. Here, current is output in proportion to position error and integrated position error as follows:

$$i_{PI} = K_P (y - y_r) + K_I \int_0^t (y - y_r)(\tau)\, d\tau \tag{5.22}$$

where i_{PI} is the current control output, K_P is the proportional gain and K_I is the integral gain and y_r is the desired reference trajectory. The gains are first approximated using a Ziegler-Nichols method [Franklin et al., 1998] and then manually refined. PI control enhances system response through increasing the response to output-command error while the integration of such errors ensures steady state errors are eliminated. Due to excessive sensor noise, a differential term is not included. To enhance the transient response, a feedorward current, $i_{PI_{ff}}$, is introduced so that the desired current output, i_d, is $i_d = i_{PI} + i_{PI_{ff}}$. Regulation about the desired current is done in a similar fashion as holding current regulation. The position based open loop feedforward current is derived as shown in Section 5.5. This controller requires current, i, and position, y, for feedback which is assumed to be available for simulation purposes. Experimental performance of a similar controller is contrasted with a flatness-based method for a linear type of actuator in [Chung, 2005]. A block diagram for the PI landing controller with a feedforward current input is shown in Figure 5.6.

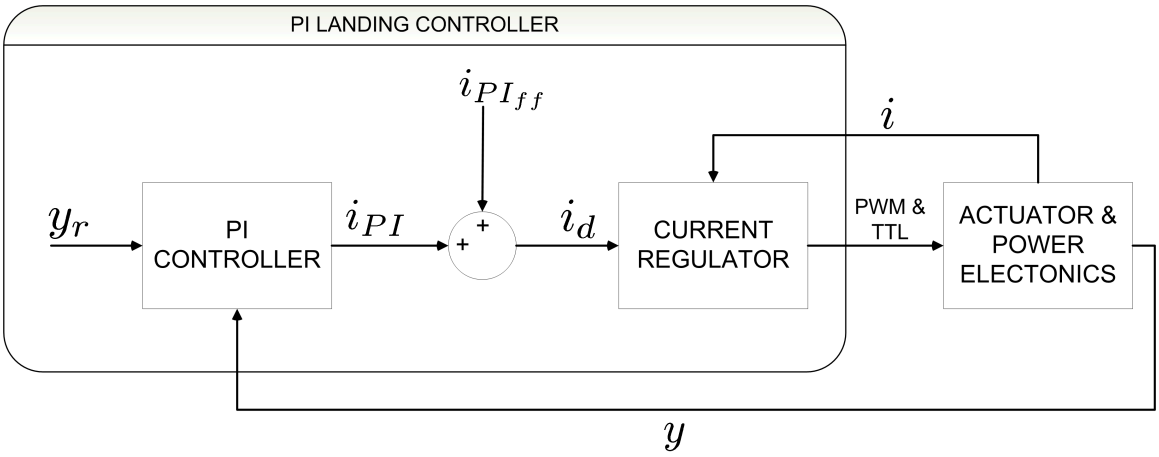

Figure 5.6: Simulated proportion-integral current landing control block diagram

5.4.5 Flatness-based Voltage Control - Nonlinear Induction

The landing controller proposed in this work uses a flatness-based landing controller as described in [Chung et al., 2007, Chladny and Koch, 2006b] to achieve exponentially convergent armature position tracking to a predetermined trajectory. Flatness based control was chosen for landing as it allows the design of a trajectory which is subject to both path and end constraints. Static state-feedback voltage control is obtained by defining position, x, as a flat output, $y = x$. States velocity, $\dot{x}$ and current, i are related to the flat output through:

$$\dot{x} = \dot{y} \tag{5.23}$$

$$i = -\frac{1}{g(y)}\left[W_{-1}(-\eta(y, \dot{y}, \ddot{y})/e) + 1\right] \tag{5.24}$$

where W_{-1} is a real-valued branch of the Lambert's function and

$$\eta(y, \dot{y}, \ddot{y}) = 1 - \frac{g^2(y)(m\ddot{y} - \mathcal{A}(y, \dot{y}, F_g))}{\psi g'(y)} \tag{5.25}$$

$$\mathcal{A}(y, \dot{y}, F_g) = -(ky + b\dot{y} - F_v + F_g) \tag{5.26}$$

Voltage is related to the third time derivative of y as follows:

$$\ddot{y} = \ddot{x} = -\frac{1}{m}\left(\dot{y}b + yk - F_v + F_g - \frac{\ell_m}{\ell_v}F_m(y,i)\right) \tag{5.27}$$

$$y^{(3)} = -\frac{1}{m}\left(\ddot{y}b + \dot{y}k + \dot{F}_g - \frac{\ell_m}{\ell_v}\dot{F}_m(y,i)\right), \tag{5.28}$$

where,

$$\begin{aligned}\dot{F}_m(y,i) =& 2\dot{y}F_m(y,i)\left(\frac{1}{(\kappa - y)} - \frac{g'(y)}{g(y)}\right) \\ &+ \frac{ig'(y)}{g(y)}(v - iR).\end{aligned} \tag{5.29}$$

Solving (5.28) and (5.29) for input voltage, v yields:

$$\begin{aligned}v =& \frac{\ell_v g(y)}{\ell_m i g'(y)}\left(\ddot{y}b + \dot{y}(k + 2F_m(y,i)(\frac{g'(y)}{g(y)}\right. \\ &\left. -\frac{1}{(\kappa - y)}) + \dot{F}_g + y^{(3)}m\right) + iR.\end{aligned} \tag{5.30}$$

The singularity at $i = 0$ is avoided through ensuring a non-zero bias current prior to landing controller engagement. Non-zero current is also a requirement for flux-based position reconstruction as described in Section 5.6.1. From (5.30) it is apparent that the state $(i, x, \dot{x})$ and input, v, may be expressed as a finite number of time derivatives of the output, y. Therefore, the system satisfies the flatness definition and therefore an open-loop solution of input, v, may be expressed as a function of reference trajectories as outlined in work such as [Fliess et al., 1999, Fliess et al., 1995]. To compensate for deviations from desired and actual trajectories, additional feedback can be implemented through defining tracking error as $\tilde{y} = y - y_d$, and linear error

dynamics:

$$k_1\tilde{y} + k_2\dot{\tilde{y}} + k_3\ddot{\tilde{y}} + \tilde{y}^{(3)} = 0 \tag{5.31}$$

Coefficients k_1, k_2 and k_3 are chosen such that the characteristic equation $P = s^3 + k_3s^2 + k_2s + k_1 = 0$ is Hurwitz. Pole placement is selected with respect to convergence rate and plant saturation (42 V and stroke limitations). Solving (5.31) for $y^{(3)}$ results in:

$$y^{(3)} = -k_1\tilde{y} - k_2\dot{\tilde{y}} - k_3\ddot{\tilde{y}} + y_d^{(3)} \tag{5.32}$$

Substitution of (5.32) into (5.30) completes the expression for closed loop voltage control. Exponential tracking of y to y_d will be achieved provided that the gains k_i are positive and chosen appropriately. As in the LTI case, the flatness controller requires either full state feedback or estimates thereof. For the purposes of controller comparison simulations, it is assumed the full state is available. In practice however, the state i is measured and y, $\dot{y}$ and gas force F_g are estimated through an integrated flux measurement and nonlinear observer (see Sections 5.6.1 and 5.8 respectively). Reference trajectories are designed subject to physical, practical and desired end condition constraints as discussed in Section 5.5 as well as in [Chladny and Koch, 2006b] and [Chung, 2005, Koch et al., 2004] for a linear motion actuator. A block diagram for the simulated flatness-based landing controller is shown in Figure 5.7.

5.4.6 Preliminary Control Law Comparison

With four potential landing control laws derived, preliminary simulations are conducted to investigate the most promising candidate to be implemented in experiments. Using a simplified version of the Simulink LPM-FEA model described in

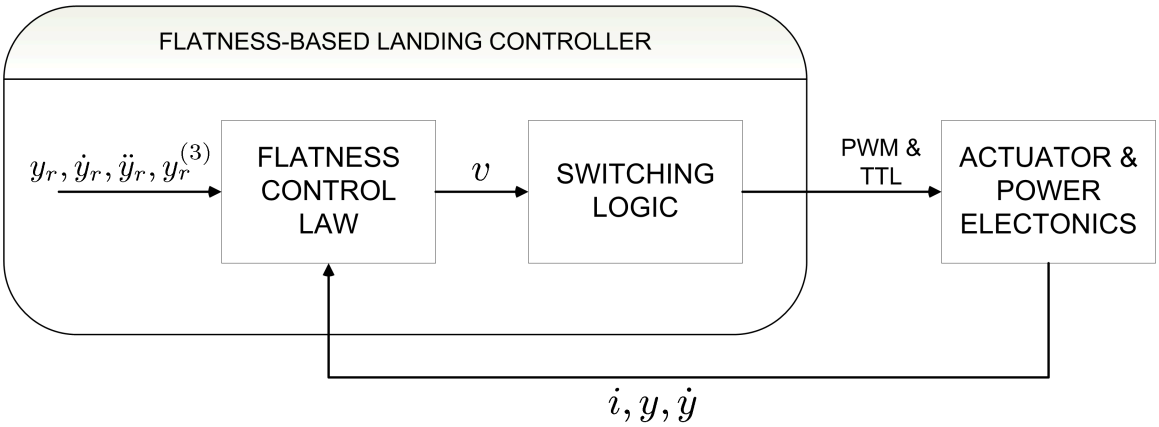

Figure 5.7: Simulated flatness-based landing control block diagram

Section 4.6, closer landing performance is investigated using specific initial current, and velocity conditions. The simplified model does not involve gas forces, disturbance feedforward controller, power electronics or state estimation (full state feedback is assumed). The landing controller is always engaged at a specific position, x_{lc}, usually 1.5 mm away from the landing magnet pole face. Voltage sources of 500 V and 42 V are simulated to predict landing performance with and without significant input saturation conditions. The LTI and flatness controllers have the same pole locations of $[-10000, -10000, -1500]$ for the purpose of comparison (and was sufficient for all controllers to land the valve). Note that because the Simulink model coil and force dynamics are based in part on the FEA simulations, model-plant mismatch is to be expected for all controllers tested. Simulated landing position and velocity tracking is provided in Figure 5.8 for initial conditions corresponding with the derived reference trajectories and a 500 V source. By comparing the two LTI controllers, it is apparent that even a linearized model that accounts for magnetic saturation provides a significant improvement with respect to impact velocity. The flatness controller has the best performance with least tracking error and an impact velocity of 0.05 m/s. Based on these results, it was apparent that the LTI linear induction controller would likely prove unsuitable.

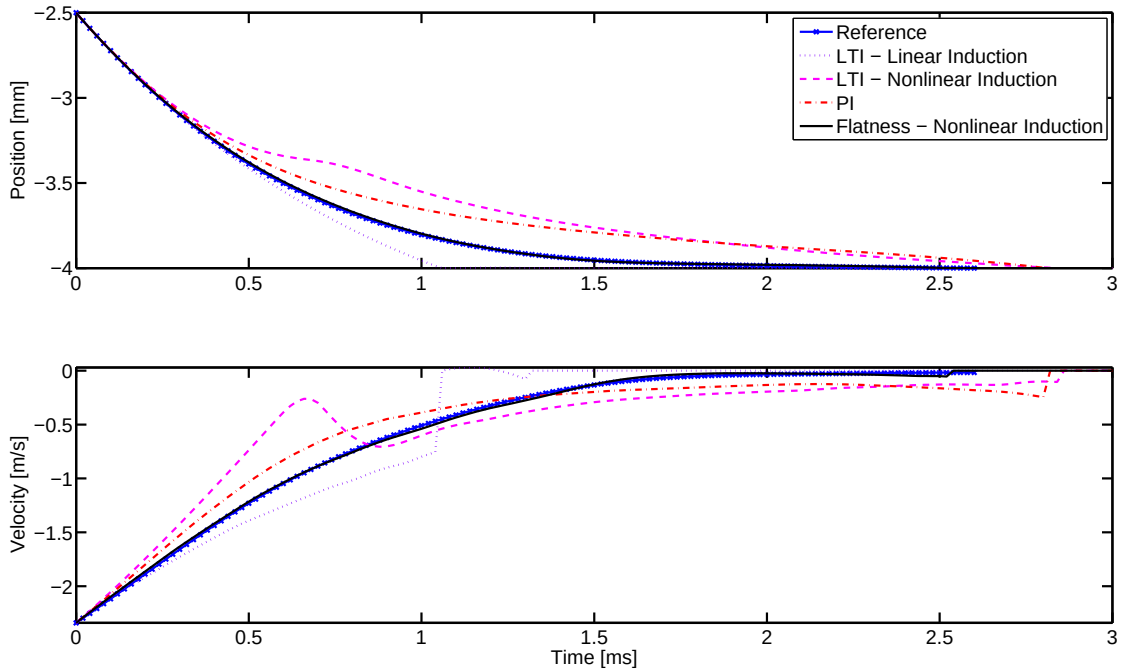

Figure 5.8: Simulated landing control performance comparison with ideal initial conditions, 500 V

Next, deviations from the ideal initial conditions are introduced to provide insight to performance under more realistic conditions. Figure 5.9 provides the landing results under a initial velocity that is both 0.5 m/s greater and less than the initial reference velocity. Beyond this range, all controllers except the flatness controller failed to land completely. Due to the relatively high voltage of 500 V, initial current variations of up to 10 A, caused insignificant performance variations and are not shown. In all large initial condition variations, the flatness controller performed best respect to tracking error and settling time. The LTI nonlinear induction controller had the best impact velocity at 0.1 m/s (0.05 m/s less than the flatness controller), but was among the longest with respect to settling time. The PI controller had the worst impact speed but better settling time than the LTI controller.

To predict performance with a more realistic source, voltage was reduced to 42 V as shown in Figure 5.10. Once again, the flatness-based controller performed best with

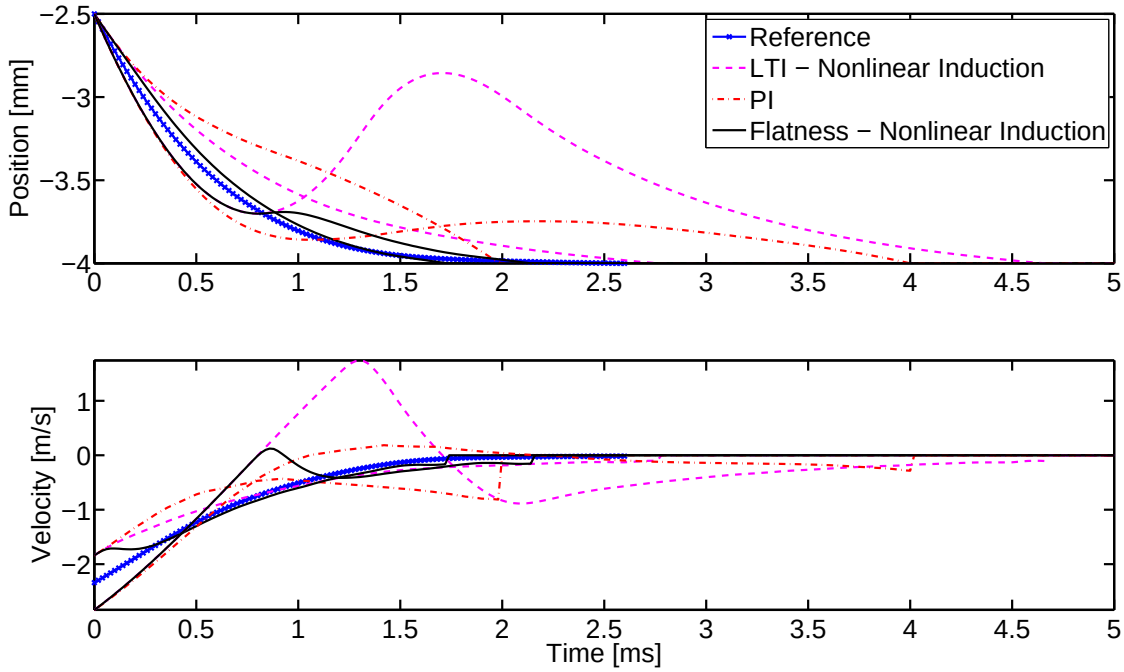

Figure 5.9: Simulated landing control performance comparison with ±0.5m/s initial velocity deviation, 500 V

respect to impact speed and settling time. The PI controller was re-tuned to accommodate the reduced voltage with an impact velocity of 0.33 m/s and considerably better tracking error than the LTI controller (which failed to land completely). Also provided in Figure 5.10 is current response and input energy. In practice, the coil current is limited to 40 A (peak) to prevent overloading. Reduced energy consumption is desired to minimize the associated parasitic engine load. In this respect, the PI and flatness controllers preformed nearly equally well.

Landing robustness to parameter variations is also of concern given the wide range of temperatures and long duration over which a vehicle engine must operate. In particular, the mechanical spring stiffness and damping are investigated as they are arguably more susceptible to environmental and manufacturing variations. In Figure 5.12, PI and flatness controller response to a ± 10% change in system spring stiffness, k_{sys}, are shown. In the case where the system stiffness is 10% less than the value used in

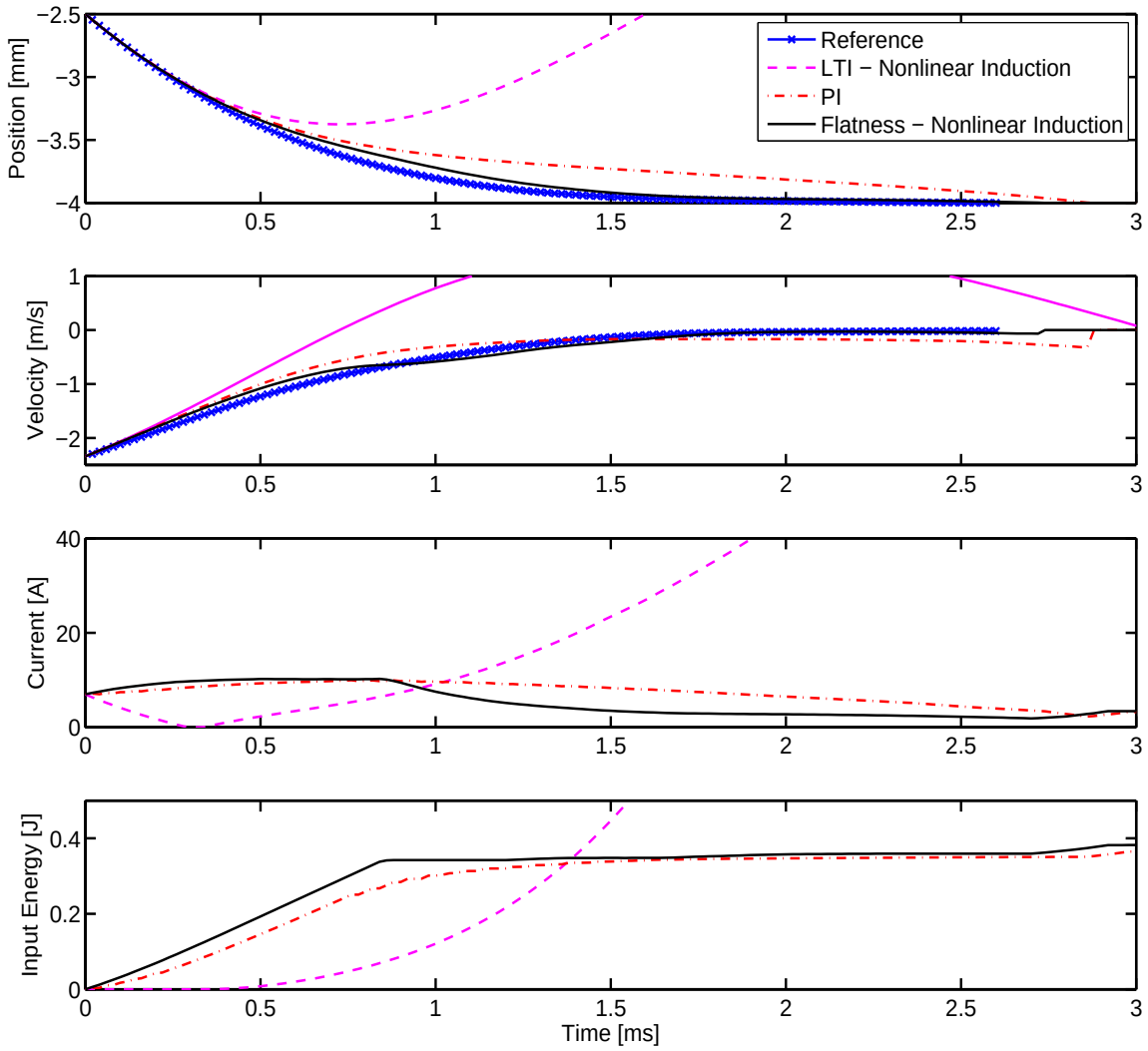

Figure 5.10: Simulated landing control performance comparison with ideal initial conditions, 42 V

the control law (and reference and PI feedforward input derivations), landing impact speeds are higher. The flatness and PI controllers had final speeds of 0.17 m/s and 0.35 m/s respectively. When the stiffness was increased, the PI controller failed to land altogether and the flatness controller exhibited a steady state bias of 0.05 mm as a result of the plant/model mismatch. Such biases are not uncommon with feedback linearization techniques where the tracking error causes a controller input that exactly matches the model/plant discrepancy. In practice, such problems may be

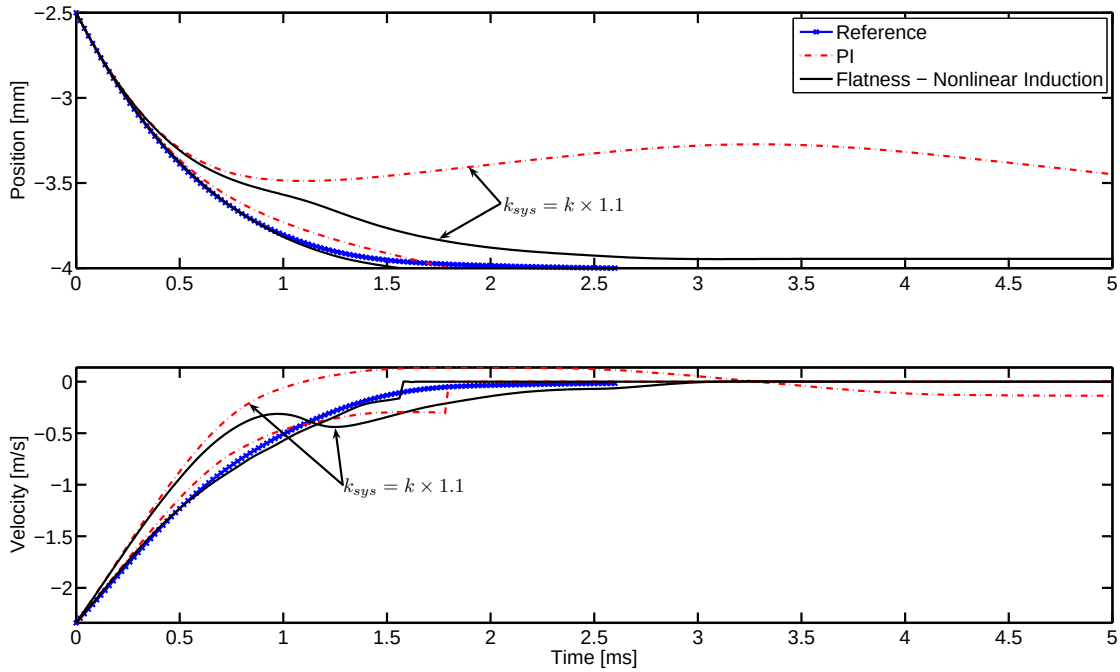

Figure 5.11: Simulated landing control performance comparison with ideal initial conditions and system spring variation of ± 10% at 42 V

overcome by introducing an additional integrator loop to eliminate any steady state errors. Fortunately, spring stiffness is more likely to vary with component wear rather than shorter term environmental changes, unlike viscous damping. To address performance alterations caused by viscous damping changes, system damping, b_{sys}, was varied by ± 500%. Due to the relatively weak force damping has, particularly at the lower speeds encountered during the landing stages of control, only a slight change in impact speed is observed for either controller. However, noticeable changes in settling time are observed, particularly for the flatness controller. Despite that, the changes in viscosity are likely to occur relatively slowly with respect to a given valve cycle. In fact, both stiffness and damping forces are linearly dependent on the system state they are relatively easy to recursively identify through on-line [Slotine and Li, 1991] or off-line methods (see Appendix B).

The result of these simulations indicate the two most promising controllers are the

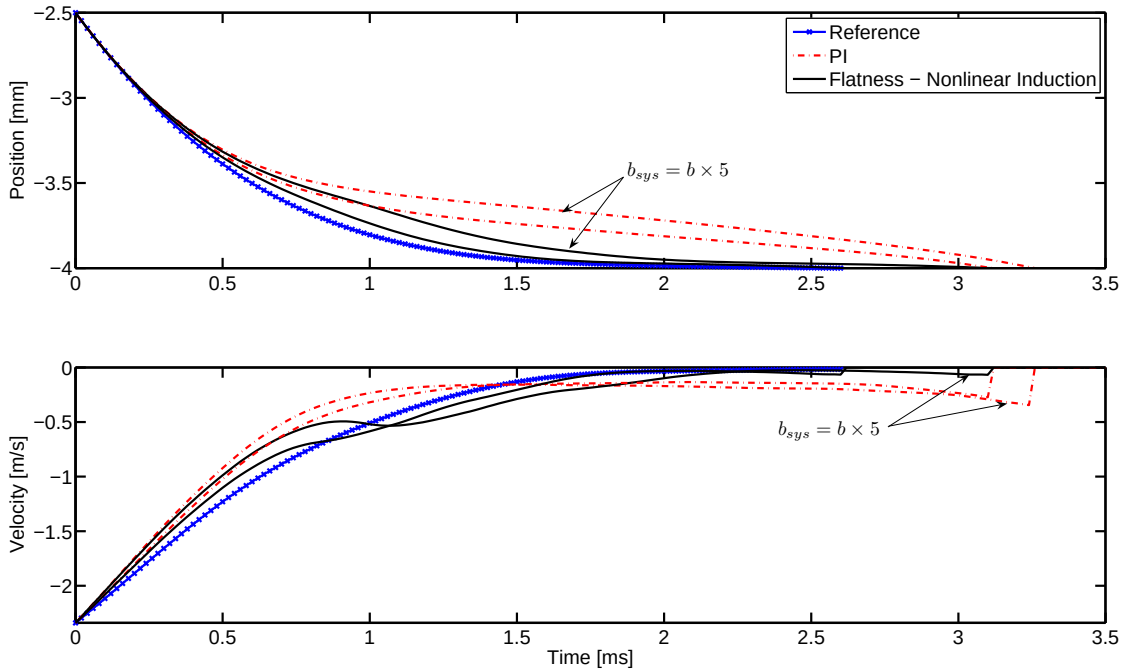

Figure 5.12: Simulated landing control performance comparison with ideal initial conditions and system damping variation of ± 500% at 42 V

flatness-based and PI algorithms. Similar conclusions are documented in [Chung, 2005] based on simulated and experimental results with a linear motion actuator. As a result, only the flatness-based landing controller is to be incorporated into the overall control strategy and testbench experiments discussed in Section 6.3.

5.5 Reference Trajectory Design

To implement the flatness based or LTI landing control algorithms, a set of reference trajectories is required. These trajectories can also be used to generate a corresponding feedforward current input for the PI controller. Optimal reference trajectories are sought to move the armature from an initial state (provided by the feedforward controller) to a open / closed state while subject to physical, practical and desired end condition constraints. A nonlinear programming procedure described in [Chung, 2005] and [Koch et al., 2004] for the closer of a linear motion actuator is

applied to both the opener and closer of the hinged actuator system used in this work. The procedure consists of the formulation of a nonlinear constrained problem to optimize a parameterized trajectory set that connects the prescribed initial and final states. By using the flat mapping between the system output and input, the method is able to account for the dynamics represented in the nonlinear induction model such as magnetic saturation, armature motion and voltage input.

5.5.1 Nonlinear Constrained Problem

Nonlinear optimization problems can generally be formulated into the form:

$$\min_X F(X) \tag{5.33}$$

$$\text{subject to: } A_{eq}\,X = B_{eq} \quad \text{(Linear Equality Constraints)} \tag{5.34}$$

$$A\,X \leq B \quad \text{(Linear Constraints)}$$

$$C_{eq}(X) = 0 \quad \text{(Nonlinear Equality Constraints)} \tag{5.35}$$

$$C(X) \leq 0 \quad \text{(Nonlinear Constraints)}$$

$$\tag{5.36}$$

where $[A,\ A_{eq},\ B,\ B_{eq},\ C(X),\ C_{eq}(X),\ X]\ \epsilon\ \mathbb{R}^n$. The problem solution process minimizes an objective function, X, subject to a nonlinear cost function, $F(X)$, while subject to sets of linear and nonlinear constraints. The solution of such nonlinear constrained problem can be difficult, requiring many iterations and functional computations [Milam, 2003]. In the method used, and originally proposed in [Koch et al., 2004], (5.34) is modified by substituting the minimization of $F(X)$ with a nonlinear feasibility problem. Specifically, a solution will be found such that a parameterized trajectory, y_d, will satisfy the imposed constraints. The constraints imposed are listed in Table 5.1 where t_0 and t_f are the times when the landing controller are respectively

Table 5.1: Reference trajectory constraints

Position (Air Gap)	Velocity
$y_d(t_0) = 1.50$ mm $y_d(t_f) = 0.00$ mm	$\dot{y}_d(t_0) = \dot{y}_0$ m/s $\dot{y}_d(t_f) \leq 0.1$ m/s $\dot{y}_d(t) \geq 0, t_0 < t < t_f$
Acceleration	Voltage & Current
$\ddot{y}_d(t_0) = -1/m\,(\dot{y}_d(t_0)b + y_d(t_0)k - F_v$ $-\ell_m F_m(y_d(t_0), i(t_0))/\ell_v)$ m/s^2 $\ddot{y}_d(t_f) = 0$ m/s^2 $\ddot{y}_d(t) > -1/m\,(\dot{y}_d(t_0)b + y_d(t_0)k - F_v)$, $t_0 < t < t_f$	$v(t) \leq 42$V, $t_0 \leq t \leq t_f$ $i(t_0) = i_0$ A

engaged and disengaged. To ensure the armature moves from the initial position, $y_d(t_0)$ to the final open / closed state, $y_d(t_f)$, the following equality constraints are imposed:

$$y_d(t_0) = 1.50 \text{ mm (Air gap)} \tag{5.37}$$

$$y_d(t_f) = 0.00 \text{ mm (Air gap)} \tag{5.38}$$

Initial and final velocity constraints are also imposed:

$$\dot{y}_{dc}(t_0) = 2.34 \text{ m/s} \tag{5.39}$$

$$\dot{y}_{do}(t_0) = 2.58 \text{ m/s} \tag{5.40}$$

$$\dot{y}_d(t_f) \leq 0.10 \text{ m/s} \tag{5.41}$$

Unique initial velocities for the opener, $\dot{y}_{do}(t_0)$, and closer, $\dot{y}_{dc}(t_0)$, are prescribed to account for the slight differences between the two magnets and spring preload bias. A final landing velocity constraint, (5.41), is imposed to minimize wear and acoustical noise as outlined in the original control objectives.

An initial coil current is also imposed to minimize the input voltage required upon

engagement of the landing controller as done in [Hoffmann et al., 2003].

$$i_o(t_0) = 5.5 \text{ A} \tag{5.42}$$

$$i_c(t_0) = 7.0 \text{ A} \tag{5.43}$$

Where again, the subscripts 'c' and 'o' differentiate between the closer and opener magnets, respectively. The imposed initial current ensures that an adequate flux level is maintained in anticipation of the landing control effort, particularly because the inductance is highest at the smaller air gaps inherent with the landing control.
The initial position and velocity constraints may be used to solve for corresponding acceleration constraints for a predetermined initial current, $i(t_0)$, through substitution into the expression for mass-spring dynamics, where:

$$\ddot{y}_{do}(t_0) = -1/m\,(\dot{y}_{do}(t_0)b + y_d(t_0)k - F_v - \ell_m F_{mo}(y_d(t_0), i(t_0))/\ell_v) \quad \text{m/s}^2 \tag{5.44}$$

$$\ddot{y}_{dc}(t_0) = -1/m\,(\dot{y}_{dc}(t_0)b + y_d(t_0)k - F_v + \ell_m F_{mc}(y_d(t_0), i(t_0))/\ell_v) \quad \text{m/s}^2 \tag{5.45}$$

$$\ddot{y}_d(t_f) = 0.0 \quad \text{m/s}^2 \tag{5.46}$$

A zero acceleration at t_f is explicitly specified so that a constant velocity of $\dot{y}_d(t_f) \leq 0.10$ is maintained until seating occurs. This is done to ensure the valve seats at an acceptable velocity even when the armature and valve are coupled through a flexible lash adjuster. Additionally, acceleration constraints may be imposed to account for the fact that the magnets are only able to impart attractive forces:

$$\ddot{y}_d(t) > -1/m\,(\dot{y}_d(t_0)b + y_d(t_0)k - F_v) \quad \text{m/s}^2, \quad t_0 < t < t_f \tag{5.47}$$

An input voltage constraint may also be imposed through the flat mapping between input voltage, v, and state provided in Equation (5.30):

$$|v(t)| \leq 42 \text{ V}, \quad t_0 \leq t \leq t_f \tag{5.48}$$

This constraint is imposed in accordance with the future 42 V on-board vehicle voltage standard [Chang et al., 2002]. In all cases, realistic constraint values (based on simulated and experimental observations) are specified to ensure a physically realizable trajectory while still satisfying the input and final state conditions.

5.5.2 Parametrization of the Flat Output Trajectory

With a nonlinear programming and constraint framework established, the trajectory set must be parameterized for a particular solution to be found. As discussed in [Chung, 2005], B-spline basis functions are used to mathematically describe a trajectory, y_d. Spline functions are chosen because they are amenable to computing continuous derivatives and are more numerically stable than higher order polynomials [van Nieuwstadt and Murray, 1995]. Sufficiently smooth reference trajectories are required to ensure a diffeomorphic mapping between the input, output and state variables. In this case, three derivatives are required to relate the flat output to the states and input (see Equation (5.30)). Therefore, the parameterized trajectory should have a continuous third time derivative.

Using the methods shown in [Löewis, 2002], a desired trajectory may be parameterized with a spline basis function by:

$$y_d(t) = \theta^T B_k(t), \quad t = t_0, \ldots, t_f \tag{5.49}$$

where θ and B_k represent vectors of spline coefficients and B-spline basis functions of order, k. Knots on an interval $[t_0, t_f]$ represent where the basis functions are joined and are specificed through a strictly increasing sequence of real numbers. In this way, a trajectory, y_d, over the interval $[t_0, t_f]$ and subject to the constraints discussed in the previous section may be determined provided $B_k(t) \neq 0$ [Boor, 1978].

The MATLAB Spline and Optimization Toolboxes are used to optimize the spline coefficients, by solving the nonlinear constrained problem via the `fmincon.m` function. In order to achieve convergence, initial guesses of the coefficients, θ, must be provided that are sufficiently close to the optimal solution. At each iteration, the `fmincon.m` function uses a sequential quadratic programming (SQP) solution method to solve a quadratic programming (QP) subproblem whose solution is used as a search direction for a line search procedure. Details of the SQP method can be found in [Gill et al., 1981]. To ensure sufficient smoothness, five, fourth order B-splines ($k = 5$) are evenly spaced at six simple knots on $[t_0 = 0, t_f]$.

Optimization of θ is done separately for the opener and closer magnets. In doing so, respective constraints (5.37) through (5.40) and (5.45) through (5.46) are passed to `fmincon.m` as linear equality constraints. Additionally, conditions (5.41) and (5.47) are imposed on θ as linear and nonlinear inequality constraints, respectively.

Convergence is knot position dependent which are in turn determined through choosing a suitable landing time from $t_0 = 0$ to $t_{fo} = 2.35$ms, and $t_{fc} = 2.60$ms for the opener and closer magnets, respectively. Given these constraints and knot positions, a trajectory that satisfies the input constraint of $|v|$ <42 V is obtained with the

following optimal spline coefficients:

$$\theta_o^T = \begin{bmatrix} 0.216 & 1.926 & 3.168 & 3.750 & 3.977 & 3.980 & 3.998 & 4.002 & 4.020 \end{bmatrix}^T \times 10^{-3} \tag{5.50}$$

$$\theta_c^T = \begin{bmatrix} 0.187 & 1.924 & 3.174 & 3.737 & 3.955 & 3.980 & 3.998 & 4.002 & 4.020 \end{bmatrix}^T \times 10^{-3} \tag{5.51}$$

Figure 5.13 illustrates the resultant set of reference trajectories and Figure 5.14 represents the corresponding voltage and current input. Note that for the purposes of comparison, the opener and closer reference trajectories are shown relative to their respective magnet pole faces. As mentioned previously, in practice the continuous voltage input is approximated by a 50 kHz PWM via the dSPACE controller and custom power electronics (see Section 6.5.14). The current input is used in the PI controller as a feedforward input to improve convergence rate.

5.6 Flux-based Position Reconstruction

Due to the low-impact speed requirement of the valve and significant combustion pressure fluctuations, a means of accurately sensing armature or valve position is required for feedback control. In [Koch et al., 2002] it was demonstrated that a sensor accuracy of at least 10 μm is required during landing. Presently, a sensor with this accuracy over a 8mm stroke length is either too expensive, unsuitable for under-hood environments or otherwise unfeasible for on-board control. In addition, the sensor response must not limit the control system and consequently stability. Therefore, the sensor must have at least an equivalent response or bandwidth of the actuator system. Methods of state reconstruction through external valve and/or armature-based position measurements have been documented. These include position or velocity mea-

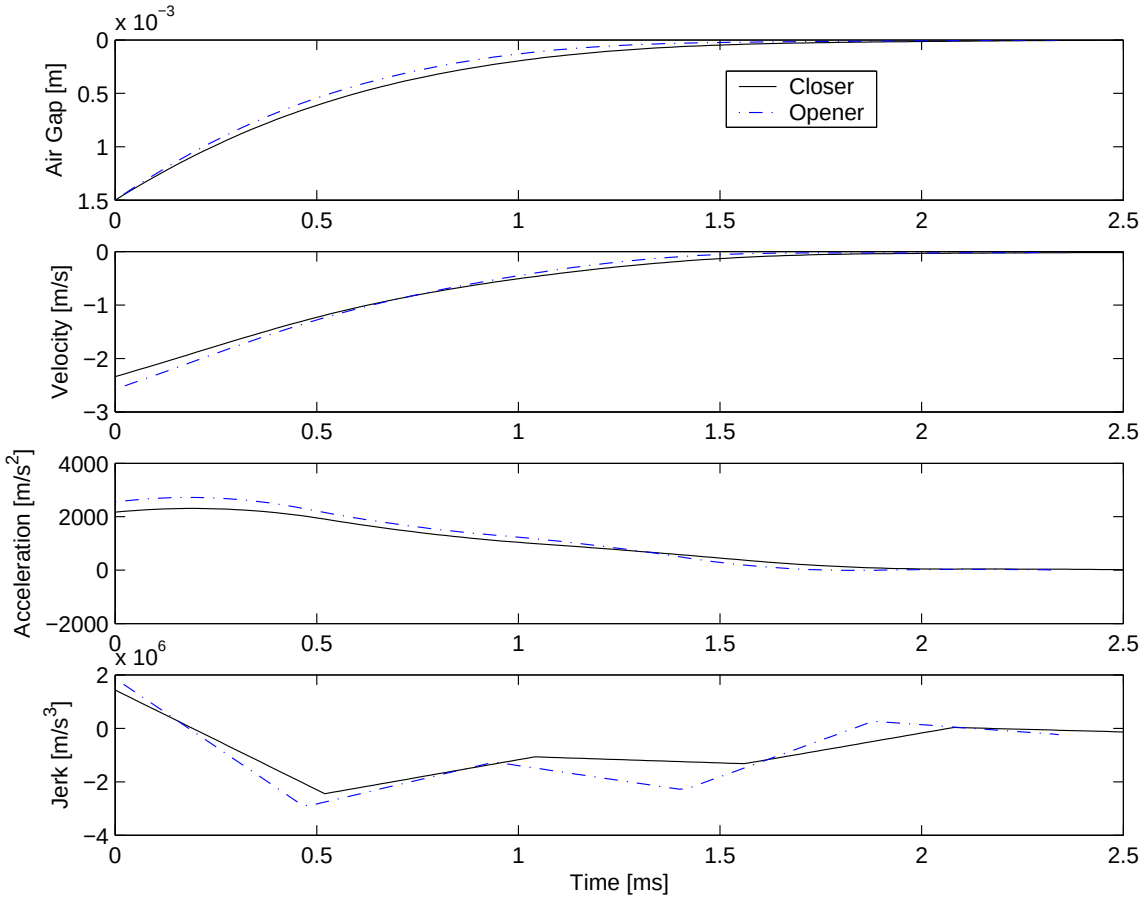

Figure 5.13: Optimized reference trajectories for the hinged actuator with nonlinear induction model

surements via linear variable differential transformer (LVDT) [Sun and Cleary, 2003], laser [Tai and Tsao, 2003, Wang et al., 2002, Stubbs, 2000] or eddy current displacement sensors [Peterson et al., 2006, Chung, 2005]. Another feedback system demonstrated uses a microphone to adaptively improve impact speeds from sound intensity measurement [Peterson and Stefanopoulou, 2004]. Although proven successful in laboratory testbench experiments, such a sensor scheme is likely not practical in an engine environment due to associated sensor cost, multiple valves in operation and other acoustic sources.

These sensors provide sufficient precision, accuracy and response, efforts are being

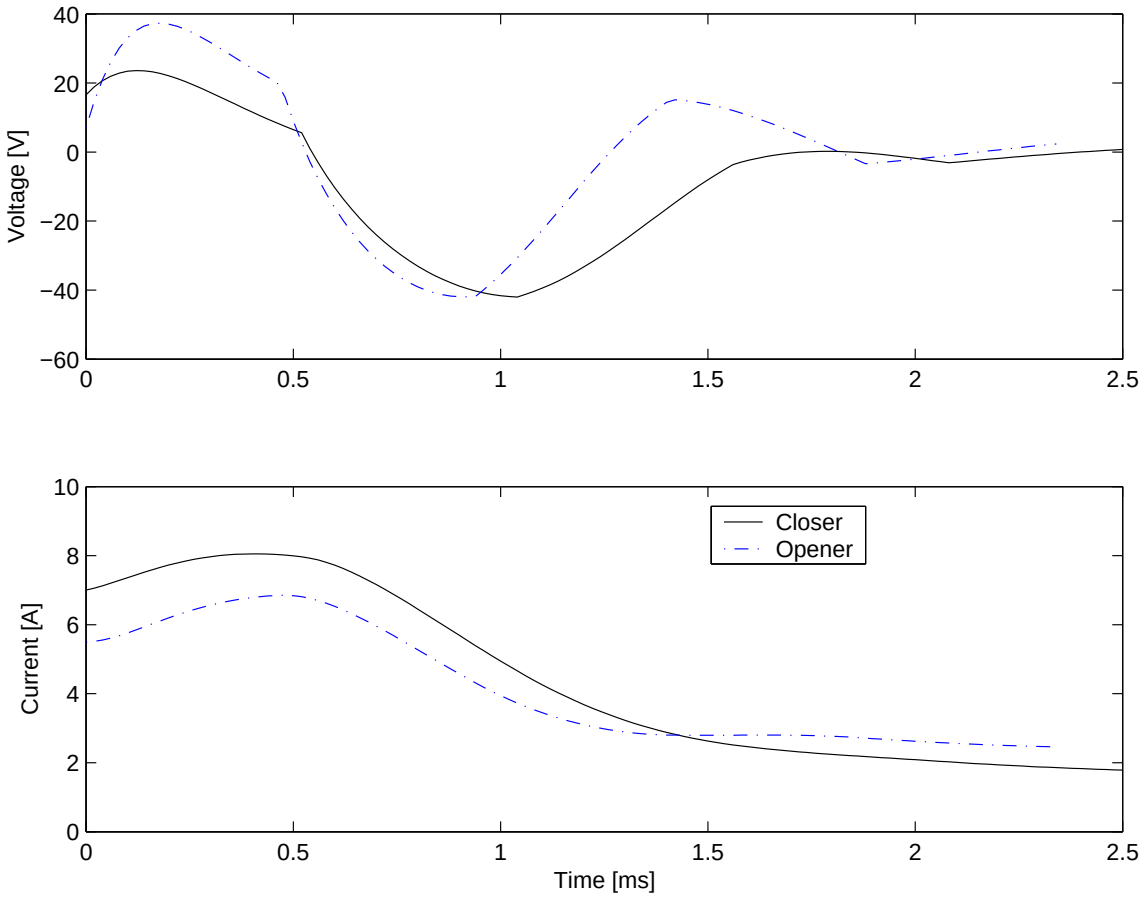

Figure 5.14: Coil input corresponding to the optimized reference trajectories for the hinged actuator and nonlinear induction model

made to develop alternative production amenable sensors or sensing methods with equivalent performance. These methods include the flux-based coil type [Chladny and Koch, 2006a, Scacchioli, 2005, Montanari et al., 2004], [Ronchi and Rossi, 2002, Rossi and Alberto, 2001, Rossi and Tonielli, 2001], [Roschke and Bielau, 1995], observer based [Lynch et al., 2003, Eyabi, 2003] and self inductive [Butzmann et al., 2000, Takashi and Iwao, 1995]. In the latter cases, it is proposed that the driving coil itself be used to relate the measured rate of change of induced coil current to the armature position and velocity. This may be done by momentarily deactivating the drive coil and relating velocity-induced currents to po-

sition. However, this method is susceptible to noise and signal processing challenges in addition to temporary loss of control authority [Butzmann et al., 2000] and thus potentially compromising to tracking performance.

Observer based state reconstruction that makes use of the measured current signal and estimated initial state conditions to predict plant output has been implemented in [Eyabi, 2003]. Using only a current measurement makes the position and velocity estimates sensitive to initial conditions and requires high gain for the relatively rapid estimation convergence required, making the estimation potentially prone to instability when subjected to excessive noise or disturbances. Thus, it is perhaps better suited to compensate for relatively slow parameter variations.

5.6.1 Flux Sensor

Flux-based coil type sensors, such as the type used in this work and first proposed in [Rossi and Tonielli, 2001], appear to be a promising method of achieving a low-cost yet high-performance position measurement. The system incorporates a secondary sensor coil concentric to each of the opener and closer magnet drive coils as shown in Figures 1.2 and 3.4. These sensor coils are terminated across high impedance analog integration circuits (see Section 6.5.7). The circuit output signal can thus be related to magnetic flux. Using this signal with the drive current signal, position may be predicted through an inductance model. In the case of devices with variable air gaps such as solenoid actuators, inductance is highly dependant on armature and hence valve position. Thus, any time-varying magnetic field produced by the excitation coil will induce an electromotive force (EMF) in the secondary coil as predicted by Faraday's law of mutual inductance. The secondary coil is measured with high impedance circuitry and thus the effect of resistance is assumed negligible. As a result, the induced voltage, v_{fc}, due to a change in excitation current or flux

may be expressed as:

$$v_{fc} = N_{fc}\frac{d\phi(i,x)}{dt} = \frac{N_{fc}}{N_{ec}}\frac{d\lambda(i,x)}{dt}, \tag{5.52}$$

where v_{fc} is the induced voltage in the flux coil, $\frac{d\phi}{dt}$ is the flux induced potential and N_{fc} and N_{ec} are the respective number of turns for the secondary flux measurement coil and excitation coil. In practice, the induced voltage is integrated (via analog circuitry) and sampled. Analog drift is assumed linear with respect to time and corrected for during online measurement through $v_{fd} = c_{fd}t$, where c_{fd} is a measured constant. Each channel is calibrated prior to excitation and the integration hardware is reset externally when the armature is at the opposite pole face of the coil in use. The reset of the integrator is particularly effective due to the periodic motion of the valve. The integrators are reset when coil current is zero (releasing magnet) or when the valve is in the open or closed holding states. The later reset requires an estimate of the initial flux condition, ϕ_o, which is obtained by using the steady state holding current measurement and the known position (since it is either fully open or closed). The integrated flux linkage measurement may be expressed as:

$$\lambda = N_{ec}(\phi_o + \frac{\int v_{fc}dt - v_{fd}}{N_{fc}}), \tag{5.53}$$

where ϕ_o is the initial flux condition prior to integration. Using the derived nonlinear induction model, a relationship between current, flux and armature position is expected to be of the form:

$$x = \frac{\beta i}{\alpha i + ln(1 - N_{ec}/\psi(\phi_o + \int v_{fc}dt/N_{fc}))} + \kappa \tag{5.54}$$

which requires a non-zero current to maintain sufficient accuracy. This restriction is also imposed in order to satisfy controllability conditions (Section 5.4.5). This

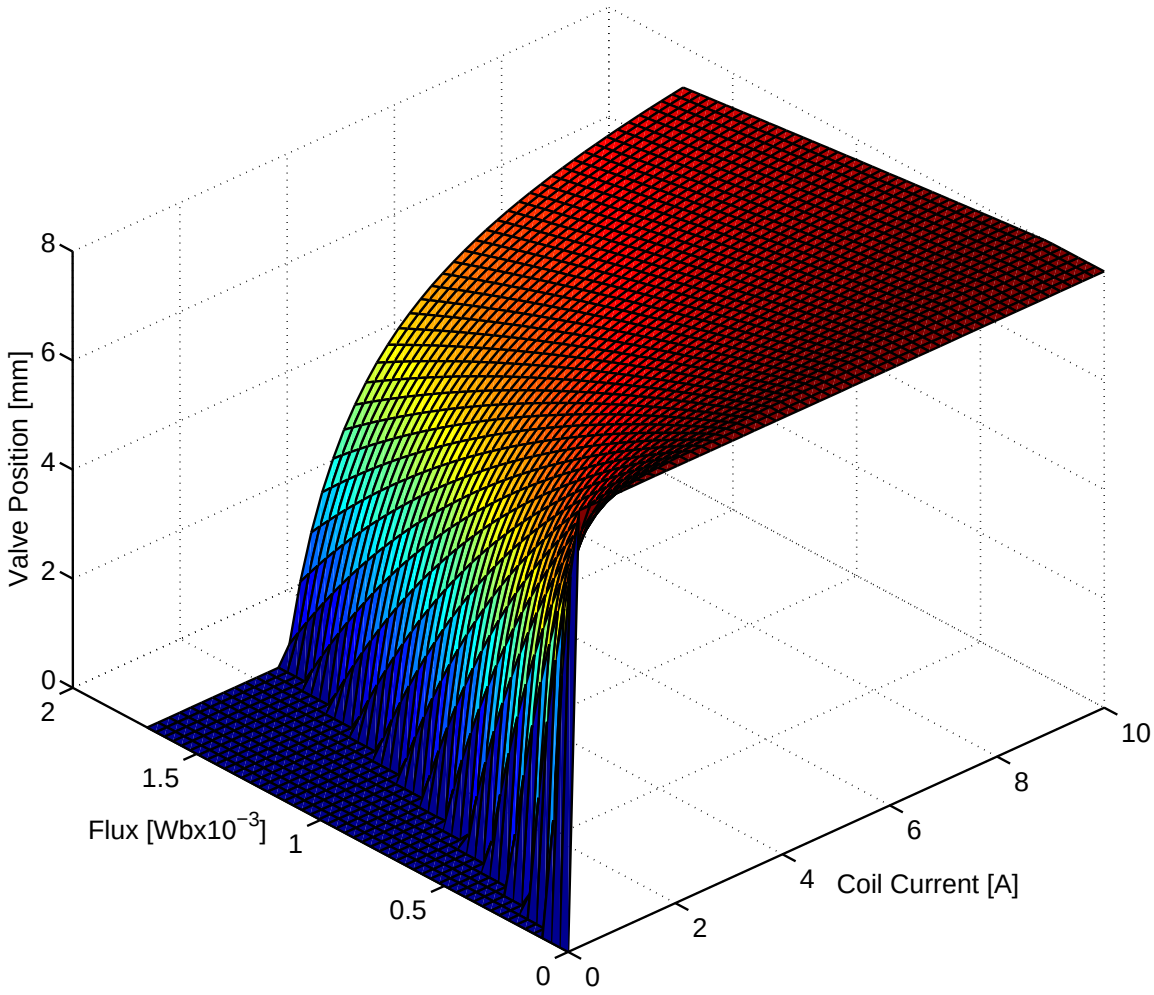

Figure 5.15: Opener position with respect to current and flux

method of position reconstruction is similar to [Montanari et al., 2004], in which two functions are used to relate reluctance and excitation to air gap. A plot of position as a function of path flux and excitation current is provided in Figure 5.15 for the opener magnet. Experimental efforts in this work have shown that improved performance can be attained over Equation (5.54) through use of a numerical look-up table with FEA results relating flux and current to position [Chladny and Koch, 2006b, Chladny et al., 2005].

5.7 Feedforward Controller

The approximate $\frac{1}{x^2}$ drop in magnetic force with air gap limits the effectiveness of a closed loop landing controller to regions close to the pole face [Tai and Tsao, 2002]. For the exhaust actuator, the lack of force authority is exacerbated by in-cylinder combustion gas forces, particularly at higher engine loads, which inhibit valve opening. Initially, these forces can only be overcome by spring force, after which, open-loop control is used to setup favorable valve motion and coil current conditions for the start of the feedback or landing control. By using the position-based gas force relation in Section 4.5.2 and a nonlinear disturbance observer (see Section 5.8), an energy based method is used to determine the required coil current output for the open-loop control. A detailed discussion of the individual system energy terms is provided in the following section to clarify the proposed feedforward technique.

5.7.1 System Energy Derivation

An essential concept to the proposed feedforward design is system energy. The armature-valve kinetic and valve spring / torsion bar potential energy may be expressed as a function of the work done to cause motion or displace the springs. The general expression for work is the amount of force, F, applied over a given path, ds:

$$W = \oint F \cdot ds \tag{5.55}$$

Given this general expression, the definitions for the spring and kinetic energy, as well as gas force, magnetic closer and opener work can be derived. Kinetic energy, W_k for an object with mass, m, velocity $\dot{x}$ and momentum, $p = m\dot{x}$ is defined as (assuming

starting from rest):

$$W_k = \int F \cdot ds = \int \dot{x} \cdot dp = \int m\dot{x}d\dot{x} = \frac{m\dot{x}^2}{2} \tag{5.56}$$

Similarly, work due to potential spring energy is:

$$W_s = \int F_s dx \tag{5.57}$$

where $F_s(x) = k(x - x_o)$ is the position dependent spring force. Thus:

$$W_s = \int_{x_1}^{x_2} k(x - x_o)dx = (\frac{kx^2}{2} - kx_o x)|_{x_1}^{x_2} \tag{5.58}$$

Force due to viscous friction is approximated as $F_f = b\dot{x}$. The work done can thus be related through:

$$W_f = \int b\dot{x}dx = b\int \dot{x}\frac{dx}{dt}\frac{dt}{dx}dx = b\int \dot{x}^2 dt \tag{5.59}$$

Using the model for simplified gas force, F_{gs}, from Section 4.5.2, work due to gas forces, W_{gs}, over an opening cycle may be expressed as:

$$W_{gs} = \int F_g dx = C_{gf}P_o A_v(c_1 x_L + \frac{c_2 x_L^2}{2} + \frac{c_3 x_L^3}{3}) \tag{5.60}$$

since the path dx is equivalent to valve lift, dx_L. Recall, γ represents the combined initial pressure, valve area and gas force coefficient, $\gamma = P_o A_v C_{gf}$, and is identified using the online disturbance observer (see Section 5.8).

Work due to the opener, W_{mo}, or closer, W_{mc}, magnets is

$$W_{m,o/c} = \int F_{mo/c}dx = \int \frac{\ell_m}{\ell_v}\frac{\psi g'(x)}{g^2(x)}\left(1 - (1 + ig(x))e^{-g(x)i}\right)dx = \frac{\ell_m}{\ell_v}W_{c,o/c} \tag{5.61}$$

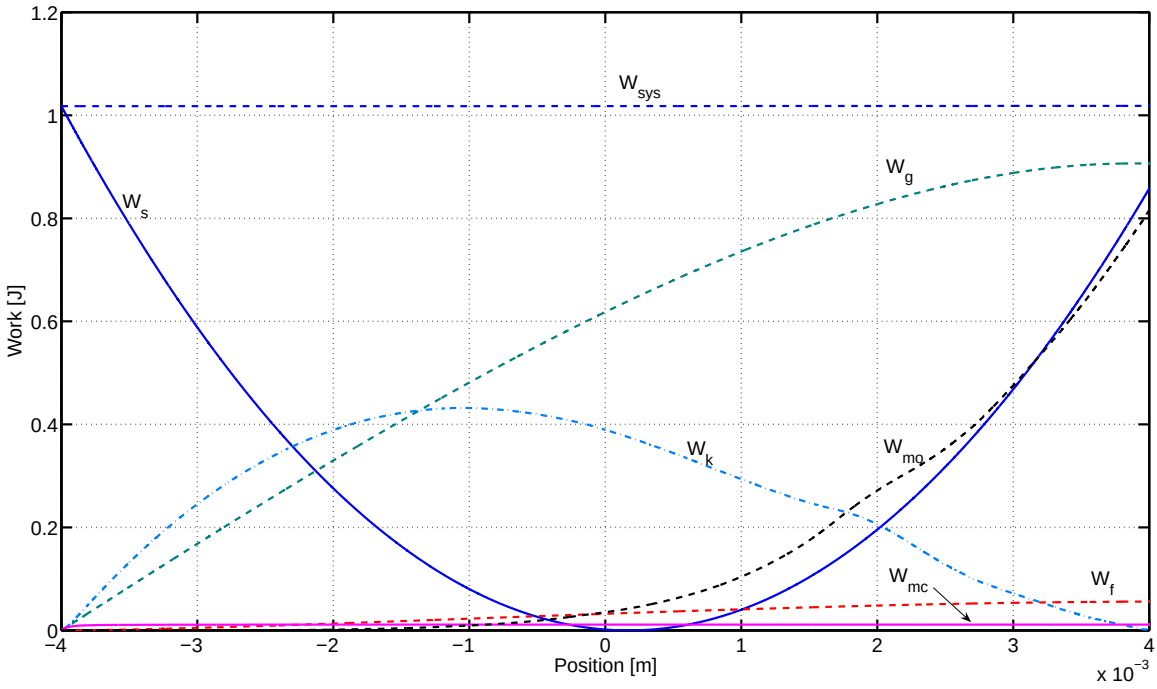

Figure 5.16: Simulated individual energy terms (5.56), (5.58), (5.59), (5.63), (5.61) and (5.62) during an opening cycle (4 bar exhaust valve opening pressure)

where W_c is magnetic co-energy.

Finally, net mechanical system energy, W_{sys}, may be expressed as the sum of the work done by the spring, kinetic energy, friction, gas force and opener and closer magnets:

$$W_{sys} = W_k + W_s + W_f + W_g + W_{m,o} + W_{m,c} \tag{5.62}$$

Provided all energy terms are accounted for, the system energy should remain constant over a given opening or closing cycle. Figure 5.16 provides an example of these terms for the valve system energy during a simulated opening cycle at a 4 bar EVO. Note that the system energy remains constant, and the dominant terms are spring, kinetic energy, magnetic opener and gas force work.

5.7.2 Feedforward Current Input

Typically, due to the characteristics of the valve and port of an engine, gas forces occur primarily in the first half of the valve stroke as indicated in Figures 4.8 and 5.16. However, the magnetic force required to compensate for gas disturbances can only be effectively applied in the later half of the valve stroke (see Figure 7.4). The work done on the valve by gas forces, W_g, can be approximated by integrating (4.33) with respect to valve lift:

$$W_{gs}(x_L) = \int_0^{x_{L_1}} F_{gs} dx_L = \gamma(c_1 L + \frac{c_2 x_L^2}{2} + \frac{c_3 x_L^3}{3}) \tag{5.63}$$

To compensate for this disturbance, a desired restoration work trajectory, W_d, is chosen as:

$$\begin{aligned} W_d(x_L) =& \gamma \int \left[c_1 + c_2(x_L - S) + c_3(x_L - S)^2\right] dx_L \\ =& \gamma x_L \left[c_1 + x_L \left(\frac{c_2}{2} + \frac{c_3}{3} x_L\right)\right. \\ & \left. - S(c_2 + c_3 x_L) + c_3 S^2 \right] \end{aligned} \tag{5.64}$$

A disturbance observer estimate is used to estimate the the initial gas force magnitude, γ, which can then be used to adjust the above trajectory. Just as the majority of the gas work occurs primarily over the first half of the valve stroke, this trajectory was chosen to mirror the simplified gas force work about the mid-stroke position so that the restoring magnetic force is applied in the latter half of the stroke. The advantages of this strategy are: the opening magnet is only used when it is most effective, thereby minimizing ohmic losses, and additionally, the disturbance estimate is not required immediately, providing time for the observer to converge.

The above technique ensures that work performed on the valve by the gas force

is recovered using the magnetic force by the end of the valve stroke. However, to expedite transition, (5.64) is adjusted so that the estimated gas work is recovered by the time the landing controller is engaged (at position $x = x_{lc}$). Thus, the desired magnetic work trajectory used with landing control, W_{dlc}, takes the form:

$$\begin{aligned} W_{dlc}(d) =& \gamma \frac{W_{gs}(S)}{W_d(x_{lc})} x_L \left[c_1 + x_L \left(\frac{c_2}{2} + \frac{c_3}{3} x_L \right) \right. \\ & \left. - S(c_2 + c_3 x_L) + c_3 S^2 \right] \end{aligned} \tag{5.65}$$

The magnetic coenergy relation is used to convert work into a desired current output. Using the flux relation in (3.76), the co-energy of the system W_c is:

$$\begin{aligned} W_c(x, i) &= \int_0^i \lambda(x, \xi) d\xi \\ &= \int_0^i \psi(1 - e^{-\xi g(x)}) d\xi \\ &= \psi \left(i + \frac{e^{-ig(x)} - 1}{g(x)} \right) \end{aligned} \tag{5.66}$$

To restore the energy lost to gas forces, the desired feedforward current, i_d, is calculated as a function of initial gas pressure and valve position by equating (5.66) and (5.65) and solving for current:

$$i_d(x, P_o) = \frac{1}{g(x)} + \frac{W_{dlc}}{\psi} + \frac{W_{-1}(-e^{\frac{-1 - g(x) W_{dlc}}{\psi}})}{g(x)} \tag{5.67}$$

Again, W_{-1} is a real-valued branch of Lambert's W function. In the real system, current is measured with a hall-effect sensor and regulated through the 'H'-bridge power electronics. As with the holding and PI controllers, the desired current, i_d, is obtained using a simple control law based on measured and desired current and a PWM signal to the power electronics. The feedforward control is engaged upon

valve release and disengaged during landing control, holding, initialization and error modes. Any discrepancy between the final feedforward current and the initial landing control current appears to be minimal, or at least manageable by the landing control algorithm as no method of current level transition is specified (or appears necessary).

5.8 Disturbance Observer

Since velocity and gas pressure are required by the feedforward and landing controllers but are not measured, they are estimated online. Improved robustness and landing performance are expected upon implementation of a gas force estimate and feedforward compensator compared to static position or time based feedforward controller. Disturbance dynamics are characterized by assuming that gas force magnitude, γ, may vary from one cycle to the next, however, it's normalized trajectory, f_1, as a function of position is typically predictable for all cycles. Therefore, all that must be identified is the initial force magnitude, γ, which is used as a constant for the entire cycle (but estimated for each new cycle). Velocity and initial force magnitude estimation are performed using a nonlinear Luenberger observer [Zeitz, 1987]. Defining the estimated state as $\hat{\mathbf{y}} = [\hat{y}\ \dot{\hat{y}}\ \hat{\gamma}]$, the observer structure is:

$$\begin{pmatrix} \dot{\hat{y}} \\ \ddot{\hat{y}} \\ \dot{\hat{\gamma}} \end{pmatrix} = \begin{pmatrix} 0 & 1 & 0 \\ \frac{-k}{m} & \frac{-b}{m} & \frac{-f_1}{m} \\ 0 & 0 & 0 \end{pmatrix} \begin{pmatrix} \hat{y} \\ \dot{\hat{y}} \\ \hat{\gamma} \end{pmatrix} + \zeta(y, i_{op}, i_{cl}) + \begin{pmatrix} \ell_{ob1} \\ \ell_{ob2} \\ \ell_{ob3} \end{pmatrix} (y - \hat{y}) \tag{5.68}$$

where

$$\zeta(y, i_{op}, i_{cl}) = \begin{pmatrix} 0 \\ \frac{1}{m}(F_v + F_{mop}(y, i_{op}) - F_{mcl}(y, i_{cl})) \\ 0 \end{pmatrix} \tag{5.69}$$

and the valve position output is represented through $y = h(x)$.

The system is locally observable provided the term $-\frac{f_1(y)}{m} \neq 0$. Although the function $f_1(y)$ does become small towards the end of the valve stroke ($f_1(4mm) = 0.01$), the gas force will have largely been dissipated by that time. Additionally, because the gas force amplitude may be considered a constant over the whole cycle, the estimated value at the time of landing control engagement ($f_1(x_{lc})$) may be used for the remainder of the valve stroke. However, simulated and experimental results have indicated that an adequate estimate may be obtained over the entire valve stroke.

Assuming negligible magnetic force modeling errors, the observer structure error dynamics are:

$$\dot{\tilde{e}}_o = \begin{pmatrix} \dot{\tilde{y}} \\ \ddot{\tilde{y}} \\ \dot{\tilde{\gamma}} \end{pmatrix} = \begin{pmatrix} -\ell_{ob1} & 1 & 0 \\ -\ell_{ob2} - \frac{-k}{m} & \frac{-b}{m} & \frac{-f_1(y)}{m} \\ -\ell_{ob3} & 0 & 0 \end{pmatrix} \begin{pmatrix} \tilde{y} \\ \dot{\tilde{y}} \\ \tilde{\gamma} \end{pmatrix} \tag{5.70}$$

Observer gains $L_o = [\ell_{ob1}, \ell_{ob2}, \ell_{ob3}]^T$ are chosen to maintain LHP poles of the characteristic equation $det(sI - (A_o - L_o C_o)) = s^3 + \lambda_2 s^2 + \lambda_1 s + \lambda_0 = 0$ where:

$$A_o = \begin{bmatrix} 0 & 1 & 0 \\ -\frac{-k}{m} & \frac{-b}{m} & \frac{-f_1(y)}{m} \\ 0 & 0 & 0 \end{bmatrix} \tag{5.71}$$

and $C_o = [1, 0, 0]$. so that the observer gains may be expressed as:

$$\ell_{ob1} = -\frac{b}{m} + \lambda_2 \quad \ell_{ob2} = -\frac{k + \ell_{ob1} b}{m} + \lambda_1 \quad \ell_{ob3}(y) = -\frac{\lambda_0 m}{f_1(y)} \tag{5.72}$$

Note that ℓ_{ob3} is a function output injection, y, in order to maintain pole placement in a similar fashion as [Löewis et al., 2000, Lévine et al., 1996].

The observer is implemented in real time by Tustin's method of integration of the estimated states:

$$\gamma[n+1] = \gamma[n] + \frac{T_s}{2}(\dot{\gamma}[n+1] + \dot{\gamma}[n]) \tag{5.73}$$

$$\dot{\hat{y}}[n+1] = \dot{\hat{y}}[n] + \frac{T_s}{2}(\ddot{\hat{y}}[n+1] + \ddot{\hat{y}}[n] + \ell_{ob2}\tilde{y}) \tag{5.74}$$

$$\hat{y}[n+1] = \hat{y}[n] + \frac{T_s}{2}(\dot{\hat{y}}[n+1] + \dot{\hat{y}}[n] + \ell_{ob1}\tilde{y}) \tag{5.75}$$

with T_s representing the sample period and

$$\dot{\gamma}[n] = \ell_{ob3}(\hat{y}[n])\tilde{y} \tag{5.76}$$

$$\ddot{\hat{y}}[n] = \frac{1}{m}(-b\dot{\hat{y}}[n] - ky[n] + f_1(y[n])\gamma[n] + \zeta(y[n], i_{op}[n], i_{cl}[n])) \tag{5.77}$$

Estimated gas force and the respective time derivative are input to the flatness control law by:

$$\begin{aligned} \hat{F}_g &= \hat{\gamma} f_1(y) \\ \dot{\hat{F}}_g &= \hat{\gamma} f_2(y, \dot{\hat{y}}) \end{aligned} \tag{5.78}$$

By including an approximation of the gas force dynamics via f_1 and γ in the observer, higher convergence rates can be expected than if gas force was to be estimated directly.

The estimation routine begins at the stroke bound, therefore initial estimates of position and velocity are known. Good performance over a wide operating range has be found by taking the initial gas force estimate, $\hat{\gamma}_0$, is taken to be 1 bar. This is because the feedforward controller may input excessive magnetic force if an overestimate of gas force is made, causing a collision between the armature and opener pole face. The landing controller has a fundamental limitation in avoiding such a situation as the

magnets can only apply attractive forces.

For valve closing, the observer order is reduced to two by assuming γ, and hence gas force, F_g and observer gain, ℓ_{ob3} are zero. Thus, aside from consideration of valve preload and magnetic forces that consider material saturation, the structure is similar to the observer proposed in [Peterson, 2005] while the valve is in transition from the open to closed states.

5.9 Summary

A comprehensive valve control methodology is presented for a hinged solenoid valve actuator. The key features are a flux-based feedback sensor, energy-based feedforward controller, a nonlinear disturbance observer and flatness-based closed-loop landing controller. Together, these components form a complete valve control system capable of soft seating control and cycle-by-cycle gas force disturbance rejection while satisfying onboard and feedback sensor constraints. Simulated and experimental testbench results of the system are presented in Chapter 7.

Chapter 6

Experimental Setup

6.1 Introduction

To ensure the finite element and lumped parameter models adequately capture the significant physical dynamics, experimental validation is undertaken. Two experiments are conducted, one involving the actuator in a material testing machine to investigate the actuator performance (magnetic force and current response), another to evaluate the control performance (impact velocities and disturbance rejection) on a testbench engine emulator. Through system identification techniques, experiments also serve to parameterize and further refine model fidelity, and thus control performance. In addition, preliminary work is undertaken to facilitate the implementation of an engine control unit (ECU) that will manage the valve actuator controllers. The following describes in detail the procedure and equipment used for the experimental testing of a hinged electromagnetic prototype actuator.

6.2 Material Testing Machine Experiments

As a method of validating the developed FEA and analytic models, the opener magnet of the hinged VVT actuator was tested using a material testing machine and associated apparatus. The actuator is constrained and the armature is manipulated

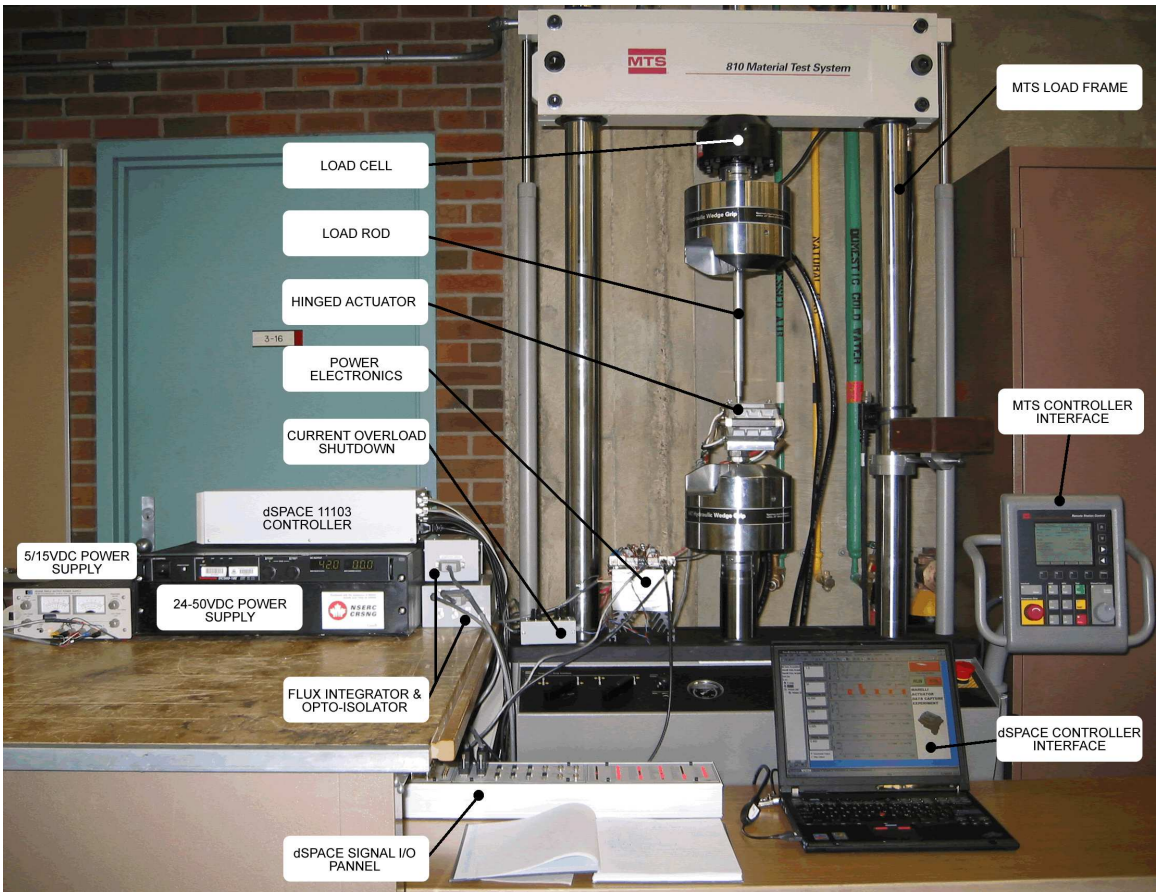

Figure 6.1: Hinged actuator performance evaluation experimental setup

to predetermined positions. At each position the magnetic force on the armature is recorded for a series of steady state and transient current inputs. The material testing machine also has a dynamic loading ability which is used as a preliminary method of investigating the flux-based position measurement. A labeled photo of the experimental apparatus is provided in Figure 6.1. A detailed description of the equipment is provided in Section 6.5 with relevant specifications listed in Table 6.2. In these experiments, only the opener portion of the actuator was tested. This is due to the difficulty in fabricating a nondestructive load cell-to-actuator adaptor capable of measuring the high tension loads that will be experienced at low closer air gaps. These experimental tests are primarily intended to validate the the FEA modeling

procedure and not to evaluate the actuator performance in its entirety. Due to the similarity between the opener and closer magnets, it is assumed that the validation of the opener will demonstrate that the closer FEA is also valid. To mitigate the potential risk of damaging the actuator, the power supply current and overload protection are used to artificially limit control input to a 'dummy' actuator. The actuator power supply current limit and overload circuit protection is only then relaxed as necessary and later, the real actuator is installed in the load frame.

6.2.1 Static Evaluation

As in the case of the FEA modeling, a steady state map of magnetic force as a function of current and position is desired for performance characterization. Digital current control is implemented in C on the dSPACE controller to regulate a desired current amplitude for a pre-specified duration (25 ms) using pulse width modulation (PWM) at a 50 kHz frequency. A Hall-effect current sensor is used for feedback. By sending appropriate switching signals, the dSPACE controller allows the measured coil current to rise to the specified level and then switches the power electronics to the 0 V mode. The power is switched on again when the current drops below a threshold level. Controller switch signals, crosshead position, actuator coil voltage, coil current and load cell signals are all recorded with the dSPACE controller at a sample rate of 50 kHz. A 5 V TTL logic signal is used to control the 42 V power transistors and is also used to trigger data recording. Measured signals are saved as MATLAB binary files (version 6.5). Table 6.1 lists the 19 current levels and 45 armature positions where force is recorded to contrast with the performance predicted by the FEA and LPMs. Because the sampling and PWM frequency are identical, voltage measurements are monitored (via a scope) at a higher rate. The naming convention of all data files are listed in Appendix C.

Table 6.1: Experimental air gap and excitation operating points

Air Gap [mm]								
0.02	0.03	0.04	0.05	0.08	0.10	0.12	0.14	0.16
0.18	0.20	0.22	0.24	0.28	0.30	0.32	0.34	0.36
0.38	0.40	0.42	0.44	0.46	0.50	0.55	0.60	0.65
0.70	0.75	0.80	0.85	0.90	0.95	1.00	1.25	1.50
1.75	2.00	2.50	3.00	3.50	4.00	4.50	5.00	6.00

Coil Excitations [Ampere-turns]									
50	100	150	200	250	300	350	400	450	500
600	700	800	900	1000	1250	1500	1750	2000	

6.2.2 Transient Evaluation

Three types of transient excitation experiments are conducted to investigate the actuator response and flux-based position sensing technique. In all cases, coil voltage, current, flux signals, crosshead postion and force data are recorded in MATLAB binary format for comparison to the transient FEA opener and LPM model results. See Appendix C for a full listing.

6.2.2.1 Step Response

Aside from validating the transient performance of the FEA and LPM models, evaluating an actuator coil response to a step voltage input provides insight to the extent which eddy-currents persist in the magnetic path material [Chladny et al., 2005]. For that reason, an experiment is conducted using the dSPACE controller where the coil current and magnetic force response to a step voltage input of a pre-specified amplitude over several positions is measured. To prevent coil damage, the step duration is gradually increased to 1.74 ms which is sufficient to reach a current amplitude of 30 A at the largest air gap (lowest inductance) and voltage amplitude tested. After the step duration period is exceeded, voltage polarity is effectively reversed (see the

power electronics Section 6.5.14) to reduce the flux and current as rapidly as possible. Voltages of 24, 42 and 50 V are selected to investigate the effect on response. Armature position is varied between 0.50 and 2.00 mm in 0.25 to 0.50 mm increments. All collected data are archived in MATLAB binary files as listed in Appendix C.

6.2.2.2 Sinusoidal Response

As an initial investigation of flux-based sensor performance, a sinusoidal current is input at various predefined armature positions. The corresponding force, crosshead position and integrated flux signals are recorded to reconstruct the position off-line. A signal with an amplitude of 5 A and frequency of 750 Hz with mean excitations of 5, 10 and 15 A are tracked by the same current controller used in the steady state experiments. As this experiment is primarily exploratory in nature, these tests were also performed at voltages of 24, 42 and 50 V for air gaps between 0.50 and 2.00 mm in 0.25 to 0.50 mm increments. All collected data are archived in MATLAB binary files as listed in Appendix C.

6.2.2.3 Response with Armature Motion

The material testing apparatus shown in Figure 6.2 can manipulate the armature position through changing the lower crosshead displacement with predefined time varying functions. This feature is used to evaluate the flux sensor performance over varying positions and current excitations. The armature position is varied sinusoidally for various mean positions, amplitudes and frequencies over various step and sinusoidal current excitations while force, crosshead position and integrated flux signals are recorded. Unfortunately, the maximum amplitude and frequency of the position was limited to 1.50 mm and 10 Hz respectively, resulting in relatively slow speeds ($<$0.1 m/s). This limitation is due to the material testing machine power and hydraulic pressure overload safeguards. As well, there is concern of destroying the

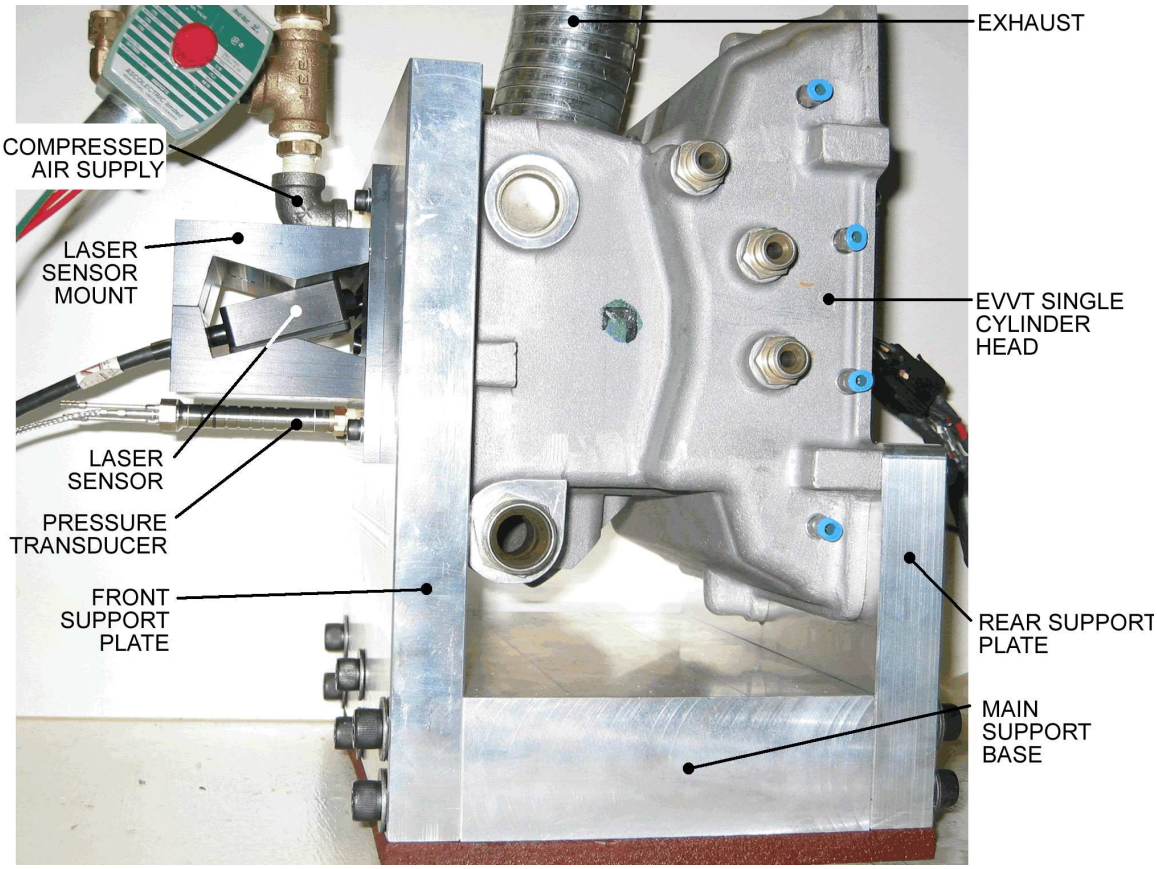

Figure 6.2: Single cylinder head test-bench setup

actuator because at higher frequencies, the stroke amplitude must be artificially increased beyond the actuator stroke bounds to compensate for the observed amplitude attenuation. Although these armature speeds and position amplitudes are relatively slow with respect to those experienced during actuation, they provide initial insight into the flux sensor performance.

6.3 Testbench Engine Emulator

A techbench method of experimentally evaluating actuator control performance is designed to avoid the added complexity of implementation on a working single cylinder engine. The designed system is located in 4-28 of the Mechanical Engineering Building at the University of Alberta. It consists of an intake and exhaust actuator

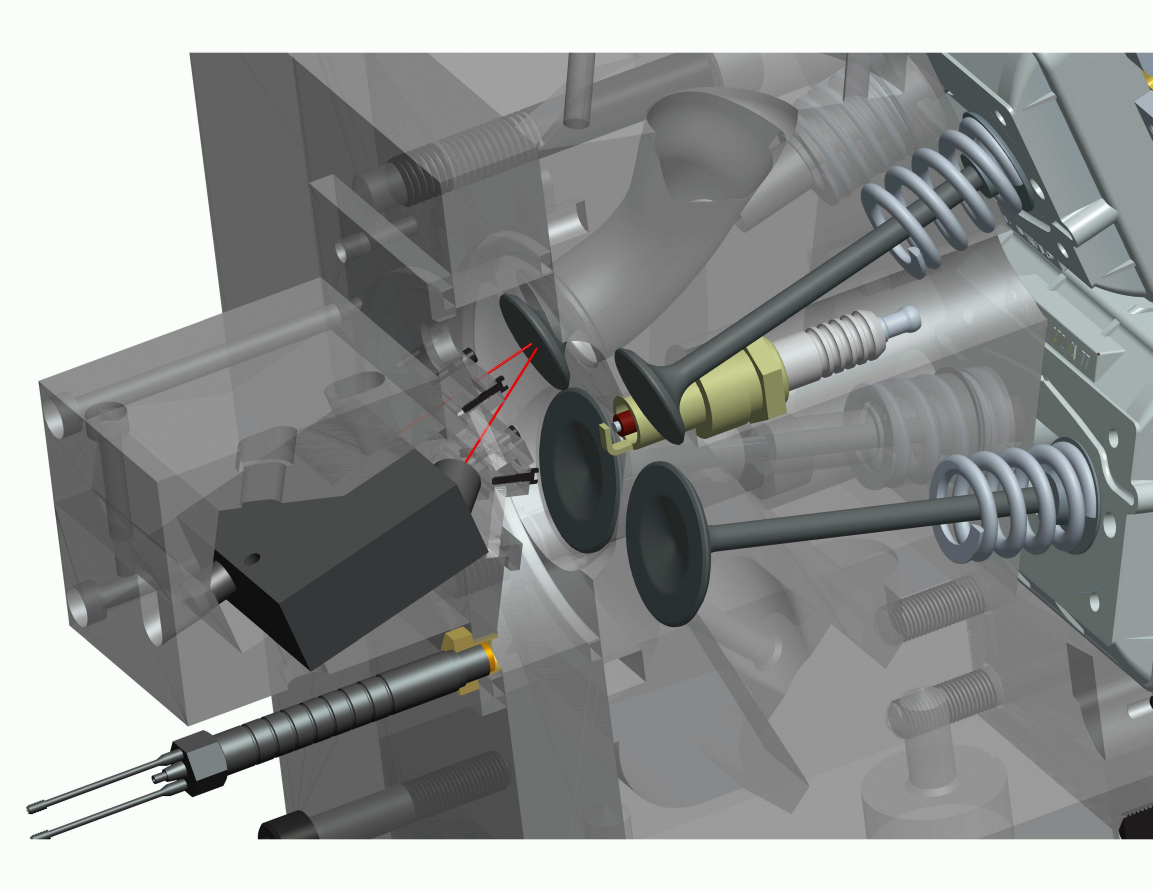

Figure 6.3: Cut-away view of testbench cavity

module (four individual actuators) mounted to a prototype single cylinder engine head. The cylinder head is donated by DaimlerChrysler AG specifically for use with the prototype actuators and single cylinder engine. Three aluminum plates are designed to constrain the cylinder head to a custom work table by as shown in Figure 6.2 and a steel sub-frame (not shown). The front support plate has a centrally located cylindrical hole with a diameter corresponding to the intended engine cylinder bore. A 3D and 2D cross-sectional representation of the cavity and associated hardware are provided in Figures 6.3 and 6.4, respectively. The cavity is pressurized with compressed air from the building supply. In order to produce realistic exhaust pressure transients, cavity volume may be varied by affixing aluminum disks (of known length and diameter) with press-fit permanent magnets to the unused valve faces. This is

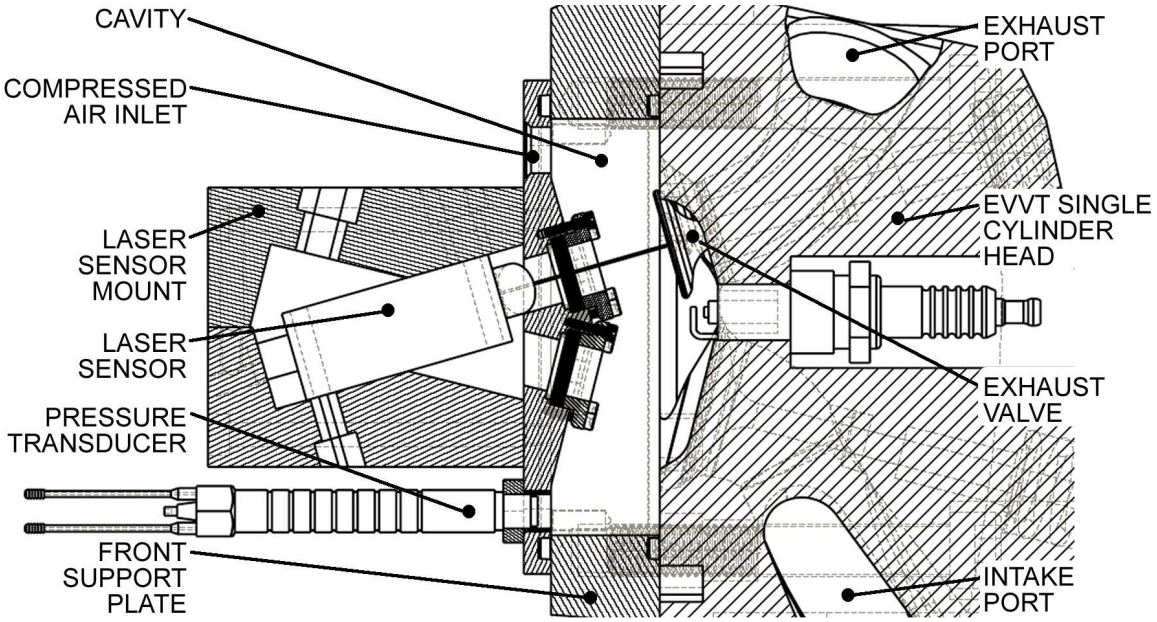

Figure 6.4: Sectional view of cylinder head test-bench cavity

possible since only one actuator is tested at a time (and therefore up to three valves not in use). The chamber is completed by a custom designed sensor mount-plate that fits into the cavity and is secured with cap screws. This plate has ports to accommodate a compressed air inlet and a pressure transducer. The mount plate contains two windows so that a position measurement can be made on any of the four valves (through repositioning of the laser sensor). An air seal is provided with o-rings around each of the windows and the cavity bore. Cavity pressure regulation is achieved by an electronic pressure regulator and a two-way solenoid valve via signals generated by the dSPACE controller. Opening pressures can be varied between 0 and 5 bar. A 48 L (11 gal) accumulator tank between the pressure regulator and two-way valve is used to mitigate pressure pulsations. The air is expelled through the exhaust port and muffler (upon actuator valve opening) as though it were exhaust gas. To accommodate the relatively continuous flow rates associated with higher emulated engine speeds, a ball valve may be manually opened in parallel with the two-way solenoid valve. As in the material testing machine experiments, actuator power is regulated

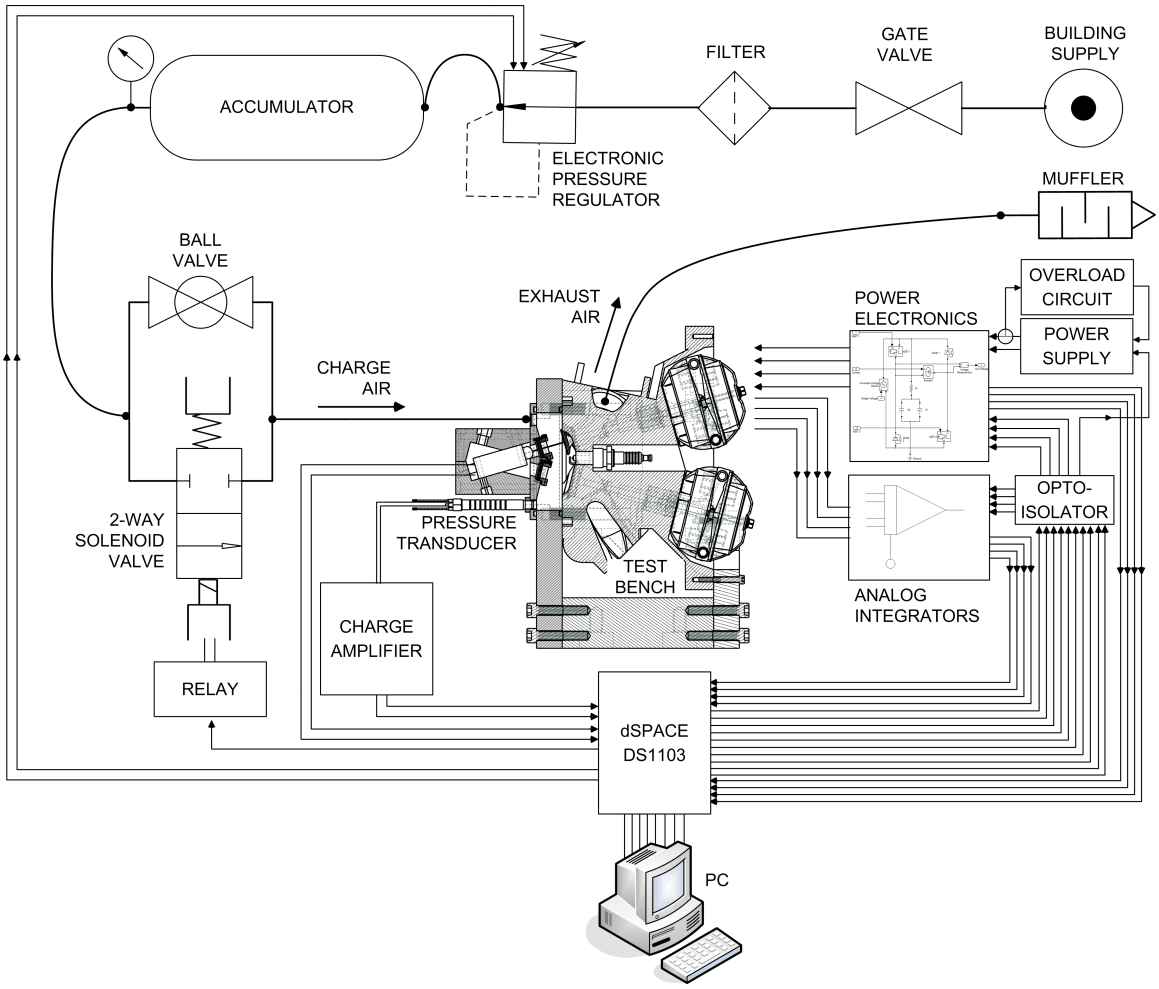

Figure 6.5: Single cylinder head test-bench setup schematic

through the same custom designed power electronics and a DC switched power supply (also configurable through the dSPACE controller). A schematic representation of the testbench system is provided in Figure 6.5. The testbench experiments are primarily focused on controlling the exhaust actuator subject to gas disturbances as control of the intake actuator is expected to be the same but without significant disturbances. Valve control of a single valve was first considered as only one laser position sensor is available. However, the laser is only used as a performance reference and is not used by the controller. As a result of the torsion and valve spring forces being balanced at a mid-stroke position, the valve lash adjusters were removed from the remaining ex-

haust and two intake valves so that the valve springs could hold the valves closed and hence seal the combustion chamber during the experiments. The tests progressed in complexity, initially with basic software and hardware checks followed by system identification of the mechanical parameters. A position-based feedforward controller and flatness landing controller were then implemented (for both the opener and closer magnets) initially using an externally mounted laser position sensor for feedback. Later, the flux-based position algorithm replaced the laser measurement for feedback with the results documented in [Chladny and Koch, 2006a]. Next, a pneumatic system used for the emulation of exhaust gas disturbances was installed. The feedforward algorithm was manually tuned to accommodate fixed opening pressures as shown in [Chladny and Koch, 2006b]. Finally, feedforward and estimation algorithms were implemented for the opener magnet to accommodate a random exhaust opening pressure between zero and 5.0 bar as shown in [Chladny and Koch, 2007]. Using the developed control strategy, landing impact velocities, transition time and energy consumption were evaluated for various pressure levels, engine speeds and voltages. All data were acquired through the ControlDesk interface and saved in MATLAB binary format (see Appendix C for a file listing and Chapter 7 for results).

Due to the relatively large number of system components and controller complexity, this test-bench validation process is critical for debugging software, coordinating the actuator controllers with the engine control unit and developing an associated software interface. In addition, it is an opportunity for validating, evaluating and improving the derived control strategies in a closely controlled environment and without risk of compromising a working engine. Note that precautions should be taken to avoid eye injury from the laser position sensor or hearing loss from expansion of the compressed air through the exhaust port. A detailed description of the equipment used is provided in Section 6.5 with relevant equipment specifications listed in Table 6.3.

To achieve independent valve timing control for a two valve single cylinder engine,

the described exhaust actuator controller and an additional DS1103 controller for the intake valve will be coordinated by a dSPACE 1404 MicroAutobox engine controller.

6.4 Preparation for Single Cylinder Engine Testing

Upon successful test bench testing, the cylinder head will be mounted to a custom designed cylinder barrel and sleeve for experimental validation on a Ricardo Mark III single cylinder research engine shown in Figure 6.6. These experiments will be used to further validate and refine the proposed actuator control strategies by contrasting performance with a modified production cam-driven cylinder head with similar combustion chamber and port geometry (not shown). Having a fully flexible valvetrain will also serve as a significant extension of the present research engine test facility capabilities. To this end, considerable work has been done to upgrade the present engine control unit with a dSPACE MicroAutobox 1404 flexible engine controller and associated interface electronics to coordinate two dSPACE DS1103 controllers (for an intake and exhaust valve actuator) in addition to fuel injector(s) and spark timing control.

6.4.1 MicroAutobox Engine Controller and Interface Electronics

A hardware interface between the dSPACE MicroAutobox 1404 engine controller and engine hardware is presently in the final stages of testing. As part of this process, a 91 conductor interface cable between the 1404 and proprietary electronic cam and crank signal conditioners, analog and digital input/out conditioners and ignition and fuel injector drivers (provided by Bazooka Electronics and Hitachi [Hitachi, 2003]) is designed and tested. A photo of the interface electronics and 1404 controller is provided in Figure 6.7. At the time of writing, the interface and 1404 unit is operating the aforementioned single cylinder engine with a conventional cam-driven valvetrain.

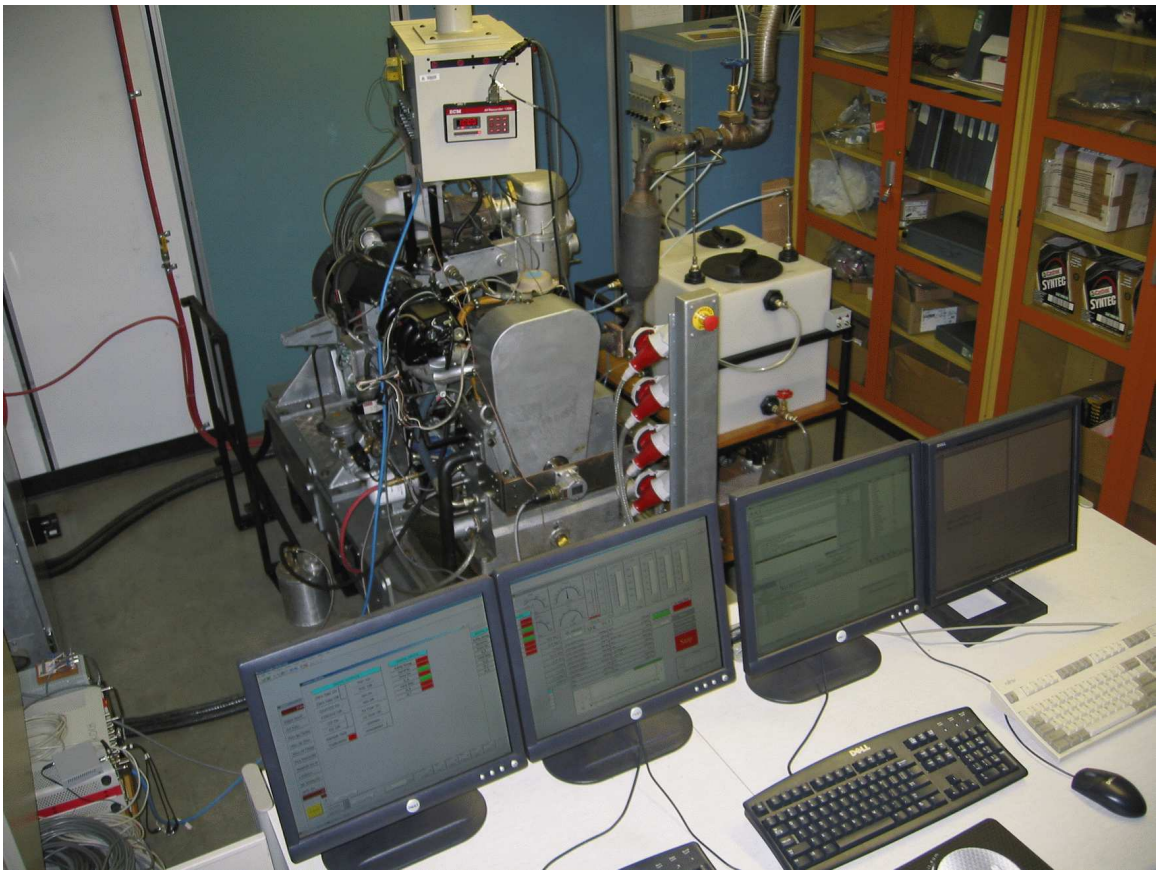

Figure 6.6: Ricardo Mark III single cylinder engine and test facility

6.5 Equipment Description

The following subsections provide detailed descriptions of the relevant equipment used in the material testing and testbench experiments.

6.5.1 Actuator Adapter and Load Rod

An adapter that attaches the actuator to the lower material testing machine crosshead was designed and fabricated from AISI 6061 T6 aluminum. The actuator was attached to the adaptor using the socket-head cap screws and mounting locations provided for normal cylinder head mounting. The adaptor is secured to the crosshead with steel ready-rod and a locknut. To manipulate the armature position with the material

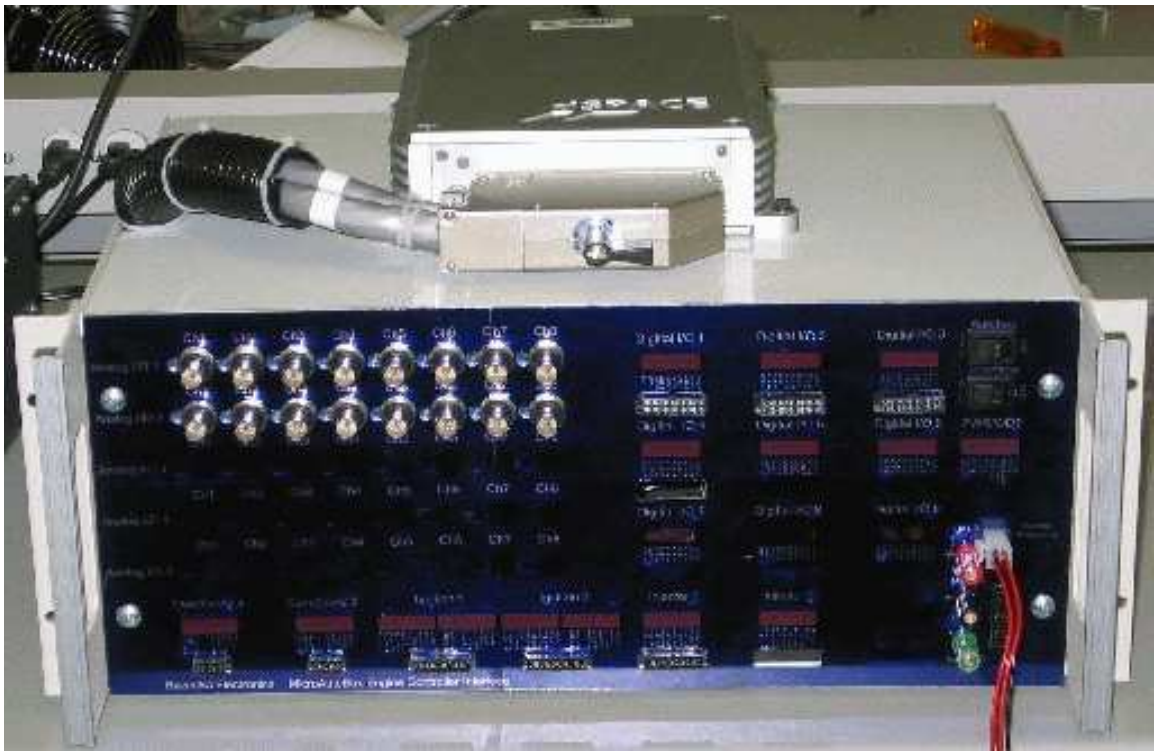

Figure 6.7: dSPACE MicroAutobox and custom interface electronics

testing machine crosshead, an aluminum load rod was fashioned to press against the armature valve lash adjuster socket. In previous experiments [Chladny, 2003], load cell measurements were observed to be affected by the actuator magnetic fields. The rod was made of sufficient length so that no detectable interference was observed in the load signal during excitation. Aluminum was chosen over steel as the construction material to minimize a flux path to the load cell.

6.5.2 Circuit Protection

To prevent significant levels of current to flow unchecked through the actuator in the event of a control or hardware failure, an overload protection circuit was constructed. The circuit consists of a low-pass filter for the coil current which generates a signal to the power supply when the low frequency current signal exceeds a variable shutoff

limit. The output lead from the primary power supply to the power electronics is measured using a Hall-effect current sensor. The shutoff threshold is manually adjusted to allow a suitable current limit. It was also deemed prudent to protect the expensive dSPACE controller from potential electrical spikes or surges that may originate from an actuator or power electronics failure. Thus, all switch signals from the dSPACE controller to the power electronics are optically isolated using a 16 channel, 10 MBit/s opto-isolator circuit (comprised of several 6N137 HCPL-2601/2611 integrated circuits).

Both the overload circuit and opto-isolator require a ± 15 V and 5 V DC power source which is provided by a HP 6236B triple output power supply. Electrical schematics of both devices are provided in [Chung, 2005].

6.5.3 Computer Hardware and Software

During the material testing machine experiments, a PC laptop running Microsoft Windows XP and dSPACE ControlDesk 2.4 was used to communicate to a standalone dSPACE DS1103 PowerPC (PPC) target controller board via a PCMCIA card and ethernet adaptor. The testbench experiments use a host PC running a Microsoft Windows XP operating System and PCI card to optically link to the DS1103 PPC target controller board. The ethernet and optical links provide a two-way communication between the PC host and controller for code uploads and data downloads. A user interface developed with dSPACE ControlDesk software provides non-realtime communication of parameters and transfer of real-time data acquisition between the DS1103 controller and the PC.

6.5.4 Current and Voltage Sensing

Both coil voltage and coil current measurement signals are generated on-board the custom power electronics (see Section 6.5.14). Coil voltage is measured by dividing

it with a differential operational amplifier circuit so that it is within the DS1103 analog to digital converter (ADC) input range. The value of the gain and resistors are chosen such that the output voltage is one fifth of the actual voltage across the coil. A schematic of the sensing system used is provided in [Chung, 2005].

Coil current is measured with a LEM LA55-P Hall-effect current sensor. The Hall-effect current sensor works by directing the magnetic field produced by a flowing current, given by $B = \frac{\mu_o I}{2\pi r}$, into a semiconducting material using a steel yoke. When a semiconducting material is exposed to a magnetic field, it produces a measurable current and voltage in proportion to the impinging field as predicted by the Hall-effect phenomenon. In order to avoid the nonlinear behavior of the yoke and the semiconducting material itself, an op-amp uses a coil that feeds back an opposing magnetic flux in the yoke in proportion to the output of the semiconducting material. Thus, any flux produced by the current intended to be measured is equally countered by the flux produced by the op-amp driven coil. The counter flux is generated by passing the op-amp current through a resistor and, N, external loops around the yoke. The op-amp voltage can then be measured since it is proportional to the current required to balance the magnetic flux produced by the line current. It is then possible to relate the op-amp voltage to the current flowing in the conductor by $V = \frac{I_{Measured} R}{N}$.

6.5.5 Cylinder Head

A single cylinder engine head (donated by DaimlerChrysler AG) is incorporated into the testbench apparatus to evaluate actuator control performance under realistic engine operating conditions but without the additional complications or risk of damaging a research test engine. The cast aluminum alloy cylinder head has four valves and a bore of 97.00 mm with a combustion chamber and valve porting similar to the Mercedes-Benz M273-E55 engine (used in the E, CLK, CL, CLS, GL and S 500/550

models, 2006 or newer). In the future, the cylinder head is to be removed from the testbench and installed on a single cylinder engine.

6.5.6 dSPACE DS1103 Controller

For both the material testing machine and testbench experiments, dSPACE control hardware is used. The system includes the DS1103 target board contained in a PX4 expansion box and connected to a CLP1103 connector/LED panel. The target board is equipped with a master 400 MHz PPC Motorola 604e microprocessor and a 20 MHz Texas Instruments TMS320F240 slave processor. Control at frequencies up to 50 kHz are used through the target board which includes 16 analog to digital converters (ADCs), 12-bit multiplexed channels equipped with four sample and hold ADC as well as four parallel 16-bit channels each equipped with individual sample and hold ADCs. Digital to analog output is available through 8, 14-bit channels in addition to 32-bit parallel I/O organized in four 8-bit groups. Each group can be programmed to be either input or output. The slave processor provides an additional 16 10-bit ADC inputs and 4 single phase PWM outputs. Complete specifications are available in [dSPACE GmBH, 2003]. Measurements of the two coil voltages, currents, flux linkage signals, laser position sensor and pressure sensor are sampled at a rate of 20 μs (50 kHz) while executing the control algorithms. A second 100 μs background task is established to accommodate lower priority processes such as an initialization routine, RPM generator and processor temperature monitoring. Although programming is available through the MATLAB Simulink / RTI environment, all algorithms are coded in C language in part to improve real-time performance. All code is compiled and downloaded from the host PC to the DS1103 board. Experiments are managed using ControlDesk 2.4 software as a convenient method of interacting with the controller and transferring data back to the PC.

6.5.7 Flux Sensor Integration Electronics

As shown in Section 5.6.1, magnetic path flux and coil current can be related to armature position through a flux linkage model. However, due to the switching of the coil current, potentially at the same rate as the sample frequency, magnetic flux cannot be measured directly. Instead, the rate of change of flux is integrated with custom analog integration circuits and then sampled through the DS1103 controller. The rate of change of flux is physically measured as the mutually induced potential in a measurement coil that is co-axially aligned with the primary excitation coil. Since a magnetic flux must be present in order to infer a position measurement, a measurement coil is in both the opener and closer electromagnets since they are not energized simultaneously. As a result, excitation current and position dependent logic is used to change between the measurement coil signals during the valve transition to maintain a continuous position measurement. Despite such additional complications, the feedback method is cost effective and practical since there are no moving parts and all components are relatively inexpensive compared to other feedback sensing methods. Integration is achieved through the use of a standard resistor-capacitor operational amplifier circuit designed by DaimlerChrysler AG and fabricated by Bazooka Electronics.

6.5.7.1 Integration Drift

Op-amp integration circuits are subject to drift. Small non-zero bias currents cause the feedback loop capacitor to accumulate charge until the op-amp output saturates. The bias results from small amounts of current at each input terminal - usually drawn from the ground plane [Chaniotakis and Cory, 2006]. The result of this bias when integrated is known as integration drift and has a tendency to affect the measured signal. Fortunately, the time required for typical valve flight is on the order of 5 ms,

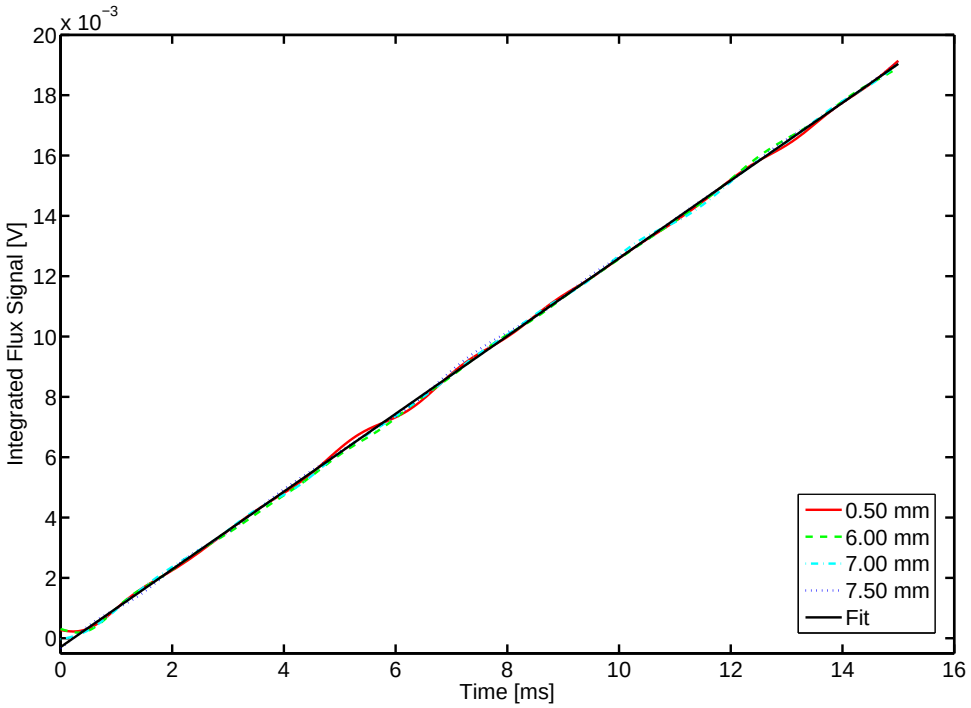

Figure 6.8: Analog Drift of the RC Integration Circuit

thus, the accumulated amount of drift over a measurement cycle is relatively small. To manage drift (and prevent saturation), the integrators are reset by temporarily grounding the measured capacitor that accumulates charge from the operational amplifier output when the valve is in the fully open or closed position (where position is known). In addition, the flux sensor range is only appropriate over a limited valve stroke range (and hence the time over which a measurement is affected by drift is even less than any given flight time). Additionally, the drift may be assumed to be linear with respect to time and therefore easily compensated for. During experimental tests, the drift was measured at several positions by first resetting the integrator and then sampling the ensuing drift. From these tests, a rate of drift was estimated and used to correct all subsequent flux measurements. Figure 6.8 illustrates the results of these tests and the resulting fit curve used to compensate all flux measurements. On

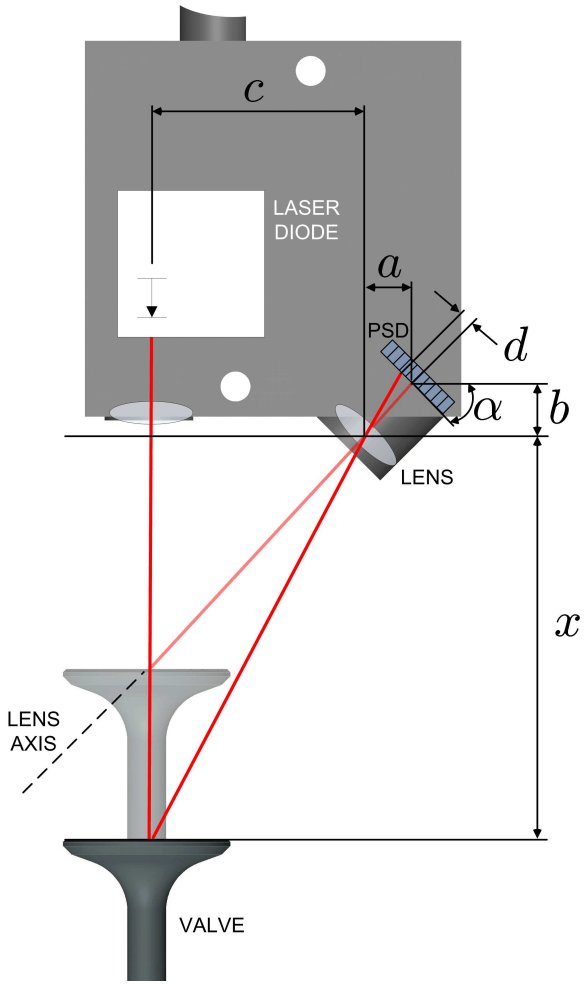

Figure 6.9: Laser sensor schematic

a production engine, this bias could be learned when the valve is in a known position (such as open or closed) or could be filtered using a high-pass filter

6.5.8 Laser Position Sensor

A non-contact method of measuring valve displacement for validation of control performance was desired. A non-contacting sensor avoids complications arising from physically attaching a sensor component to the valve such as altering the system mass. Additionally, an optical method is ideal because of the compressed air pressure

transients within the cavity. A Micro-Epsilon LD1627-10 laser transducer is selected to monitor valve position. By using a triangulation method and a semiconductor optoelectronic position sensitive device (PSD) a position resolution of 6 μm (noise) and frequency response of up to 37kHz over a 10 mm stroke is possible. The sensing principal works by projecting a point of laser light onto a target which is then reflected diffusely. A lens then focusses the light on the PSD. The PSD then outputs an analog voltage signal related to the impinging laser light position on a sensing surface. Figure 6.9 indicates a schematic of the triangulation method. The following indicates how a change in valve position, Δx is related to a change in position of laser light impingement on the PSD surface, Δd [Song et al., 2006]:

$$\Delta x = \frac{x^2}{b(a+c)\cos\alpha - b\sin^2\alpha}\Delta d \tag{6.1}$$

A gauge pressure change from atmospheric to 6 bar will alter the refractive index of the air from approximately 1.0003 to 1.0015 [Picard and Fang, 2003]. According to the manufacturer, a change in refractive index causes a DC offset in position output and that the aforementioned change is insignificant (less than 100 ppm) [Micro-Epsilon, 2007]. However, the tempered 3.0 mm plate glass window (refractive index of 1.4740) does cause a static DC offset of approximately 0.2 mm and is compensated for prior to testbench experiments.

Compared with a charge coupled device (CCD), a PSD has higher sensitivity, response and a continuous sensing surface. However due to the analog nature of the generated signal, it is more adversely affected by environment noise. It is important to emphasize that the output position signal cannot by used in a real engine but is used to validate the flux-based position sensors. To conserve the laser diode life, power is switched off via the DS1103 controller when not in use.

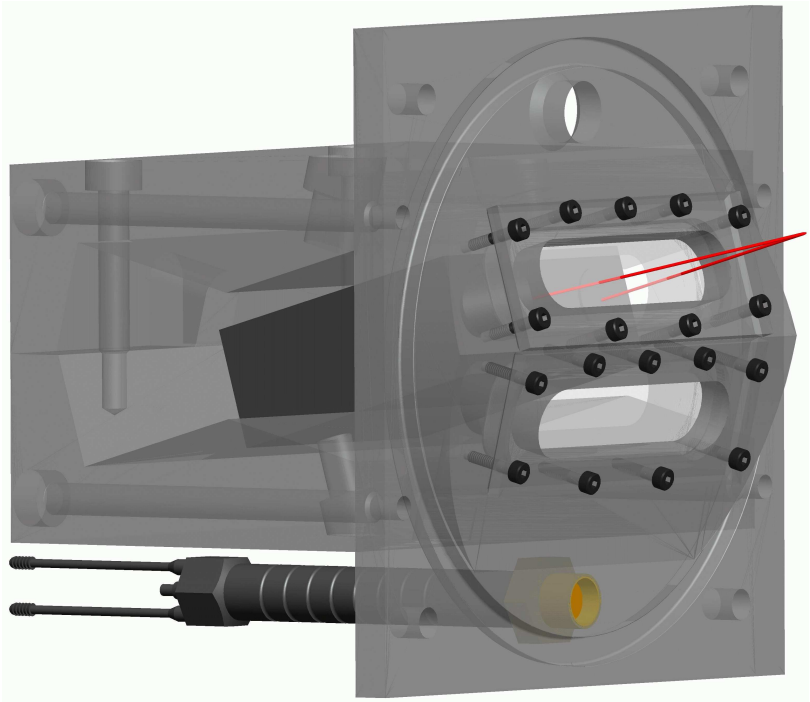

Figure 6.10: Laser and pressure sensor mounting assembly

6.5.9 Laser and Pressure Sensor Mount

A laser sensor mount was designed to for the LD1627-10 to accommodate measurement of any four of the cylinder head valves. The incident beam on the valve face is aligned with the valve axes to minimize measurement errors caused by misalignment. The mount is easily removed and realigned through a high tolerance fit between the mount plate and front support plate cavity. Sensor noise attributed to ambient light variations is minimized through a relatively enclosed design and a black anodized surface finish. Compressed air inlet and pressure measurement ports are also provided. Removable tempered glass windows are provided for optical access to the valve faces. The complete assembly is shown in Figure 6.10.

6.5.10 Load Cells

To measure armature force in the material testing machine experiments, a Strainsert FL1U-2SGKT flat strain gauge load cell is installed between the load rod and crosshead. The load cell strain gauge bridge is balanced and conditioned using a Vishay 2100 strain gauge conditioner and amplifier system. Measurements from a second load cell that was already installed in the load frame are also recorded. However, the second load cell is of a higher capacity and situated above the crosshead and therefore less sensitive to lower excitation levels. This larger load cell is used to calibrate the smaller capacity Strainsert as it had previously been calibrated with a proving ring.

6.5.11 Material Testing Machine

The material testing machine used is a MTS 810 servohydraulic system with 318.10 load frame and SilentFlo 505.07 hydraulic power unit located in 3-26 of the Mechanical Engineering Building at the University of Alberta. The axial displacement control capability of the machine is used in all tests. The load frame is adjusted to allow for ample clearance for the load rod, load cell and load cell adaptor to be installed. After the rod, load cell and adaptors are installed into the load frame, the armature position is set through the manual position control knob on the user interface control unit. Upon sufficient change in crosshead displacement, the actuator armature stem contacts the fixed load rod. Further change in the crosshead position overcomes the torsion bar force and displaces the armature to a desired position. Great care should be taken to not exceed the actuator 8 mm stroke limit to prevent the crosshead from damaging the actuator. Specific positions are set and recorded by using the crosshead position sensor and user display. The control unit also allows for cyclical position control as discussed in Section 6.2.2.3.

6.5.12 Pressure Regulator and Two-way Solenoid Valve

Compressed air is regulated in the testbench cavity using a Wilkerson ER1 electromechanical pressure regulator and a 2-way ASCO 104R solenoid valve. The pressure regulator has a built in pressure transducer and control hardware to regulate a pressure set-point via a 0-10 V analog signal input. In this way, pressure can be varied through ControlDesk and the DS1103 hardware. Although this regulator is ideal for setting a nominal pressure, it has a relatively slow response and is significantly upstream from the testbench cavity. Thus, the solenoid valve is attached as closely as possible to the cavity inlet port so as to more precisely control the pressure level on a cycle-by-cycle basis. A simple control algorithm uses the pressure transducer signal for feedback to regulate the internal cavity pressure at a preset level (specified through ControlDesk) by opening and closing the solenoid. Through coordination of the regulator and solenoid set points, a wide variety of exhaust valve opening pressures at different speeds can be tested. At higher emulated engine speeds, a ball valve that is in parallel with the solenoid valve can also be adjusted to provide a higher flow rate (at the sacrifice of having to use the slower pressure regulator).

6.5.13 Pressure Transducer and Charge Amplifier

To measure testbench cavity pressure transients, a Kistler 6061B pressure transducer and Sundstrand 507 charge amplifier are used as shown in 6.5. Early tests used a Kistler 6043A60 sensor mounted to the pressure mount. This was later exchanged for a 6061B which is compatible with a measurement port provided in the cylinder head. A pressure signal is required for cavity pressure regulation as well as to validate and improve gas force disturbance models and estimation algorithms. A pressure measurement is not used for actuator landing control or disturbance rejection because production engines are not equipped with such sensors. A piezoelectric pressure

transducer is used because they exhibit superior frequency response, ruggedness and insensitivity to magnetic fields when compared to other pressure sensing methods. A change in pressure causes a thin membrane to apply force in a single direction on a piezoelectric crystal. An electric charge is then produced in proportion to crystal deformation. This charge is then measured and amplified through the charge amplifier (as in an op-amp integrator circuit). The charge amplifier outputs an analog voltage in proportion to accumulated charge from the piezoelectric pressure transducer. As in the case of the flux integration circuits, the charge amplifier is subject to drift over time and is thus externally reset by the DS1103 controller. The transducer and charge amplifier were calibrated for a 10 V output corresponding to a pressure of 6 bar (90 psi) using a a Bundaberg 280L hydraulic pressure calibration stand.

6.5.14 Power Electronics

The relatively high current demands of the hinged actuator requires the control signals from the DS1103 to be amplified. A switched H-bridge configuration for driving the actuator coils is used because of the relative simplicity and low cost of such circuits. A set of custom H-bridge power electronics were designed and built by Bazooka Electronics Ltd. to supply the actuator with the necessary electrical power in a coordinated and repeatable fashion. These circuits are designed to switch up to 50 V up at frequencies up to 50 kHz. The actuator opener and closer coils, opto-isolator signal lines, voltage and current measurement signal lines as well as a 3 kW and 35 W power supplies were connected to the custom power electronics. The electronics provide three basic output modes of +42 VDC, 0 VDC and −42 VDC to the coil. These three modes are achieved with two high speed voltage-controlled insulated gate bipolar transistors (IGBT IRG4BC40W), T1 and T2, and two flyback diodes, D_1 and D_2. Inputs to the transistors for each of the three modes are shown in the H-bridge power circuit representation provided in Figure 6.11. Here, a digital

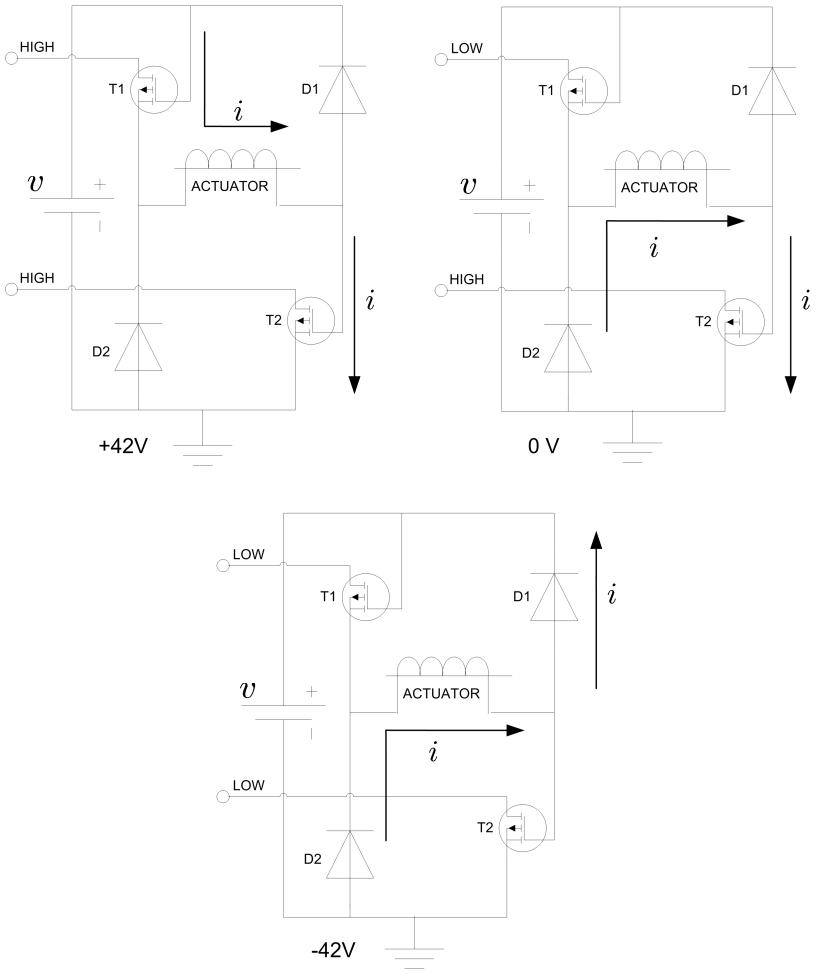

Figure 6.11: Power electronic modes

high input closes the transistors.

In +42 V mode, transistors T1 and T2 are closed and current flows from the power supply, through the actuator and to ground.

After the coil is energized, an effective potential of 0 V may be applied by setting transistors T1 open and T2 closed. This results in the coil current to 'free-wheel' through diode D2 with a net potential difference across the actuator of 0 V.

Also available is a -42 V mode. After the coil is energized, T2 may be opened so that the only current path available is through diodes D2 and D1. This mode is used to drive the current down at a faster rate than the 0 V mode due to the effective change

in polarity. For example, it is used when releasing the armature in order to reduce the magnetic force quickly and subsequently achieve faster valve travel time. It should be noted that when T2 is open, the mode is the same regardless of the state of T1. A 50 kHz PWM signal from the DS1103 controller board controls T1 (+42 and 0 V modes) while a digital TTL output signal regulates T_2. With sufficiently fast switching frequencies and a relatively high inductance, it is reasonable to assume that PWM duty cycle variation can regulate an average linear voltage output as done in [Peterson and Stefanopoulou, 2004, Deng and Nehl, 1998, Pawlak and Nehl, 1988].

6.5.15 Power Supplies

Actuator power in both the material testing and testbench experiments is provided with Sorensen programmable switching power supplies. In the material testing experiments a DCS60-18E 1 kW model was used and in the testbench setup, a larger DCS80-37 3 kW supply is used. Both supplies convert a 60 Hz AC source into a variable DC power source. The testbench supply is remotely shutdown via the DS1103 controller and through a connection to an external overload circuit that monitors the supply current output. Although the 1 kW and 3 kW power supply outputs are respectively rated to maximum 18 A and 37 A of continuous current, it was observed that both supplies are capable of providing short term (10 ms or less) currents in excess of 50 A at 50 V (with a 'dummy' actuator load). Thus, actuator performance is not expected to be limited by the supplies.

All other hardware accessories such as the electronic pressure regulator, opto-isolation, analog integration, power electronic and current overload protection circuits are powered through a linear 35 W HP 6236B triple output supply.

6.6 Summary

The above sections provide a brief summary of the hardware and procedure used to conduct the experimental studies. Using an axial material testing machine, custom H-bridge power electronics are interfaced with a switching power supply and high speed controller to investigate the static and transient force and current response of a hinged prototype actuator. Actuator force is measured with a load cell and magnetic path flux was inferred through analog integration electronics. Additional testbench experiments are conducted to evaluate actuator control performance under emulated engine conditions. Emphasis is placed on the study of the exhaust valve actuation to address the issue of gas force disturbance rejection. Both experiments are essential in validating developed models and qualifying and tuning the control algorithms prior to implementation on a single cylinder research engine. The apparatus components and relevant specifications for the material testing and testbench experiments are listed in Tables 6.2 and 6.3, respectively.

Table 6.2: Material Testing Machine Experimental Equipment

Item	Description	Relevant Specs.
Prototype Actuator	Valve actuator RAM 113 050 02 77 Provided by DaimlerChrysler AG	8.00 mm (0.315") stroke
Actuator Adaptor	Connects the actuator to the MTS crosshead	AISI 6061 T6 AL plate
Actuator-Load Cell Rod	Transfers load from the armature to the load cell	13mm (1/2")ϕ x 300mm (12") 6061 T6 Aluminum bar
Load Cell Adaptor	Fixes the load cell to the MTS load frame	6061 T6 Aluminum
Actuator Power Supply	Sorensen DCS60-18E programmable switching power supply	0-60V, 0-18A Max output: 1 kW
Accessory Power Supply	Hewlett Packard 6236B triple output linear supply for power and miscellaneous electronics	+6V, ±-20V 35 W
Power Electronics	Custom H-Bridge driver for actuator current control with on board current hall-effect sensor	Switching $\leq$ 50 kHz Max: 55V @ 50A IGBT IRG4BC40W
Flux Measurement Electronics	Custom analog integration circuits for position feedback board current hall-effect sensor	Four channel with external reset Cap.: 200V @ 70 A
Load Cell	Strainsert FL1U-2SGKT flat load cell	Cap.: 4448 N Acc.: 1% FS
Load Cell (in load frame)	MTS 661 20E-03 load cell	Cap.: 100 kN Acc.: 1% FS
Load Frame	MTS 318.10 Axial Load Frame and SilentFlo 505.07 hydraulic unit	Cap.: 100 kN (22 kip)
Load Controller	MTS 810 servohydrauic system and TestStar IIs controller	-
Strain Gauge Conditioner	Vishay 2100 provides load cell excitation and calibration	1-12V Excitation Gain: 100-2100
Host PC	IBM ThinkPad notebook for data collection / control interface	1.2 GHz CPU 512 Mb RAM
Controller	dSPACE DS1103 with PX4 enclosure PCI card and 400 MHz processor	16Bit sampling to 50 kHz,
Misc. Electronics	16 X 10 Mbit/s opto-isolator Variable overload protection	IC HCPL-2601
Misc. Hardware	Various connectors, leads and fasteners to connect hardware	-

Table 6.3: Testbench Experimental Equipment

Item	Description	Relevant Specifications
Prototype Actuator	Hinged exhaust valve actuator No. RAM 113 050 02 77 provided by DaimlerChrysler AG	8.00 mm (0.315") stroke
Single Cylinder Head	Model No. HAM 113 016 L003 provided by DaimlerChrysler AG	Four valve Vol: 60.2 cm^3
Controller	dSPACE DS1103 with PX4 enclosure PCI card and 400 MHz processor	16 Bit sampling to 50 kHz,
Flux Measurement Electronics	Custom analog integration circuits for position feedback	Four channel with external reset
Valve Position Sensor	Micro-Epsilon LD1627-10 laser triangulation (PSD type) 10 mm	Freq. resp: 37 kHz Res.:6 μm (noise)
Pressure Sensor	Kistler 6061B piezoelectric transducer for M10x1 port	Natural Freq: 90 kHz Sensitivity: -25 pC/bar Max pressure: 300 bar
Charge Amplifier	Sundstrand 507, adjustable sensitivity of 0.01 to 110 pC/V	Max Freq. 350 kHz
Power Electronics	Custom H-Bridge driver for actuator current control with on board current hall-effect sensor	Switching $\leq$ 50 kHz Max: 55V @ 50 A IGBT IRG4BC40W
Actuator Power Supply	Sorensen DCS80-37 programmable switching power supply	0-80 V, 0-37 A Max output: 3 kW
Accessory Power Supply	Hewlett Packard 6236B triple output linear supply for power and miscellaneous electronics	+6V, $\pm$-20 V 35 W
Pressure Regulator	Wilkerson ER1, 1/2" NPT ports Step response: 600 ms (nominal)	0-10 V input Max pressure: 10.3 bar
Host PC	Windows XP desktop computer for data collection and control interface. Dual monitor output.	AMD Athlon XP 1800 1.53 GHz CPU 1 GB Ram
Misc. Pneumatics	Parker F602 filter, 48L vessel Bourdon tube indicator, flexible hose (1/2") and various fittings	-
Misc. Electronics	16 X 10 Mbit/s opto-isolator Variable overload protection	IC HCPL-2601
Misc. Hardware	Various connectors, leads and fasteners to connect hardware	-

Chapter 7

Results

7.1 Introduction

In the preceding chapters, finite element, Simulink and lumped parameter models are provided for a prototype hinged solenoid variable valve timing actuator. The models are used to predict the actuator steady state and transient response in part to evaluate the performance of the various models. Experiments to validate the derived models and a comprehensive control strategy are conducted. The following sections highlight key simulated and experimental findings.

7.2 Simulated and Measured Actuator Response

Prior to control development, extensive simulation and experimental studies are conducted to characterize the actuator performance. The simulations include the finite element analysis, lumped parameter-FEA hybrid model (Simulink) and state space lumped parameter model (LPM) as discussed in Chapter 4. Associated experimental measurements are made using a material testing apparatus described in Section 6.2. Two significant types of studies are conducted, namely, steady state performance and transient performance. The following sections briefly summarize these results.

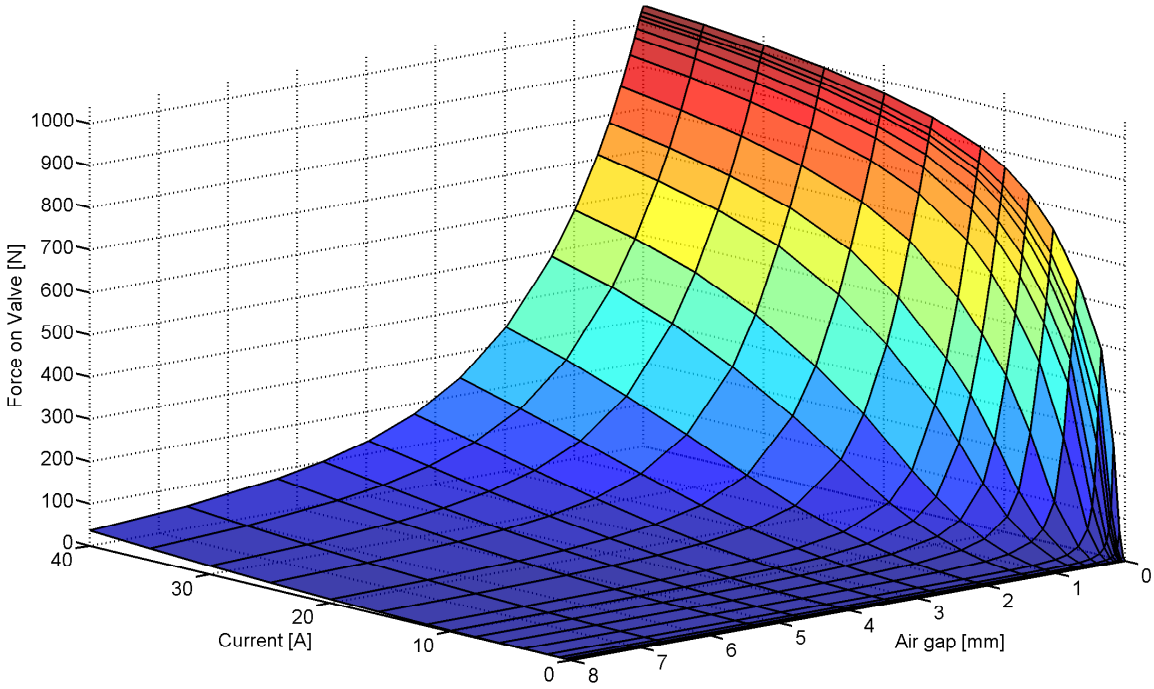

Figure 7.1: FEA simulated opener force as a function of respective air gap and steady state current

7.2.1 Static Performance Evaluation

Static force and magnetic flux as a function of position and current are simulated using an FEA model (Section 4.3) and measured experimentally (6.2.1) over a relatively wide range of armature positions and current levels. Figures 7.1 and 7.2 indicate the simulated and measured steady state force response for the opener magnet. The simulated force response of closer magnet is provided in 7.3. Figure 7.4 compares measured and simulated armature valve force as a function of position and various steady state excitation. Also plotted is the combined torsion bar and valve spring force, kx, from (4.19), which in the range shown, opposes the magnetic force. A plot of the difference between the simulated and measured results over the tested operating points is provided in Figure 7.5. Good agreement between the measured and simulated response is observed with a maximum deviation at low air gaps and

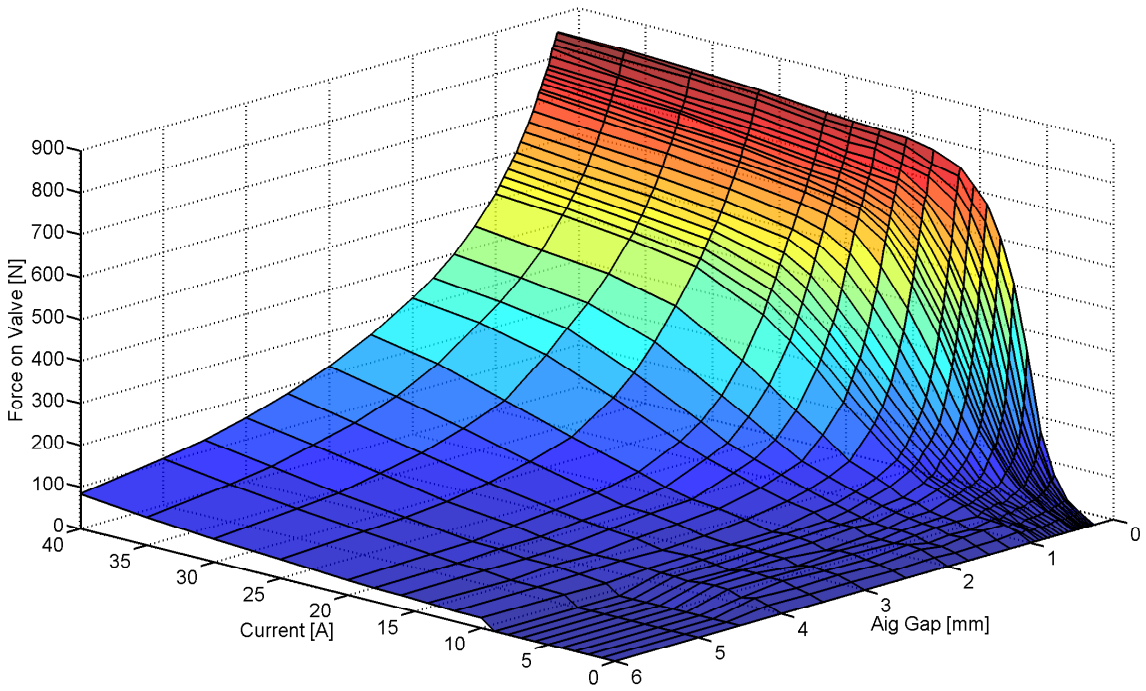

Figure 7.2: Experimentally measured opener force as a function of respective air gap and steady state current

higher current excitations. This is most likely due to the armature deflecting and thereby reducing the air gap (assumed rigid in the FEA studies). In fact, at air gaps less than 0.5 mm, one portion of the armature could be heard contacting the pole face thus making such force measurements erroneous. This was also observed during similar measurements performed for a linear actuator in [Chladny, 2003]. During normal operation, deflection is likely less significant because the armature is not rigidly constrained as done in the static tests. In [Clark et al., 2005], similar experimental and simulated discrepancies are observed despite a 3D FEA model being conducted. Regions beyond 6 mm and currents below 10 A provided insufficient force to be detectable by the load cells. Both the simulated and measured response indicate the effect of material saturation as the force does not continue to increase quadratically with respect to current as a linear induction model suggests. Experimental results for the closer magnet are not available as it is not readily possible to make force

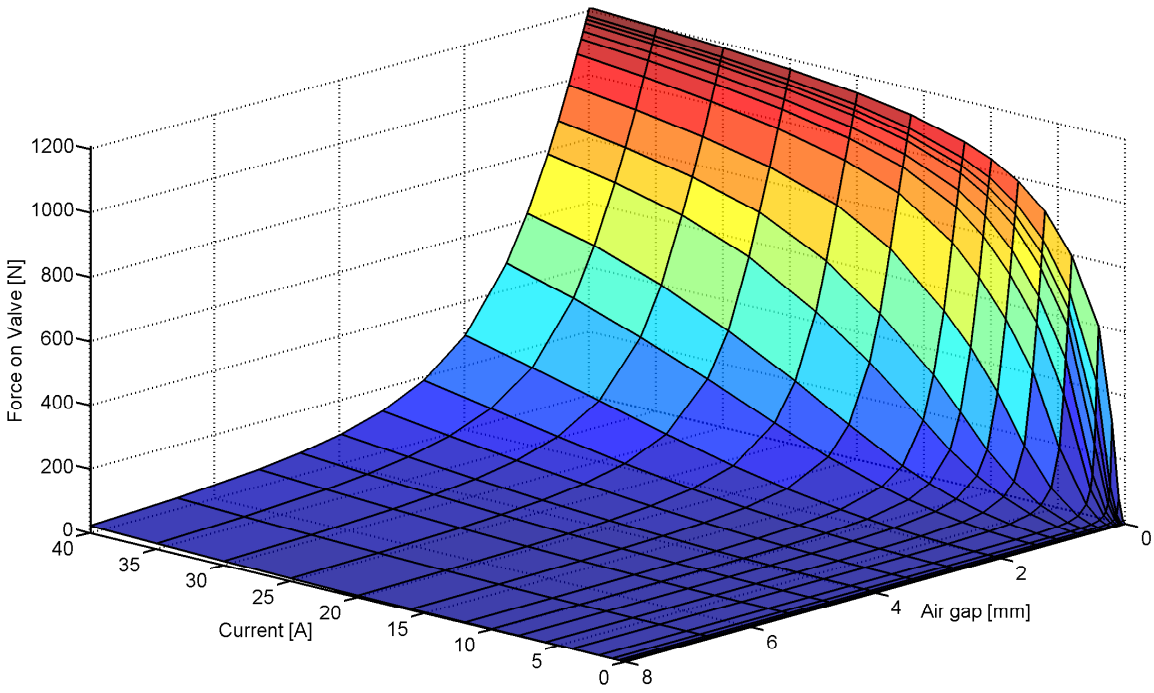

Figure 7.3: FEA simulated closer force as a function of respective air gap and steady state current

measurements in a non-destructive fashion. However, due to the similarity between the opener and closer magnets, it is expected that the simulated model is also capable of closely representing the actual closer response.

Provided the FEA models have sufficient fidelity, the numerical data can be used directly in a LPM-FEA hybrid model or to parameterize a LPM through fitting techniques as discussed in Chapter 4. As shown in the following sections, these models (which use steady state data) can predict transient performance with good accuracy and with considerably less computational demands than a FEA.

7.2.2 Transient Performance Evaluation

Although good steady state model performance may be demonstrated, transient force and current response to a time varying voltage input is also important for model based control design. In particular, the LPMs so far have neglected the effects of eddy cur-

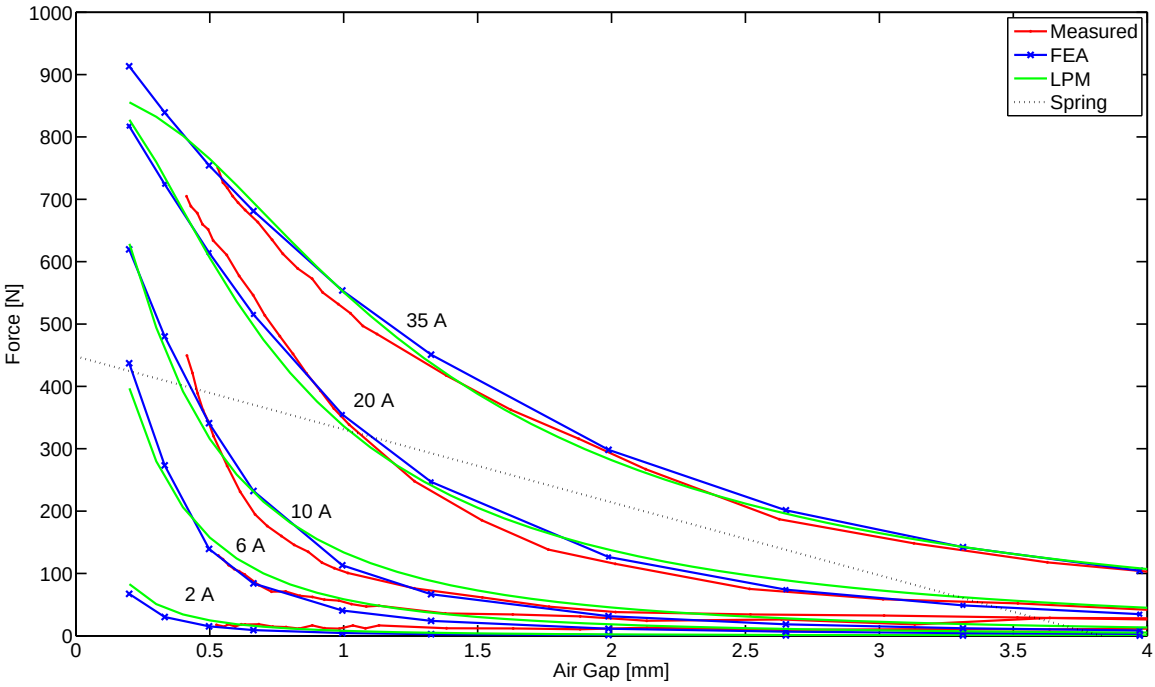

Figure 7.4: Opener magnet measured, FEA and LPM valve force as a function of armature position and various steady state currents

rents. Although these effects cannot be directly measured, their effect on coil current response is apparent (if significantly present) when comparing actual response to a model that does not account for them [Chladny et al., 2005]. To investigate if eddy current effects are significant to the actuator performance, experiments are conducted as described in Chapter 6, Section 6.2.2.1 where a relatively short step voltage is applied and then reversed until current returns to zero over various armature positions. Transient FEAs are also conducted using the measured voltage input for comparison purposes. The FEA models are capable of predicting eddy current response using the material conductivity specification for the laminate sheet of which the actuator is constructed. Therefore the FEA models provide insight to how significant eddy currents are for the actuator considered (and if necessary, may be used to parameterize a secondary eddy current model [Chladny et al., 2005]).

Figures 7.6 through 7.10 compare the measured, FEA, LPM-FEA hybrid and LPM

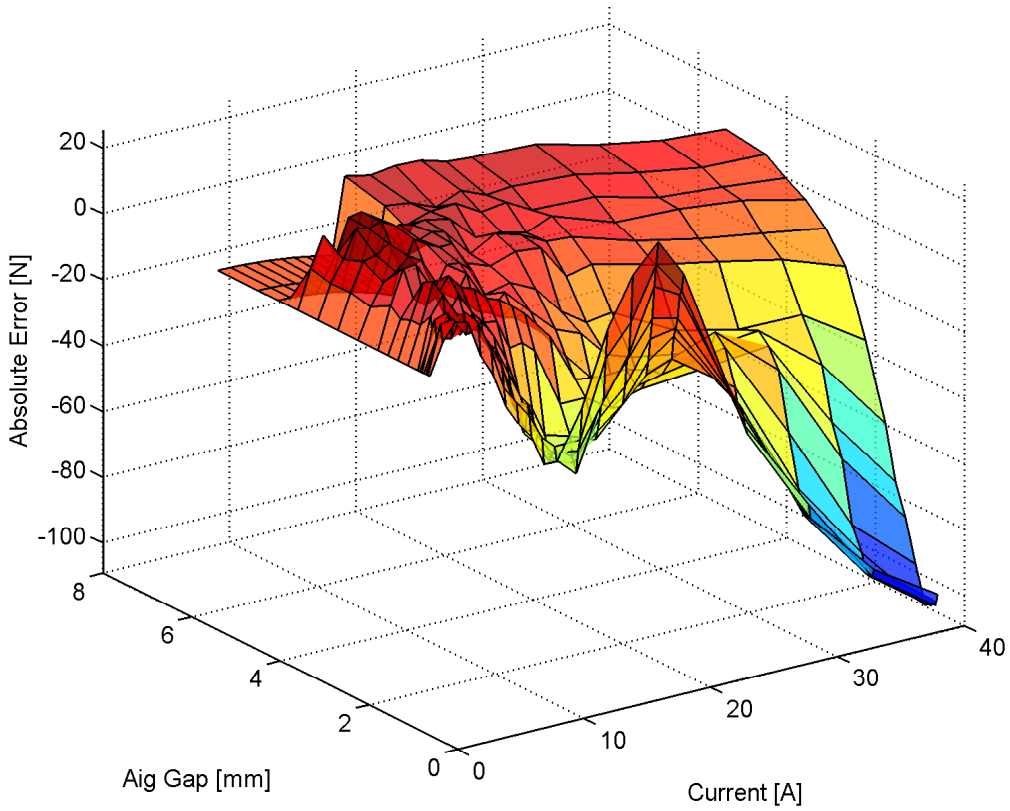

Figure 7.5: Opener magnet simulated and measured force error as a function of armature position and various steady state currents

current and force response at respective air gaps of 0.50, 0.75, 1.00, 1.50 and 2.00 mm. Also indicated are measured and modeled voltage inputs as an approximation is used for the modeled input to simplify the data input, particularly for the FEA. These results indicate an overall good agreement between all models and experimental measurements with a 14% over prediction of peak current by the LPM-FEA hybrid model and a 15% peak force under prediction by the LPM model, both of which occur at a 0.50 mm air gap position. In fact, all models performed poorest at the lower air gaps tested. This is likely due to the armature deflecting enough to reduce the nominal air gap where as it is assumed rigid in the models. If this were the case, a slower current response and higher peak force should be measured as a result of the higher inductance associated with a smaller air gap. Indeed, this is the case as agreement

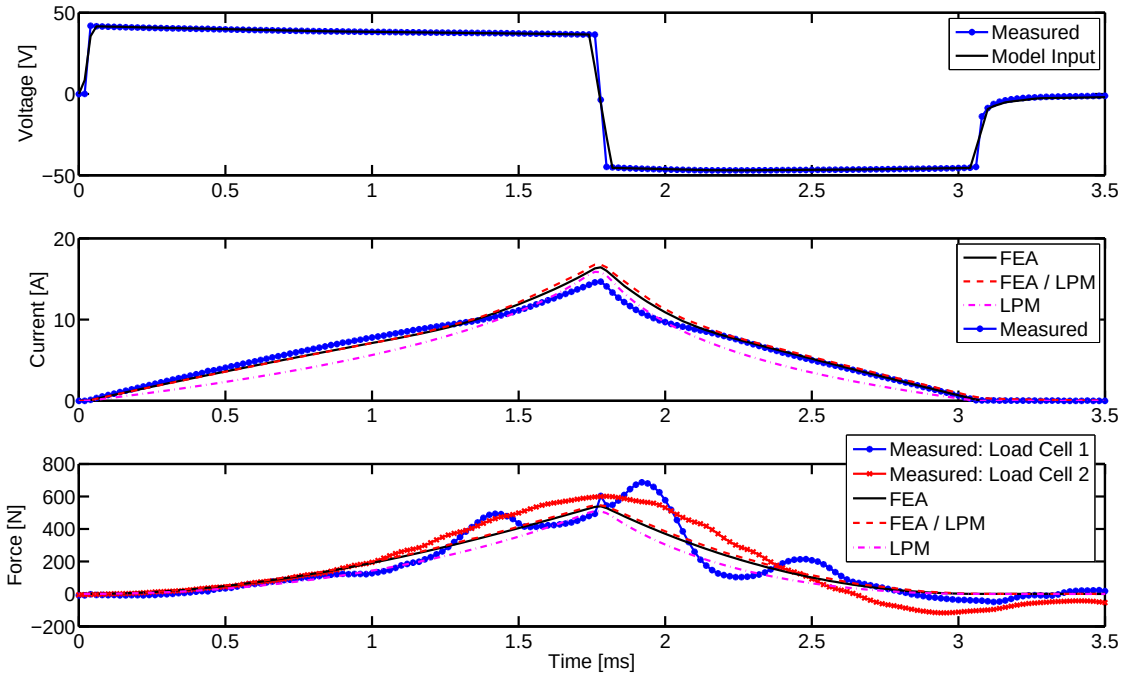

Figure 7.6: Simulated and measured response of the opener magnet, 42 V, 0.50mm airgap

between peak current and force improves with larger air gaps (smaller forces and hence less deflection). Also apparent is the effect of the transient loading on the load cell and frame structure. As mentioned in Chapter 6, the signals from two load cells are recorded. Load cell 1 is a lower capacity unit located between the load rod and material testing machine crosshead. Load cell 2 is a higher capacity (and less sensitive) unit situated between the load crosshead and frame. Their relative location is apparent with load cell 2 having a smoother response, likely due to the inertia of the crosshead acting as a mechanical filter. Similarly, the relatively large mass of the cross head causes a temporary tensile (negative) load upon polarity reversal. Despite these force measurement complications, the general trend across the different operating points suggests good agreement. Of greater concern is agreement with transient current response since the steady state measurements have already demonstrated good force-current model performance. Overall model performance is as expected with a

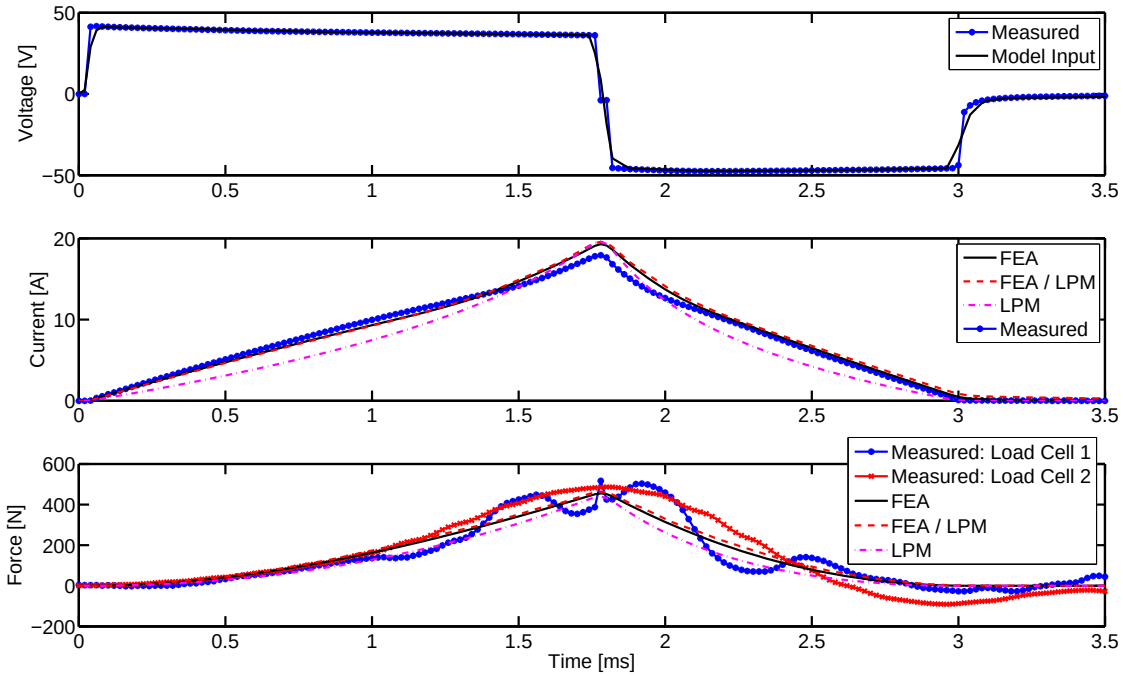

Figure 7.7: Simulated and measured response of the opener magnet, 42 V, 0.75mm airgap

general degradation in performance with respect to model simplicity. However, the degradation is relatively modest suggesting the assumption of negligible eddy currents is valid. Although the FEA provides the best overall current and force prediction, the LPM-FEA hybrid and LPM models take only seconds to simulate (as opposed to hours). Despite the LPM exhibiting the lowest overall agreement, it is the only model that is amenable to analytical control design techniques.

Although the FEA has proven instrumental in providing data for LPM development, it is the only method capable of producing potentially revealing qualitative results. Figures 7.11a through 7.11f illustrate opener flux lines over time for the same step voltage input shown in Figure 7.9 corresponding to an air gap of 1.50 mm. These figures provide insight to the nature of the fringing and leakage air paths, something that may assist in the development of reluctance network models. Additionally, due to the transient nature of the study, appreciation of the eddy current skin effect (see

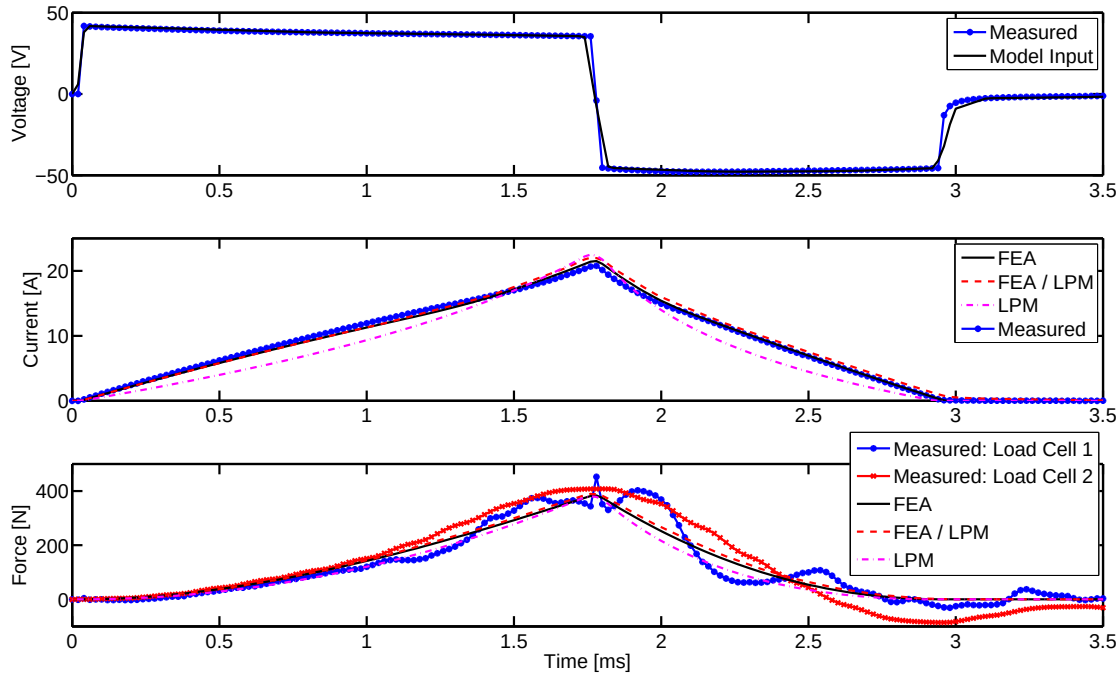

Figure 7.8: Simulated and measured response of the opener magnet, 42 V, 1.00mm airgap

Appendix A.5) can also be made. Compared to similar transient studies conducted in [Chladny, 2003], the observed skin effect is relatively modest. Similar to the flux lines, contour plots of magnetic flux density are as shown in Figure 7.12. Such plots are likely quite useful to an actuator path designer as they provide insight as to where the material is most likely to saturate first (and hence offer no further use to field manipulation or intensification). For example in Figure 7.12b, it is apparent that saturation is most likely to occur first in the back iron path corners (likely exacerbated by the eddy current skin effect) and later (Figure 7.12e) in the pole face corners (due to the relatively small amount of material through which fringing is likely). Thus, it may be possible to further enhance the magnetic efficiency of the device through the addiction of small radii at the inside of the back iron legs (where the inner coil is wound) likely at an increase of manufacturing costs or overall actuator volume and mass.

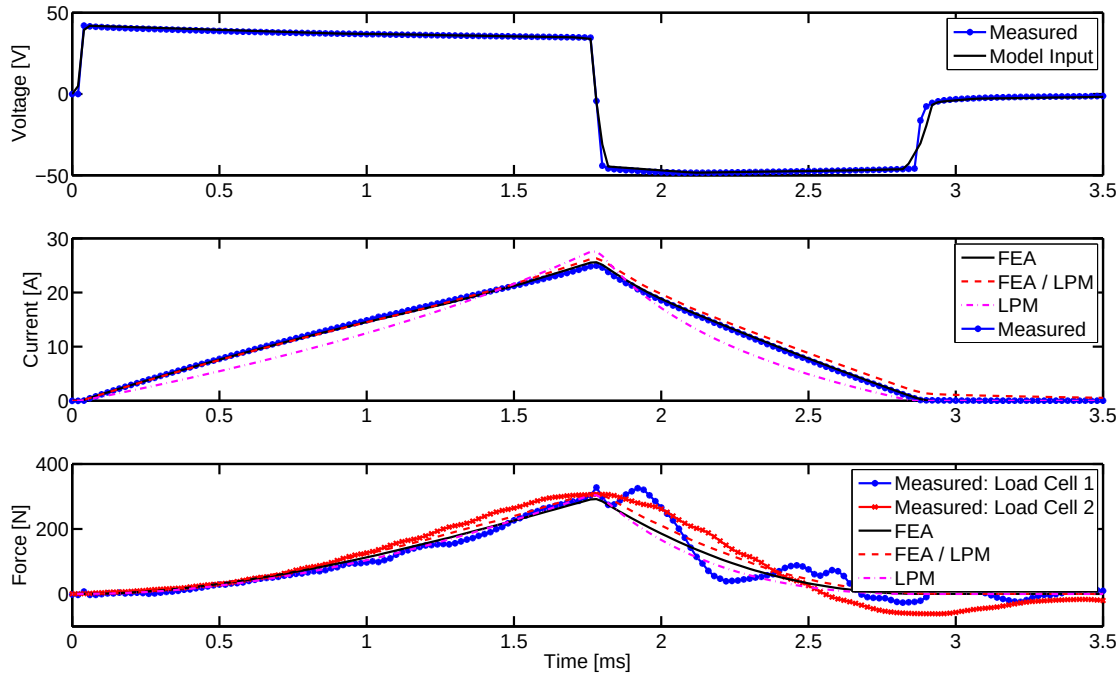

Figure 7.9: Simulated and measured response of the opener magnet, 4 2V, 1.50mm airgap

7.2.3 Preliminary Flux Sensor Evaluation

As a preliminary method of evaluating the flux sensor performance, the material testing machine crosshead position controller is set to induce a sinusoidal armature motion. During this time, a step load is input through regulation of coil current about a predefined set-point as discussed in Section 6.2.2.3. In this way, insight may be gained to armature position measurements by comparing the crosshead position output and the reconstructed position based on flux and coil current measurements using the technique in Section 5.6.1. Figure 7.13 shows the results at a crosshead frequency of 10 Hz and amplitude of 0.50 mm. Minimum air gap is set to 0.50 mm. Similarly, Figure 7.14 provides results of a test conducted at a frequency of 4 Hz but with an amplitude of 1.50 mm and a minimum air gap of 1.00 mm. In both tests, reasonable agreement is observed between the reconstructed position and measured

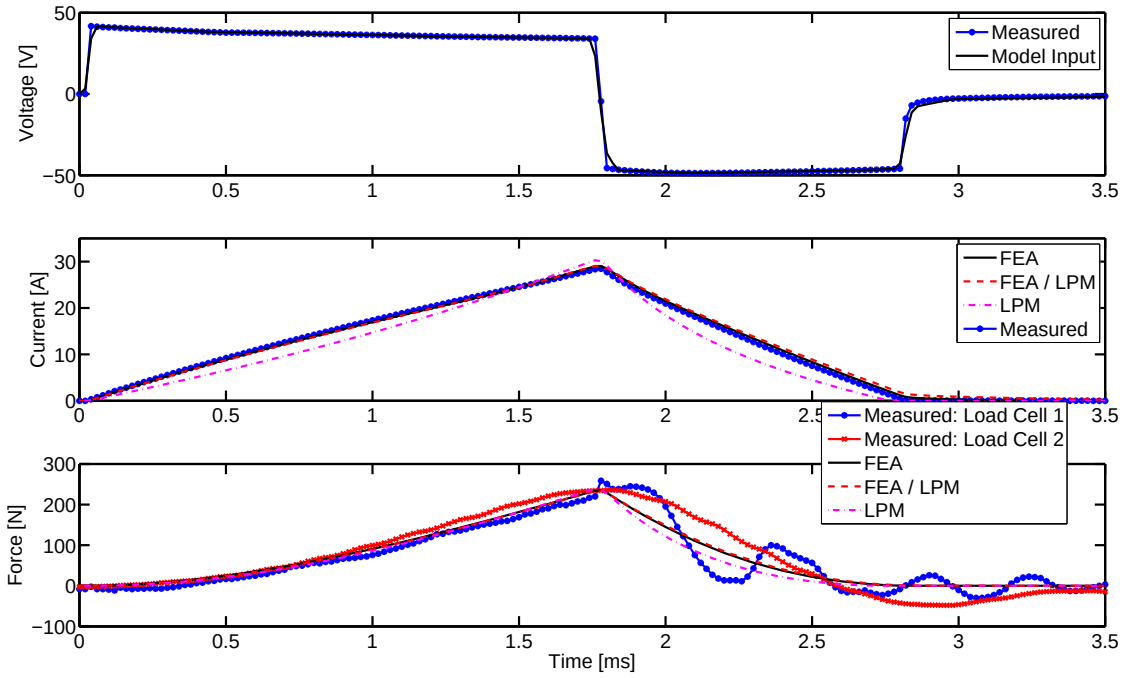

Figure 7.10: Simulated and measured response of the opener magnet, 42 V, 2.00 mm air gap

crosshead position. Aside from initial field build up (at t< 1.5 ms), a maximum deviation of approximately 0.7mm is observed for the 10 Hz case. It is unclear if the discrepancy is a result of the reconstruction technique or an actual deviation as a result of armature or load frame dynamics. The time required to establish a field sufficiently strong enough to make an accurate measurement is significant and suggests that a bias current will be required, particularly at low air gaps. Although these experiments serve only as a preliminary indication that it is possible to reconstruct position from flux and current measurements, they are not overly useful in that even at 10Hz, the motion is relatively slow compared to a normal valve opening or closing cycle (which typically occurs within 5 ms). Recording time is limited to approximately 70 ms due to concerns of saturating the op-amp integration circuit and damaging the coil.

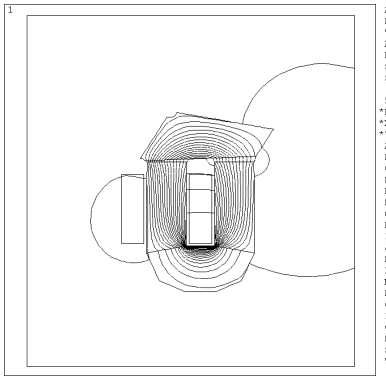

(a) t=0.2 ms

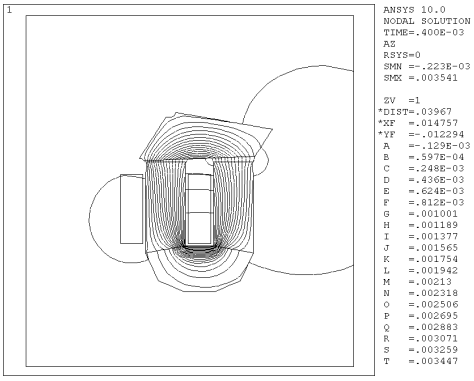

(b) t=0.4 ms

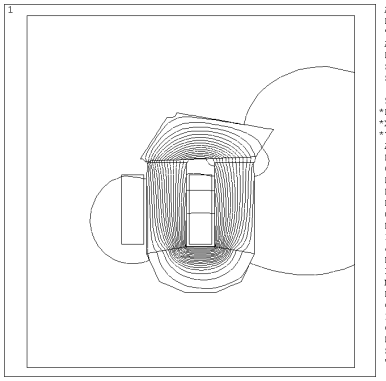

(c) t=0.6 ms

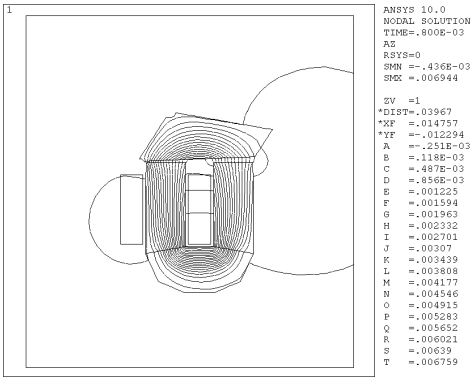

(d) t=0.8 ms

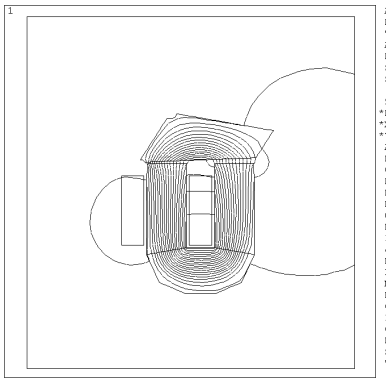

(e) t=1.0 ms

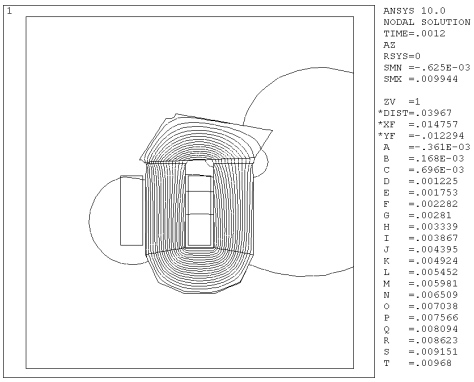

(f) t=1.2 ms

Figure 7.11: Opener flux lines for a 1.50 mm air gap and 42 V step input at: 0.2, 0.4, 0.6, 0.8, 1.0 and 1.2 ms

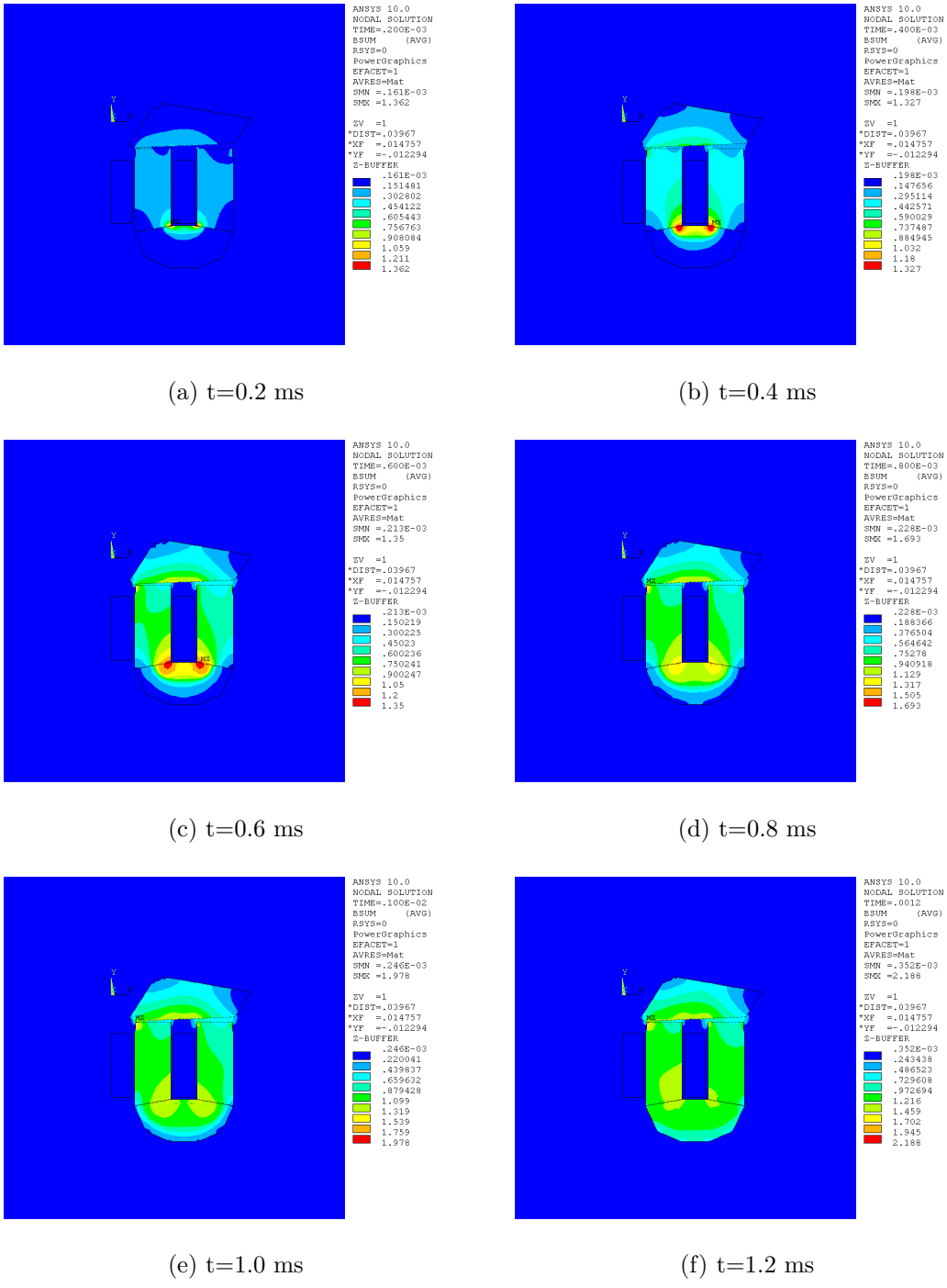

Figure 7.12: Opener flux density contour plots for a 1.50 mm air gap and 42 V step input at: 0.2, 0.4, 0.6, 0.8, 1.0 and 1.2 ms

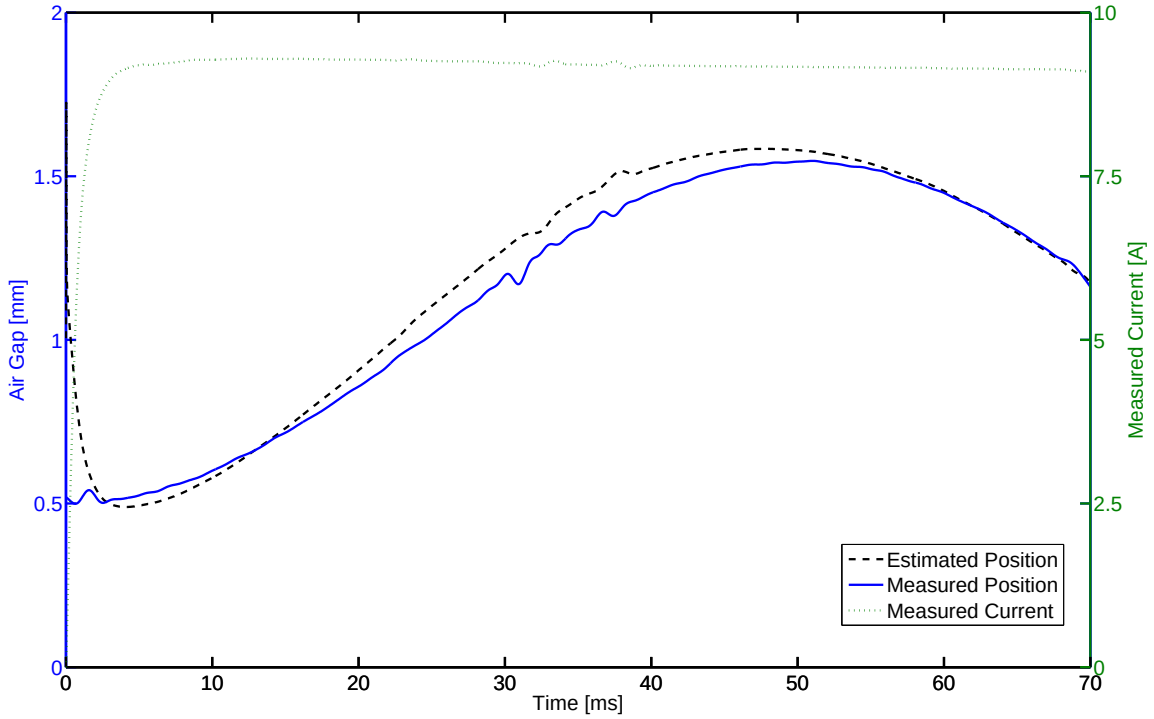

Figure 7.13: Measured and estimated air gap during 10 Hz, 0.50 mm amplitude, 1.00 mm mean crosshead motion

7.3 Simulated and Measured Controller Performance

Upon validation of the various magnetic models, the LPM-FEA hybrid model is extended to include spring-mass and gas force dynamics as described in Section 4.6. The model is instrumental in the development of a comprehensive control strategy capable of addressing the issues of unknown gas force disturbances and soft seating while subject to a 42 V source and production amenable feedback sensors. The model is validated through comparison with relatively simple open-loop testbench experiments. Upon successful simulated controller performance, the developed control software is coded in C and compiled on a dSPACE DS1103 controller. The following sections provide an overview of the simulated and measured testbench experiments.

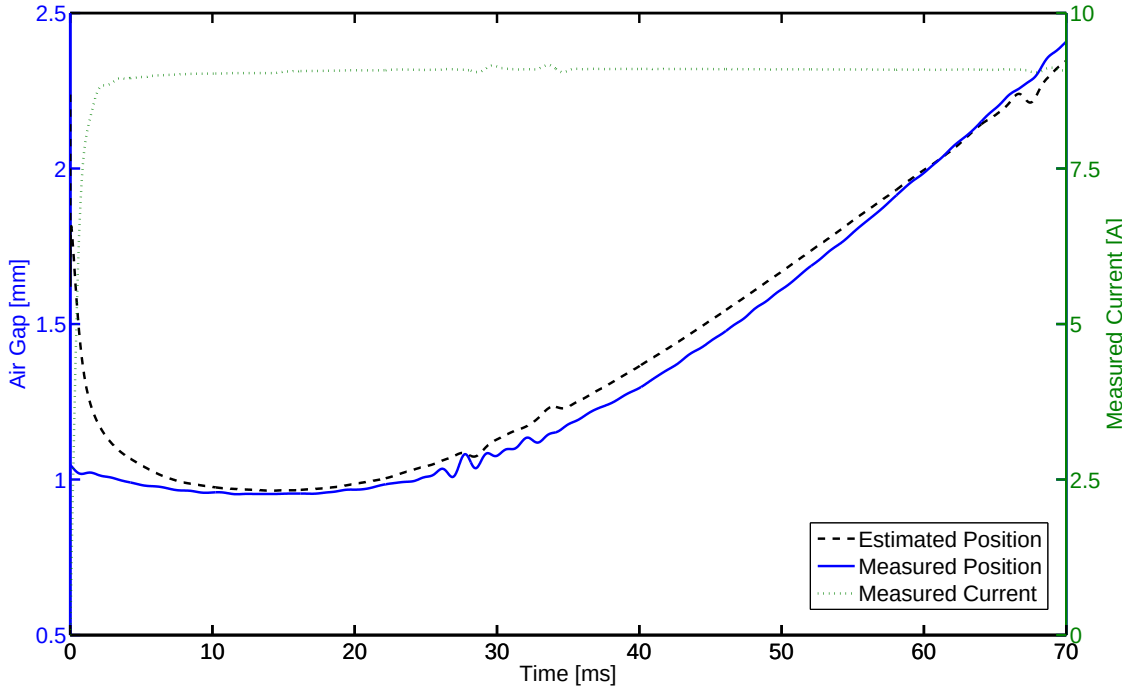

Figure 7.14: Measured and estimated air gap during 4 Hz, 1.50 mm amplitude, 2.5 mm mean crosshead motion

7.4 Testbench System Model Validation

Prior to feedback control implementation on the designed testbench (described in Section 6.3), a model of the complete actuator system is developed using the MATLAB-Simulink environment and acquired FEA data. The model accounts for bridge drive circuits, mechanical and electromagnetic response. The model also approximates exhaust gas forces as a means to evaluate feedforward requirements under a variety of blowdown pressures. The model is then validated through comparison to increasingly sophisticated testbench experiments. For example, Figure 7.15 contrasts the simulated and experimental results of a pressurized release where the closer holding current is simply switched off and the cavity depressurization and valve oscillation are observed. Later, when a landing controller is implemented, the pressure trace and digital outputs from the dSPACE controller are recorded and used as the model

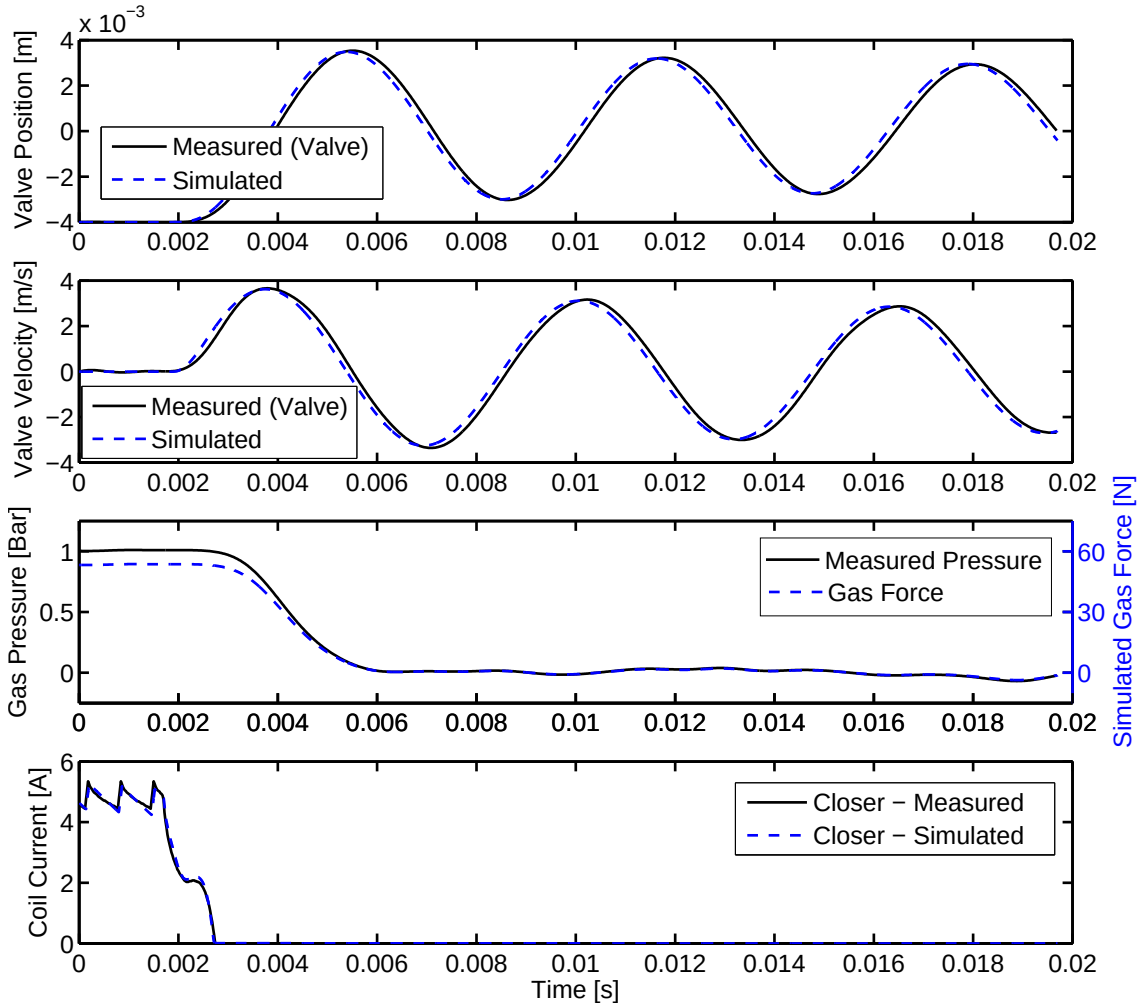

Figure 7.15: Simulated LPM-FEA and experimental free opening, 1 bar blowdown pressure

input (open-loop simulation) as shown in Figures 7.16 and 7.17. Here, gas force is simulated as valve area times cavity pressure and gas force coefficient, $F_g = A_v P C_{gf}$. The simulation results suggest reasonable agreement given the simple gas force model and the lack of a controller in the simulations. Specifically, a maximum of 1.5% displacement and velocity peak error among the various simulations is observed. The primary discrepancy is due to a 0.25 ms delay (maximum) between the measured and simulated results. This may be due to static friction force that is unaccounted for in the model. Given that these results are obtained simply through using the same ini-

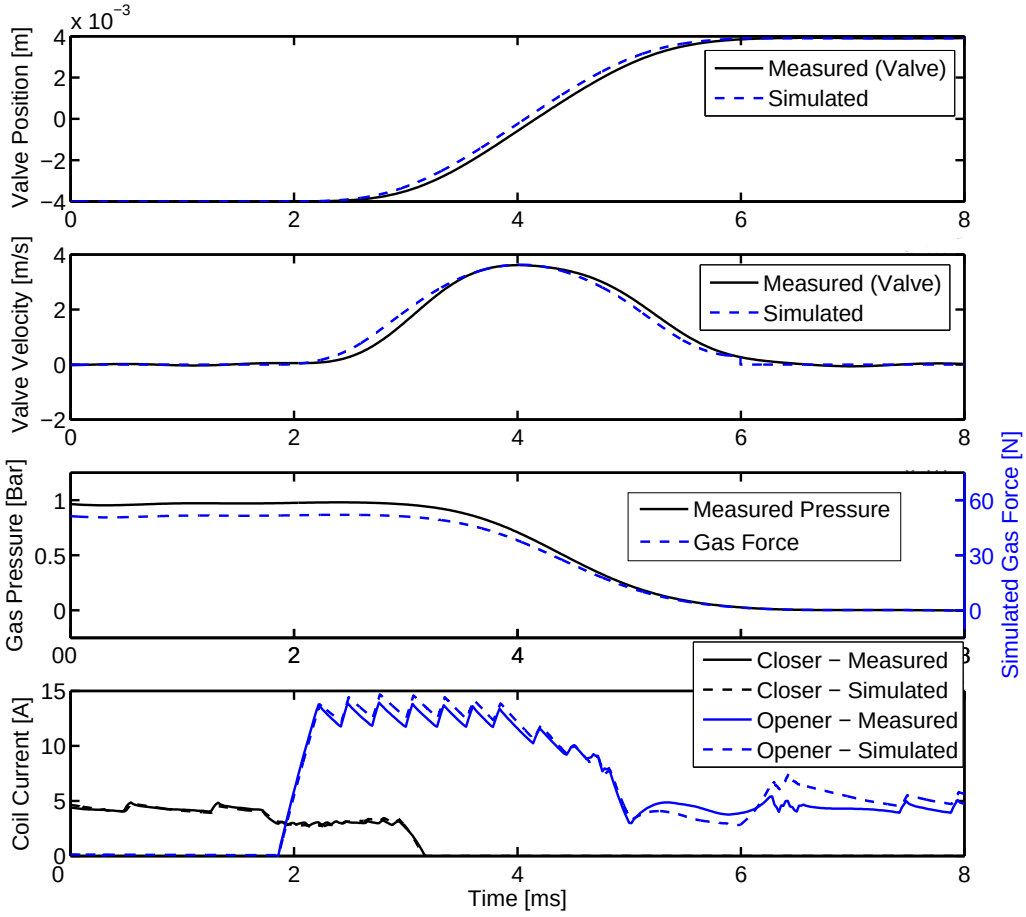

Figure 7.16: Simulated LPM-FEA and experimental valve opening, 1 bar blowdown pressure

tial conditions and experimental switch signals (simulation is thus run in open-loop) the model is expected to be valid for controller design purposes.

7.4.1 Open-loop Feedforward Control

Initially, only tuned open-loop feedforward controllers are used to setup appropriate initial conditions for the flatness-based landing controller. Figure 7.18 demonstrates typical landing performance (opening and closing) over a pressure range of 0.25 to 4.5 bar using the flux-based position and velocity estimation and open-loop feedforward

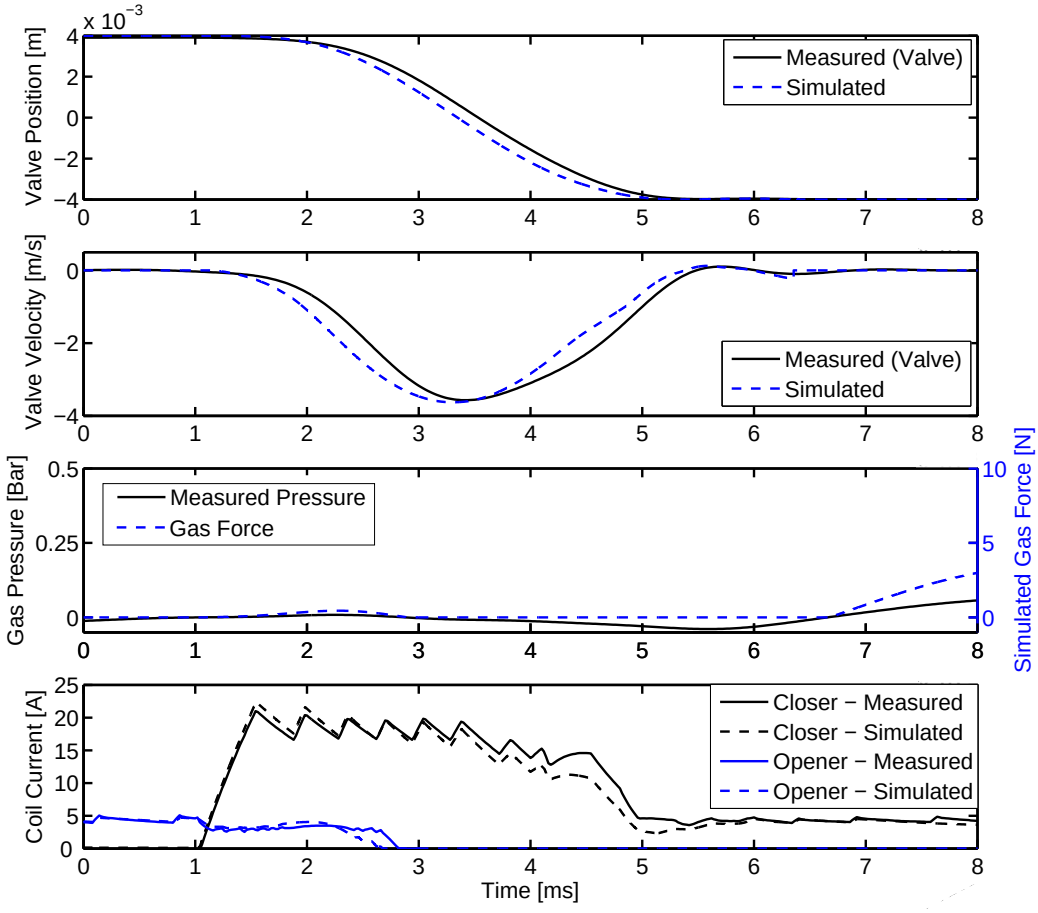

Figure 7.17: Simulated LPM-FEA and experimental valve closing, 1 bar blowdown pressure

method. It is found that with tuning at each pressure level, landing velocities of $\leq$ 0.1m/s are consistently attainable. Figure 7.19 illustrates similar performance is attainable at higher test-bench speeds as well. However, at speeds greater than 3000rpm, exhaust pressures are limited to approximately 1 bar due to compressed air supply restriction on the testbench.

Although the manually tuned method appears acceptable, potentially large impacts and / or actuation failure can result with even modest ($\pm$0.5 bar) changes in opening pressure.

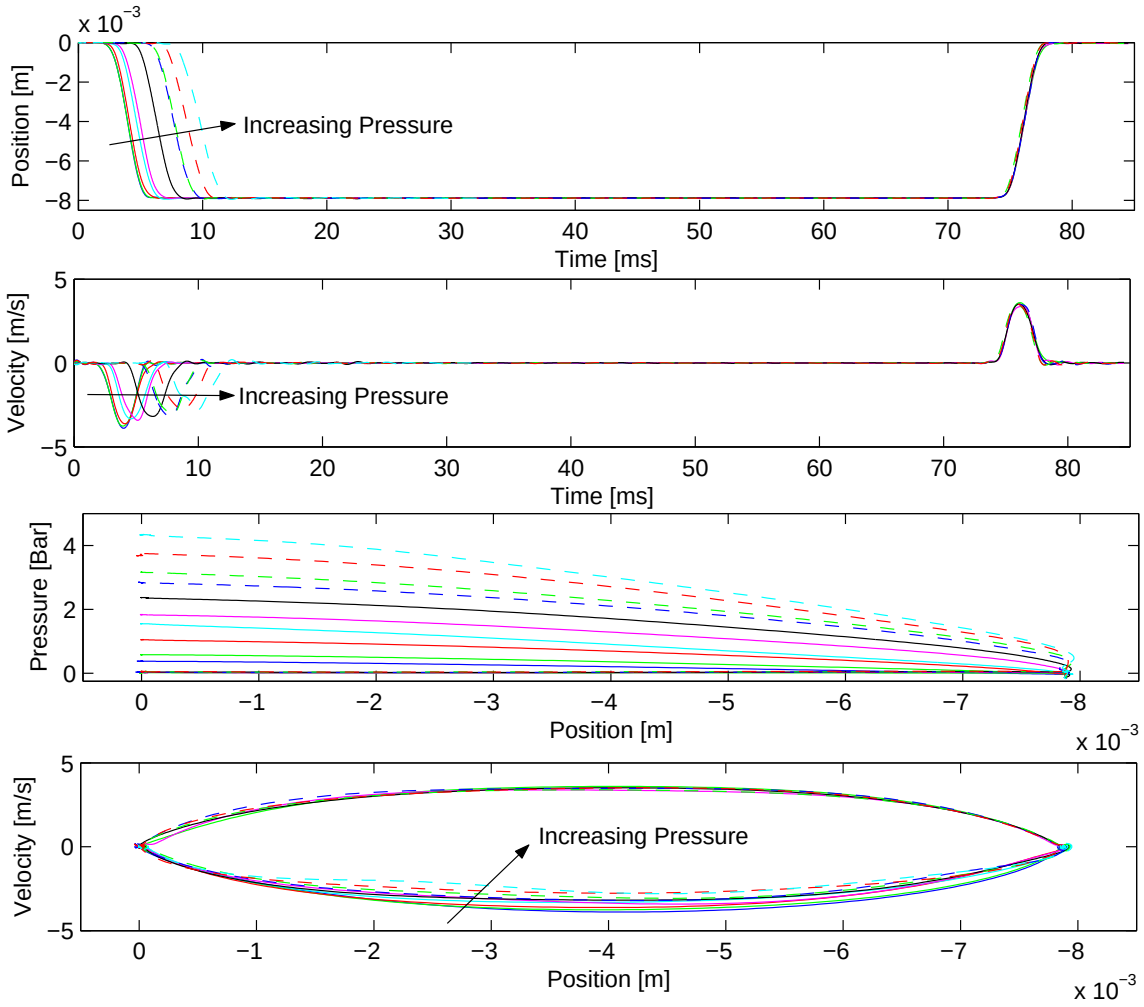

Figure 7.18: Full cycle plots over a 0.25 to 4.5 bar pressure range, 250 rpm

7.4.2 Observer Convergence

Since velocity and gas pressure measurements are unavailable for control, they are estimated through the observer discussed in Section 5.7. The observer structure is first simulated and tuned independently of a feedback controller using measured position data for simple testbench experiments as shown in 7.15. Later, the observer is combined with a feedforward and landing controller first in simulation and then coded and re-tuned on the testbench hardware. Figures 7.20 and 7.21 indicate typical position, velocity and gas pressure estimates at respective EVO pressures of

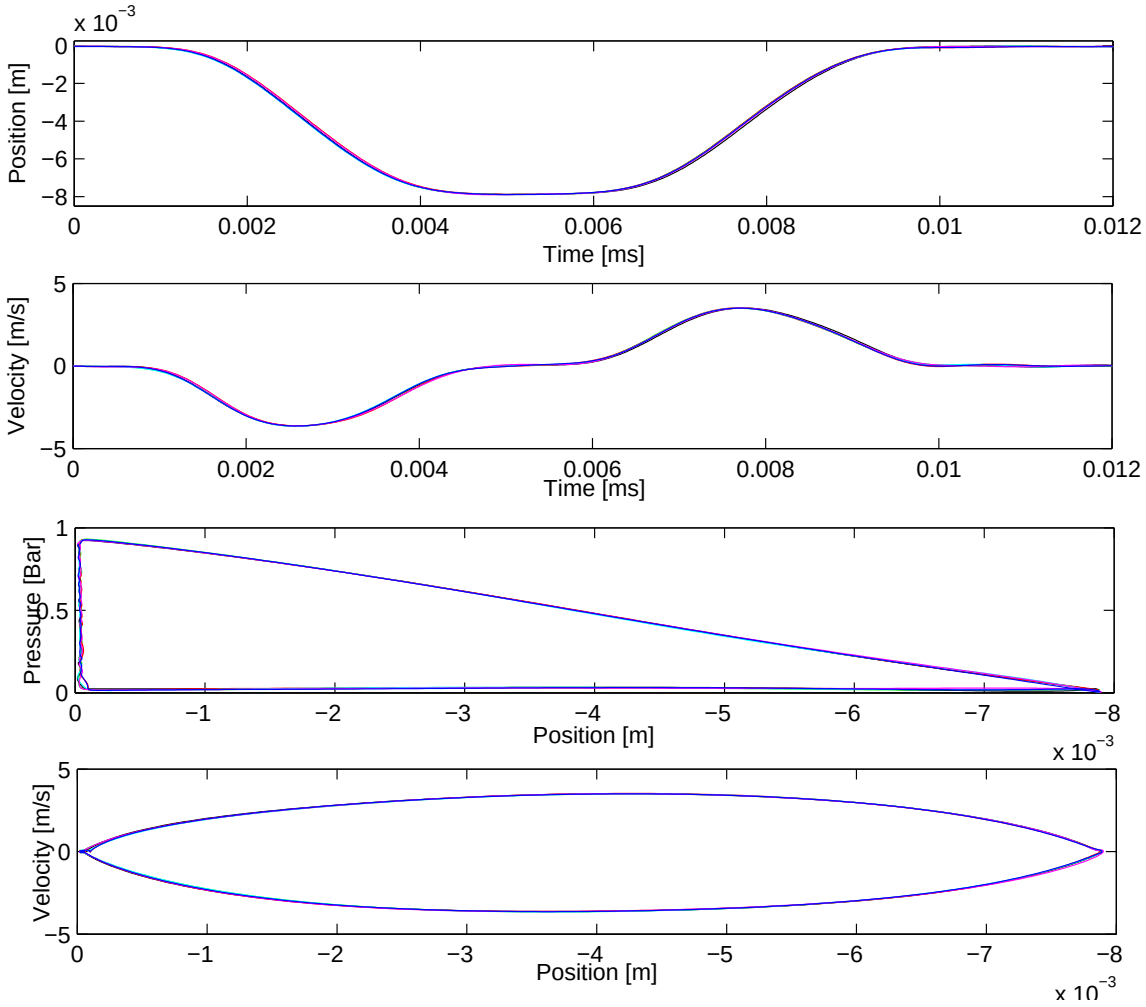

Figure 7.19: Flatness voltage landing control via flux feedback - 3500 rpm, 1 bar blowdown, 6 cycles

1 and 5 bar. Although gas force is actually used in the feedforward and feedback routines, the force estimate is converted to a pressure for direct comparison with measured pressure (since valve gas force is not measured directly). Also shown is the measured flux-based position signal in which all estimates (with current) are made. Convergence performance in the case of the simulated results is significantly better than the measured cases. This is largely due to a relatively noisy flux-based position signal, particularly at the early stages of valve opening where a change in armature position has only a moderate influence on path flux. This problem is intensified at

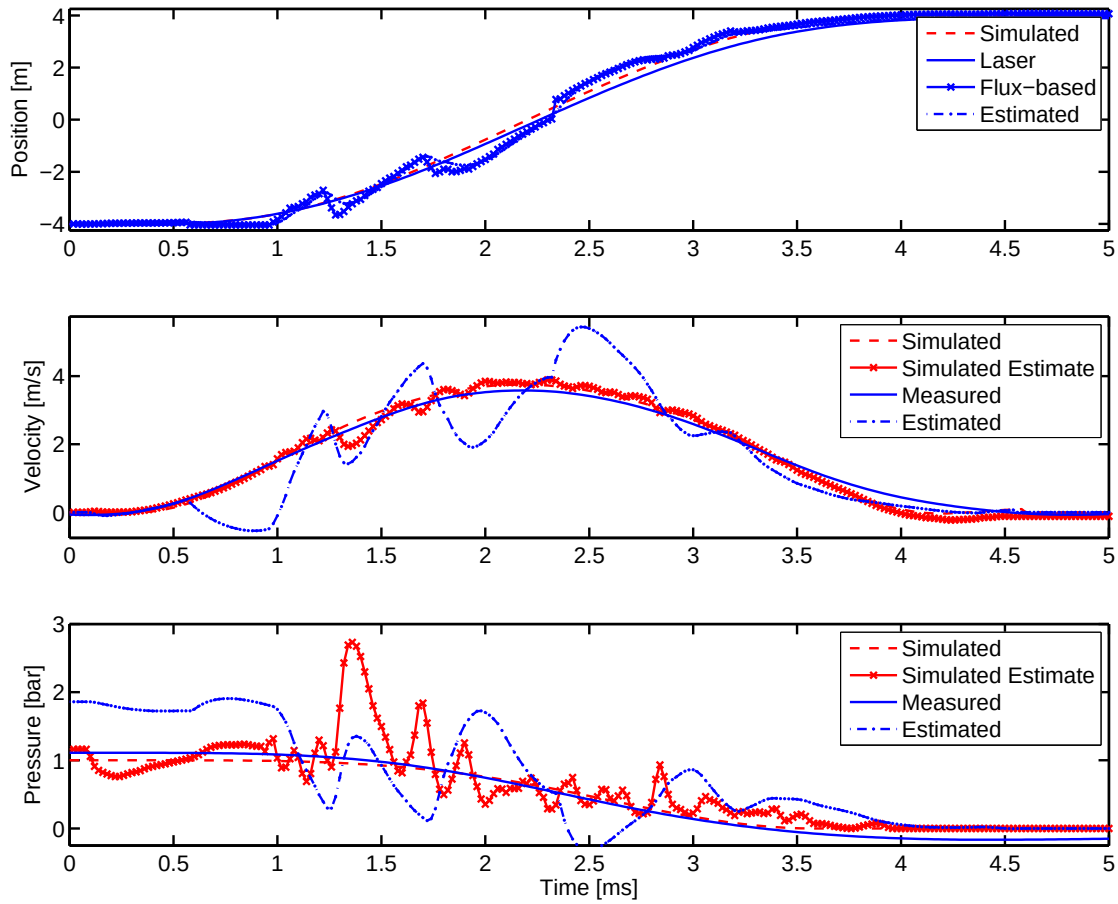

Figure 7.20: Simulated and experimental estimated position, velocity and pressure convergence, 1 bar

larger EVO pressures as the valve opens so slowly that a opener bias current is imposed to maintain a position signal (albeit a relatively poor one). In the later half of the valve opening stroke, the flux-based signal improves as do the respective estimates. Despite the degraded estimation accuracy in the early opening stages, good control performance is still possible in part because of the way in which the feedforward controller is designed. Specifically, consideration is given to the low magnetic force authority at distances of 4 mm away or greater from the pole face so that a relatively low (and thus less noisy) feedforward current is demanded during the early stages of valve opening. Figure 7.22 indicates desired and actual feedforward currents for EVOs of 1 and 5 bar for both the simulated and measured cases. Upon release, a constant

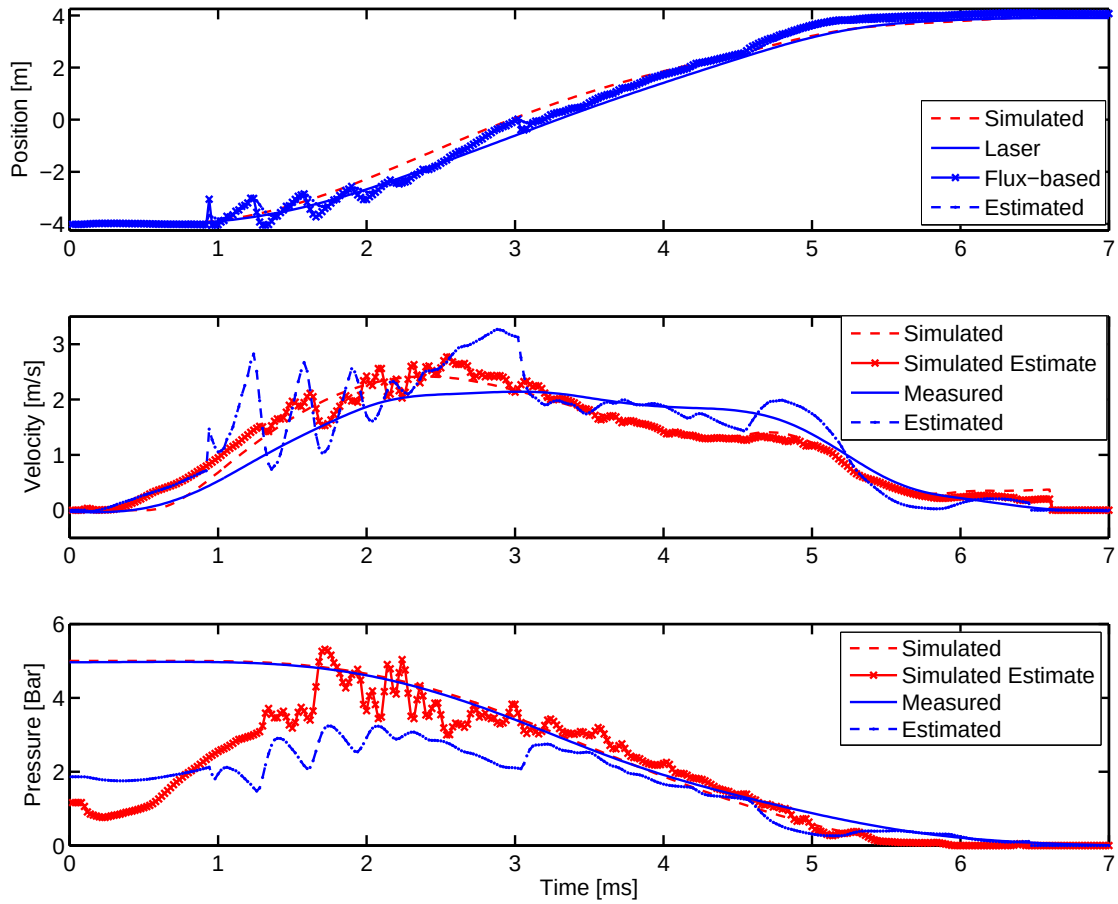

Figure 7.21: Simulated and experimental estimated position, velocity and pressure convergence, 5 bar EVO

bias current is applied in anticipation the requirement of a position measurement.

7.4.3 Gas Disturbance Rejection

Plots of simulated and measured position, velocity and gas pressure are shown in Figure 7.23. Also shown are individual gas pressure estimates. In this figure, eight consecutive cycles are shown where initial pressure is alternated between 1 and 5 bar to demonstrate the observer and feedforward controller's ability to compensate for large cycle-to-cycle pressure variations. In both simulation and experiment, no changes are made to the controller parameters, gains or initial gas force estimates between cycles. Similar results are obtained for random initial pressure tests. Convergence

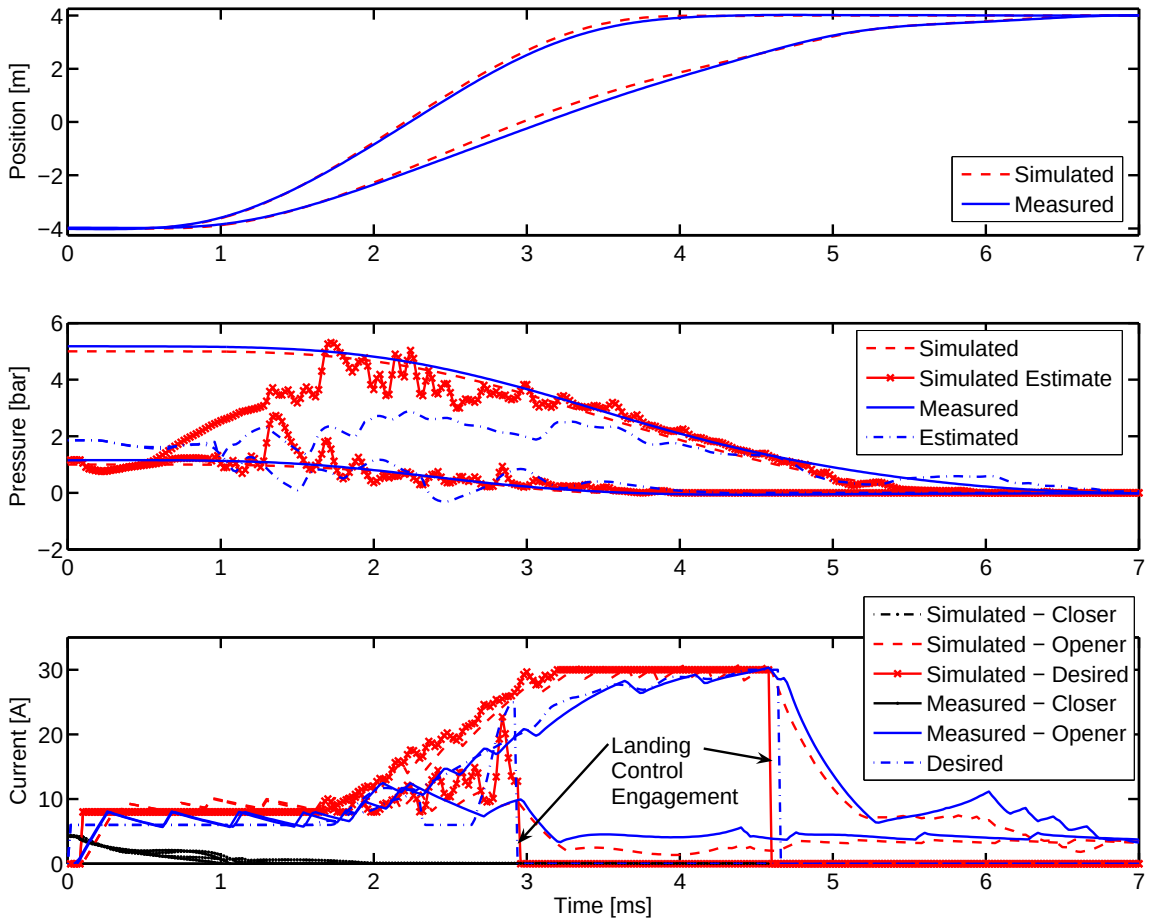

Figure 7.22: Simulated and experimental position, pressure, current and desired feed-forward current at 1 and 5 bar EVO

of γ is provided for the same cases, this time measured gas pressure is converted into an equivalent initial pressure by dividing measured pressure by function $f_1(x)$. Overall, there is good agreement between simulated and experimental results. In simulation, gas force estimation is initially very good with rapid convergence in the first two millimeters of lift. However, deviation from the true value is observed in the later portion of the stroke, likely due to model-plant mismatch bias and weak observability. Gas pressure convergence is not as rapid in the experimental case due to a poorer quality position signal (noise is not modeled in the simulation) and thus lower gains are assigned. Position signal quality is poorer at high pressures as the slower valve motion required the need to switch from the closer position coil (zero

current) to the opener early on in the valve stroke (where the flux-based position performance is most sensitive to noise). Despite this, convergence is rapid enough to provide adequate feedforward current and the overall experimental performance is very good. The phase plane plot in Figure 7.23 indicates a maximum opening impact speed of 0.17 m/s in one of the 5 bar cycles. Such results are excellent considering pressure variations from 1 to 5 bar are being applied alternatively for each of the eight consecutive cycles to approximate an engine misfire.

7.4.4 Simulated and Measured Control Performance

The flux-based feedback sensor, observer, feedforward and landing controllers are implemented to provide a comprehensive valve actuation strategy. The routines are first tested using the detailed actuator and power electronics Simulink model and then implemented in real-time on the testbench. Upon demonstration of successful landing control at predefined EVO pressures, the proposed disturbance estimation and energy-based feedforward method is implemented. Simulated and experimental performance results of these tests (again using flux-based feedback) are shown in Figure 7.25 with respect to position, velocity, pressure and coil current. These results illustrate the comprehensive control performance in simulation and in experiment over a relatively wide range of exhaust gas pressures. The effectiveness of the combined control strategy is experimentally demonstrated with an average impact velocity below 0.1 m/s with a standard deviation of 0.06m/s (over two hundred cycles). Transition times (defined by the time from when the control command is given to open to the point of impact) vary significantly with pressure with typical maximum and minimum times of 6.2 ms and 4.1ms for the 5 bar and 1 bar cases respectively. If transition time is calculated as the time taken for the valve to move from the 98% closed to 98% open position (-3.84mm to 3.84mm) [Peterson, 2005], then typical maximum and minimum times are 4.5ms and 3.0ms for the respective 5 and 1 bar cases.

To be sure acceptable landing performance is consistent and repeatable, impact speeds are recorded from 200 cycles at three pressure levels. Due to data acquisition memory limitations, the recording time is limited to two seconds. As a result, the cycles that occur during the time to download and save a two second interval (at most, 30 seconds) are not recorded. The engine speed (emulated) of the tests determines how many recording intervals are required to total 200 valve cycles. Again, for higher pressure EVOs, a slower speed is required to accommodate compressed air flow rate limitations. Figures 7.26 through 7.28 show the opener and closer impact velocities over 200 recorded cycles at 1, 3 and 5 bar EVO pressures, respectively. In all cases, an average impact velocity of 0.1 m/s with an approximate standard deviation of 0.05 m/s are achieved with exception of the opener at 5 bar EVO pressure. Here, a slightly higher average impact velocity is obtained with a significantly higher average impact speed of 0.104 m/s and standard deviation of 0.09 m/s is observed. Also worthy of note is the difference in distribution between the 5 bar EVO case and all others. The 5 bar opener distribution is somewhat polarized between relatively low impacts and higher impacts while the other cases conform closer to a normal distribution. It is suspected that this is a result of heightened sensitivity to variations in initial conditions and estimation errors for the higher pressure cases. Or in other words, the controller performance tends to either be exceptionally good, or in the event of even moderate initial condition variations, higher impacts are observed.

7.5 Simulated Multi-cylinder Exhaust Manifold Pressure Disturbances

The gas disturbances considered thus far have been highly idealized to simplify the estimation process while attempting to capture the main dynamic effect. It is acknowledged that multi-cylinder exhaust manifold pressure variations can be significant and difficult to measure and predict [Macián et al., 2004]. It is suspected that

the proposed disturbance observer will be able to accommodate large variations in back pressure provided they are slowly varying with respect to a valve event. However, if a relatively large pressure disturbance occurs mid-stroke of valve opening, it is unknown how experimental landing performance may be affected. Several simulations are provided to lend insight to performance under such conditions in Figure 7.29. The simulations suggest that although performance is compromised with respect to impact velocity and opening time, such disturbances may still be manageable (particularly given the abrupt timing and magnitude simulated). One conceivable extension of the testbench apparatus would be to inject volumes of compressed air into the exhaust stream to investigate the subsequent control performance subject to exhaust manifold variations.

7.6 Summary

The previous sections summarize and highlight the key results of the modeling and control of a prototype solenoid valve actuator. The proposed modeling techniques have been validated through quasi-static and testbench experiments. Feedback and state estimates are made through a magnetic flux signal measurement and estimator. This technique is sufficient for implementation in a production under-hood environment and cost effective compared to eddy current, LVDT and laser based sensors of sufficient resolution and bandwidth. Using a disturbance observer and feedforward controller, large EVO pressure variations may be identified and rejected on a cycle-by-cycle basis ensuring soft seating over a wider range of operating modes. Additionally, the flatness-based landing controller provides suitable tracking over a wide range of initial conditions while restricted to a 42 V source.

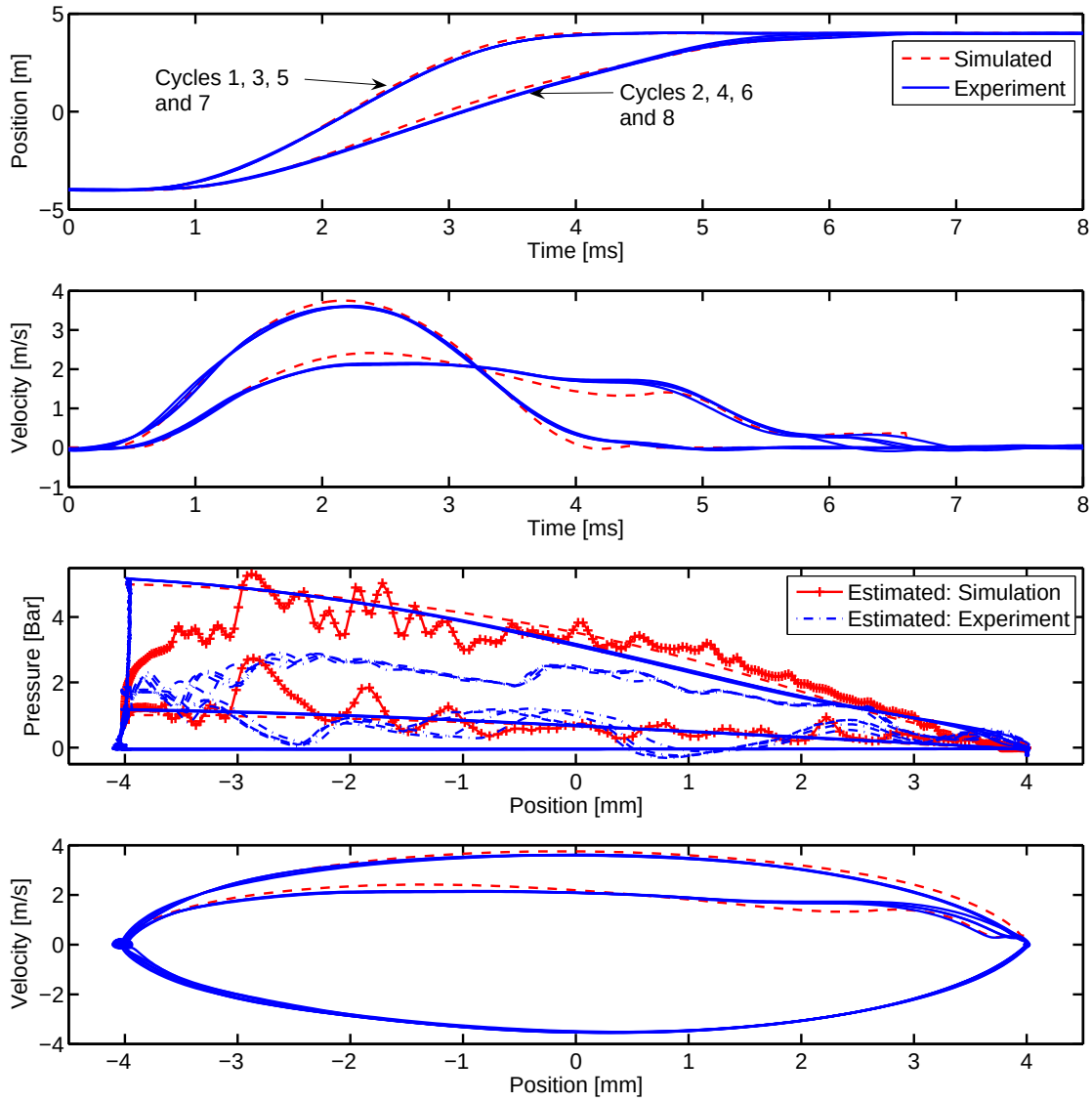

Figure 7.23: Simulated and measured opening cycles with cyclic pressure variations between 1 and 5 bar

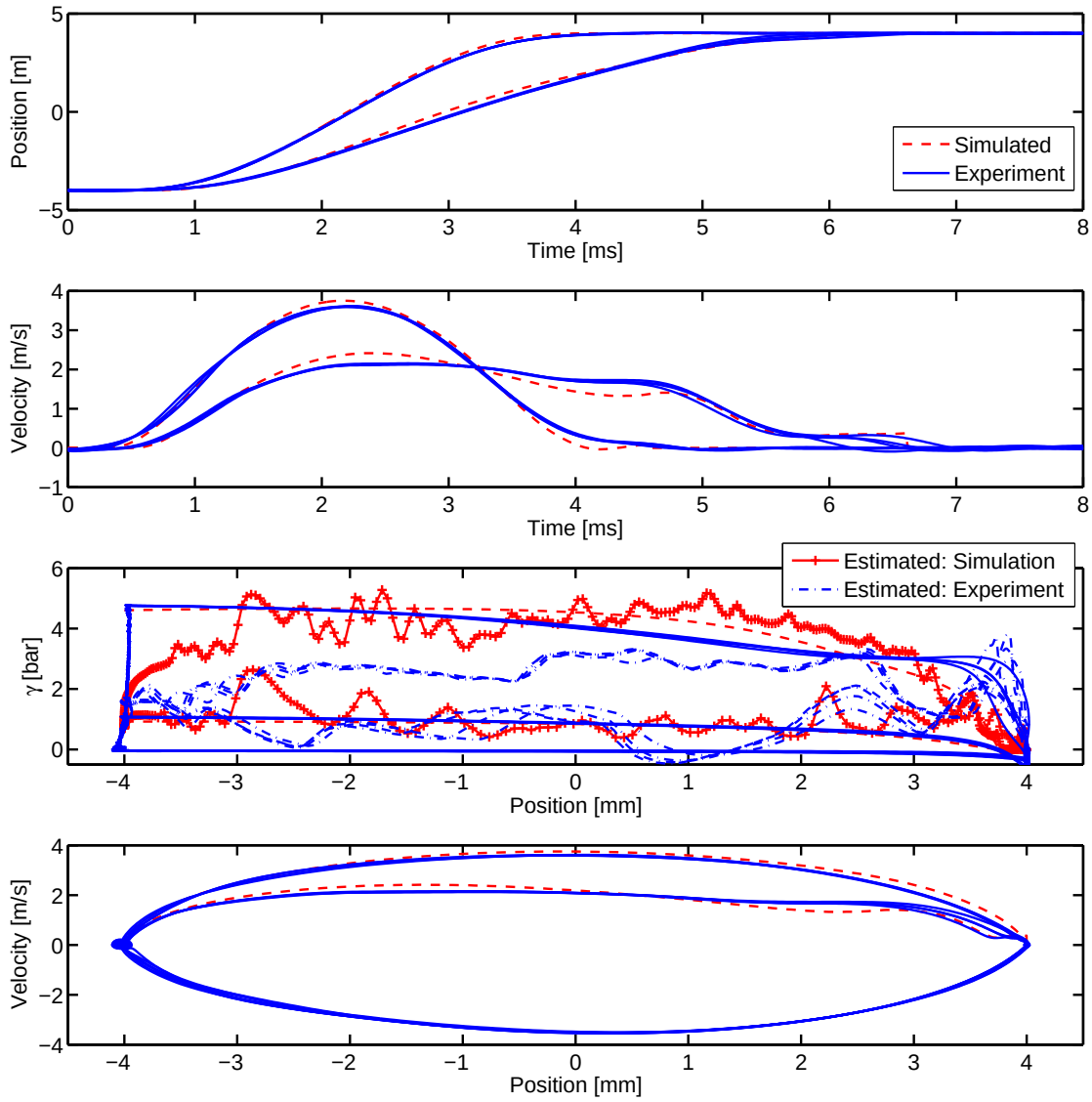

Figure 7.24: Simulated and measured opening cycles with cyclic pressure variations between 1 and 5 bar

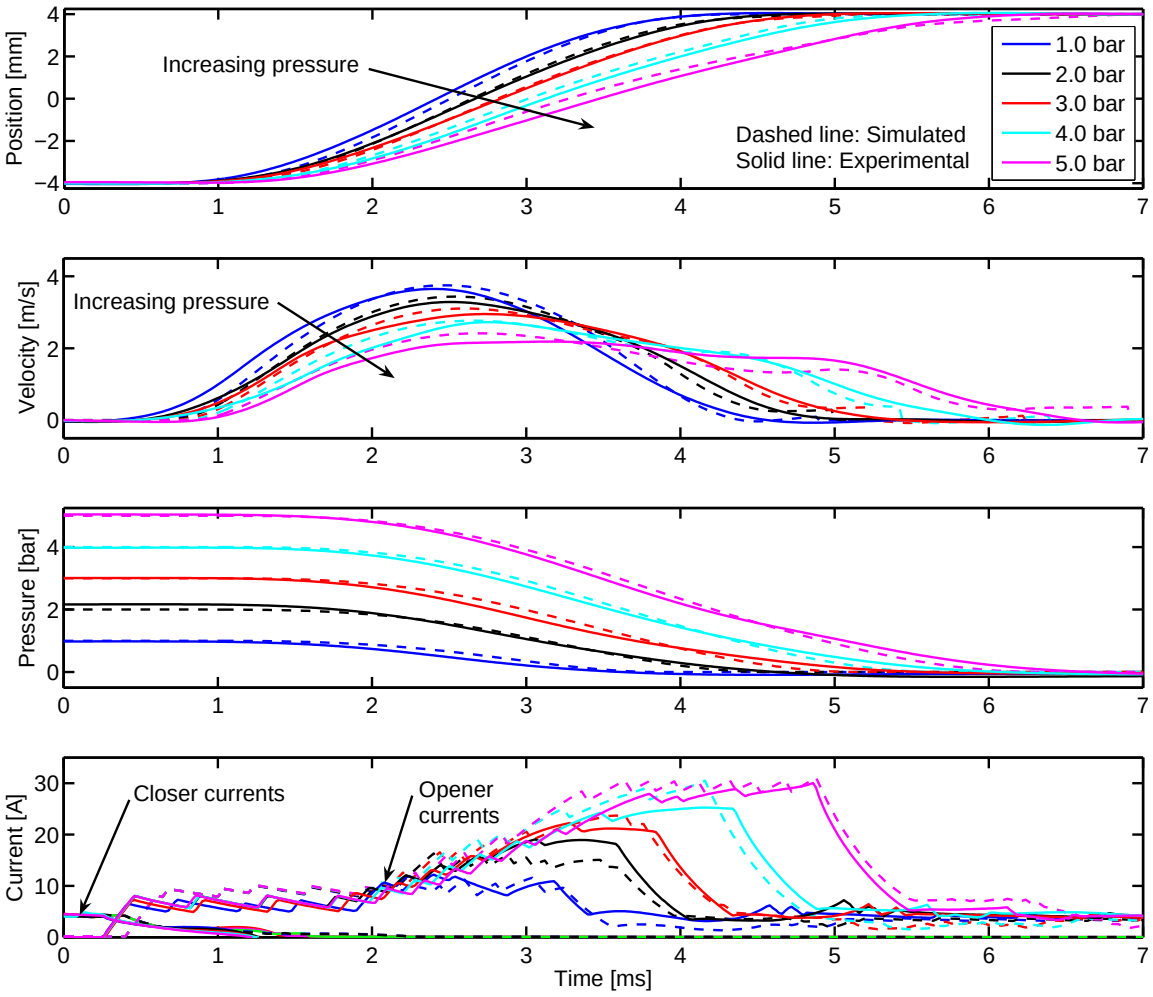

Figure 7.25: Simulated and experimental feedforward and landing results for 1 to 5 bar EVO pressures using flux-based feedback and observer disturbance rejection

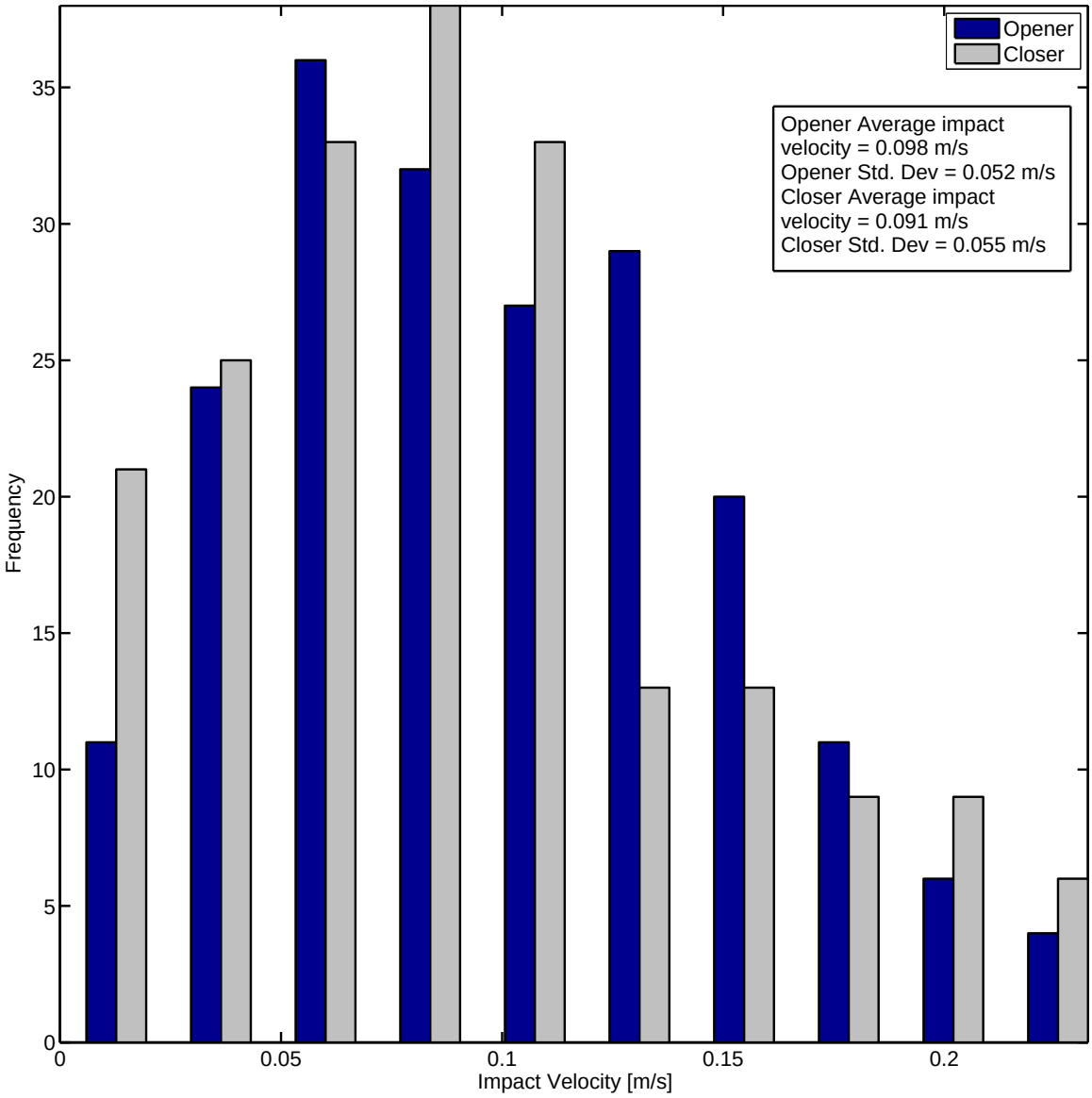

Figure 7.26: Experimental impact velocity histogram at 1 bar, 200 cycles

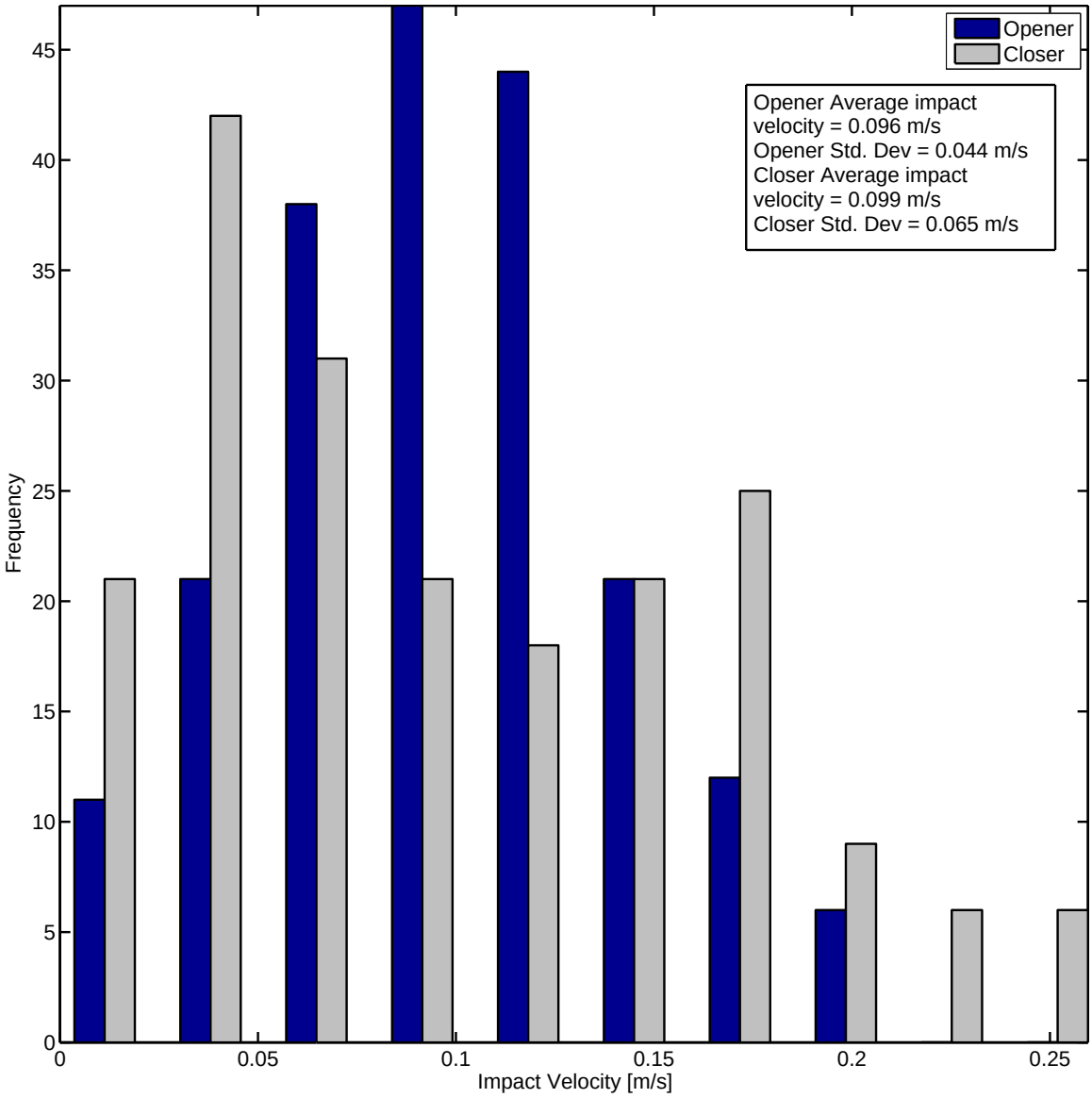

Figure 7.27: Experimental impact velocity histogram at 3 bar, 200 cycles

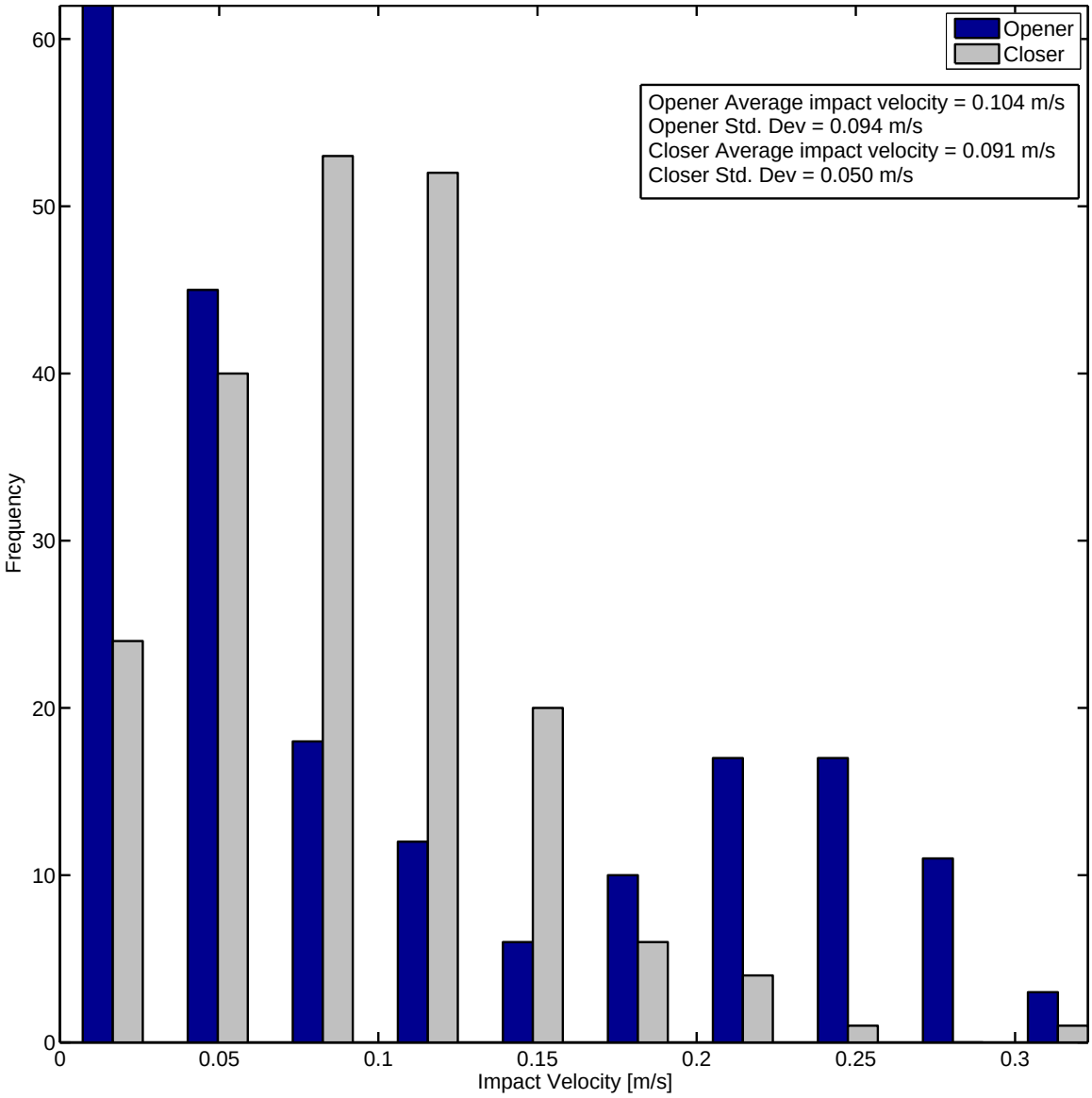

Figure 7.28: Experimental impact velocity histogram at 5 bar, 200 cycles

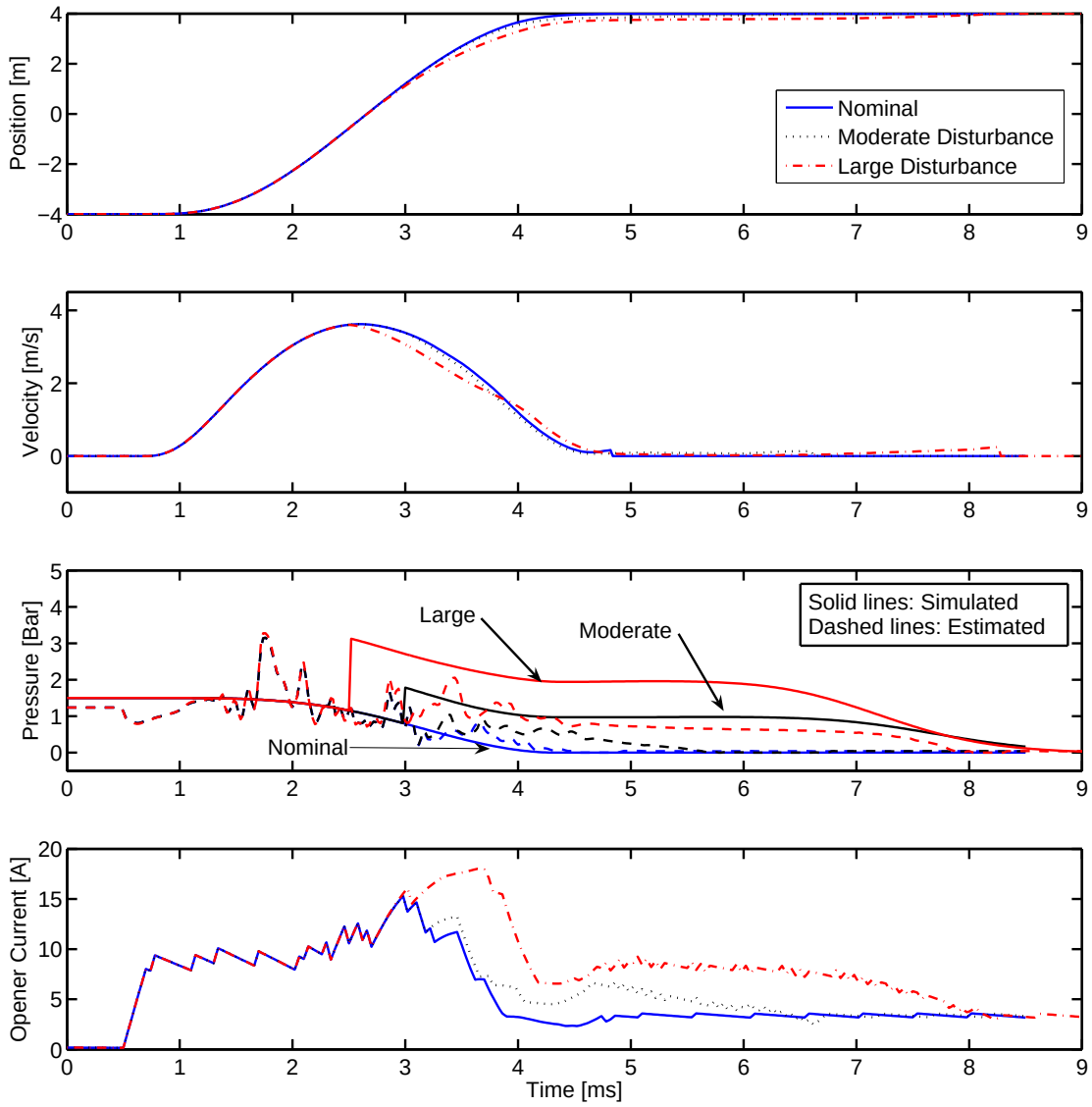

Figure 7.29: Simulated 1.5 bar disturbance response with secondary mid-stroke pressure disturbances

Chapter 8

Conclusions and Further Research

Due to the many stringent constraints and requirements inherent to using solenoid variable valve timing actuators, the design, control and implementation of the devices has proven to be exceptionally challenging. The multi-disciplinary nature of the problem has also likely impeded development. Without considering the myriad challenging issues already facing any emerging automotive technology such as ecconomics, mass production, environmental impact and safety, the successful implementation of solenoid gas exchange valve actuators involves insights of electricity, magnetism, heat transfer, vibrations, fluid mechanics and control system theory. The preceding work presents a comprehensive modeling and control strategy for such actuators that accounts for the electrical, mechanical and nonlinear magnetic aspects of the actuators system. The control method is based on a foundation of extensive and accurate simulations as a means of maximizing control performance while simultaneously reducing the debugging, tuning and risk associated with hardware implementation. Specifically, 2D FEA models have been developed to characterize actuator magnetic response and are used to parameterize lower-order lumped parameter models that are amenable for control design. All models have been validated with equivalent experiments. Through careful analysis of simulated performance, a control strategy has been designed that is capable of achieving the low impact velocity

constraint while rejecting variable gas force disturbances and being subject to realistic power source and feedback sensing techniques. Based on this work, the following conclusions may be made:

1. Sufficiently accurate FEA models of the closer and opener magnets are developed to parameterize lower-order (albeit still nonlinear) dynamic lumped parameter models that account for magnetic saturation effects and gas force disturbances. All models are validated using experimental techniques of increasing complexity and operational realism.

2. As a means of simulating the dynamic response of the actuator system, the electromagnetic FEA results are directly incorporated with a mechanical LPM into a modular simulation environment. This LPM-FEA hybrid model provides a means of investigating the effects of external parameters on the overall actuator performance while avoiding the computational demands of a FEA. For example, the model is extended to include the influence of combustion gas forces and switched voltage waveforms. This high fidelity model is capable of predicting an entire valve actuation cycle making it instrumental in development of a comprehensive control strategy.

3. To simplify initial control hardware implementation, a testbench engine emulator was designed and fabricated. The apparatus incorporates a production-realistic cylinder head and compressed air cavity that may be electronically pressure regulated to produce transient gas force disturbances consistent with an operating engine. This unique method of testing provides an intermediate step to single cylinder engine experiments that allows for tuning and debugging in a controlled environment without the additional complications or risk of working within a research engine test cell.

4. A method for position feedback through magnetic flux and current measurements is presented and demonstrated sufficient performance for use with an estimator and closed-loop landing controller.

5. A one dimensional compressible flow model is further simplified as a strictly valve position dependent phenomenon. In doing so, it may be used in a nonlinear observer capable of cycle-by-cycle gas force disturbance estimation. Once an estimate of gas force magnitude is available, it may be compensated for through an energy recovery based feedforward method. The combined estimation and feedforward technique are demonstrated on a custom testbench experiment to provide suitable initial landing control conditions for a closed-loop landing controller to successfully open an exhaust actuator.

6. A flatness-based closed loop landing controller is demonstrated both in simulation and experiment to exponentially track predefined reference trajectories. The trajectories are parameterized using B-spline basis functions and optimized subject to practical motion and voltage constraints. Through simulation, the flatness-controller is shown to exhibit superior performance with respect to impact speed, transition time, parameter variations and input saturation when compared to LTI and PI based controllers.

7. Both the feedforward and nonlinear landing controllers are successfully demonstrated while subject to subject to practical physical constraints and gas force disturbances using the aforementioned feedback sensing and disturbance identification techniques.

8. The method of disturbance characterization, identification and control techniques are sufficiently generic to be applied to other valve actuator types.

8.1 Further Research

In order to further enhance the proposed control process and continue on the path of engine implementation, the following highlights possible areas of future work.

8.1.1 Engine Implementation

1. Evaluation of the proposed control scheme on an operating single cylinder research engine. Work includes coordination of the intake and exhaust valve controllers with the engine control unit, online diagnostics and error handling and further performance evaluation.

8.1.2 Control Development

1. To address the issue of compensating for slowly varying system parameters (such as friction and spring stiffness) a method of online parameter estimation could be developed. The disturbance observer presented is not expected to necessarily compensate for such changes due to the way such parameters interact with the flatness based landing control law.

2. Provided sufficient computational resources are available, the presented control strategy could be augmented with an adaptive scheme that adjusts feedback gains, open-loop feedforward control parameters (closer) or compensates for slowly time varying model parameters, such as changes in viscosity.

3. The landing controller used in this study tracks only one set of predefined trajectories. Improved landing performance and efficiency could likely be achieved if a wider variety of trajectories were available or generated recursively online, again subject to available computational resources.

8.1.3 Alternative Actuators

1. With recent advancements of motor driven and hydraulic valve actuators, a survey and categorization of various potential prototype candidates could provide decisive insight for which technology is most likely to prove superior with respect to efficiency, manufacturing / implementation cost and performance.

Bibliography

[A. Warburton et al., 2005] A. Warburton, L. F., Scott, J., Butler, N., and Wygnanki, W. (2005). Intelligent Valve Actuation (IVA) System for Gasoline and Diesel Engines. *SAE paper 2005-01-0772*.

[Alexander, 2006] Alexander, D. (2006). Valeo pushes engine valves. *SAE Automotive Engineering International*, page 42.

[Allen and Law, 2002] Allen, J. and Law, D. (2002). Production electro-hydraulic variable valve-train for a new generation of I.C. engines. *SAE paper 2002-01-1109*.

[Amato and Meuller-Heiss, 2001] Amato, G. and Meuller-Heiss, M. (2001). Power stage partitioning for E-VALVE applications. *SAE paper 2001-01-0239*.

[ANSYS Inc., 2005] ANSYS Inc. (2005). Ansys theory reference. *Release 10*.

[Ashley, 2003] Ashley, S. (2003). Artificial muscles. *Scientific American*.

[Atkins and Koch, 2003] Atkins, M. and Koch, C. (2003). A well-to-wheel comparison of several powertrain technologies. *SAE paper 2003-01-0081*.

[Barros da Cunha et al., 2000] Barros da Cunha, S., Hedrick, J., and Pisano, A. (2000). Variable valve timing by means of a hydraulic actuation. *SAE paper 2000-01-1220*.

[Blair, 1999] Blair, G. (1999). *Design and Simulation of Four-Stroke Engines*. Society of Automotive Engineers.

[Boor, 1978] Boor, C. D. (1978). *A Practical Guide to Splines*. Springer-Verlag, New York.

[Borgmann et al., 2004] Borgmann, K., Frhlich, K., Hall, W., Hofmann, R., Melcher, T., and Bock, C. (2004). The High-Performance Powertrain of the X5 4.8is. *SAE paper 2004-08-0100*.

[Braune et al., 2006] Braune, S., Liu, S., and Mercorelli, P. (2006). Design and control of an electromagnetic valve actuator. *2006 IEEE CCA/CACSD/ISIC Conference*, pages 1657–1662.

[Butzmann and Melbert, 2003] Butzmann, S. and Melbert, J. (2003). Method for controlling an electromechanical actuator. *US Patent 6,648,297*.

[Butzmann et al., 2000] Butzmann, S., Melbert, J., and Koch, A. (2000). Sensorless control of electromagnetic actuators for variable valve train. *SAE paper 2000-01-1225*.

[C. R. Ferguson, 2000] C. R. Ferguson, A. T. K. (2000). *Internal Combustion Engines*. John Wiley and Sons, Inc.

[Canada, 2005] Canada, E. (2005). Canada's Greenhouse Gas Inventory: 1990-2003. Technical report.

[Çengel and Boles, 1993] Çengel, Y. and Boles, M. (1993). *Thermodynamics: An Engineering Approach*. McGraw-Hill, 2nd edition.

[Chang et al., 2002] Chang, W. S., Parlikar, T. A., Seeman, M. D., Perreault, D. J., Kassakian, J. G., and Keim, T. A. (October 2002). A new electromagnetic valve actuator. *IEEE Workshop on Power Electronics in Transportation, Auburn Hills, MI*, pages 109–118.

[Chaniotakis and Cory, 2006] Chaniotakis, M. and Cory, D. (2006). Op amp (cont.); active filters; superdiode, log, antilog filters. In *Course 6.071J, Introduction to Electronics, Signals, and Measurement*, number 30 in Op Amp Lecture Notes. Massachusetts Institute of Technology OpenCourseWare.

[Chen et al., 2005] Chen, L., Mercorelli, P., and Liu, S. (2005). A Kalman Estimator for Detecting Repetitive Disturbances. *2005 American Control Conference*, pages 1631–1636.

[Chillet and Voyant, 2001] Chillet, C. and Voyant, J. (2001). Design-oriented analytical study of a linear electromagnetic acutator by means of a reluctance network. *IEEE Trans. Magn.*, 37:3004–3011.

[Chladny, 2003] Chladny, R. (2003). Modeling and simulation of automotive gas exchange valve solenoid actuators. *M.Sc. thesis, Dept. Mechanical Engineering, University of Alberta*.

[Chladny and Koch, 2006a] Chladny, R. and Koch, C. (2006a). A Magnetic Flux-Based Position Sensor for Control of an Electromechanical VVT Actuator. *2006 American Control Conference*, pages 3979–3984.

[Chladny and Koch, 2007] Chladny, R. and Koch, C. (2007). Flatness-Based Tracking of an Electromechanical VVT Actuator with Disturbance Observer Feed-Forward Compensation. *Manuscript accepted from publication in IEEE Trans. Contr. Syst. Technol.*

[Chladny and Koch, 2006b] Chladny, R. and Koch, C. (October 2006b). Flatness-Based Tracking of an Electromechanical VVT Actuator with Magnetic Flux Sensor. *2006 IEEE CCA/CACSD/ISIC Conference*, pages 1663–1668.

[Chladny et al., 2005] Chladny, R., Koch, C., and Lynch, A. (2005). Modeling automotive gas-exchange solenoid valve actuators. *IEEE Trans. Magn.*, 41:1155–1162.

[Chung, 2005] Chung, S. (2005). Flatness-based voltage end control of a gas exchange solenoid actuator for IC engines. *M.Sc. thesis, Dept. Mechanical Engineering, University of Alberta.*

[Chung et al., 2007] Chung, S., Koch, C., and Lynch, A. (2007). Flatness-based feedback control of an automotive solenoid valve. *To be published in IEEE Trans. Contr. Syst. Technol.*

[Clark et al., 2005] Clark, R., Jewell, G., Forrest, S., Rens, J., and Maerky, C. (2005). Design Features for Enhancing the Performance of Electromagnetic Valve Actuation Systems. *IEEE Trans. Magn.*, 41:1163–1168.

[Cope and Wright, 2006] Cope, D. and Wright, A. (2006). Electromagnetic Fully Flexible Valve Actuator. *SAE paper 2006-01-0044.*

[Corless et al., 1996] Corless, R., Gonnet, G., Hare, D., Jeffrey, D., and Knuth, D. (1996). On the Lambert W function. *Advances in Computational Mathematics*, 5:329–359.

[Deng and Nehl, 1998] Deng, F. and Nehl, T. W. (1998). Analytical modeling of eddy-current losses caused by pulse-width-modulation switching in permanent-magnet brushless direct-current motors. *IEEE Transactions on Magnetics*, 34(5):3728–3736.

[dSPACE GmBH, 2003] dSPACE GmBH (2003). DS1103 PPC Controller Board Features Release 4.0.

[Dugdale et al., 2005] Dugdale, P., Rademacher, R., Price, B., Subhedar, J., and Duguay, R. (2005). Ecotec 2.4L VVT: A Variant of GMs Global 4-Cylinder Engine. *SAE paper 2005-01-1941*.

[Energy Information Agency (EIA), 2006] Energy Information Agency (EIA) (2006). Global Oil Consumption. http://www.eia.doe.gov.

[Euler, 1779] Euler, L. (1989 (orig. date 1779)). De serie lambertina plurismique eius insignibus proprietatibus. *Leonhardi Euleri Opera Omnia, Ser. 1 Opera Mathematica, Bd 6*.

[Eyabi, 2003] Eyabi, P. (2003). Modeling and sensorless control of solenoid actuators. *Ph.D. thesis, Dept. Mechanical Engineering, Ohio State University*.

[Eyabi and Washington, 2006a] Eyabi, P. and Washington, G. (2006a). Modeling and sensorless control of an electromagnetic valve actuator. *Mechatronics*.

[Eyabi and Washington, 2006b] Eyabi, P. and Washington, G. (2006b). Nonlinear Modeling of an Electromagnetic Valve Actuator. *SAE paper 2006-01-0043*.

[Flierl and Klüting, 2000] Flierl, R. and Klüting, M. (2000). The third generation of valvetrains - New fully variable valvetrains for throttle-free load control. *SAE paper 2000-01-1227*.

[Fliess et al., 1992] Fliess, M., Lévine, J., Martin, P., and Rouchon, P. (1992). On differentially flat nonlinear systems. *Proceedings of the IFAC-Symposium NOLCOS 1992, Bordeaus, France*, pages 408–412.

[Fliess et al., 1994] Fliess, M., Levine, J., Martin, P., and Rouchon, P. (1994). Nonlinear control and Lie-Backlund transformation: Toward a new differential standpoint. *Proc. 33rd IEEE Conf. Decision and Control*, pages 339–344.

[Fliess et al., 1995] Fliess, M., Lévine, J., Martin, P., and Rouchon, P. (1995). Flatness and defect of non-linear systems: Introductory theory and examples. *Int. J. Control*, 61(6):1327–1361.

[Fliess et al., 1999] Fliess, M., Lévine, J., Martin, P., and Rouchon, P. (1999). A Lie-Bäcklund approach to equivalence and flatness of nonlinear systems. *IEEE Trans. Auto. Contr.*, 44(5):922–937.

[Franklin et al., 1998] Franklin, G., Powell, D., and Workman, M. (1998). *Digital Control of Dynamic Systems*. Addison Wesley.

[Gecim, 1993] Gecim, B. (1993). Analysis of a lost-motion-type hydraulic system for variable valve actuation. *SAE paper 930822*.

[Giglio et al., 2002] Giglio, V., Iorio, B., Police, G., and di Gaeta, A. (2002). Analysis of advantages and of problems of electromechanical valve actuators. *SAE paper 2002-01-1105*.

[Gill et al., 1981] Gill, P. E., Murray, W., and Wright, M. H. (1981). *Practical Optimization*. Academic Press, London.

[Gladel et al., 1999] Gladel, P., Kreitmann, F., Meister, O., Stolk, T., and Gaisberg, A. V. (1999). Aktor zur elektromagnetischen Ventilsteuerung. *German Patent Application DE19961608 A1*.

[Golovatai-Schmidt et al., 2004] Golovatai-Schmidt, E., Schwarzenthal, D., Geiger, U., Haas, M., and Scheidt, M. (2004). Technologies for variable valve trains; a contribution to modern S.I. engines. *SAE paper 2004-34-0005*.

[Gottschalk, 2006] Gottschalk, B. (2006). OICA President Gottschalk: Automotive industry is a key sector with a high rate of innovation worldwide. *International Organization of Motor Vehicle Manufacturers (OICA)*.

[Gould et al., 1991] Gould, L., Richeson, W., and Erickson, F. (1991). Performance evaluation of a camless engine using valve actuators with programmable timing. *SAE paper 910450*.

[Griffiths, 1999] Griffiths, D. (1999). *Introduction to Electrodynamics*. Prentice Hall.

[Gunselmann and Melbert, 2003] Gunselmann, C. and Melbert, J. (2003). Improved robustness and energy consumption for sensorless electromagnetic valve train. *SAE paper 2003-01-0030*.

[Hara et al., 2000] Hara, S., Hidaka, A., Tomisawa, N., Takemura, S., and Nohara, T. (2000). Application of a variable valve event and timing system to automotive engines. *SAE paper 2000-01-1224*.

[Hartwig et al., 2005] Hartwig, C., Josef, O., and Gebauer, K. (2005). Dedicated intake actuator for electromagnetic valve trains. *SAE paper 2005-01-0773*.

[Haskara et al., 2004] Haskara, I., Kokotovic, V., and Mianzo, L. (2004). Control of an elctro-mechanical valve actuator for a camless engine. *International Journal of Robust and Nonlinear Control*, 14:561–579.

[Henry, 2001] Henry, R. (2001). Single-cylinder engine tests of a motor-driven variable-valve actuator. *SAE paper 2001-01-0241*.

[Heywood, 2006] Heywood, J. (2006). Fueling Our Transportation Future. *Scientific American*, pages 60–63.

[Heywood, 1988] Heywood, J. B. (1988). *Internal Combustion Engine Fundamentals*. McGraw-Hill.

[Hitachi, 2003] Hitachi (2003). Private Communication.

[Hoffmann et al., 2003] Hoffmann, W., Peterson, K., and Stefanopoulou, A. (2003). Iterative learning control for soft landing of electromechanical valve actuator in camless engines. *IEEE Trans. Contr. Syst. Technol.*, 11:174–184.

[Ilic'-Spong et al., 1987] Ilic'-Spong, M., Marino, R., Peresada, S., and Taylor, D. (1987). Feedback linearizing control of switched reluctance motors. *IEEE Trans. Auto. Contr.*, 32(5):371–379.

[Isidori, 1997] Isidori, A. (1997). *Nonlinear Control Systems*. Springer Verlag.

[Kawase et al., 1991] Kawase, Y., Kikuchi, H., and Ito, S. (1991). 3-D nonlinear transient analysis of dynamic behavior of the clapper type DC magnet. *IEEE Trans. Magn.*, 27(5):4238–4241.

[Kim et al., 1997] Kim, D., Anderson, M., Tsao, T., and Levin, M. (1997). Dynamic model of a springless electrohydraulic valvetrain. *SAE paper 970248*.

[Koch et al., 2002] Koch, C., Lynch, A., and Chladny, R. (2002). Modeling and control of solenoid valves for internal combustion engines. *2nd IFAC Conf. on Mechatronic Systems*, pages 317–322.

[Koch et al., 2004] Koch, C., Lynch, A., and Chung, S. (2004). Flatness-based automotive solenoid valve control. *6th IFAC Symp. Nonlin. Contr. Systems (NOLCOS)*, pages 1091–1096.

[Konrad, 1998] Konrad, R. (1998). Verfahren zur Bewegungssteuerung für einen ankers eines elektromagnetishen Aktuators. *German Pat. Appl. 19834548 A1.*

[Koopmans et al., 2003] Koopmans, L., Ström, H., Lundgren, S., Backlund, O., and Denbratt, I. (2003). Demonstrating a SI-HCCI-SI Mode Change on a Volve 5-Cylinder Electronic Valve Control Engine. *SAE paper 2003-01-0753*.

[Kreyszig, 1993] Kreyszig, E. (1993). *Advanced Engineering Mathematics*. John Wiley & Sons.

[Lambert, 1758] Lambert, J. H. (1758). Observationses variae in mathesin puram. *Acta Helvetica, physicomathematico-anatomico-botanico-medica, Basel*, 3:128–168.

[Lambrechts et al., 2004] Lambrechts, P., Boerlage, M., and Steinbuch, M. (2004). Trajectory planning and feedforward design of electromechanical motion systems. *Control Engineering Practice*, 13:145–157.

[Lancefield et al., 1993] Lancefield, T., Gayler, R., and Chattopadhay, A. (1993). The practical application and effects of a variable event valve timing system. *SAE paper 930825*.

[Landau and Lifshitz, 1984] Landau, L. D. and Lifshitz, E. M. (1984). *Electrodynamics of Continuous Media*. 2nd edition.

[Lequesne, 1990] Lequesne, B. (1990). Fast acting, long-stroke solenoids with two springs. *IEEE Trans. Ind. Applicat.*, 26:848–856.

[Lequesne, 1996] Lequesne, B. (1996). Permanent magnet linear motors for short strokes. *IEEE Trans. Ind. Applicat.*, 32:161–168.

[Lequesne, 1999] Lequesne, B. (1999). Design and optimization of two-spring linear actuators. *European Trans. on Electrical Power*, 9:377–383.

[Lévine, 2004] Lévine, J. (2004). On flatness necessary and sufficient conditions. *6th IFAC Symp. Nonlin. Contr. Systems (NOLCOS)*, pages 125–130.

[Lévine et al., 1996] Lévine, J., Lottin, J., and Ponsart, J.-C. (1996). A nonlinear approach to the control of magnetic bearings. *IEEE Trans. Contr. Syst. Technol.*, 4(5):524–544.

[Li and McEwan, 1993] Li, E. and McEwan, P. (1993). 3d to 2d transformation solution of transient eddy current electromagnetic fields in an actuator. *IEEE Transactions on Magnetics*, 29:1733–1736.

[Ljung, 1987] Ljung, L. (1987). *System Identification: Theory for the User*. Prentice-Hall, Englewood Cliffs, NJ.

[Ljung, 2004] Ljung, L. (2004). *System Identification Toolbox for use with Matlab: User's Guide Version 6*. MathWorks, Inc., Natick, Mass.

[Löewis, 2002] Löewis, J. (2002). *Flachheitsbasierte Trajektorienfolgeregelung elektromechanischer Systeme*. PhD thesis, TU-Dresden.

[Löewis et al., 2000] Löewis, J., Rudolph, J., and Woittennek, F. (2000). Discrete-time flatness-based control of an electromagnetically levitated rotating shaft. *Proc. Math. Theory Networks Systems (MTNS 2000)*.

[Longstaff and Holmes, 1975] Longstaff, K. and Holmes, S. (1975). Internal combustion engines. *U.S. Patent No. 3,882,833*.

[Lynch et al., 2003] Lynch, A., Koch, C., and Chladny, R. (2003). Nonlinear observer design for sensorless electromagnetic actuators. *3rd International Conference on Dynamics of Continuous, Discrete and Impulsive Systems, May 2003*.

[Macián et al., 2004] Macián, V., Luján, J. M., Bermúdez, V., and Guardiola, C. (2004). Exhaust pressure pulsation observation from turbocharger instantaneous speed measurement. *Meas. Sci. Technol.*, pages 1185–1194.

[Martin, 1992] Martin, P. (1992). *À l'étude des systèmes diffèrentielement plats*. PhD thesis, École des Mines de Paris.

[Martin et al., 1997] Martin, P., Murray, R., and Rouchon, P. (1997). *Flat Systems*.

[Maxwell, 1864] Maxwell, J. C. (1864). A Dynamical Theory of the Electromagnetic Field. *Philosophical Transactions of the Royal Society of London*, 155:459–512.

[Melgoza and Rodger, 2002] Melgoza, E. and Rodger, D. (2002). Comparison of table models of electromagnetic actuators. *IEEE Trans. Magn.*, 38:953–956.

[Mercorelli et al., 2003] Mercorelli, P., Lehmann, K., and Liu, S. (2003). Robust flatness based control of an electromagnetic linear actuator using adaptive PID controller. *Proceedings of the IEEE Decision and Control Conference*, pages 3790–3795.

[Mercorelli and Liu, 2005] Mercorelli, P. and Liu, S. (2005). Model predictive control of transistor pulse converter for feeding electromagnetic valve actuator with energy storage. *Proceedings of the 44th IEEE Conference on Decision and Control, and the European Control Conference*, pages 6794–6799.

[Mianzo et al., 2005] Mianzo, L., Newton, S., Z., and Popovic (2005). Integrated control and power electronics for an electro-mechanical valve actuation system. *2005 IEEE/ASME International Conference on Advanced Intelligent Mechatronics*, pages 485–491.

[Micro-Epsilon, 2007] Micro-Epsilon (2007). Internal communication.

[Milam, 2003] Milam, M. (2003). *Real-Time Optimal Trajectory Generation for Constrained Dynamical Systems*. PhD thesis, University of Alberta.

[Montanari et al., 2004] Montanari, M., Ronchi, F., Rossi, C., and Tonielli, A. (2004). Control of a camless engine electromechanical actuator: Position reconstruction and dynamic performance analysis. *IEEE Trans. Ind. Electron.*, 51:299–311.

[Moro et al., 2001] Moro, D., Ponti, F., and Serra, G. (2001). Thermodynamic analysis of variable valve timing infuence on SI engine efficiency. *SAE paper 2001-01-0667*.

[Murray et al., 1995] Murray, R., Rathinam, M., and Sluis, W. (1995). Differential Flatness of Mechanical Systems: A Catalog of Prototype Systems. *1995 ASME Intl Mech Eng Congress and Expo*.

[Nakamura et al., 2001] Nakamura, M., Hara, S., Yamada, Y., Takeda, K., Okamoto, N., Hibi, T., Takemura, S., and Aoyama, S. (2001). A continuous variable valve event and lift control device (VEL) for automotive engines. *SAE paper 2001-01-0244*.

[Niţu et al., 2005] Niţu, C., Grămescu, B., and Niţu, S. (2005). Application of electromagnetic actuators to a variable distribution system for automobile engines. *Journal of Materials Processing Technology*, 161:253–257.

[Ohata and Butts, 2005] Ohata, A. and Butts, K. (2005). Towards a concurrent engine system design methodology. *2005 American Control Conference*, pages 3296–3302.

[OICA, 2005a] OICA (2005a). World Motor Vehicle Production by Country and Type: Cars 2004 - 2005. *International Organization of Motor Vehicle Manufacturers (OICA)*.

[OICA, 2005b] OICA (2005b). World motor vehicle production by country and type: Light commercial vehicles 2004 - 2005. *International Organization of Motor Vehicle Manufacturers (OICA)*.

[Parlikar et al., 2005] Parlikar, T., Chang, W., Qiu, Y., Seeman, M., Perreault, D., Kassakian, J., and Keim, T. (2005). Design and experimental implementation of an

electromagnetic engine valve drive. *IEEE/ASME Transactions on Mechatronics*, 10:482–494.

[Pawlak and Nehl, 1988] Pawlak, A. M. and Nehl, T. W. (1988). Transient finite element modeling of solenoid actuators: The coupled power electronics, mechanical and magnetic field problem. *IEEE Transaction on Magnetics*, 24(1):270–273.

[Payne, 1899] Payne, D. (1899). Electically controlled valve gear for gas or other motors. *U.S. Patent 623,821*.

[Peterson, 2005] Peterson, K. (2005). Control methodologies for fast and low impact electromagnetic actuators for engine valves. *Ph.D. Thesis, University of Michigan*.

[Peterson et al., 2006] Peterson, K., Grizzle, J., and Stefanopoulou, A. (2006). Nonlinear control for magnetic levitation of automotive engine val(v)es. *IEEE Trans. Contr. Syst. Technol.*, 14(2):346–354.

[Peterson and Stefanopoulou, 2004] Peterson, K. and Stefanopoulou, A. (2004). Extremum seeking control for soft landing of an electromechanical valve actuator. *Automatica*.

[Peterson et al., 2002] Peterson, K., Stefanopoulou, A., Megli, T., and Haghgooie, M. (2002). Output observer based feedback for soft landing of electromechanical camless valvetrain actuator. *2002 American Control Conference*, pages 1413–1418.

[Picard and Fang, 2003] Picard, A. and Fang, H. (2003). Methods to determine the density of moist air. *IEEE Trans. Instrum. Meas.*, 52:504–507.

[Piron et al., 1999] Piron, M., Sangha, P., Reid, G., Miller, T., D.Ionel, and Coles, J. (1999). Rapid computer-aided design method for fast-acting solenoid actuators. *IEEE Trans. Ind. Applicat.*, 35:991–999.

[Pischinger and Kreuter, 1984] Pischinger, F. and Kreuter, P. (1984). Electromagnetically operating actuator. *U.S. Patent No. 4,455,543*.

[Pischinger et al., 2000] Pischinger, M., Salber, W., van der Staay, F., Baumgarten, H., and Kemper, H. (2000). Benefits of the electromechanical valve train in vehicle operation. *SAE paper 2000-01-1223*.

[Prieto et al., 2005] Prieto, R., Oliver, J., and Cobos, J. (2005). Study of non-axisymmetric magnetic components by means of 2D FEA solvers. *IEEE Power Electronics Specialists Conference (PESC)*, pages 1074–1079.

[Qiuz et al., 2004] Qiuz, Y., Parlikarz, T., Chang, W., Seemanz, M., Keimy, T., Perreaulty, D., J., and Kassakian (2004). Design and experimental evaluation of an electromechanical engine valve drive. *Proceedings of the IEEE Power Electronics Specialists Conference*, pages 4838–4843.

[Rathinam and Sluis, 1995] Rathinam, M. and Sluis, W. (1995). A test for differential flatness by reduction to single input systems. *CDS Technical Report - CDS95-018. California Institute of Technology*.

[Richeson and Erickson, 1989] Richeson, W. and Erickson, F. (1989). Pneumatic actuator with permanent magnet control valve latching. *U.S. Patent No. 4,852,528*.

[Ronchi and Rossi, 2002] Ronchi, F. and Rossi, C. (2002). Sensing device for camless engine electromagnetic actuators. *Proceedings of the IEEE International Conference on Industrial Electronics Control and Instrumentation (IECON)*, pages 1669–1674.

[Roschke and Bielau, 1995] Roschke, T. and Bielau, M. (1995). Verfahren zur modellbasierten Messung und Regelung von Bewegungen an elektromagnetischen Ak-

toren. *Technische Universitaet Dresden German Patent Application DE 19544207 A1.*

[Rossi and Alberto, 2001] Rossi, C. and Alberto, T. (2001). Method and device for estimating the position of an actuator body in an electromagnetic actuator to control a valve of an engine. *Magneti Marelli European Patent Application EP 1152129 A1.*

[Rossi and Tonielli, 2001] Rossi, C. and Tonielli, A. (2001). Method and device for estimating the position of an actuator body in an electromagnetic actuator to control a valve of an engine. *European Patent Application EP 1152129 A1.*

[Scacchioli, 2005] Scacchioli, A. (2005). Hybrid regulation of electromagnetic valves in automotive systems. *Ph.D. thesis, Dept. of Electrical Engineering, University of L`Aquila.*

[Schechter and Levin, 1996] Schechter, M. and Levin, M. (1996). Camless engine. *SAE paper 960581.*

[Schernus et al., 2002] Schernus, C., van der Staay, F., Janssen, H., Neumeister, J., Vogt, B., Donce, L., Estlimbaum, I., Nicole, E., and Maerky, C. (2002). Modeling of exhaust valve opening in a camless engine. *SAE paper 2002-01-0376.*

[Schmitz, 1995] Schmitz, G. (1995). Verfahren zur Regelung der Ankerauftreffgeschwindigkeit an einen elektromagnetischen Aktuator durch extrapolierende Abschätzung der Energieeinspeisung. *German Pat. Appl. 19807875 A1.*

[Schmitz and Novotny, 1965] Schmitz, N. and Novotny, D. (1965). *Introductory Electromechanics.* The Ronald Press Company.

[Shahbakhti et al., 2007] Shahbakhti, M., Lupul, R., and Koch, C. R. (2007). Predicting hcci auto-ignition timing by extending a modified knock-integral method. *SAE paper 2007-01-0222*.

[Shampine and Reichelt, 1997] Shampine, L. and Reichelt, M. (1997). The MATLAB ODE Suite. *SIAM Journal on Scientific Computing*, 18:1–22.

[Shen et al., 2006] Shen, Y., King, E., and Pfahl, U. (2006). Influences of Intake Charge Preparations on HCCI Combustion in a Single Cylinder Engine with Variable Valve Timing and Gasoline Direct Injection. *SAE paper 2006-01-3274*.

[Slotine and Li, 1991] Slotine, J. and Li, W. (1991). *Applied Nonlinear Control*. Prentice Hall.

[Song et al., 2006] Song, H., Wang, X., Ma, L., Cai1, M., and Cao, T. (2006). Design and Performance Analysis of Laser Displacement Sensor Based on Position Sensitive Detector (PSD). *4th International Symposium on Instrumentation Science and Technology (ISIST)*, 48:217–222.

[Stolk and Gaisberg, 2001] Stolk, T. and Gaisberg, A. (2001). Elektromagnetischer aktuator. *German Patent Application DE 10025491 A1*.

[Stubbs, 2000] Stubbs, A. (2000). Modeling and controller design of an electromagnetic engine valve. *Master's thesis, University of Illinois at Urbana-Champaign*.

[Sun and Cleary, 2003] Sun, Z. and Cleary, D. (2003). Dynamics and control of an electro-hydraulic fully flexible valve actuation system. *Proceedings of the American Control Conference*, 4:3119–3124.

[Tai and Tsao, 2001] Tai, C. and Tsao, T. (2001). Quite seating control design of an electromagnetic engine valve actuator. *Proc. 2001 ASME Ineternational Mechanical Engineering Congress and Exposition*.

[Tai and Tsao, 2002] Tai, C. and Tsao, T. (2002). Control of an electromechanical camless valve actuator. *Proceedings of the American Control Conference*, pages 262–267.

[Tai and Tsao, 2003] Tai, C. and Tsao, T. (2003). Control of an electromechanical actuator for camless engines. *Proc. 2003 American Control Conference*.

[Takahashi et al., 1991] Takahashi, N., Nakata, T., Fujiwara, K., and Nishimura, T. (1991). Factors affecting errors due to 2-D approximate analysis of 3-D magnetic fields with eddy currents. *IEEE Transactions on Magnetics*, 27(2):5223–5225.

[Takashi and Iwao, 1995] Takashi, D. and Iwao, M. (1995). Valve drive device for internal combustion engine and initial position setting method for valve element. *Japan Patent Application JP 0224624*.

[Theobald et al., 1994] Theobald, M., Lequesne, B., and Henry, R. (1994). Control of engine load via electromagnetic valve actuators. *SAE paper 940816*.

[Trajkovic et al., 2006] Trajkovic, S., Milosavljevic, A., Tunestål, P., and B.Johansson (2006). FPGA Controlled Pneumatic Variable Valve Actuation. *SAE paper 2006-01-0041*.

[Trout, 2001] Trout, S. (2001). Material Selection of Permanent Magnets, Considering Thermal Properties Corretly. *Electrical Insulation Conference and Electrical Manufacturing and Coil Winding Conference*, pages 365–370.

[Turner et al., 2004] Turner, J., Bassett, M., Pearson, R., Pitcher, G., and Douglas, K. (2004). New Operating Strategies Afforded by Fully Variable Valve Trains. *SAE paper 2004-01-1386*.

[van Nieuwstadt et al., 1994] van Nieuwstadt, M., Rathinam, M., and Murray, R. M. (1994). Differential flatness and absolute equivalence. *Proceedings of the 33rd Conference on Decision and Control, Lake Buena Vista, FL*, pages 326–333.

[van Nieuwstadt and Murray, 1995] van Nieuwstadt, M. J. and Murray, R. M. (1995). Approximate trajectory generation for differentially flat systems with zero dynamics. *Proceedings of the 34th Conference on Decision and Control, New Orleans, LA*, pages 4224–4230.

[Vaughan and Gamble, 1996] Vaughan, N. and Gamble, J. (1996). The modeling and simulation of a proportional solenoid valve. *ASME Dynamic Systems, Measurment and Control*, 118:120–125.

[W. Hoffmann and A. Stefanopoulou, 2001] W. Hoffmann and A. Stefanopoulou (2001). Valve position tracking for doft landing of electromechanical camless valvetrain. *Int. Federation of Automatic Control (IFAC), Advances in Automotive Control*.

[Wang et al., 2002] Wang, Y., Megil, T., Haghgooie, M., Peterson, K., and Stefanopoulou, A. (2002). Modeling and control of electromechanical valve actuator. *SAE paper 2002-01-1106*.

[Wang et al., 2000] Wang, Y., Stefanopoulou, A., Haghgooie, M., Kolmanovsky, I., and Hammoud, M. (2000). Modeling of an electromechanical valve actuator for a camless engine. *Proc. AVEC 2000. 5th Int. Symposium on Advanced Vehicle Control*.

[Weddle and Leo, 1998] Weddle, C. and Leo, D. (1998). Embedded actuation systems for camless engines. *Proceedings of the International Conference on Adaptive Structures and Technologies*.

[Wilson et al., 1993] Wilson, N., Watkins, A., and Dopson, C. (1993). Asymmetric valve strategies and their effect on combustion. *SAE paper 930821*.

[Wolters et al., 2003] Wolters, P., Salber, W., Geiger, J., and Duesmann, M. (2003). Controlled auto ignition combustion process with an electromechanical valve train. *SAE paper 2003-01-0032*.

[Woodson and Melcher, 1968] Woodson, H. and Melcher, J. (1968). *Electromechanical Dynamics Part I: Discrete Systems*. John Wiley & Sons.

[Xiang, 2002] Xiang, J. (2002). Modeling and control of a linear electro-mechanical actuator (LEMA) for operating engine valves. *IEEE Ind. Applicat. Conf.*, 3:1943–1949.

[Zeitz, 1987] Zeitz, M. (1987). The extended Luenberger observer for nonlinear systems. *Systems & Control Letters*, 9:149–156.

Appendix A

Supplemental Theory

A.1 Vector Differential Calculus Operations & Notation

The following briefly summarizes the notation used to denote mathematical operations commonly used in the electromagnetic discipline, especially with Maxwell's equations.

A.1.1 Gradient of a Scalar Function

The gradient allows the derivation of vector fields from scalar functions, the latter of which are computationally easier to handle. For example, the gradient of a scalar function $s(x, y, z)$, results in

$$\nabla s = \frac{\partial s}{\partial x}\mathbf{i} + \frac{\partial s}{\partial y}\mathbf{j} + \frac{\partial s}{\partial z}\mathbf{k} \tag{A.1}$$

where x, y and z are Cartesian coordinates. The geometric interpretation of the gradient is such that ∇s points in the direction of maximum increase of s and the magnitude $\|\nabla s\|$ gives the slope or rate of increase along the maximum direction.

A.1.2 Divergence of a Vector Field and the Laplacian Operator

A useful operation in defining field quantities is the divergence operator, $\nabla\cdot$. Consider a differentiable vector function $\mathbf{v}(x, y, z)$, where x, y and z are Cartesian coordinates and the components of $\mathbf{v}$ are given by v_1, v_2 and v_3 as:

$$\mathbf{v}(x, y, z) = v_1\mathbf{i} + v_2\mathbf{j} + v_3\mathbf{k} \tag{A.2}$$

Then the divergence of $\mathbf{v}$ may be expressed as:

$$\nabla \cdot \mathbf{v} = \left(\frac{\partial}{\partial x}\mathbf{i} + \frac{\partial}{\partial y}\mathbf{j} + \frac{\partial}{\partial z}\mathbf{k}\right) \cdot (v_1\mathbf{i} + v_2\mathbf{j} + v_3\mathbf{k}) = \frac{\partial v_1}{\partial x} + \frac{\partial v_2}{\partial y} + \frac{\partial v_3}{\partial z} \tag{A.3}$$

Note that $\nabla \cdot \mathbf{v}$ depends only on $\mathbf{v}$ and the points in space, not on the choice of coordinate system.

If a scalar function $s(x, y, z)$ is able to be differentiated twice, the divergence of a gradient may be expressed as:

$$\nabla \cdot \nabla s = \frac{\partial^2 s}{\partial x^2} + \frac{\partial^2 s}{\partial y^2} + \frac{\partial^2 s}{\partial z^2} \tag{A.4}$$

This operation is also known as the Laplacian of $s(x, y, z)$ where the Laplacian operator is denoted by ∇^2 and may be written as:

$$\nabla^2 = \Delta = \nabla \cdot \nabla = \frac{\partial^2}{\partial x^2} + \frac{\partial^2}{\partial y^2} + \frac{\partial^2}{\partial z^2} \tag{A.5}$$

The geometric interpretation of divergence is the measure of how much a vector spreads or diverges from a given point. A point of positive divergence can be thought of as a 'source'. Similarly, a negative point of divergence can be considered a 'sink'.

A.1.3 Curl of a Vector Field

Again consider a differentiable vector function $\mathbf{v}(x, y, z)$ as before. The curl of $\mathbf{v}$ in a right handed Cartesian coordinate system is then defined as:

$$\nabla \times \mathbf{v} = \left(\frac{\partial v_3}{\partial y} - \frac{\partial v_2}{\partial z}\right)\mathbf{i} + \left(\frac{\partial v_1}{\partial z} - \frac{\partial v_3}{\partial x}\right)\mathbf{j} + \left(\frac{\partial v_2}{\partial x} - \frac{\partial v_1}{\partial y}\right)\mathbf{k} \tag{A.6}$$

Although curl is defined in terms of coordinates, it is not dependant on the coordinate system. The result of the curl operation can be considered a measure of how much the vector $\mathbf{v}$ rotates about a specified point. The curl of a gradient is always zero. For any scalar function $s(x, y, z)$ that is twice differentiable

$$\nabla \times (\nabla s) = 0 \tag{A.7}$$

Thus it may be observed that gradient fields are irrotational. Similarly, the divergence of a curl is also always zero, $\nabla \cdot (\nabla \times \mathbf{v}) = 0$.

A.2 Maxwell's Equations Derived

The following entails a brief overview of the empirical laws of electricity and magnetism in order to provide a very basic derivation of Maxwell's equations.

A.2.1 Coulomb's Law

Coulomb derived an inverse squared relation from measurements he made experimentally with an electrical torsion bar.

$$\mathbf{f} = \frac{qQ\mathbf{r}}{4\pi\epsilon_0|r|^3} \tag{A.8}$$

This expression describes the force, $\mathbf{f}$ [Newtons], experienced by a point charge, q [coulombs], when brought towards another point charge of like sign, Q. Where $\mathbf{r}$[m], is a position vector from one point charge to another, and ϵ_0 is the free space permittivity constant ($8.854\text{x}10^{-12}\frac{F}{m}$). Similarly, the electric field intensity, $\mathbf{E}$ [volts per meter], of charge Q may be expressed as:

$$\mathbf{E}(\mathbf{r}) = \frac{Q\mathbf{r}}{4\pi\epsilon_0|r|^3} \tag{A.9}$$

Since electric charge occurs in multiples of the elementary unit of charge, $1.60\text{x}10^{-19}$C, charge density may be expressed as:

$$\rho_e(\mathbf{r}) = \lim_{\delta V \to 0} \frac{1}{\delta V} \sum_i q_i \tag{A.10}$$

which expresses a continuum model of a sum of charges at a point located by $\mathbf{r}$ enclosed by a small volume, δV. Where δV is considered infinitesimally small when compared to the considered system's dimensions yet large enough to contain a large number of charges, q_i.

In such instances, one may assume that all charges on such a volume will experience the same electric field. Thus, for the repulsion force of a body containing a number of charges one may average the force to derive an electric force density, $\mathbf{F}$. Where,

$$\mathbf{F} = \rho_e\mathbf{E} \tag{A.11}$$

A.2.2 Gauss's Law of Electricity

An often more convenient way to relate charge density and electric field intensity is through the integral form of Gauss's Law, which is implied by Coulombs law,

$$\oint_S \epsilon_0 \mathbf{E} \cdot \mathbf{n} da = \int_V \rho_e dV \tag{A.12}$$

where $\mathbf{n}$ is the unit vector normally directed from area S which encloses volume V. It can be seen that in the case of a point charge, Equation A.12 reverts to that of Coulombs law, Equation A.8 where the surface S may be taken as a sphere centered at the location of point charge Q. A differential form of Equation A.12 may be obtained by applying the divergence theorem,

$$\oint_S \mathbf{v} \cdot \mathbf{n} da = \int_V \nabla \cdot \mathbf{v} dV \tag{A.13}$$

to result in the following:

$$\int_V (\nabla \cdot \epsilon_0 \mathbf{E} - \rho_e) dV = 0 \tag{A.14}$$

Since the integrated volume is arbitrary, one may state:

$$\nabla \cdot \mathbf{E} = \frac{\rho_e}{\epsilon_0} \tag{A.15}$$

Which is in fact one of Maxwell's equations. Both Oersted and Gauss experimented with electromagnetism and its forces upon objects such as a compass needle.

A.2.3 Gauss's Law for Magnetism

Gauss's law for magnetism is a formalized means of stating the observation that unlike electricity, free magnetic poles do not exist (at least they have yet to be observed). This implies that the net magnetic flux passing through any closed surface, S, is always zero.

$$\Phi_B = \oint_S \mathbf{B} \cdot \mathbf{n} da = 0 \tag{A.16}$$

Or, again recognizing the surface is arbitrary and applying the divergence theorem, the relation may be expressed in differential format as,

$$\nabla \cdot \mathbf{B} = 0 \tag{A.17}$$

This relation represents another of Maxwell's equations.

A.2.4 Conservation of Charge

Observed experimental evidence has shown that electric charge is always conserved. For example, an equal and opposite charge is observed on a previously neutral atom when an electron is removed. When this concept is applied to an arbitrary volume, V, enclosed by a smooth surface, S, any flow rate of charge out of the surface must be balanced by the rate of which charge decreases in the volume. A continuum variable, current density, $\mathbf{J}$ $[\frac{C}{m^2 s}]$ is often used to express this charge flow rate. The sign indicates direction of flow of positive charge and its magnitude indicates the net rate of charge flow per unit area. Mathematically this observation may be expressed as:

$$\oint_S \mathbf{J} \cdot \mathbf{n} da = -\frac{d}{dt} \int_V \rho_e dV \tag{A.18}$$

or, in differential format (again utilizing the divergence theorem) as:

$$\nabla \cdot \mathbf{J} + \frac{\partial \rho_e}{\partial t} = 0 \tag{A.19}$$

A.2.5 Ampére's Law

As a means to relate the magnetic effect of time varying electric fields and currents. Maxwell extended the original expression by adding the far right hand side term, known as displacement current, to account for influence of time varying electric fields displacing electrons and thus generating current.

$$\nabla \times \mathbf{B} = \mu_0 \mathbf{J} + \mu_0 \frac{\partial \epsilon_0 \mathbf{E}}{\partial t} \tag{A.20}$$

The later format is another of Maxwell's equations.

A.2.6 Faraday's Law of Induction

Faraday discovered that time varying magnetic fields induce an emf. He infered from this that time varying magnetic fields must produce time varying electric fields. Experimentally this was performed by thrusting a permanent bar magnet through a loop of wire and observing the induced current. The emf was equal to the change of flux

$$\varepsilon = \oint \mathbf{E} \cdot d\mathbf{l} = -\frac{d\Phi}{dt} \tag{A.21}$$

And **E** is related to a change B by the equation

$$\oint_C \mathbf{E} \cdot d\mathbf{l} = -\frac{d}{dt} \int_S \mathbf{B} \cdot \mathbf{n} da \tag{A.22}$$

Or by applying Stoke's theorem, in differential form as:

$$\nabla \times \mathbf{E} = -\frac{\partial \mathbf{B}}{\partial t} \tag{A.23}$$

The latter format is known as Faraday's Law and completes the set of Maxwell's equations.

A.3 Other Relations of Interest

The following describes other relations which may be referred to through the course of this work.

A.3.1 Biot-Savart Law

The Biot-Savart Law is a means to assist in calculating the field produced by an arbitrary current density. As can be imagined, the solution to many of the aforementioned equations may be challenging even for relatively simple geometry. The Biot-Savart Law discritizes a current density into elements which may be individually solved to calculate the field, $d\mathbf{B}$, due to each current element, $d\mathbf{l}$.

A.3.2 Lenz's Law

Lenz's Law is a means by which to predict the direction of induced currents by means of energy conservation. Although, the same results may be achieved by scrutinizing Faraday's law, Lenz's law is perhaps a more intuitive procedure for predicting currents in a closed loop produced by a changing magnetic field. Essentially it states that the induced current will appear in a direction that opposes the change that produced it.

A.3.3 Lorentz Force

The Lorentz force, f, is defined as the force imposed on a test charge, q, that is moving with velocity, v while moving through electric field, E and magnetic field, B. This relation is quantified by:

$$\mathbf{f} = q\mathbf{E} + q\mathbf{v} \times \mathbf{B} \tag{A.24}$$

A single moving charge, $q\mathbf{v}$ may be expressed as a current. Thus the first term is a force on a static charge and the second term is the force on a current. As mentioned earlier, we are generally not concerned with electrostatics. Further, when considering the average contribution the force may be expressed as current density and the magnetic field as shown:

$$\mathbf{F} = \mathbf{J_f} \times \mathbf{B} \tag{A.25}$$

A.4 Magnetic Materials

When considering the design of electromagnetic actuators, how a material behaves in the presence of a magnetic field is of great importance. The orbiting electrons of a particular atom within any material cause small but significant electric currents, which in turn cause small magnetic fields. The spin of the electron about its own axis also contributes to this current. The way in which the atom's magnetic fields interact with each other determines the overall magnetic behavior. For example, the fields produced by the electron spins of most materials are random and cancel out. Other materials may have regions which have aligned spins and thus an overall net field exists. The orientations are susceptible to external fields where the net magnetic field may be decreased, or enhanced depending on the new orientation. Generally, there are three major classifications of magnetic materials, diamagnetic, paramagnetic and ferromagnetic. Diamagnetic materials are characterized by resisting an applied external field. The effect is slight, but still measurable. For example, a typical relative permeability of a diamagnetic material may be 0.9. Paramagnetic materials align so that there is a slight but measurable increase in the applied field. A typical relative permeability may be on the order of 1.1. Ferromagnetic material possesses the ability to greatly enhance an external field, with relative permeabilities ranging from 100 to

1,000,000. As the regions of common orbital spin align, the external field is intensified, after which, the material is said to be saturated and then behaves as though no material were present, or takes on permeability of free space. This saturation limit is of great concern when controlling solenoid actuators as the armature material will most likely be saturated at low air gaps, where accurate control is most desired. The effect is also significant as the transition from high permeability to free space permeability is nonlinear, making accurate analytic performance estimates extremely challenging. It should also be noted that once magnetized, the aligned regions do not instantaneously return to their initially demagnetized state, nor does flux density follow the same magnetization path. This phenomena is known as magnetic hysteresis. Although this may complicate even a low frequency analysis, it is often of greater concern with the design of higher frequency devices such as transformers. Hysteresis is often negligible in systems with air gaps, especially at low flux densities, as the energy required to magnetize the gap is several orders greater than any losses incurred through magnetic domain realignment. The field strength required to return a material to a demagnetized space is referred to as coercive force. Ferromagnetic permeability is also sensitive to temperature, with a sharp drop at what is referred to as the Curie temperature. This temperature typically corresponds with a phase change (change in crystalline structure).

Despite the complex properties of ferromagnetic materials, their high permeability allows flux to be constrained to a predefined path just as one would use wires to connect an electrical circuit. In fact, in many circumstances magnetic systems may be analyzed as a circuit problem rather than a field problem as discussed in Section 3.3.

A.5 Eddy Currents

Eddy currents are characterized as local circulating currents which exist in the core material. These are physically existing currents produced within the material due to a time varying core flux. They may be thought of as a short circuit consisting of coil wrapped around the external core material path in that the change in flux induces a current which in turn generates its own magnetic flux in the opposite sense (obeying Lenz's law) and ultimately opposes the change or rise of flux of the overall circuit. Thus, the observed flux rise or magnetization curve will be lower than the that of the static case. The energy difference between the static and rapid field buildup is defined through resistive losses and hence heating. In summary, the two effects of eddy currents are: an internal MMF is generated which tends to counteract the applied MMF, an irreversible heating loss of energy with the i^2 losses in the core. Thus greater changes in flux tend to generate more losses. A widening of the hysteresis loop is an indication of the eddy current magnitudes. They may be minimized by using materials with low conductivity and by laminating the core structure (through thin sheets or sintered powder metallurgy techniques). In the actuator studied, laminations are used to increase the circulating path length thereby breaking the eddy current paths into many smaller loops with lower magnitude and subsequently reduce the counter flux generated. Eddy currents are not to be confused with the electrodynamic Amperian currents generated by electron spin which are used to explain material magnetism. The eddy current counter flux tends to constrain the applied or useful flux path density to the edge of the material, also know as the skin effect. The skin depth, δ may be approximated as a function of the material conductivity, σ, excitation frequency f, material permeability, μ through the following relation:

$$\delta = \frac{1}{\sqrt{\pi \mu \sigma f}} \qquad \text{[Landau and Lifshitz, 1984]} \tag{A.26}$$

A.6 The Lambert W Function

The solution of a feedforward current trajectory as well as the parametrization of the coil current state, i, with the flat output, y, and respective time derivatives, requires the algebraic solution of of the Lambert W function [Corless et al., 1996] as discussed in Chapter 5. This expression was first introduced by Euler in 1779 [Euler, 1779] after studying Lambert's transcendental equation in [Lambert, 1758]. This multi-valued relation is defined to be the inverse of the function $w \mapsto we^w = z$, $z \in \mathbb{C}$. It thus provides a solution to:

$$W(z)e^{W(z)} = z \tag{A.27}$$

When restricted to only real, negative arguments, Equation (A.27) has a unique real solution represented by the principal branch, W_0, as shown in Figure A.1. For all real z in the range $0 > z > -1/e$, the function is multi-valued with two real solutions that are represented by the W_0 and W_{-1} branches. For $i \geq 0$, only the principal real branch, $W_{-1}(z)$, is considered since the argument z varies from -1 to -∞ in all instances that it is invoked in this study.

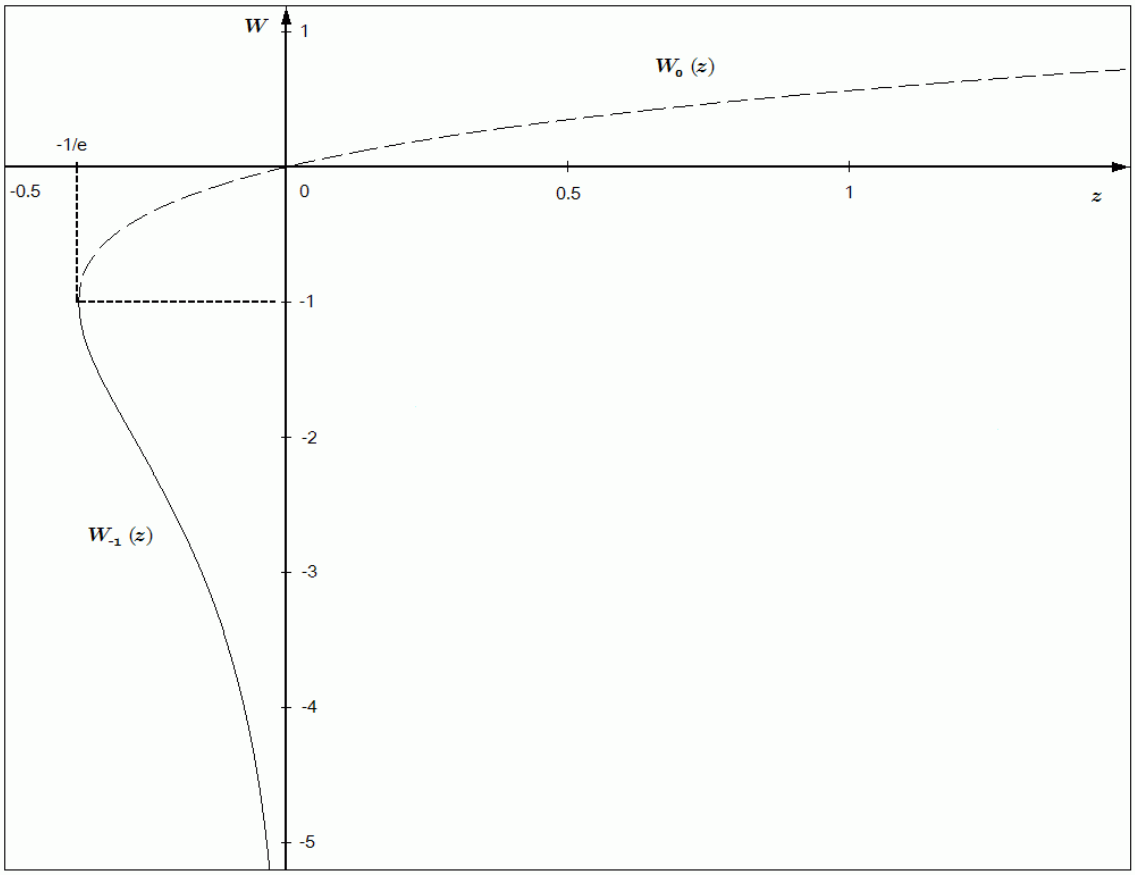

Figure A.1: Two real branches of the Lambert W function [Chung, 2005]

Appendix B

Actuator Properties and Specifications

B.1 Introduction

The following provides key actuator properties and data.

B.2 Magnetic Data

Linear relative permeabilities for the back iron leg, μ_{irnlg} and root portions, μ_{irnrt} and armature, μ_{arm}, are estimated from the induction curves for the respective materials as plotted in Figures B.1 and B.2. Since the linear permeability of steel is approximately 1000 times greater than air, the steel material properties are expected to be of little significance in the inductance calculation at large air gaps (or prior to the onset of saturation). Upon material saturation, the steel permeability is the same as free space, μ_0 or air, and hence the reluctance of the steel flux path lengths become as significant as the air gaps. Saturation is expected to occur at relatively large excitation levels and small air gaps, as it is at those operating points where the magnetic field intensity will be greatest.

Table B.1 lists pertinent results of LPM fitting and manufacturer material data for both opener and closer magnets. The armature and core are made from 0.3 mm thick sheets of silicon steel alloy. The material is provided by Vacuumschmelze Hanau and

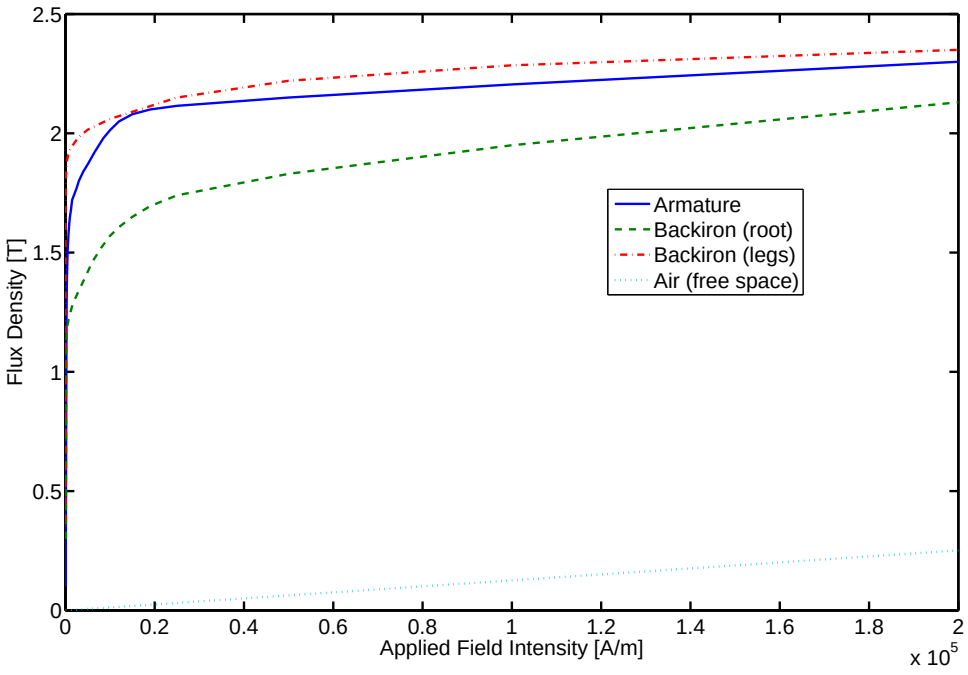

Figure B.1: Induction curves of the various materials used in the hinged actuator magnetic path (large field)

their respective trade names are VX17.1 and ORSI H100-30.

B.3 Mechanical Data

The parameters for the spring mass and gas force models are derived through measured and system identification techniques. The following sections provide a brief summary of the techniques used to measure key parameters. All relevant parameters are listed in Table B.2.

B.3.1 Torsion Bar Force Measurement

As part of the actuator performance evaluation, the torsion bar force as a function of armature position was measured. Figure B.3 illustrates the measured torsion bar response.

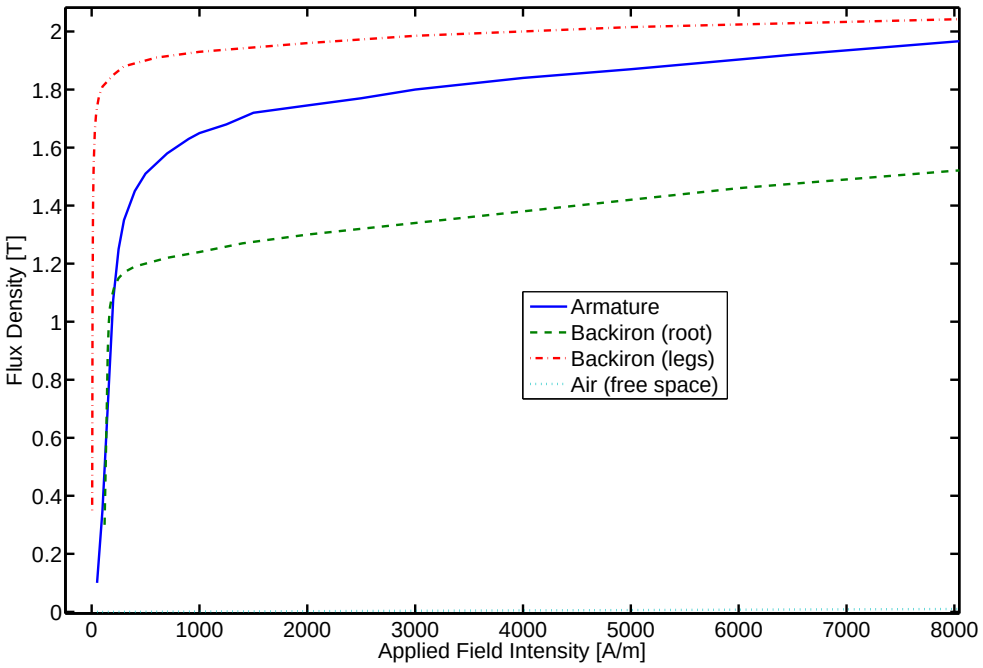

Figure B.2: Induction curves of the various materials used in the hinged actuator magnetic path (small field)

B.3.2 Testbench System Identification

A greybox model of the mechanical system was created with MATLAB's System Identification Toolbox [Ljung, 1987, Ljung, 2004] to identify the effective moving mass, spring stiffness, viscous damping and spring pre-load parameters. The actuator is closed then released and the unforced position and velocity response data are recorded. Three sets of data are collected for both a 'cold' and 'warm' operating condition. In the 'cold' case, the free response is recorded after being unused for 24 hrs. In the 'warm' case, the actuator is run for approximately 3000 cycles immediately before recording the response. For each operating case, two data sets are used to generate predictive error method models. Upon which, the model performance is contrasted with the third data set as shown in Figures B.4 and B.5. The proposed mechanical model appears to be a valid with a minimum agreement of approximately 97% among

Table B.1: Magnetic and Electric Lumped Model Parameters

Parameter	Opener	Closer
ψ [Wb]	0.1354	0.1184
β [m/A]	7.6801×10^{-5}	5.7479×10^{-5}
κ [m]	4.1042×10^{-3}	4.0700×10^{-3}
α [A^{-1}]	8.3263×10^{-3}	3.5562×10^{-3}
Resistivity [Ωm]		
Armature	5.0×10^{-3}	5.0×10^{-3}
Core	2.0×10^{-3}	2.0×10^{-3}
Coil (copper)	3.0×10^{-8}	3.0×10^{-8}
R [Ω]	0.51	0.46
ℓ_m [m]	19.4×10^{-3}	20.8×10^{-3}
N_{fc} [turns]	10	10
N_{ec} [turns]	50	50

the various data sets when contrasted with validation data. It is observed that the parameter that varied most significantly was friction with an increase of 5.9% from the cold to the warm operating conditions.

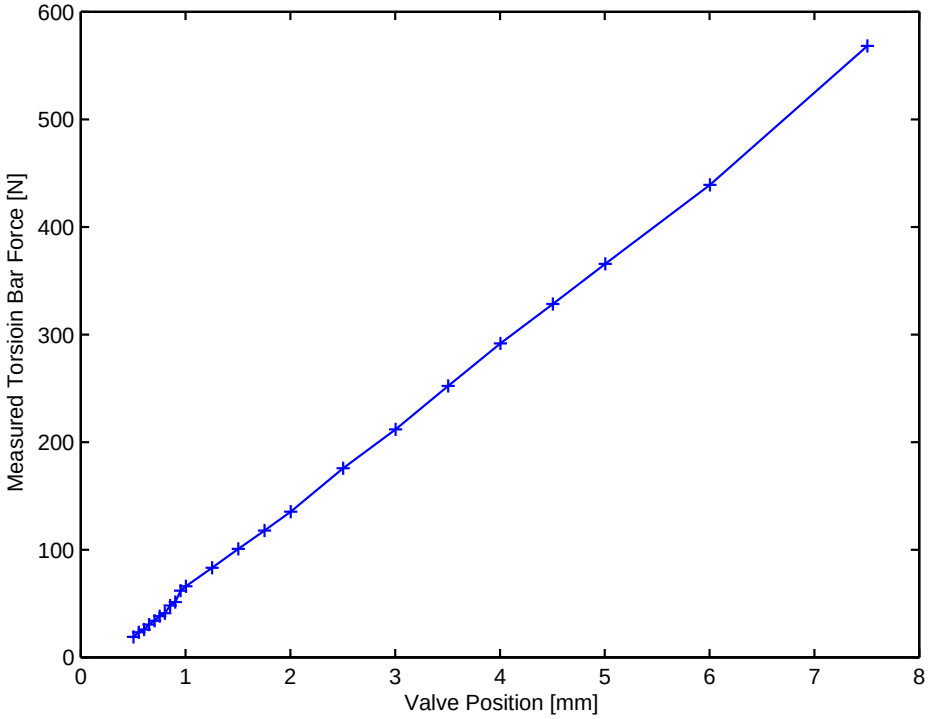

Figure B.3: Torsion Bar Force Exerted on Valve Vs. Valve Position

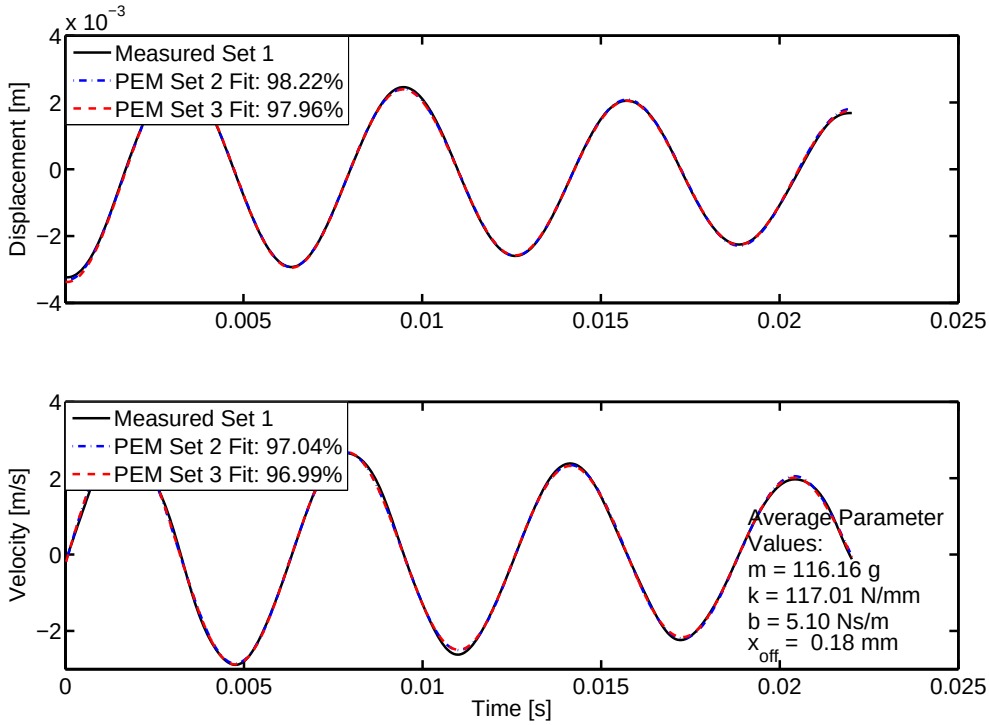

Figure B.4: Measured and predicted response during 'cold' operation

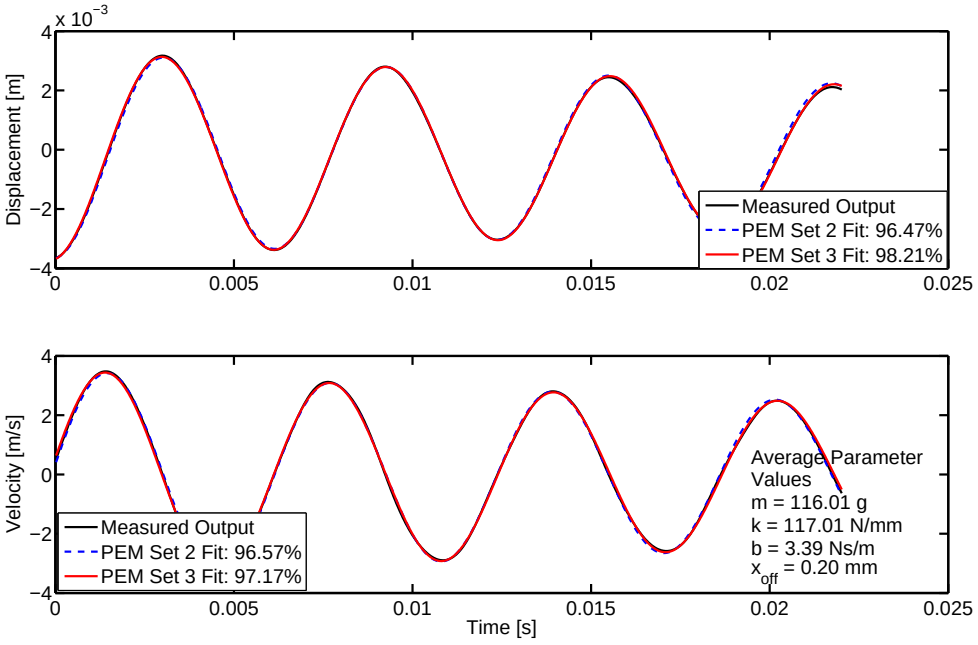

Figure B.5: Measured and predicted response after approximately 3000 cycles

Table B.2: Mechanical Lumped Model Parameters

Parameter	Opener	Closer
m [kg]	0.116	
m_v [kg]	0.037	
I_o [kg m^2]	6.190× 10^{-5}	
b [Ns/m]	3.390	
b_v [Ns/m]	1.700	
$\hat{b}$ [Nsm/rad]	0.010	
k [N/m]	117.010× 10^3	
k_v [N/m] [Ωm]	40.000× 10^3	
$\hat{k}$ [Nm/rad]	112.000	
F_v [N]	23.402	
S [m]	8.00× 10^{-3}	
ℓ_v [m]	38.0× 10^{-3}	
A_v [m^2]	5.309 x 10^{-4}	-
C_d [-]	0.9	-
C_{gf} [-]	0.8	-
c_1 [-]	0.997	-
c_2 [1/m]	31.875	-
c_3 [1/m^2]	-11437.500	-

Appendix C

Program and Data File Summary

C.1 Introduction

The following lists all model, command, program and data files that were used and generated over the course of this work.

C.2 ANSYS Static Command and Result Files

Table C.1: ANSYS static command and result files

File Description	File Name
2D armature geometry used by ANSYS macro files	armature.igs
2D opener geometry used by mopnrmac.tex	obkirn.igs
2D opener geometry used by mclsrmac.tex	cbkirn.igs
Pro/E file used to create 2D geometry files	ansyssection.prt
ANSYS master command file (opener)	mopnr.tex
ANSYS master command file (closer)	mclsr.tex
ANSYS macro command file (opener)	mopnrmac.tex
ANSYS macro command file (closer)	mclsrmac.tex
Output torque result file (opener)	torque1op.res
Output force in x-direction result file (opener)	forcex1op.res
Output force in y-direction result file (opener)	forcey1op.res
Output flux result file (opener)	flxopen.res
Output torque result file (closer)	torque1cl.res
Output force in x-direction result file (closer)	forcex1op.res
Output force in y-direction result file (closer)	forcey1op.res
Output flux result file (closer)	flxclose.res
MATLAB file used to process ANSYS result files	linpost.m
MATLAB output ANSYS results file (opener)	opentab.m
MATLAB output ANSYS results file (closer)	clostab.m
MATLAB LPM parameter fitting script (opener)	openerparam.m
MATLAB LPM parameter fitting script (closer)	closerparam.m
MATLAB Model script called by nlinfit.m	nlinforfit.m

C.3 ANSYS Transient Command and Result Files

Table C.2: ANSYS transient command and result files

File Description	File Name
ANSYS master command file (opener)	mopnrtrans.tex
ANSYS macro command file (opener)	mopnrtransmac.tex
ANSYS transient result file (opener)*	transopnr_X42VXXXmm.rst

$*$ - transopnr_42VXXXmm represents the air gap in millimeters $\times 10^2$ for the corresponding experimental input.

C.4 Simulink Models and Parameter Files

Table C.3: Simulink lumped parameter model files

File Description	File Name
Simulink parameter file for all models	param.m
Simulink full dynamic model	fullsim.mdl
Simulink simplified landing control model	simpland.mdl
Simulink hybrid and LPM transient magnetic model	transientcomp_simple.mdl
Exhaust valve opening simulation results files*	fdfwdflxFBXXbar_rwTB_X.mat
Exhaust valve opening simulation results files**	fdfwdflxFBXXbar_rwEXXXXrpm_X.mat

$*$ - fdfwdflxFBXXbar_rwTB_X represents the EVO pressure and case number.

$**$ - fdfwdflxFBXXbar_rwEXXXXrpm_X.mat represents the EVO pressure, simulated engine speed and case number.

C.5 Trajectory Optimization Files

Table C.4: MATLAB files used for generating landing control reference trajectories

File Description	File Name
Main script (opener)	trajgen.m
Main script (closer)	trajgen_cl.m
Open loop current output function (opener)	nc.m
Open loop current output function (opener)	nc_cl.m

C.6 Material Testing Machine Experimental Program and Data Files

In all files, the following signals are recorded: crosshead position (0.5"/V), small load cell (51lb/V), large load cell (40lb/V), commanded opener coil current, actual opener coil current (0.2A/V), opener coil voltage (0.2V/V), opener sensing coil signal (integrated) and H-bridge TTL switch signals. $*$ - s_25_XX_XXX represents a 25 ms step

Table C.5: Material testing machine experimental and raw fata files

File Description	File Name
ControlDesk experiment file	...\MTScurrent\MTSDataAcquisition.cdx
ControlDesk interface layout file	...\MTScurrent\test.lay
dSPACE make file (to be compiled)	...\MTScurrent\fr.mk
Variable mapping file	...\MTScurrent\fr.trc
Compiled dSpace Executable File	...\MTScurrent\fr.ppc
Most recent parameter settings file	...\MTScurrent\mtspar2.par
Control program Files	...\MTScurrent\src\$*$.c
Steady state raw data files *	...\step\s_25_XX_XXX.mat
Transient voltage input raw data files **	...\impulse\i_XX_XXX_XXX.mat
Sinusoidal current input raw data files ***	...\sinusoid\f_XX_XXX_XXX.mat
Armature motion raw data files †	...\sinusoid\m_XXX_XX_XXX_XX_a.mat

input at a current level of XX amps and XXX indicating air gap in mm $\times 10^2$.

$**$ - i_XX_XXX_XXX represents the switched voltage level, input duration in ms $\times 10^2$ and air gap in mm $\times 10^2$.

$***$ - f_XX_XXX_XXX represents the switched voltage level, current input frequency in kHz $\times 10^2$, mean current level amps and air gap in mm $\times 10^2$.

†- m_XXX_XX_XXX_XX_a represents the armature amplitude in mm $\times 10^2$, displacement frequency in Hz, minimum air gap in mm $\times 10^2$ and the current input in amps. A suffix of '_a' indicates the armature is moving away from the pole face during recording, otherwise it is moving towards it.

C.7 Testbench Experiment and Data Files

In all files, the following signals are recorded: laser position (1.00mm/V), pressure transducer (9psi/V), reconstructed position, commanded opener feedforward coil current, estimated position, estimated velocity, estimated gas force, actual coil currents (0.2A/V), sensing coil signals (integrated), analog integrator reset signal, control state, CPU task execution time and H-bridge TTL switch signals. Older data files also contain recorded coil voltages (0.2V/V). Caution should be used in interpreting such signals as they may be erroneous due to aliasing since both the sampling and PWM carrier frequencies are at a rate of 50KHz. As a result, the commanded switch signals are better indicators of coil voltage as they are control outputs, not sampled inputs. $*$ - XXXX represents the emulated engine rpm, X indicates the EVO pressure in bar and XX indicates the data set number.

$**$ - XbarXbar indicates the respective minimum and maximum EVO pressure and XXXX is the emulated rpm with X indicating the data set number.

Table C.6: Testbench experimental and raw data files

File Description	File Name
ControlDesk experiment file	...\dSPACECode\fluxrev5\ValveControl3a.cdx
ControlDesk interface layout files:	...\dSPACECode\fluxrev5\plotters.lay ...\dSPACECode\fluxrev5\control.lay ...\dSPACECode\fluxrev5\anschwingen.lay
dSPACE make file (to be compiled)	...\dSPACECode\fluxrev5\fr.mk
Variable mapping file	...\dSPACECode\fluxrev5\fr.trc
Compiled dSpace Executable File	...\dSPACECode\fluxrev5\fr.ppc
Most recent parameter settings file	...\dSPACECode\fluxrev5\bk1_hand_flt4.par
Control program Files	...\dSPACECode\fluxrev5\src*.c
Landing control with open-loop feedforward files *	flatnessXXXXrpmXbar_XX.mat
Nominal data files with disturbance observer *	flxflataff_XXXXrpm_Xbar_XX.mat
Switched pressure data files **	dp_XbarXbarXXXXrpm_X.mat

C.8 Primary Testbench Control Program Files

The following lists the primary C program files that contain the key feedforward, estimation, position reconstruction and landing control algorithms.

Table C.7: Primary testbench control program files

File Description	File Name
Task manager	tasks.c
Control state manager (state machine)	control.c
Data acquisition, gas pressure controller and flux-based reconstruction	hw_inter.c
FEA data for flux-based position measurement	fluxdat.h
Feedforward and landing controllers	ctrl_traj.c
State and disturbance estimation	filter.c

C.9 Primary Analysis and Postprocessing Files

The following MATLAB files are various scripts used to help automate the data process, plotting and analysis of the material testing machine and testbench results.

Table C.8: Files and scripts used to compile and analyze experimental results

File Description	File Name
Analog integrator drift fitting and plots	drftcalc.m
Material testing machine static data processing and plotting	stplt.m
Multiple cycle data segmenter and statistical analysis	flatVaffmultipressplot.m
Simple landing control simulation results plotter	simplandplot.m
Gas force model comparison and plotting	press_comp_plt.m
Flux-based position sensor sensitivity analysis	fluxsens.m
System ID main script	mechid.m
System ID greybox model file	sprngms.m
System ID results plotter	sysidplot.m